WARSAW UNIVERSITY OF TECHNOLOGY

SCIENTIFIC DISCIPLINE IN CHEMICAL SCIENCES

FIELD OF EXACT AND NATURAL SCIENCES

Doctoral dissertation

M.Sc. Eng. Claudia Janeth LIMACHI NINA

Sustainable and green batteries: Fluorine-free Lithium-ion cells

Supervisors

Dr. hab. inż. Leszek Niedzicki

Prof. Dr. Michel Armand

WARSAW 2024

A mi familia: a mis padres, Martín y Petrona, y a mis hermanitas, Paola y Yessica. Su amor incondicional, ejemplo, apoyo y confianza en mí han sido mi mayor fuente de fortaleza. Son mi inspiración constante.

To Marek, for his unwavering support and patience throughout this journey. Your encouragement and understanding have been truly invaluable to me.

ACKNOWLEDGMENTS

I would like to express my deepest gratitude to everyone who supported me throughout my PhD journey. First and foremost, I am profoundly thankful to my supervisors, Prof. Michel Armand and Prof. Leszek Niedzicki, for their enduring support and mentorship. A special thank you to Prof. Władysław Wieczorek for his invaluable assistance and warm welcome. His support has made a significant difference. A heartfelt thanks goes to Marta Cabello for both her personal and scientific support. I feel incredibly fortunate to have had the opportunity to work with and learn from all of you. I truly appreciate all you have done.

I would also like to extend my appreciation to Prof. Christian Masquelier for allowing me to join such an inspiring community. The chance to learn and grow within this environment was truly a dream come true. My gratitude to Louise Vrand and Béatrice Messana for their endless assistance and great organization.

To my friends, you made this journey far more wonderful than I could have ever imagined. Thank you to Klaudia, Aleksandra (Ola), Maciej, Mariana, Armando, mi hermano Jazer, Nail, Pempa, and Agin. Your friendship and inspiration meant the world to me. I am also amazingly thankful to Lian, Mattia, Yawen, Kushbu, Oscar, Anu, Cleo, Athira, Miguel M., Stiven, Amna, Ali, Andrea, Susanna, and Michał. The conversations during lunch, weekend plans, and hiking trips while in Vitoria made my experience memorable. A special note of appreciation to the entire prototyping group at CIC EnergiGUNE—Guillermo, Silvia, Nerea, Javier, Nastasiya, Maia, June, and Idoia—your support and kindness were indeed valuable.

I want to express my sincere gratitude to everyone involved in the DESTINY program. It has been an incredible opportunity to meet and learn from such an exceptional group of professors and colleagues.

Thank you all, from the bottom of my heart, for being a part of this extraordinary journey. Your kindness and support have made this experience truly special and meaningful.

ABSTRACT

Current commercial LIBs rely on fluorinated salts, solvents, and additives, which pose significant environmental challenges. Removing fluorine from LIBs is critical, not only to minimize environmental hazards but also to simplify recycling and enhance sustainability. Fluorinated compounds, such as lithium hexafluorophosphate (LiPF$_6$), dominate electrolyte formulations despite releasing harmful substances like HF under certain conditions. While fluorine is crucial for performance, alternative fluorine-free salts, such as lithium 1,1,2,3,3-pentacyanopropenide (LiPCP) are proposed in this PhD Thesis. LiPCP offers excellent thermal and chemical stability, making it a viable replacement in battery electrolytes. In parallel, the use of fluorine-free binders, like carboxymethyl cellulose, and styrene-butadiene rubber offers further improvements in battery performance, cost, and recyclability. Therefore, this research investigates the development of fluorine-free electrolytes compatible with aqueous-processed electrodes. Developed cathodes include cobalt-free cathode materials such as lithium iron phosphate (LFP) and lithium manganese-iron phosphate (LMFP). Anodes are composed of synthetic graphite (SG) and silicon oxide composites (SOX). Such materials allow us to address the environmental concerns and resource availability of lithium-ion batteries.

Properties of the LiPCP-based electrolyte was screened with various organic carbonate solvents, and the optimal mixture was found to be 30:70 wt.% EC:DMC. It achieved conductivities of 9.6 mS·cm^{-1} for 0.8m LiPCP and 12.3 mS·cm^{-1} for 1m LiPF$_6$ at 20°C. Vinylene carbonate was selected as a SEI stabilizing additive, and the electrolyte demonstrated stability up to 4.4 V vs. Li$^+$/Li.

Optimized LiMn$_{0.6}$Fe$_{0.4}$PO$_4$ achieved 70 mAh·g^{-1} at C/10 after 40 cycles at 87:10:3 (LMFP:KB:CMC) ratio. This cathode was not investigated further due to insufficient performance.

LFP slurry formulations were improved from 87:10:3 (LFP:KB:CMC) to 93.5:5:0.75:0.75 (LFP:KB:CMC:SBR), increasing the solid content and improving areal capacity to ~2 mAh·cm^{-2}. For synthetic graphite electrodes, slurries were improved from 95:3:2 (SG:CB:CMC) to 95:2:1:2 (SG:C-45:CMC:SBR) resulting in mass loading of ~2.3·mAh·cm^{-2} and a N/P ratio of 1.1–1.4. The silicon oxide composite electrodes were also refined, improving slurry composition to 92:6:1:1 (SOX:C-45:CMC:SBR) and achieving mass loading of ~2.4 mAh·cm^{-2}.

Conductivity measurements showed that electrode conductivity decreased with increasing thickness. The density and mechanical stability improved after calendering. The

LFP/synthetic graphite configuration was tested in both coin and pouch cells. In coin cells, specific capacity averaged 60 mAh·g^{-1} at C/10 and an N/P ratio of 1.18. Pouch cells exhibited an initial specific capacity of 84 mAh·g^{-1}, stabilizing at 63 mAh·g^{-1} after 64 cycles. In contrast, the LFP/silicon oxide composite system showed lower capacities and worse coulombic efficiency.

Galvanostatic cycling in two- and three-electrode cells revealed potential instability of the LiPCP electrolyte at low voltages. Reduction occurred below 2 V, likely contributing to fading capacity due to crystal formation on the electrode surfaces. While LiPCP reduces the formation of harmful fluorinated species, further optimization of solvent mixtures or electrolyte additives is needed to enhance stability at low potentials.

In summary, this study demonstrates the viability of fluorine-free lithium-ion cells at both laboratory and pre-pilot scales. The electrochemical characterization suggests comparable performance with conventional systems. While offering a more sustainable and environmentally friendly alternative, with enhanced recyclability and potential for wider scalability.

Keywords: Fluorine-free lithium salts, green chemistry, sustainability, aqueous electrodes; scaling-up Li-ion cells.

ABSTRAKT

Komercyjne baterie litowo-jonowe zawierają fluorowane sole, rozpuszczalniki i dodatki, które stanowią znaczące wyzwanie w kontekście ich przyjazności środowisku. Usunięcie fluoru z ogniw litowo-jonowych jest kluczowe nie tylko ze względu na minimalizację zagrożenia dla środowiska, ale również w celu uproszczenia recyklingu baterii. Fluorowane związki, takie jak heksafluorofosforan litu ($LiPF_6$) dominują wśród składów elektrolitów pomimo iż pod pewnymi warunkami mogą generować niebezpieczne związki np. HF. Mimo że fluor jest kluczowym pierwiastkiem dla zapewnienia parametrów elektrolitu, bezfluorowa alternatywa, jaką jest 1,1,2,3,3-pentacyjanopropenid litu (LiPCP), została zaproponowane w tej rozprawie doktorskiej. LiPCP zapewnia doskonałą stabilność termiczną i chemiczną, co potencjalnie pozwala tej soli zastąpić $LiPF_6$ w elektrolitach bateryjnych.

Jednocześnie wykorzystanie bezfluorowych lepiszczy, takich jak karboksymetyloceluloza (CMC) czy kauczuk butadienowo-styrenowy (SBR) pozwala na dalszą poprawę wydajności ogniwa, jego kosztu i podatności na recykling. Z tego względu te badania obejmują opracowanie bezfluorowych elektrolitów, które są kompatybilne z elektrodami wytwarzanymi z użyciem wody jako rozpuszczalnika. Wśród opracowanych katod są elektrody nie zawierające kobaltu takie jak fosforan litowo-żelazowy (LFP) i fosforan litowo-manganowo-żelazowy (LMFP). Anody są na bazie syntetycznego grafitu (SG) oraz kompozytów z tlenkiem krzemu (SOX). Zastosowanie takich materiałów pozwala rozwiązać problemy wpływu na środowisko i ograniczeń dostępności materiałów dla ogniw litowo-jonowych.

Wstępne badanie elektrolitu bazującego na LiPCP w różnych kombinacjach węglanów organicznych pozwoliło wyłonić mieszaninę EC:DMC (30:70 w/w) jako optymalną. W tej mieszaninie uzyskano odpowiednio 9,6 $mS \cdot cm^{-1}$ dla 0,8m LiPCP oraz 12,3 $mS \cdot cm^{-1}$ dla 1m $LiPF_6$ w 20°C. Węglan winylenu został wybrany jako dodatek stabilizujący SEI, a elektrolit wykazał stabilność elektrochemiczną wynoszącą 4,4 V vs. Li/Li^+.

Zoptymalizowane $LiMn_{0.6}Fe_{0.4}PO_4$ pozwoliło uzyskać 70 $mAh \cdot g^{-1}$ przy prądzie C/10 po 40 cyklach przy składzie 87:10:3 (LMFP:KB:CMC). Ta katoda nie była dalej badana ze względu na niezadowalającą wydajność.

Kompozycja masy elektrodowej z LFP została poprawiona z 87:10:3 (LFP:KB:CMC) do 93,5:5:0,75:0,75 (LFP:KB:CMC:SBR), zwiększając zawartość materiału aktywnego i podnosząc pojemność do ~2 $mAh \cdot cm^{-2}$. Dla syntetycznego grafitu skład masy został poprawiony z 95:3:2 (SG:CB:CMC) do 95:2:1:2 (SG:C-45:CMC:SBR), co przełożyło się na

pojemność wynoszącą ~2,3 mAh·cm^{-2} i zapewniającą stosunek N/P równy 1,1-1,4. Katody z kompozytu z tlenkiem krzemu również zostały dopracowane uzyskując pojemność 2,4 mAh·cm^{-2} przy składzie 92:6:1:1 (SOX:C-45:CMC:SBR).

Pomiary przewodności elektronowej pokazały, że przewodność elektrod maleje z ich grubością. Kalenderowanie natomiast przekłada się na poprawę gęstości i właściwości mechanicznych elektrod. Układ elektrod SG/LFP został przetestowany zarówno w ogniwach guzikowych jak i w ogniwach kieszeniowych. Dla ogniw guzikowych przy prądzie C/10 i stosunku N/P równym 1,18 uzyskano średnią pojemność wynoszącą 60 mAh·g^{-1}. W ogniwach kieszeniowych uzyskano pojemność 84 mAh·g^{-1}, która spadła i ustabilizowała się po 64 cyklach na poziomie 63 mAh·g^{-1}. Układ SOX/C/LFP wykazał gorszą pojemność i niższą wydajność kulombowską od układu SG/LFP.

Galwanostatyczne ładowanie-rozładowanie ogniw w układach dwu- i trójelektrodowych ujawniło niestabilność LiPCP przy niskich potencjałach. Poniżej ok. 2 V zaobserwowano redukcję, która prawdopodobnie przyczyniła się do nieodwracalnego spadku pojemności oraz wzrostu kryształów na powierzchni elektrod. Chociaż LiPCP eliminuje powstawanie szkodliwych związków fluoru, dalsza optymalizacja mieszanin rozpuszczalników oraz składu dodatków jest niezbędna do poprawy stabilności przy niskich potencjałach.

Podsumowując, wykonane badania dowodzą możliwości uzyskania bezfluorowych ogniw litowo-jonowych, zarówno w skali laboratoryjnej jak i pre-pilotażowej. Elektrochemiczna charakteryzacja zbadanych systemów sugeruje wydajność porównywalną do systemów komercyjnych. Jednakże oferują one bardziej zrównoważoną i przyjazną środowisku alternatywę z lepszym potencjałem recyklingu i skalowalności.

Słowa kluczowe: bezfluorowe sole litowe, zielona chemia, zrównoważony rozwój, wodne elektrody, powiększanie skali ogniw litowo-jonowych

LIST OF ABBREVIATIONS

AM	Active material
AM_f	Active material pH during slurry preparation at the end
AM_o	Active material pH during slurry preparation at the beginning
AN	Acetonitrile
C45	Super C45 carbon black
CM	Conductive material/conductive additive
CMC	Carboxymethyl cellulose
CMR	Carcinogenic, mutagenic, and toxic to reproduction
CV	Cyclic voltammetry
DEC	Diethyl carbonate
DMC	Dimethyl carbonate
EAC	Environmentally assisted cracking
EC	Ethylene carbonate
EIS	Electrochemical impedance spectroscopy
EMC	Ethyl methyl carbonate
EPA	Environmental protection agency
ES	Energy storage
EV	Electric vehicle
GCD	Galvanostatic charge discharge
GITT	Galvanostatic intermittent titration technique
KB	Ketjenblack EC600JD conductive carbon black
LFP/ $LiFePO_4$	Lithium iron phosphate
LFP_f	LFP pH during slurry preparation at the end
LFP_o	LFP pH during slurry preparation at the beginning
$LiAlCl_4$	Lithium tetrachloroaluminate
$LiAsF_6$	Lithium hexafluoro arsenate
LIB	Lithium-ion battery
$LiB(C_4H_9)_4$	Lithium tetrabutylborate
$LiB(C_6H_5)_4$	Lithium tetraphenylborate
$LiB(CH_3)_4$	Lithium tetramethylborate
LiBETI	Lithium bis(perfluoroethanesulfonyl)imide
$LiBF_4$	Lithium tetrafluoroborate
LiBOB	Lithium bis(oxalato)borate
$LiC(SO_2CH_3)_3$	Lithium tris(alkanesulfonyl)methide
$LiClO_4$	Lithium perchlorate
LiDFOB	Lithium difluoro(oxalato)borate
LiFOP	Lithium tetrafluoro(oxalato)phosphate
LiFSI	Lithium bis(fluorosulfonyl)imide
LiPCP	Lithium 1,1,2,3,3-pentacyanopropenide
$LiPF_6$	Lithium hexafluorophosphate
$LiSO_3CF_3$	Lithium trifluoromethanesulfonate

LiTBP	Lithium tris(1,2–benzenediolato(2)-O,O′)phosphate
LiTFSI	Lithium bis(trifluoromethanesulfonyl)imide
LiTOP	Lithium tri(oxalato)phosphate
LMFP/ $LiMn_{1-x}Fe_xPO_4$	Lithium manganese iron phosphate
L_n	Thickness number, n
LSV	Linear sweep voltammetry
LTO/ $Li_4Ti_5O_{12}$	Lithium titanate
N/P	Negative/positive capacity ratio
NG	Natural graphite
NMP	N-methyl-2-pyrrolidone
OCV	Open circuit voltage
PC	Propylene carbonate
PFAS	Per- and polyfluoroalkyl substances
PTFE	Poly(tetrafluoroethylene)
PVdF	Poly(vinylidene difluoride)
RLB	Rechargeable lithium batteries
rpm	Revolution per minute
SBR	Styrene butadiene rubber
SC	Supercapacitor
SEI	Solid electrolyte interface
SEM	Scanning Electron Microscope
SG	Synthetic graphite
S_n	Slurry number, n
SOX / SiOx/C	Silicon oxide composite
Super P	Super P carbon black
TM	Transition metal
V	Potential/Voltage (volt)
VC	Vinylene carbonate
VEC	Vinylethylene carbonate

TABLE OF CONTENTS

1. IMPORTANCE AND OBJECTIVES OF DEVELOPING GREEN AND MORE SUSTAINABLE LITHIUM-ION CELLS

1.1. General background

Energy storage technologies are pivotal in modern energy systems, balancing supply and demand, and ensuring reliability. The spectrum of these technologies includes mechanical storage (like pumped hydro and flywheels), thermal storage, and electrochemical storage, among others [1]. Among electrochemical solutions, lithium-ion batteries (LIBs) have emerged as the leading technology due to their high energy density, efficiency, and long cycle life. LIBs store energy through reversible electrochemical reactions involving lithium cations moving between the anode and cathode. This technology is widely used in portable electronics, electric vehicles (EVs), and grid storage applications [2, 3].

The development of LIBs traces back to the 1970s when initial research explored the potential of LIBs. In 1991, Sony commercialized the first LIB, marking a significant milestone in portable energy storage. This breakthrough resulted from the combined work of John B. Goodenough, Stanley Whittingham, and Akira Yoshino, who laid the foundation with their discoveries in materials and electrochemical principles [4, 5]. Goodenough's development of the cobalt oxide cathode and Yoshino use of carbon-based anodes were crucial innovations [6]. Over the decades, continued advancements in electrode materials, electrolyte formulations, and manufacturing processes have significantly improved the energy density, safety, and cost-effectiveness of LIBs, leading to their widespread adoption in various sectors [7].

Current advancements in LIB technology focus on increasing energy density, reducing costs, and enhancing safety. Innovations such as solid-state electrolytes, silicon anodes, and advanced cathode materials are at the forefront, promising better performance and longer lifespans. However, conventional LIBs face environmental challenges, including the extraction and processing of raw materials like lithium, cobalt, and nickel, which have significant ecological and social impacts [8, 9]. Additionally, the recycling of LIBs remains a complex and costly process due to the current battery chemistry and configuration, contributing to electronic waste considerably [10, 11]. Efforts are being made to develop green and sustainable battery chemistries and improve recycling technologies to mitigate these environmental issues and ensure the sustainable growth of the energy storage sector.

1.2. Problem statement

Current commercial LIBs use fluorinated salts, solvents, and electrolyte additives. The main hazards of fluorinated compounds include potential toxicity, negative environmental impact, and they complicate the recycling. The most frequently used commercial batteries' electrolyte is the fluorinated salt lithium hexafluorophosphate ($LiPF_6$), which contains $75 \cdot wt.\%$ of fluorine. The PF_6^- anion can release toxic substances like HF and POF_3 in the presence of even traces of moisture, high temperatures, or acids [12-14].

Fluorinated compounds are present not only in electrolytes but also in electrodes, particularly poly(vinylidene difluoride) (PVdF), which is used in electrode fabrication as a binder, which involves the use of a hazardous, teratogenic and irritating solvent N-methyl-2-pyrrolidone (NMP) solvent, both used in the most common commercial electrodes [15-18].

Furthermore, the growing awareness and concern about the environmental and health impacts of per- and polyfluoroalkyl substances (PFAS) have led to significant regulatory actions [19]. For instance, the European Union has proposed a comprehensive ban on all non-essential PFAS by 2025 and across all uses by 2030 [20]. Similarly, the United States Environmental Protection Agency (EPA) has been working on regulations to limit PFAS in industrial uses. Canada is also working with initiatives to restrict these substances under the Canadian Environmental Protection Act [19]. These bans emphasize the urgent need for developing sustainable alternatives in various industries, including energy storage. In this context, the development of fluorine-free batteries becomes not only a technological advancement but also a crucial step towards a safer and more sustainable society [19, 20].

The new generation of LIBs targets sustainable and greener chemistries, with a special focus on cobalt-free cathode materials [21, 22]. Critical raw materials such as Cobalt (Co) and Nickel (Ni) are classified as carcinogenic, mutagenic, and toxic to reproduction (CMR) [23]. Cobalt, in particular, is a major cost driver and raises significant moral and environmental concerns due to questionable mining conditions. There are, however, alternative electrode materials that do not include critical resources. Phospho-olivine-type cathode materials like $LiFePO_4$ (LFP) and $LiMn_xFe_{1-x}PO_4$ (LMFP) with $0 \leq x \leq 1$ are considered eco-friendly since they are abundant elements [24, 25]. Furthermore, the high structural stability of the polyanionic phosphate network and the relatively low operational voltage window, which prevents unwanted parasitic reactions of the battery electrolyte, allow long cycle and span life for olivine-based LIBs [25].

The current most widely used commercial anodes in LIBs are primarily based on natural or synthetic graphite (SG). While graphite has proven reliable, it faces significant limitations in terms of energy density, which restricts the overall capacity of the battery. Furthermore, the extraction and processing of natural graphite (NG) pose serious environmental concerns, including habitat destruction, pollution from mining operations, and high energy consumption during purification. SG, although more controllable in production, is energy-intensive to manufacture, contributing to a larger carbon footprint. Additionally, the relatively modest capacity of graphite (372 mAh·g^{-1}) limits the performance improvements needed to meet the growing demands of electric vehicles (EVs) and grid energy storage [26-28].

In contrast, SG and silicon oxide composite (SOX) offer an advanced solution to these challenges. Silicon oxide (SiO$_x$) significantly boosts energy density due to its higher theoretical capacity (up to 2000 mAh·g^{-1}), enabling longer driving ranges in EVs and more efficient energy storage. The use of silicon oxide also reduces reliance on vast amounts of graphite, potentially alleviating some environmental pressures associated with graphite mining. Furthermore, this composite approach mitigates silicon natural volume expansion during charge/discharge cycles, which leads to structural damage and performance degradation. SG and SOX not only enhance battery efficiency, and stability, but also contribute to reducing the environmental impacts of battery production and extending battery lifespans—ultimately making LIBs more sustainable and efficient for the future [29-31].

1.3. Research objectives

This doctoral project aims to study a novel fluorine-free lithium salt for electrolyte preparation, find, fabricate and optimize compatible aqueous-processed electrodes (both anode and cathode), optimize the fluorine-free lithium-ion (Li-ion) cell and assembly coin and pouch cells, to demonstrate the viability at larger scale of the novel fluorine-free electrolyte for aqueous-processed olivine-type phosphate cathode materials, SG, and silicon oxide/carbon composite (SOX) anode materials. In a sentence, this research aims to design, optimize and scale up a fluorine-free Li-ion cell, which key factors are the performance and sustainability.

Key tasks to achieve the main objectives involve:

- Preparation and determination of the organic carbonate solvents for the electrolyte, conductivity measurements of electrolyte solutions at various concentrations and temperatures by means of the electrochemical impedance spectroscopy (EIS).

- Cyclic voltammetry studies to find electrode/electrolyte compatibility. Fabrication and optimization of aqueous-processed electrodes for coin and pouch cells assembly.

- Measurements of viscosity and pH and the evaluation of the electrode resistance and developing electrode sheets through optimization of their composition, mass loading and electrode thickness (wet and dry). Electrochemical characterization for determination of optimum full cells for scaling-up to pouch cells.

- Surface characterization on the electrodes of the pouch cells before and after cycling.

- For the fabrication of electrodes for pouch cells, main tasks involve preparation of the slurry in a homogenizer, along with casting, calendering, sealing, welding, and electrolyte filling equipment at a pre-pilot scale.

1.4. Research methodology overview

As electrolyte, anode and cathode were prepared within this doctoral project, the fluorine element was removed from all battery components and subsequently, the fluorine-free batteries were manufactured, and their performance was tested. For better understanding and analysis, this research project was divided into 3 parts:

❖ *Characterization and study of the novel electrolyte,* determination of organic carbonate solvents choice and optimal formulation, electrochemical stability window of various electrolyte compositions, and impedance spectroscopy for conductivity determination.

❖ *Electrodes fabrication*, study of various slurry compositions at various binder, conductive materials (conductive additives, conductive agents, CMs), active materials (AMs) ratios. Stability and reversibility of the electrodes prepared through the aqueous-based processes with the optimized electrolyte were investigated through the measurement of cyclic voltammetry. Parameters such as solid content, pH, and viscosity of the slurry; electrode resistance, mass loading (areal capacity), wet and dry thickness of electrodes sheets, and the effect of the calendering were measured.

❖ *Electrochemical and surface evaluation,* to evaluate the fluorine-free Li-ion cell with the optimized electrolyte and electrode determined, galvanostatic cycling aims to study the rate capability in coin-cells, and cycling stability in both, coin and pouch cells. Surface characterization of the electrodes used in pouch cells before and after cycling using SEM/EDX was performed to analyze surface roughness, topography, cracks, and distribution of components on the electrode surface.

2. INTRODUCTION – ENERGY STORAGE

Environment and energy are two key factors that have a direct effect on human being lifestyle [32, 33]. Nowadays one of the main challenges is the so-called energy transition for fighting climate change and reducing global warming due to the huge amount of carbon dioxide released into the atmosphere [34]. The energy transition implies the replacement of fossil fuels such as coal, natural gas, oil by alternative renewable sources of energy: solar radiation, wind, ocean waves, biomass, geo-thermal and hydroelectricity, among others [35]. which represent energy sources that are intermittent and widely spread over the area. Photovoltaic cells and windmills are a very attractive source of energy for electricity production. However, both sources are discontinuous, therefore, energy storage systems are required to supply energy for dark/cloudy or windless periods [36]. Energy storage devices are systems storing some form of energy than can be used later to perform given operations. All forms of energy storage are either potential energy (e.g. capacitive in capacitor/supercapacitor or gravitational in hydroelectric pumped storage), kinetic energy (e.g. rotational in rotating flywheel) or inner energy (e.g. chemical/electrochemical in battery/flow cells or thermal in thermal/solar thermal energy storage), of which the summary is shown in Table 1, [36].

Thus, chemical energy storage is realized by storing various chemical elements able to react when in contact, producing energy from bonding energy differences.

Electrochemical energy storage technology is a technology that converts electric energy and chemical energy into energy storage and releases it through chemical reactions [2].

The society is becoming more dependent on electricity, thus, the development of technologies to store directly or indirectly this secondary energy form will be the key for the twenty-first century to meet the rising demand for modern applications [32].

Furthermore, the importance of considering these systems capable of storing energy is high due to their effect on the economy and the most basic issues in industrialized countries, in the economical, environmental, technological, and political terms.

To meet these requirements, extensive research has been done by developing power sources, such as LIBs, and supercapacitors (SCs) [37].

Chemical	Electrical	Biological
$\Delta G = \Delta H - T\Delta S$ Hydrogen Biofuels Liquid nitrogen Oxyhydrogen Hydrogen peroxide	$E_{p,e} = \dfrac{1}{4\pi\varepsilon_o}\dfrac{Q_1 Q_2}{r}$ Supercapacitor Superconducting magnetic energy storage	Starch Glycogen
Electrochemical	**Mechanical**	**Thermal**
Batteries Flow batteries Fuel cells	$E_P = -\displaystyle\int F dS$ Compressed air Flywheel Hydraulic accumulator Hydroelectric Spring	$\Delta q = \displaystyle\int C_v dT$ Ice storage Molten salt Cryogenic liquid air Seasonal thermal store Solar pond Steam accumulator Fireless locomotive

Table 1.　　Classification of energy storage methods

Living in a transition time towards a carbon-neutral society provides us with various challenges in different disciplines, including the field of electrochemical energy storage. LIBs that are the most common energy storage for electric vehicles, mobile electronic devices and home energy storage, have been commercially available since 1990.

Fluorinated salts, solvents and electrolyte additives for electrolyte preparation are the main components of the electrolyte for current commercial LIBs. Moreover, fluorinated, expensive, and not-easy-to-recycle binders as well as toxic solvents are used for electrode fabrication. Therefore, potential toxicity, negative environmental impact, and difficulties in recycling at the end of LIBs life are the main and most common consequences of fluorinated compound applications [38, 39].

Batteries consist of three main components, namely cathode, anode, and electrolyte [40]. The ionic conductivity of the electrolyte strongly influences LIB performance. It depends on the speed at which lithium cations migrate across the cell and relates to their solvation structure. The choice of solvent can greatly impact both the solvation and diffusivity of lithium cations. The most commonly used salt is $LiPF_6$, which fluorine content is 75% by mass. Due to its poor stability, PF_6^- anion in the presence of moisture, high temperature or acids releases toxic gases such as HF and POF_3. Consequently, it requires the use of special electrolyte additives for scavenging moisture and HF, which increases the battery price [41, 42]. However, the temperature issue is not easily solved so LIBs' upper operation temperature limit is typically 60°C due to $LiPF_6$ instability above that temperature. This is why numerous salts have been developed and reported for use in LIBs in order to substitute $LiPF_6$. For instance, a fluorine-

free lithium salt, that is commercially available and well-known, is lithium perchlorate ($LiClO_4$), which has no fluorine content, exhibits high solubility in aprotic solvents, high conductivity, good electrochemical stability, and acceptable solid electrolyte interface (SEI) layer formation [43]. However, the high oxidation state of the Cl^{VII} atom makes it highly explosive in organic solutions [44]. Other proposed salts so far contain fluorine.

Electrolyte additives are one of the most effective methods for the improvement of LIB performance. The electrolyte additives can facilitate the formation of SEI on the electrode surface Additionally, they can reduce irreversible capacity and gas generation during SEI formation and improve long-term cycling that way. Functional additives can also protect cathode material against dissolution and degradation, as well as improve the physical properties of electrolytes such as ionic conductivity, viscosity, and wettability. In terms of safety, electrolyte additives can reduce the flammability of organic electrolytes, and protect against or increase tolerance towards overcharge [45].

Alternatives to commonly industrially used electrode chemistries for the new generation of LIBs target sustainable and greener growth. Such chemistries are cobalt-free materials for cathodes, and synthetic carbonaceous materials like SG for anodes (instead of the NG, which is mined), [46, 47]. At present, more than 60% of mined cobalt is destined for battery cathodes. With the predicted growth of the battery market, shortages in the supply of cobalt are likely to occur. Such problems may also arise within the supply chain of critical raw materials such as lithium, nickel, and NG. Moreover, the 2023 report from the European Commission shows lists of strategic and critical raw materials, where cobalt and NG have been included since 2020 [48].

The binder material represents around 2–5% of the total mass of the electrode, and it has an important influence on the performance, cost, environmental impact, and recycling possibility of the battery [49, 50]. Currently, binders are not only required to meet bonding characteristics but also to contribute to the better electrode-electrolyte contact by minimizing the resistance, and to the stabilization of the cell during the SEI layer formation. High thermal, chemical and electrochemical stability under extreme conditions is required from the binder [51]. Hence, the development of fluorine-free electrolytes that work with aqueous-processed electrodes represents greener, safer, lower-cost, and straightforward electrode fabrication. Furthermore, it reduces the environmental impact during recycling of the battery components at the end of life by hydrometallurgical or pyrometallurgical processes [13, 52].

3. LITHIUM BATTERIES AND LITHIUM-ION BATTERIES

In the mid of 1960s a new generation of electrochemical systems was developed. Lithium metal foil as the anode and a lithium salt in a nonaqueous solution as the electrolyte were the main components of this new system. Basically, the charge transport consists of a simple reaction where one electron is released through the external circuit and one ion is introduced into the porous structure of the cathode [53, 54].

$$Li \rightarrow Li^+ + e^- \qquad (3.1)$$

Lithium is a very attractive element in the field of energy storage as the lightest metal (molar weight of 6.941 $g \cdot mol^{-1}$ and density 0.51 $g \cdot cm^{-3}$). The specific capacity of lithium metal is 3860 $mAh \cdot g^{-1}$ and the Li^o/Li^+ redox couple has the highest electroactivity with a standard redox potential of –3.04 V against H_2/H^+ (*vs* SHE).

Thus, the voltage of lithium batteries is significantly higher than that of Pb-acid and Ni-metal hydride, due to lithium being the most electropositive element found in nature [55].

Lithium does not exist in the form of pure metal in nature due to very high reactivity with air, nitrogen and water. Lithium is extracted commonly from ore or brine salt-lakes. Lithium batteries are characterized by high specific energy, high efficiency and long life [56].

3.1. Li-ion batteries

In the mid of 1970s secondary lithium cells working with lithium-insertion compounds as positive electrodes were developed [57, 58]. There are two main approaches in the design of rechargeable lithium batteries. The first system involves an insertion compound as positive material and a lithium-metal foil as the negative electrode, it is the so-called lithium-metal battery. The second system, called lithium-ion battery – LIB, consists in working with two open-structured materials as electrodes, where the lithium cations are transported from one electrode to the other during the charge/discharge process. Therefore, LIB does not contain lithium metal, it involves only charged species Li^+ ions, hence the name. LIB contains a high-voltage (cathode) and a low-voltage (anode) electrode hosts versus Li^o/Li^+ redox couple [4].

The principle of a LIB starts with a fresh cell which is assembled in a discharged state. Therefore, in the initial state, the positive electrode framework is full of Li^+, while the anode (most commonly graphite) is empty [32].

During the charging process, Li^+ ions are released from the positive electrode, migrate through the electrolyte and build in the structure of the negative electrode, while electron circulate through the external circuit. Throughout the process, the positive electrode is oxidized losing *x* electrons and the negative electrode is reduced capturing *x* electrons and vice versa for the discharge process [59].

Currently, electrolyte is most often a mixture of alkyl carbonates as solvents (which are aprotic) with lithium hexafluorophosphate salt ($LiPF_6$) to provide ionic conductivity for the lithium cations' transport. The ionic conductivity is achieved by dissolving lithium salts in aprotic solvents [60].

The characteristics of the cathode and the anode components are described in detail in the following chapters, along with binders and solvents, which are also required for electrode fabrication. Table 2 presents a list of the most popular LIB technologies that have been developed so far into mass commercialization [61-63].

Table 2. **Main characteristics of various cathodes for Li-ion battery technologies**

Battery	Energy Density Wh/kg	Cyclability Cycles	Advantages	Disadvantages
LCO	150 – 190	500 – 1000	Widely studied and well-known behaviour, low-self discharge, high discharge voltage	High cost, safety issues, supply of cobalt issues
LMO	100 – 140	1000 – 1500	Highly safe, cobalt-free	Low energy density, Mn dissolution
LFP	90 – 140	Up to 2000	Highly safe, cobalt-free	Low energy density
NCA	200 – 250	1000 – 1500	Low cobalt content	Capacity fade at high temperatures
NMC	140 – 200	1000 – 2000	Low cobalt content	Safety issues at high Ni content

The two electrodes are separated by a porous membrane known as the separator, which is soaked with the liquid electrolyte. The electrolyte is a good ion conductor of lithium cations; however, it is also an electronic insulator, mandatory as any transport of electrons through the electrolyte will result in self-discharge.

Wide research and development effort have been undertaken to achieve a global goal in battery technology, which is the development of LIBs with higher energy density, while keeping the cost lower and lower [64].

4. NONAQUEOUS ELECTROLYTES FOR LITHIUM-ION BATTERIES

There are three main components of a typical battery system: cathode, anode and electrolyte, all of which have a direct effect on electrochemical performance.

The role of the electrolyte on the energy storage field is vital for battery stability, safety, and performance. The synthesis and characterization of new lithium salts have been crucial for the electrolyte development in the last decades. Currently $LiPF_6$ is the most commonly used lithium salt for commercial LIBs working with graphite as the anode.

However, new electrolyte formulations are required for the new LIB-related technologies, such as Si alloy anodes, Li-air, Li-S and the main goal for battery recycling. In this sense, lithium salts for electrolytes either as a substitute for $LiPF_6$ or as an additive are needed to meet the new goals towards greener and more sustainable LIBs [65].

In the 1970s batteries used electrolytes formulations with available lithium salts such as $LiClO_4$, $LiAlCl_4$, $LiBF_4$, $LiPF_6$, and $LiAsF_6$. During that period the main goal was to stabilize the stripping/plating of Li metal [66]. Among these studied salts, $LiPF_6$ was not the best candidate for Li metal batteries [67]. Additionally, $LiPF_6$ was problematic when carbon was used as the anode. $LiPF_6$ was not the most common and viable salt for lithium battery electrolytes until carbon coke replaced Li metal (later replaced by graphite) and the solvents were optimized for the assembly of LIBs commercialized by Sony in 1991 [68, 69].

Initially efforts were made to develop anions for electrolyte lithium salts based on stronger superacids. These were defined as more acidic than mineral Brønsted acids or more acidic than sulfuric acid, based on Gillespie. The stronger the acidity, the weaker the coordination of the anions is with the associated protons (H^+ cations) [36, 70].

The most well-known acid compounds include:

$$HF\ (365.7) < HNO_2\ (330.5) < HCl\ (328.0) < HBr\ (318.2) < HNO_3$$
$$(317.8) < HI\ (309.3) < H_2SO_4\ (302.2) < HSO_3F\ (299.8) < HClO_4\ (285 \pm 8)$$
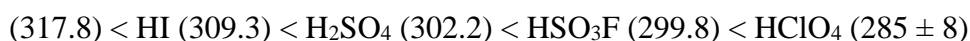
(values in brackets are experimental gas-phase acidities (ΔG_{acid}) in kcal mol^{-1} units). Interestingly, a greater delocalization of the charge on the chlorine atom relative to the fluorine results in HSO_3Cl being stronger acid than HSO_3F [71-73].

Replacement of the acid protons with Li^+ cations in given acids yields corresponding lithium salts. During the past 30 years, efforts have been made to develop new lithium salts, however, none of these new salts have offered significant advantages over the most commercially available $LiPF_6$ for LIBs [74].

4.1. Salt properties for electrolyte formulations

It is noteworthy that electrolyte is a medium responsible for ionic transport. Therefore, the properties of electrolyte such as ionic and electronic conductivity, viscosity, interfacial properties, thermal stability have significantly effect on the battery performance [75, 76]. Therefore, salts for electrolyte preparation have to meet some important requirements as shown below:

- **Ionic conductivity** – a fast Li^+ cation transport is desired in terms of the overall battery reaction, as the limitations to Li^+ cation mobility throughout the bulk electrolyte is one of the main sources of impedance from the battery [77, 78]. The influence of the lithium salt's anion on the conductivity is due to the variations on the Li^+ cation solvation and ionic association interactions, which result from the differences in anion structure and coordination strength [79].
- **Salt solubility** – adequate solubility is critical for the electrolyte preparation, as too low or too high lithium salt concentrations in the solvent(s) effective charge deficit will cause poor ionic conductivity or salt precipitation, respectively [37, 80].
- **Stability**– electrolytes should not react with other components from the cell within a wide electrochemical stability window during the charge/discharge process [80, 81]. Therefore, the electrochemical potential stability window is vital, as well as the range of electrolyte's operating temperatures.
- **SEI formation**– the lithium salt affects directly to the SEI layer formation, composition, and stability between the electrodes and electrolyte through the degradation/reaction between each other [55, 82].
- **Hydrolysis stability**– anions tend to hydrolyze when they are in contact with water, even more critically at higher temperatures, forming HF from the most common commercially used electrolyte, $LiPF_6$. Thus, dry conditions of storage of lithium salts for electrolytes in LIBs result in additional costs. Interestingly, the HF formation can be also the result of the reaction of the anions with solvents molecules (H^+) [83, 84].

Other important characteristics to be considered include low cost, recyclability, and low toxicity. The lack of these properties makes the lithium salt not viable for commercial applications. Additionally, solvents, optimized salt concentration, and electrolyte additives for the electrolyte formulation are essential for battery performance and applications [85].

4.2. Fluorine-containing lithium salts

Lithium salts have a direct effect on the chemical/electrochemical stability and ionic conductivity. Furthermore, the oxidation of the anions in the electrolyte often controls the upper voltage limitation for the electrochemical stability window of the whole cell, while the reduction of the solvent determines its lower voltage limitation. Commercially available lithium salts for electrolyte preparation with fluorine content are as follows:

- ***LiPF$_6$,*** Lithium hexafluorophosphate, is the most commonly commercially used in LIBs. It presents high conductivity values in aprotic solvents. LiPF$_6$–based electrolytes form stable interface with the Al current collector at high potential [86] and when working with carbonate solvents it forms a stable SEI with graphite electrodes [87]. Among its drawbacks the P–F bond is unstable, the salt tends to hydrolyze easily [88, 89] and it has a relativity low thermal stability [86, 87]. The principal concern associated with this salt is the presence of HF and its negative impact on the cell performance [89-91].

- ***LiAsF$_6$,*** in the 1970s and 1980s lithium hexafluoroarsenate was extensively studied. Interestingly, it was found that it improves the efficiency of Li metal plating/stripping. Its properties are very similar to LiPF$_6$ but exhibits a superior conductivity to LiPF$_6$ [92]. Although the As^V oxidation state is not toxic, the As^{III} and As^0 states, which will be formed at the negative electrode, are extremely toxic. As a consequence, its application at industrial level has been limited [93]. Additionally, arsenic is not abundant enough for a widespread application (world annual production is only 60 000 tons, [94, 95]).

- ***LiBF$_4$,*** lithium tetrafluoroborate has a lower conductivity compared to LiPF$_6$ [96]. The B–F bond is quite more stable than P–F bond. Therefore, LiBF$_4$ is not prone to hydrolysis, and it is more thermally stable than LiPF$_6$. However, this lithium salt passivates Al at high potential [97]. Although it has a low solubility, this salt has been used in high- and low-temperature applications to reduce the SEI layer formation. It has been also used as an additive to electrolytes with LiPF$_6$ [87, 96].

- ***LiSO$_3$CF$_3$,*** Lithium trifluoromethanesulfonate (triflate—commonly abbreviated as "CF$_3$SO$_3$") was widely investigated mainly for polymer electrolytes [98]. This salt has a high thermal stability [99], and it does not tend to hydrolyze due to the C–F bond stability. However, its conductivity is much lower than that of LiPF$_6$ [83, 100] and it highly corrosive towards the Al current collector at high potentials [97].

- **LiDFOB**, Lithium difluoro(oxalato)borate has a higher solubility than LiBOB (described further below) in linear carbonate solvents. However, compared to $LiBF_4$, LiTFSI, and $LiPF_6$, it is still visibly lower. Electrolytes with LiDFOB have higher conductivity than LiBOB [101], however, this conductivity is lower than that of the $LiPF_6$ or $LiClO_4$. One important characteristic to highlight is the formation of a stable cathode layer at elevated temperatures and potentials like at 60°C and at 5 V *vs.* Li/Li$^+$. Additionally, among analog salts to [44], the conductivities for the $LiB(CO_2C(CF_3)_2O)_2$, $LiBF_2(CO_2C(CF_3)_2O)$, $LiB(CO_2CH(CF_3)O)_2$, and $LiB(CO_2CH_2C(CF_3)_2O)_2$ salts were 7.0, 8.3, 6.3, and 1.9 mS·cm^{-1} at 25°C, respectively [96, 102].

- **LiTFSI,** Lithium bis(trifluoromethanesulfonyl)imide salt has many acronyms, such as LiTFSI, LiTFSA, $LiNTf_2$, $LiTf_2N$, etc. Imide and amide are the most well-known terms. Electrolytes with this salt exhibit lower conductivity than $LiPF_6$–based electrolytes. On the other hand, TFSI$^-$ anions have a high thermal stability, and due to its stable C–F bonds is less vulnerable to hydrolysis [103, 104].

  However, LiTFSI in aprotic solvent–base electrolytes are highly corrosive for Al current collector at high potential [105, 106].

Anions conjugated from Brønsted–Lewis superacids represent the core lithium salts used for commercial lithium batteries. The acidity order determined from QC calculations is as follows: HBF_4 (287.7) < HPF_6 (276.6) < $HTaF_6$ (268.3) < $HAlCl_4$ (257.4) < $HSbF_6$ (255.5) (DFT–calculated ΔG_{acid} values in kcal mol^{-1}), [73, 107]. $LiBF_4$ and $LiPF_6$ have been widely used for lithium batteries research, with $LiPF_6$ being the most frequently used for commercial LIBs. $LiTaF_6$-based electrolytes showed poor stability when cycling with Li metal. $LiSbF_6$ has a similar conductivity value to $LiPF_6$, but it is very corrosive to metals. Li_2SiF_6 and Li_3AlF_6 present very low conductivities, which can be attributed to their low solubility in aprotic solvents [108].

4.2.1. Advanced salts -Imides, methides, and phosphorylimides

Fluorination of the imide (amide) anions produce lithium salts for electrolytes highly soluble in aprotic solvents. Fluorinated sulfonyl imide salts and LiTFSI were patented in 1990 by Armand [109, 110]. LiTFSI has been widely studied among this class of anions. Adding to that, LiTFSI's analog lithium bis(perfluoroethanesulfonyl)imide (LiBETI), $LiN(SO_2C_2F_5)_2$ has also been broadly examined, reporting more than 200 publications about this lithium salt.

LiBETI salts have lower conductivity than $LiPF_6$ or LiTFSI, however, LiBETI has a very high thermal stability, it does not undergo hydrolysis with aprotic solvents, and it does not corrode aluminum at high potential [106, 109, 111, 112]. In recent years, anions with fluorosulfonyl groups ($-SO_2F$) have gained attention from researchers. The most notorious salt among them is lithium bis(fluorosulfonyl)imide (LiFSI), $LiN(SO_2F)_2$ [113]. This salt presents a conductivity value higher than that of $LiPF_6$. However, the S–F bond (similar to C–F) possess a lower stability, a lower thermal and hydrolytic stability than C-F bond [99, 114]. Furthermore, at high potential it corrodes the aluminum [115].

Asymmetrical anions for electrolytes may also be interesting to consider due to their high solubility. LiFNFSI for example presents high thermal stability (>200°C), high conductivity and the corrosion to Al at high potential cannot be considered as severe. LiFNFSI also exhibit better cycling (more stable, better capacity retention) than $LiPF_6$ at high temperatures such as 60°C. Asymmetric imide anions with carbonyl groups such as $TSAC^-$ like $N(COCF_3)(SO_2CF_3)^-$ has also been reported [116, 117]. However, it presents poor electrochemical stability. In general, various variants of imide anions have been studied and most of them do not show any significant advantage comparing to $TFSI^-$ and $BETI^-$ anions.

4.3. Fluorine-free lithium salts

A number of fluorine-free Li-salts for LIB electrolytes were tested over time, however, they do not meet characteristics to be commercialized as primary salts for the replacement of the $LiPF_6$. Some of them are effective as electrolytes additives, though [95, 118].

- *$LiB(CH_3)_4$*, Lithium tetramethylborate is stable in air atmosphere, but lithium tetrabutylborate ($LiB(C_4H_9)_4$) is pyrophoric [119]. In the former salt, the Li^+ cations are coordinated by the methyl hydrogens, however, working with longer alkyl chains is less favorable, making the anions more reactive. Lithium tetraphenylborate ($LiBPh_4$) ($LiB(C_6H_5)_4$) is stable only when Li^+ cations are fully solvated.

- *$LiClO_4$,* Lithium perchlorate was extensively used in battery electrolyte research in the 1970s and 1980s due to several advantages, including its high ionic conductivity, excellent solubility in aprotic solvents, and good thermal and electrochemical stability. Additionally, it exhibits favorable SEI-forming properties, which contribute to its performance in batteries [120, 121]. However, electrolytes containing $LiClO_4$ typically do not passivate the aluminum (Al) current collector as effectively as electrolytes containing $LiPF_6$, which can lead to issues with the corrosion [115, 122]. Another major

drawback is that the chlorine atom in the ClO_4^- anion is at the high oxidation state (Cl^{VII}), making it a strong oxidizing agent and potentially explosive [123, 124]. This safety concern has largely limited the use of $LiClO_4$ in commercial battery applications [121].

- ***Lithium salts with nonfluorinated alkyl sulfonate*** such as $LiSO_3CH_3$ or benzenesulfonate such as $LiSO_3(C_6H_5)$ anions possess notably low solubilities and conductivities in aprotic solvents [36].

- ***Lithium salts with oligoether sulfate anions*** are soluble in EC:DMC mixtures, however, they have much lower conductivities ($<10^{-3}$ S·cm^{-1} at 30°C) than $LiPF_6$–based electrolytes [125, 126].

- ***LiC(SO₂CH₃)₃***, lithium tris(alkanesulfonyl)methide salts have poor solubility in EC:DMC (<0.1 M), although they are highly soluble in DMSO (~ 0.5 M). However, it is important to highlight that with the length increasing of the alkyl chain (from methyl to ethyl, $LiC(SO_2C_2H_5)_3$) the solubility increases [127, 128].

4.3.1. Salts–organoborates, –phosphates, and –aluminates

Barthel and Gores reported in 1995 a new class of chemical, electrochemically, and thermally stable lithium salts free of fluorine. These salts were based on boron chelate complex anions such as lithium bis(1,2–benzenediolato(2-)-O,O′)borate (LiBBB). LiBBB salt has high solubility but low oxidative stability. The conductivity of these salts in electrolytes increases in the order of LiBBPB < LiBSB < LiBNB ~ LiBBB. It is important to highlight that all these salts have lower conductivity than $LiPF_6$, LiTFSI or LiBETI [128, 129].

The first more promising organoborate salt was lithium bis(oxalato)borate (LiBOB) [130, 131]. The first publication about this salt took place in 2001 by Xu and Angell [132]. LiBOB electrolytes have lower conductivity than $LiBF_4$ [133], it hydrolyzes slowly, it has high electrochemical stability (>4.5 V *vs.* Li/Li$^+$), and high thermal stability [134]. This salt has been considered as a main salt for $LiPF_6$ replacement and as additive electrolyte (for $LiPF_6$–based electrolytes). Importantly, during cycling up to 5 V *vs.* Li/Li$^+$) LiBOB presents a very stable capacity retention. Regardless, low conductivity, poor solubility in typical battery solvents and unsolved issues with long-term SEI layer stability with some electrode materials result in lack of LiBOB commercial application [130, 133, 134].

Another interesting organoborate salt such as $LiB(CO_2)_2C(CF_3O)_2$ showed that it does not undergo hydrolysis, and it is thermally stable at 100°C and this salt in the electrolyte does not corrode the Al at high potential [122, 135].

- **LiTBP,** lithium tris(1,2–benzenediolato(2)-O,O′)phosphate salt has a thermal stability lower than 200°C. However, adding a methyl group to produce lithium tris(4-methyl-1,2-benzenediolato(2)- O,O′)phosphate (Li4-MLTBP) the conductivity and thermal stability improve. As any other salts, when they are fully fluorinated, properties such as conductivity and electrochemical stability increase in most of the cases [136].

- **LiTOP,** lithium tri(oxalato)phosphate salt possesses a high conductivity and high electrochemical stability [137]. After fluorination of this salt lithium tetrafluoro(oxalato)phosphate salt (LiFOP) was obtained. This salt was first formed when mixing LiPF$_6$ and LiBOB. It is worth highlighting that LiFOP has similar electrochemical stability and conductivity to LiPF$_6$ [136]. Due to the oxalates group present, this salt improves the capacity retention of MCMB/NMC cells [138].

However, these lithium organophosphate salts were not used individually as a main electrolyte and mixed with LiPF$_6$ as additives to enhance the cycling efficiency over the range of high cycle numbers.

4.3.2. Advanced lithium salts –other anions

Alkali metal bis(trifluoromethyl) amides, –phosphides, and –arsenides (MN(CF$_3$)$_2$, MP(CF$_3$)$_2$, and MAs(CF$_3$)$_2$) – all have a high nucleophilic reactivity [139].

Trifluoromethanol (HOCF$_3$) is unstable at room temperature due to the formation of HF [65, 89],

$$HOCF_3 \rightarrow O = CF_2 + HF \tag{4.1}$$

MOCF$_3$ salts (M = K, Rb, and Cs) are prepared by the following reaction,

$$O = CF_2 + MF \leftrightarrow MOCF_3 \tag{4.2}$$

Other salts were prepared in a similar way,

$$O = CFR_F + MF \leftrightarrow MOCF_2R_F \tag{4.3}$$

$$O = C(CF_3)_2 + MF \leftrightarrow MOCF(CF_3)_2 \tag{4.4}$$
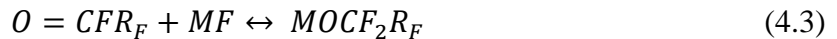
with M = Rb or Cs and R$_F$ = –CF$_3$, –C$_2$F$_5$, or –C$_3$F$_7$. Cesium salts tended to be more stable than rubidium salts. LiOCH(CF$_3$)$_2$ and LiOC(CF$_3$)$_3$ salts are both volatile at 50°C [36].

Among the family of Lewis acid groups, the most promising one for electrolyte applications is lithium bis(trifluoroborane)imidazolide (LiC$_3$N$_2$H$_3$(BF$_3$)$_2$). This salt has high solubility up to 2 M in EC:EMC (1:3/v:v), a conductivity of 5.1 mS·cm^{-1} at 20°C [140], and

quite high oxidative stability up to > 4.5 V vs. Li/Li$^+$ in DMC. Li/LiNi$_{0.2}$Co$_{0.8}$O$_2$ cells with this electrolyte show a better performance compared to LiPF$_6$-based electrolytes [141].

The gas-phase acidity values calculated for methanides with –NO, –NO$_2$, and –CN substituents are as follows: QC–calculated (ΔG$_{acid}$ values in kcal·mol^{-1}) relative to CH$_4$ (407.1): HCH$_2$NO (353.5), HCH(NO)$_2$ (318.5), (Figure 1b), HC(NO)$_3$ (303.9) (Figure 1c), HCH$_2$NO$_2$ (348.5), HCH(NO$_2$)$_2$ (311.5) (Figure 1e), HC(NO$_2$)$_3$ (298.0) (Figure 1f), HCH$_2$CN (363.9), HCH(CN)$_2$ (322.9) and HC(CN)$_3$ (288.8) (Figure 1k), [112].

The addition of a single –NO$_2$ group is expected to increase the acidity of the system more than adding a single –CN group. However, the triple substitution with –CN groups is more effective at increasing the acidity than for the –NO, –NO$_2$ groups due to the lack of steric hindrance [38].

Despite the strong electron–withdrawing properties of nitro or nitroso groups, these groups have been not used for the electrolytes due to their energetic characteristics [111, 142]. For example, lithium dinitrosomethanide (LiCH(NO)$_2$) (Figure 1b) is stable at room temperature, however, it has been reported that it is very sensitive to the temperature changes, highly explosive and toxic.

Additionally, mixtures of –NO, –NO$_2$, and –CN anions substituents have also been considered (Figure 1g–i), however, this type of substituents are also highly energetic.

Furthermore, lithium salts with the dicyanamide anion (LiDCA) (LiN(CN)$_2$) (Figure 1j), tricyanomethanide (LiTCM) (LiC(CN)$_3$) (Figure 1k), and tetracyanoborate (LiTCB) (LiB(CN)$_4$) (Figure 1l) were used for lithium battery applications [143]. Compared to the most common commercial lithium salts' anions, these new anions present limited electrochemical stability [144].

Figure 1 presents in detail examples of nitroso-, nitro-, and cyano-substituted anions for the synthesis of Li-salts for the preparation of electrolytes.
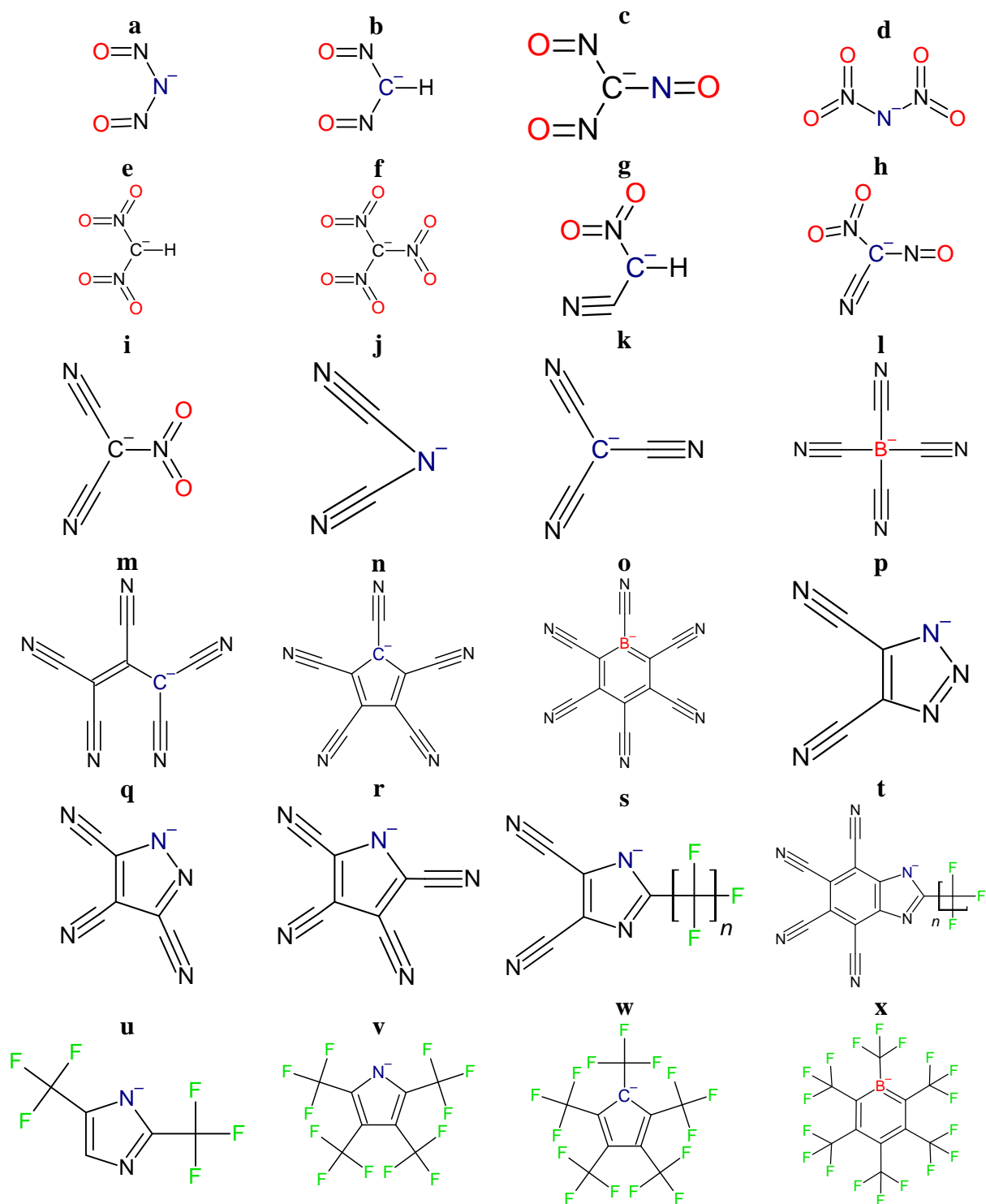
Figure 1. Examples of nitroso-, nitro-, and cyano-substituted anions: (a) $N(NO)_2^-$, (b) $CH(NO_2)_2^-$, (c) $C(NO)_3^-$, (d) $(NO_2)_2^-$, (e) $CH(NO_2)_2^-$, (f) $C(NO_2)_3^-$, (g) $CH(NO_2)(CN)^-$, (h) $C(NO)(NO_2)(CN)^-$, (i) $C(NO_2)(CN)_2^-$, (j) $N(CN)_2^-$ (DCA⁻), (k) $C(CN)_3^-$ (TCM⁻), (l) $B(CN)_4^-$ (TCB⁻), (m) $C(CN)_2=C(CN)C(CN)_2^-$, (n) $C_5(CN)_5^-$, (o) $C_5B(CN)_6^-$, (p) $C_2N_3(CN)_2^-$ (DCTA⁻), (q) $C_3N_2(CN)_3^-$, (r) $C_4N(CN)_4^-$, (s) $C_3N_2(CN)_2(C_nF_{2n+1})^-$ (TDI⁻) ($n = 1$), (PDI⁻) ($n = 2$) and HDI⁻ ($n = 3$), (t) $C_7N_2(CN)_4(C_nF_{2n+1})^-$, (u) $C_3N_2(C_2H_5)(CF_3)_2^-$, (v) $C_4N(CF_3)_4^-$, (w) $C_5(CF_3)_5^-$, and (x) $C_5B(CF_3)_6^-$

The QC-calculated gas-phase acidity (ΔG_{acid} values in kcal·mol^{-1}) of 1,1,2,3,3–pentacyanopropene ($C(CN)_2=C(CN)CH(CN)_2$) (267.2) (Figure 1m) and pentacyano-cyclo-pentadienide ($HC_5(CN)_5$) (250.1) [145, 146], (Figure 1n) are some of the values calculated among the cyanocarbon acids, which are thought to be some of the strongest acids known.

- The lithium salt with the 4,5–dicyano–1,2,3–triazolate anion (DCTA$^-$) or also known as 1,2,3–triazole–4,5–dicarbonitrile (TADC$^-$) (Figure 1p) was first reported by Michot in 1995. Alkali and alkali earth salts with DCTA$^-$ anion have shown high thermal stability (>350°C) [147, 148].

- The lithium salt with the pyrazole–3,4,5–tricarbonitrile anion (PATC$^-$) (Figure 1q) was not widely studied as an electrolyte salt [36].

- The acid with tetracyanopyrrolide anion (TCP$^-$) (Figure 1r) was reported in 1962 and the sodium salt with this anion was also reported [147]. Additionally, trifluoromethane–substituted versions of the $C_5(CN)_5^-$ and TCP$^-$ anions have been reported (Figure 1v, w), however, lithium salts has been only reported for $LiC_5(CF_3)_5$ [113, 149].

Lithium salts with the 4,5–dicyano–2–(trifluoromethyl)imidazolide (TDI$^-$) and 4,5–dicyano–2–(pentafluoroethyl)imidazolide (PDI$^-$) anions were reported by Niedzicki in 2009 [150]. The acid with TDI$^-$ (HTDI) was first reported by Begland in 1974. Thus, including the lithium salt with the 4,5–dicyano–2–(n-heptafluoropropyl)imidazolide (HDI$^-$) anion (Figure·1s), [40, 151].

There lithium salts (LiTDI, LiPDI, and LiHDI) have high thermal stability (>250°C), negligible hydrolysis, and high oxidative stability on Pt electrodes (4.8 V vs. Li/Li$^+$). However, TDI$^-$ and PDI$^-$ have lower conductivity than LiPF$_6$-based electrolyte (Table 3). Moreover, a computational study has shown that the related 4,5,6,7–tetracyano–2–fluoroalkyl benzimidazole anions (Figure 1t) might have encouraging properties [142, 152].

Table 3. **Conductivity of electrolytes with various lithium salts at 20°C and 1 M in EC:DMC (50:50 wt.%), [36]**

Lithium salt (anion)	Conductivity (mS·cm^{-1})
PF$_6^-$	10.8
N(SO2CF3)$_2^-$	9.0
PDI$^-$	6.3
TDI$^-$	6.7
DCTA$^-$	2.7

Other types of anions, which do not fit in with the previous groups have been also reported, however, not enough information about their properties is available (Table 4).

Table 4.   Conductivities and Al passivation potential of electrolytes with
various lithium salts at 25°C and 1 M salt in PC:DME (1:1 v:v), [36]

Lithium salt (anion)	Conductivity (mS·cm^{-1})	Al potential (V vs. Li/Li$^+$)
PF$_6$-	15.0	> 5.0
N(SO2CF3)$_2^-$	12.0	3.7
N(SO2C2F5)$_2^-$	9.5	4.4
N(SO2CF3)(CN)$^-$	7.2	< 4.2
N(SO2C4F9)(CN)$^-$	5.6	> 4.2
C(SO2CF3)(CN)$_2^-$	12.5	4.7
C(SO2C4F9)(CN)$_2^-$	8.3	> 5.0

4.4.   Solvents for electrolytes

Solvents have a strong effect on the ionic transport capability of the electrolyte and the conductivity is an important parameter to be measured. The conductivity can be related to the viscosity citing that "a high conductivity is achieved for electrolytes with a low viscosity", however, this is highly inaccurate. Instead, both properties originate from the molecular-level interactions between the ions and solvent (i.e., solution structure). These properties are thus only indirectly correlated with one another. It is worth pointing out that the choice of aprotic solvent or solvent mixtures greatly impacts the conductivity of an electrolyte [153].

It is known that there are numerous lithium salts and organic solvents, however, most of them do not fulfill the characteristics for commercial purposes:
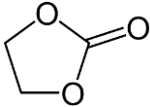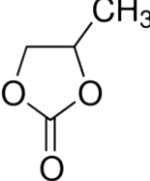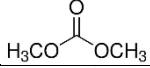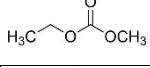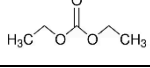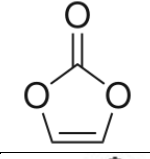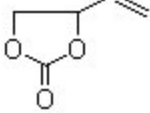
- High ionic conductivity
- High chemical and electrochemical stability
- Wide operational temperature range
- High safety
- Compatibility with the electrodes

Most of the liquid electrolytes used in commercial LIBs are based on organic solvents (see Table 5). Lithium salts are commonly dissolved in cyclic or linear carbonate solvents. However, due to the recent market demands in the field of energy storage, characteristics such as higher power and energy density, and the impact to the environment are very important parameters to consider.

Ethylene Carbonate (EC) is a cyclic organic carbonate with a high boiling point (248°C) and dielectric constant (~90), making it highly effective at dissolving lithium salts. EC is solid

at room temperature but forms a stable SEI on graphite anodes, crucial for LIB performance. It is often mixed with low-viscosity solvents like DMC to improve electrolyte conductivity and reduce viscosity. **Propylene Carbonate (PC)** is a cyclic carbonate with a lower dielectric constant (64) and melting point (-48°C), staying liquid at room temperature. It efficiently dissolves lithium salts but causes exfoliation in graphite anodes, limiting its use in LIBs with graphite. However, it is useful in other lithium chemistries and enhances electrolyte properties when mixed with additives [154].

Table 5.   **Physical properties of typical organic solvents, [154]**

Name	Molecular weight $g \cdot mol^{-1}$	d, $g \cdot cm^{-3}$	ε_T	η, mPa·s	Chemical structure
Ethylene Carbonate (EC)	88	1.32 (40°C)	90 (40°C)	1.9 (40°C)	
Propylene carbonate (PC)	102	1.20	65	2.5	
Dimethyl carbonate (DMC)	90	1.06	3.1	0.59	
Ethyl methyl carbonate (EMC)	104	1.01	3.0	0.65	
Diethyl carbonate (DEC)	118	0.97	2.8	0.75	
Vinylene carbonate (VC)	86.05	1.36	-	-	
Vinylethylene Carbonate （VEC）	86.05	1.12	-	-	

Dimethyl Carbonate (DMC) is a low-viscosity linear carbonate with a low boiling point (90°C) and dielectric constant (3.1). It enhances electrolyte conductivity when combined with high-dielectric solvents like EC. DMC is valued for reducing electrolyte viscosity and improving ion mobility. **Ethyl Methyl Carbonate (EMC)** is a linear carbonate with a slightly higher boiling point (110°C) than DMC and similar low viscosity. Though it has a low dielectric constant (2.9), EMC improves electrolyte conductivity, making it effective in balancing dielectric strength and conductivity. **Diethyl Carbonate (DEC),** with

a boiling point of 126°C, features a low dielectric constant (2.8) and viscosity. DEC is effective in cold environments or applications needing higher power density.

Vinylene Carbonate (VC), a cyclic carbonate with a boiling point of 240°C, acts as an additive in LIB electrolytes, forming a stable SEI on graphite anodes. Its reactivity enhances battery life and stability, especially at higher voltages, making VC a valuable electrolyte stabilizer. **Vinylethylene Carbonate (VEC)** is a reactive cyclic carbonate used as an additive to form a stable SEI. It improves electrolyte stability at high voltages and temperatures, enhancing capacity retention and cycling stability [155].

4.4.1. Fluorinated organic solvents

Fluorine-containing organic solvents present high electronegativity and low polarizability of the fluorine atom. It is worth highlighting that partially fluorinated organic solvents show higher polarity than fully fluorinated organic solvents.

- *Fluorinated linear carboxylates,* these types of compounds were considered for low temperature applications. The reduction potentials were found c.a. 0.87 – 1.41 vs. Li/Li$^+$. Decreasing the reduction potential increases the reversibility of the graphite electrode, obtaining a higher charge capacity.
  However, studies have shown exothermic reactions in most of the fluorinated carboxylates, making them less useful for LIBs [156, 157].
- *Fluorinated cyclic carbonates,* the most common solvents of this type are based on ethylene carbonate (EC) and propylene carbonate (PC), due to favorable physical and electrochemical properties of nonfluorinated analogs, such as the wide electrochemical stability window. By direct fluorination of EC, 4-fluoro-1,3-dioxolan-2-one (fluoroethylene carbonate, FEC) was obtained [157]. Due to its properties this solvent was used as an electrolyte additive for LIBs [158]. Currently, it is successfully used at the industrial level.
- *Fluorinated linear carbonates,* dimethyl carbonate (DMC), ethyl methyl carbonate (EMC), and diethyl carbonate (DEC) are the most common co-solvents for EC and PC. By direct fluorination of DMC, three types of partially fluorinated DMCs except *gen-*DFDMC were obtained. In terms of the conductivity of 1 mol·dm^{-3} LiPF$_6$ in EC equimolar solutions were in the DFDMC<FDMC<DMC order influenced by their viscosities. Fluorination of EMC and DEC produce 2-fluoroethyl methyl carbonate (FEMC), 2,2-difluoroethyl methyl carbonate (DFEMC), methyl 2,2,2- trifluoroethyl

carbonate (TFEMC), ethyl 2-fluoroethyl carbonate (FDEC), ethyl 2,2-difluoroethyl carbonate (DFDEC), and ethyl 2,2,2-trifluoroethyl carbonate (TFDEC), [159]. Conductivities of 1 mol·dm^{-3} LiPF$_6$/EC:FEMC or EC:FDEC at 25°C are lower than those of EC:EMC or EC:DEC. However, the cycling efficiencies and discharge capacity retentions of 1 mol·dm^{-3} LiPF$_6$/EC:FEMC or EC:FDEC at 25°C were higher than those in EC:EMC or EC:DEC, respectively. Electrolytes containing a partially fluorinated aliphatic carbonates have shown high reversible capacity, forming thin film layer and low charge transfer resistance as a result.

Fluorinated organic solvents perform in varied ways depending on the electrolyte composition. In general, the conductivity of the electrolyte decreases due to the higher viscosity, there is a good SEI layer formation, which results in low-capacity fading. Adding to that, the nonflammability of solvents increases directly with the number of fluorine atoms, however, the solubility of lithium salts decreases. The structure of selected groups of solvents are shown in Figure 2.
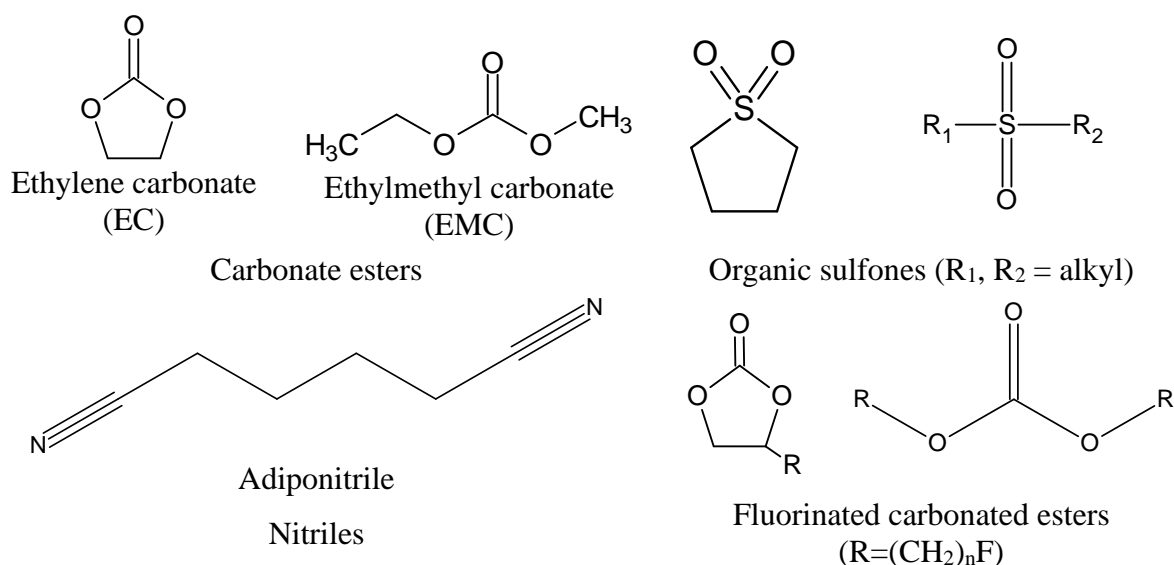
Figure 2. Chemical structures of (a) carbonate esters, (b) organic sulfones, (c) nitriles, (d) fluorinated carbonate esters

4.4.2. Phosphorus-containing organic solvents

Organic solvent-based electrolytes most commonly used in LIBs are highly flammable, causing safety concerns in general. Therefore, various approaches have been developed to establish safer electrolytes [14]. These new alternatives can be solid polymer electrolyte (lithium salt in polymer, most commonly a polyether-based one), [77]; room-temperature ionic

liquids (RTIL), [160, 161]; flame-retardant co-solvents or additives [45]; inorganic solid electrolytes well conducting at room temperature [162].

Table 6 shows fundamental properties of non-flammable electrolyte systems to produce safer LIBs. However, meeting these characteristics do not ensure a higher or better battery performance, [163, 164].

Table 6. **Classification of nonflammable electrolytes for LIBs**

Category	Composition	Example	Characteristics
Organic electrolyte solutions (with nonflammable components)	Nonflammable components as co-solvents or additives	Fluorinated esters Organic phosphorus compounds	High ionic conductivity: trade-off between nonflammability and electrode performances
Polymeric solid electrolytes	Polymer complexes with lithium salts (LiX)	LiX/Poly(ethylene oxide) (PEO) LiX/PEO-grafted polymer	Low ionic conductivity at lower temperature; low Li^+ transport number
Polymeric gel electrolytes	Polymer complexes swollen with organic solutions	LiX/alkylcarbonate/PEO with nonflammable component	High ionic conductivity; trade-off between nonflammability and electrode performances
Ionic liquids	Ionic liquids (IL) dissolving lithium salt (LiX)	LiX/IL: 1-ethyl-3 methyllimidazolium fluorisulfonylamide (EMIFSA)	High ionic conductivity; low-rate capability of electrode performances
Inorganic solid electrolytes	Li^+ - containing oxides, sulfides, glass, ceramics	Li_2S-P_2S_5 glass, $Li_{10}GeP_2S_{12}$ crystal	High ionic conductivity; high Li^+ transport number; low interfacial properties

Polymeric gels composed of non-flammable organic solvents [95], inorganic-ceramic electrolytes dispersed in polymeric matrices [43], ionic liquids mixed with nonflammable, and low-viscosity organic solvents [165, 166] are proposed as practical electrolytes for LIBs.

Phosphorus-containing organic compounds are well known and used as fire-retardant materials to suppress the flammability of organic polymers.

- *Alkylphosphates,* and related compounds were proposed as flame-retardant additives and/or co-solvents. Trimethylphosphate (TMP) works as a flame-retardant additive or co-solvent in a mixed alkyl carbonate-based electrolyte solution. The amount of TMP in the electrolyte solution is enough to achieve nonflammability of the mixture depends on the electrolyte composition and the characteristics of the other solvents. For example, in the EC+TMP system, the amount of 20 vol.% is enough, however, for the EC+EMC

(1:1 by mass), at least 30 wt.% is required [167]. Additionally, the presence of the TMP in the electrolyte formulation will affect the viscosity of the solution, decreasing the conductivity of the electrolyte as a result. However, for $LiBF_4$ conductivity can increase until certain TMP content as is shown in Table 7 [163],

Table 7.   **Ionic conductivity of 1 mol·dm^{-3} LiPF$_6$ and LiBF$_4$ solutions as a function of TMP content in EC+DMC (1:1 by vol.) at 25°C**

TMP content/ vol%	Conductivity (mS·cm^{-1}), LiBF$_4$	Conductivity (mS·cm^{-1}), LiPF$_6$
0	5.8	11.9
20	6.5	11.3
40	8.2	10.2
50	8.6	9.7
60	8.7	9.1
80	7.8	8.0
100	5.5	5.0

The addition of TMP increases the thermal stability in a full-cell system (LiCoO$_2$/graphite). However, TMP on the graphite surface causes irreversibility during the charge-discharge process, meaning that a non-compact SEI layer is formed when TMP is used. Some mechanisms are proposed to explain the TMP behavior as a fire-retardant additive, they are shown in Figure 3,

1. Thermal decomposition of organic compounds

$$RH \rightarrow R \cdot + H \cdot \quad (1)$$

$$H \cdot + O_2 \rightarrow HO \cdot + O \cdot \quad (2)$$

$$HO \cdot + H_2 \rightarrow H \cdot + H_2O \quad (3)$$

$$O \cdot + H_2 \rightarrow HO \cdot + H \cdot$$
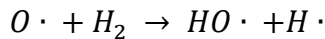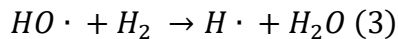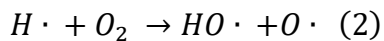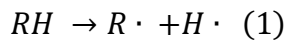
2. Evolution of P-containing radical from TMP

$$TMP_{gas} \rightarrow (P) \cdot$$
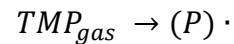
3. Trapping H· by radical (P)·, suppressing the reaction of step (2)

$$(P) \cdot + H \rightarrow (P)H$$

Terminating the chain-reaction

Figure 3.   A proposed mechanism for suppressing the decomposition reactions by addition of a phosphorus-containing compound

- *Fluoroalkylphosphates or fluorinated alkylphosphates* present high flame-retardant properties. Jow and co-workers reported some of them: tris(2,2,2-trifluoroethyl) phosphate (TFP), bis(2,2,2-trifluoroethyl)-methyl phosphate (BMP) and (2,2,2-trifluoroethyl)diethyl phosphate (TDP). Among them, TFP presents high

nonflammability and good compatibility with graphite. In general, the fluorinated alkyl phosphates show high nonflammability [168].

- **Phosphorus-containing general compounds,** alkylphosphites are a part of the family of phosphorus-containing organic esters. Trimethylphosphite (TMPi) was first reported as flame-retardant additive in $LiPF_6/EC+DEC$. Its advantage to the process is unclear, but the thermal stability is improved after using it as an additive [136].

Arylphosphates are also possible candidates of flame-retardant additives. Adding 5 wt.% of 4-isopropyl phenyl diphenyl phosphate (IPPP) to $LiPF_6/EC+DEC$ showed positive effects on the thermal stability, improving the exothermic behavior of the electrolyte [169]. Therefore, characteristics such as flammability and cell (electrodes) performance are important to choose the most suitable solvents, co-solvents and additives.

Tables 8–12 show examples of the effect of the temperature, solvents and mixture compositions on the electrolyte conductivity.

Table 8. **Conductivity of electrolytes with various lithium salts at 25°C and 0.1 M salt in PC:DME (1:2 v:v), [36]**

Lithium salt (anion)	Conductivity $(mS \cdot cm^{-1})$	Molecular weight $g \cdot mol^{-1}$
PF_6^-	4.4	152
$CO_2CF_3^-$	0.4	120
$SO_3CH_3^-$	-	102
$SO_3CF_3^-$	2.3	156
$SO_3C_4F_9^-$	2.3	306
$SO_3(C_6H_5)^-$	$0.1 - 0.2$	164
$SO_3(C_6F_5)^-$	1.1	254
$SO_3C_8F_{17}^-$	1.9	506
$C(COCF_3)_2^-$	0.8	215
$N(SO_2CF_3)_2^-$	4.0	287
$N(SO_2C_2F_5)_2^-$	3.8	387
$N(SO_2C_4F_9)(SO_2CF_3)^-$	3.5	437
$N(SO_2CF_3)(C_6F_4SO_2F)^-$	3.0	347
$N(SO_2CF_3)(SO_2C_8F_{17})^-$	3.2	637
$N(SO_2OCH_2CF_3)_2^-$	3.0	347
$N(SO_2OCH_2CF_2CF_3)_2^-$	3.0	447
$N(SO_2OCH_2CF_2CF_2H)_2^-$	2.9	411
$N(SO_2OCH(CF_3)_2)_2^-$	3.1	483
$C(SO_2CF_3)_3^-$	3.6	418
$C(SO_2OCH_2CF_3)_3^-$	2.9	508
$B(C_6H_3-3,5-(CF_3)_2)_4^-$	2.7	870
$PO_2(C_2F_5)_2^-$	0.6	308

Table 9. Conductivity of electrolytes with various lithium salts at 20°C and 1 M salt in EC:EMC (25:75 v:v), [36]

Lithium salt (anion)	Conductivity (mS·cm^{-1})	Lithium salt (anion)	Conductivity (mS·cm^{-1})
PF_6^-	8.52	BF_4^-	2.91
$BF_3(CF_3)^-$	3.21	$BF_3(C_2F_5)^-$	3.31
$BF_2(CF_3)_2^-$	4.02	$BF_2(C_2F_5)_2^-$	4.62
$BF(CF_3)_3^-$	5.11	$BF(C_2F_5)_3^-$	6.89
$B(CF_3)_4^-$	7.52	$B(C_2F_5)_4^-$	8.55
$FB_3(SO_2CF_3)^-$	4.47	$BF_3(SO_2C_2F_5)^-$	3.98
$BF_2SO_2CF_3)_2^-$	5.83	$BF_2(SO_2C_2F_5)_2^-$	5.23
$BFSO_2CF_3)_3^-$	7.62	$BF(SO_2C_2F_5)_3^-$	7.18
$BSO_2CF_3)_4^-$	8.55	$B(SO_2C_2F_5)_4^-$	8.21

Table 10. Conductivity of electrolytes with various lithium salts at 20°C and 1 M salt in EC:DMC and EC:DEC (1:1 w:w), [36]

Lithium salt (anion)	Conductivity (mS·cm^{-1})	Lithium salt (anion)	Conductivity (mS·cm^{-1})
In EC:DMC		In EC:DEC	
PF_6^-	9.41	PF_6^-	6.09
$SO_3CF_3^-$	2.51	$SO_3CF_3^-$	1.63
$N(SO_2CF_3)_2^-$	6.18	$N(SO_2CF_3)_2^-$	4.24
$N(SO_2C_2F_5)_2^-$	5.45	$N(SO_2C_2F_5)_2^-$	3.95
$N(SO_2C_4F_9)_2^-$	3.63	$N(SO_2C_4F_9)_2^-$	2.34
$N(SO_2CF_3)(SO_2C_4F_9)^-$	1.55	$N(SO_2CF_3)(SO_2C_4F_9)^-$	1.10
$N(SO_2C_2F_5)(SO_2C_4F_9)^-$	3.11	$N(SO_2C_2F_5)(SO_2C_4F_9)^-$	2.28
$N(SO_2C_3F_6SO_2)^-$	6.86	$N(SO_2C_3F_6SO_2)^-$	4.95

Table 11. Conductivity of electrolytes with various lithium salts at 25°C and 0.3 M salt in PC:DME and PC:2-MeTHF (1:1 equimolar), [36]

Lithium salt (anion)	Conductivity (mS·cm^{-1})	Lithium salt (anion)	Conductivity (mS·cm^{-1})
In PC:DME		In PC:2-MeTHF	
PF_6^-	9.23	PF_6^-	6.57
$N(SO_2CF_3)_2^-$	8.05	$N(SO_2CF_3)_2^-$	5.97
$N(SO_2C_2F_5)_2^-$	7.55	$N(SO_2C_2F_5)_2^-$	5.48
BBB^-	4.21	BBB^-	3.07
BNB^-	4.25	BNB^-	2.97
BSB^-	2.45	BSB^-	1.28
$BBPB^-$	1.09	$BBPB^-$	0.92

Table 12. Conductivity of electrolytes with various lithium salts at 20°C and 1 M salt in EC:DMC (50:50 w:w), [36]

Lithium salt (anion)	Conductivity (mS·cm^{-1})	Lithium salt (anion)	Conductivity (mS·cm^{-1})
PF_6^-	10.8	BBB^-	6.7
$N(SO_2CF_3)_2^-$	9.0	BNB^-	2.7
$N(SO_2C_2F_5)_2^-$	6.3		

4.5. Electrolyte additives

The concept of "functional electrolytes" was first introduced in 1999, aiming to control the SEI layer formation and improving battery performance by adding minimum amounts of additives, anode additives, cathode additives, and overcharge prevention additives. Currently, such electrolytes are essential for better and safer battery performance [65, 170].

The most common electrolyte base composition (to which additives are added) is a mixture of cyclic carbonates (i.e. ethylene carbonate (EC), and propylene carbonate (PC)) and linear carbonates (i.e. dimethyl carbonate (DMC), ethyl methyl carbonate (EMC), and diethyl carbonate (DEC)), to which a certain amount of lithium salt is added.

4.5.1. Electrolyte additives for anodes

Electrolyte additives for anodes can be classified as follows,

- ***Compounds with unsaturated carbon–carbon bond,*** Sanyo Electric Company in 1992 found that vinylene carbonate (VC) can be used as a solvent for the electrolyte formulation in lithium batteries [45], this solvent is best-known as an additive at present. Its main use is stabilization of the SEI layer on the anode with EC-DMC-based electrolytes. Thanks to double bonds it can polymerize at low potential but before EC or DMC would decompose. The resulting polymer is a good backbone of the SEI layer [171]. In 1997, Ube Industries found out that with small amounts of VC, it is also possible to suppress the PC decomposition at the graphite anode [172]. Furthermore, in 1993, Shu et al. from the National Research Council of Canada reported that by adding high concentrations (0.5 M) of 12–crown–4 ether, the formation of complexes with Li in PC suppresses the co-intercalation into the graphite layer [173]. However, this complex formation will not specifically control the SEI layer formation. Even though Ube Industries, Ltd. discovered in 1995 that phenylene carbonate can be used as an additive to allow the use of PC with graphite anodes [174], at that time it was established that PC does not work with graphite anodes. Around 1997, the concept of suppressing the PC decomposition by controlling the anode/electrolyte interface with additives was established and widely used in the field of LIBs. In 1998, Mitsui Chemicals discovered that PC in 4,4–dimethyl–5–methylene–1,3–dioxolan–2–one can be used with graphite anodes [65] and they also discovered that vinyl ethylene carbonate can be used as an additive [155]. Additionally, the same year, 1998, Ube Industries explored from double– to triple–bond compounds and discovered that alkyne compounds such as methyl

propargyl carbonate, propargyl acetate, and 2–butyne–1,4–diol dimethyl decarbonate suppress the PC decomposition.

- *Carboxylic acid anhydrides,* Panasonic in 1991 discovered that by adding acetic anhydride and benzoic anhydride, the reduction of the water content or the residual alkali within batteries is made possible, and as a result the battery performance deterioration is prevented [127, 175]. Also, adding succinic anhydride and maleic anhydride the PC decomposition is suppressed when cycling graphite anodes.

- *Cyclic sulfonates (Sultones),* in 1996, Sony Corporation discovered that 1,4–butane sultone (5–50%) can substitute EC as a solvent [175]. In 1997, Ube Industries, Ltd. found that cyclic monosulfonic esters (sultones), such as 1,3–propane sultone (PS) suppresses PC decomposition. Later, it was found that the combination of PS and VC can be used as additives [176]. PS is registered as a CMR (carcinogenic, mutagenic, or toxic for reproduction) substance, known for its mutagenicity. The volume of PS used for cell fabrication is much smaller than NMP, another CMR substance, so theoretically can substitute it.

4.5.2. Electrolyte additives for cathodes

In this section, additives for cathodes are categorized as follows,

- *Sulfur–containing compounds with active site poisoning function*, Fujifilm in 1996 discovered that sulfides containing phenyl groups can work as electrolyte additives, such as 4,4′–dimethoxydiphenyl sulfide, and 1,2–bis(p-methoxyphenylthio)ethane [177]. Sulfur–containing additives for cathodes have shown the following three results, (*1*) The potential on the electrode surface is not uniform, there are microscopic regions with considerably higher potential (overvoltage regions), where radicals of oxygen can be generated. Therefore, the presence of additives can hinder the formation of such decomposition products. (*2*) The range for the oxidation potential was between +3.8 and +4.3 V *vs*. Li/Li$^+$, working with metallic lithium as the reference electrode, with additives the potential was between +3.9 and +4.2 V *vs*. Li/Li$^+$. (*3*) Some of the formed decomposition products remain adherent to the cathode. In 1998, Ube Industries discovered more electrolyte additives belonging to this group such as methyl oxo(phenylthio)acetate, S,S′–diphenyl dithiooxalate, S–phenyl O–methyl thiocarbonate and S, S′–diphenyl dithiocarbonate [35].

4.5.3. Electrolyte additives for safety improvement

With the current requirements of increasing the battery capacity, safety is another characteristic that must be considered. For example, when the battery is overcharged, the whole system becomes thermally unstable, which causes an exothermic reaction followed by an internal shorting and gas release, with the possibility of thermal runaway in the battery. Therefore, this section presents the following electrolyte additives [45].

Additives for overcharge prevention, when LIBs are overcharged, excess lithium is extracted from the cathode, which produces the release of oxygen, and the crystal structure of active material becomes unstable. When the anode and cathode become thermally unstable, they oxidize the organic solvents in the electrolyte. As a consequence, sudden exothermic reactions occur, and the cell safety is compromised by producing undesirable heat. Even though there are safety procedures, such as shutdown, the application of additives for overcharge mitigation/prevention have shown effective results [173].

- *Anisole compounds,* the so-called "redox shuttle additives" consume the excess electric current through a redox process, among these additives are, 1,3,5–trimethoxybenzene, 2,6–dimethoxytoluene, and 3,4,5–trimethoxytoluene [36]. Adding to that, in 1995 Sony Corporation found new additives such as 2–chloro–p–xylene, 4–chloroanisole, 2,4–difluoroanisole, 3,5–difluoroanisole, and 2,6–difluoroanisole for this application [178].

- *Alkylbenzenes and halogen–containing benzene compounds*, the polymerization of this type of additive is believed to form an insulating layer on the surface of the cathode. These aromatic additives polymerize at higher potentials than the maximum cell operating potentials, increasing the internal resistance of the battery. These aromatic compounds were found by NEC Moli Energy in 1995, biphenyl, 3–chlorothiophene, and furan [45]. Furthermore, cumene and cyclohexylbenzene were found by Fujifilm Corporation in 1996 [156]. The same year, Hitachi Maxell discovered additives such as fluorobenzene, 1,2–difluorobenzene, and 1,3,5–trifluorobenzene. Later in 1997, the same company discovered that trimellitates, such as tris(2–ethylhexyl)trimellitate can be used as an overcharge mitigation electrolyte additive [167].

  Monomer additives, such as pyrrole, begin to polymerize when maximum potential is reached, and as a consequence a conductive frame (of limited electronic conductivity) is formed between the electrodes. That way the excess current is lost

through the slow self-discharge. Furthermore, 2,2–diphenylpropane and 2–fluorobiphenyl can be used alternatively as additives for such application [65], they were found by NEC Moli Energy in 1997.

In 1999, Sanyo Electric Company and Ube Industries, Ltd. discovered that esters containing biphenyl groups, such as 4–acetoxybiphenyl [179], diphenyl ether [179], 1,2–diphenoxyethane, 1,4–diphenoxybenzene, o–terphenyl, m–terphenyl, and p–terphenyl [180], can be used as electrolyte additives. In 1998, the same companies reported cumene and cyclohexylbenzene, the advantage of these additives are the tertiary carbon adjacent to the phenyl group. When the internal gas pressure rises considerably, these additives cut off the charge current [181].

Non-flammable solvents and additives, organic phosphates, phosphazenes, and other additives are improving safety. In 1990, Mitsubishi Chemical Corporation discovered solvents with high flash point, such triesters of phosphoric acid (triethyl phosphate) and esters of phosphoric acid at more than 15 vol.% [14, 95, 164, 167].

Additives for wettability improvement, phosphates containing long–chain aliphatics and aromatics, such as tris(2–ethylhexyl) phosphate, and triphenyl phosphite were found by Asahi Kasei in 1989. Later, electrolyte additives such as dodecyl methyl carbonate, methyl 1–methylpropyl carbonate, methyl sec–butyl carbonate, methyl 2,2–dimethylpropanoate, ethyl 2,2–dimethylpropanoate, butyl 2,2–dimethylpropanoate, and hexyl 2,2–dimethylpropanoate [182, 183] were discovered between 1995 and 2000.

Additives of corrosion inhibition, it was discovered by Ube Industries that working with small amounts of dinitriles such as adiponitrile reduces the battery corrosion [35]. Later, it was found that succinonitrile, sebaconitrile combined with 2–fluorotoluene and 3–fluorotoluene can be used as electrolyte additives [36]. Succinonitrile is also effective for Cu current collector protection.

Even although various nitrile compounds were discovered and explored, their applicability vary considerably depending on their structure. For example, the melting point of adiponitrile and succinonitrile are at 3°C and 57°C, respectively.

4.6.   Properties and developments of various electrolytes

There are various types of electrolytes developed with a focus on sustainability and lower cost, although, they are still in the early stages of development [156, 184, 185].

4.6.1. Organic liquid electrolytes

This type of electrolyte has been widely used and studied in the past few decades due to their high ionic conductivity, and good stability with various electrodes. However, thermal and electrochemical stability, as well as their general safety are characteristics of concern. Therefore, recent investigations of organic liquid electrolytes are studying possibilities to solve these issues. This would be possible either through the use of electrolyte additives or by designing new lithium salts. Furthermore, it was found that highly concentrated electrolytes are beneficial for the SEI formation on the anode, improve stability of the current collector, improve the thermal stability and the oxidation stability, as well as the rate capability, and widen the electrochemical window [172, 186].

4.6.2. Aqueous liquid electrolytes

Due to the growing interest in developing highly safe electrolytes, high-rate charge/discharge capabilities, low–cost and environmental–friendly battery systems, aqueous electrolytes have attracted attention. Aqueous liquid electrolytes possess higher ionic conductivity than organic liquid–based electrolytes and lower cost due to use of inexpensive water (no cost/energy of moisture removal). Current research on aqueous electrolytes aims at improving the stability of water due to its narrow operational electrochemical window, around 1.23 V *vs* SHE and hinder the irreversible structural changes of the electrodes [18, 95, 187]. Recently, the highly concentrated aqueous electrolytes, also known as "water–in–salt" electrolyte (WiSE), have shown promising results, such as a wider electrochemical window, low solvent activity, low flammability, and high chemical stability [188, 189].

4.6.3. Ionic liquid electrolytes

Ionic liquid–based electrolytes are composed of an ionic liquid and metal salts [165], which are often used in experimental metal ion batteries due to their ultralow volatility, high ionic conductivity, high thermal stability, low flammability, and wide electrochemical window (up to 6 V *vs*. Li/Li$^+$). However, its applicability in the industry has still a long way to go due to their high cost. Additionally, its high viscosity and often also high surface tension results in poor battery performance, and low-rate capability. Also, a relatively unstable SEI layer is formed between the electrolyte and the electrode [166, 190-192].

4.6.4. Solid-state electrolytes (polymer and inorganic solid electrolytes)

Characteristics such as low weight, low cost, the flexibility/buffering of volume changes during the charge/discharge process, nonflammability and the suppression of detrimental effects (such as electrolyte leakage) suggest that solid polymer electrolytes (SPEs) are the most promising candidates for high–performance batteries [77]. However, the ionic conductivity for this type of electrolytes is notably low, this parameter being the most challenging and critical to be improved. Adding nanoparticles and blending various polymers are among many strategies proposed to improve the SPEs' ionic conductivity.

Inorganic solid electrolytes are another alternative, this type of solid electrolytes has been extensively investigated in the last decades. As a consequence of these studies various types of inorganic solid electrolytes have been reported [186]. In contrast to solid polymer electrolytes high conductivities can be reached, sensitive to the composition and the structure of the inorganic solid; however, this is not fully understood. Based on their high safety properties (no dendrite growth), solid electrolytes seem ideal candidates. However, for their viability at the industrial level it is necessary to solve the problems of processing them to be thin on a large surface considering their brittleness, and that of the loss of contact of the batteries in operation due to the volume changes of the intercalation electrodes. Some issues arise also from high sensitivity to any atmosphere impurities (moisture, carbon dioxide, etc.) of LLZO and other most notable inorganic solid electrolyte materials.

To sum it up, electrolytes form a critical part of the design of high–performance and safe batteries. Moreover, each type of electrolyte has unique properties. As a consequence, a good understanding of their characteristics (advantages and drawbacks) is significant for further development and the design of suitable electrolytes for a specific battery type.

4.7. Criterion for the design of new lithium salt for electrolytes

Properties or features of salts which would make them promising candidates for commercial battery electrolytes include the following [193]:

a) *Simplified synthesis,* for this purpose low-cost and nontoxic reagents are important aspects to be considered. Fulfilling these requirements will allow us to handle all the reagents, products, emissions and solid/liquid waste in a facile way and lower the overall costs of salt manufacturing [194].

b) **Reduced hazards,** when the synthesis is in process, some reagents, intermediate products or the final product can be highly toxic or have undesirable properties, making them unsuitable for commercial batteries. Additionally, the side reactions when a cell failure occurs should be considered. For example, when $LiPF_6$ reacts with carbonate at high temperatures and while in contact with the electrode materials then highly toxic fluoro-organic products could be released to the environment [40]. ***Therefore, the elimination of fluorine from the anions is a worthy goal, when not only is the battery performance a priority, but also the impact on the environment.***

c) **Hydrolysis,** $LiPF_6$ undergoes hydrolysis in contact with water. Hence, the costs for synthesis, storage and general handling are very expensive. Thus, developing salt, which does not tend to hydrolyze (or any intermediate would during any step of the synthesis) would minimize additional costs at the industrial level.

d) **Thermal stability,** the stability of lithium salts at high temperatures, or during cycling at high temperatures (as primary salts or additives) such as 60°C is one of the most important characteristics to meet in this field.

e) **Solvents compatibility,** the main commercial lithium salt for electrolytes is $LiPF_6$. This salt was optimized for cyclic/acyclic carbonates solvents in electrolytes for LIBs. However, when a different solvent is used, such as GBL with $LiPF_6$ some side reactions can occur, and the electrolyte solution turns black/brown. Thus, new salt requires confirming its stability with typical solvents and/or looking out for new solvents which may have better properties and cannot be used with $LiPF_6$.

f) **Performance at low-temperature,** $LiPF_6$ in a mixture of carbonate solvents do not perform well at low temperatures. Therefore, the design and development of stable salts at low temperatures without any crystallization such as LiFSI, LiTFSI or LiBETI is preferential for commercialization purposes. For instance, LiFSI is used in commercial batteries added to $LiPF_6$ to improve the low temperature performance. It is not used on its own because of its corrosion of the aluminum current collectors.

g) **SEI formation,** the decomposition of lithium salts to form the protective layer is desirable. The formation of HF in electrolytes with $LiPF_6$ at high temperatures and potential can be treated as a very problematic characteristic. Replacing $LiPF_6$, the addition of HF and/or water scavengers or the formation of artificial protective layers are alternatives to mitigate this problem.

Summarizing, through time new characteristics are vital to meet, which means not only the performance of the battery. Nowadays, it is crucial to consider the scalability of the proposed system, lifetime, safety, cost, electrolyte compatibility and stable performance with noncritical raw materials. Adding to that, recyclability at the battery end of life and its impacts on the environment are also very important characteristics to consider.

Finally, as it was mentioned, the lithium salt, solvents and electrolyte additives play an important role as part of the electrolyte and each of them has an effect on the performance. Figure 4 [156] shows the effect of each component on the electrolyte.
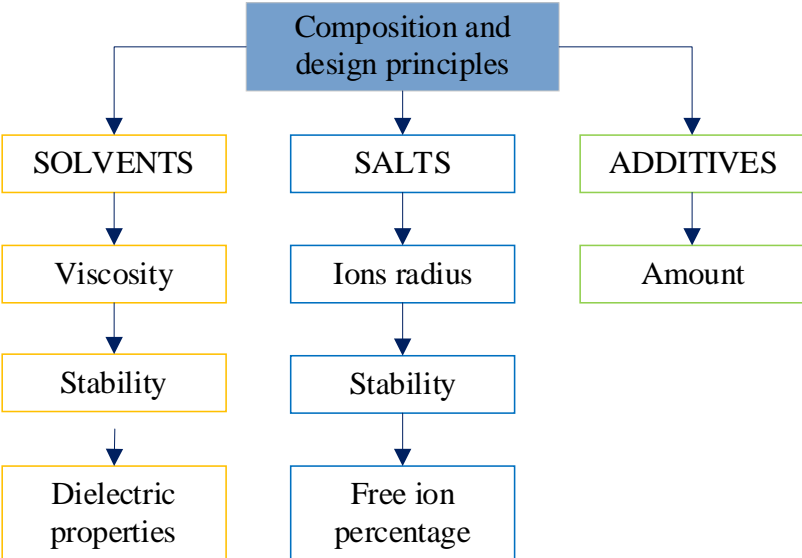
Figure 4.   Composition and design principles

5. ELECTRODES – CATHODE MATERIALS

Positive electrode material (also known as cathode material) is one of the key components of LIBs. This component plays an important role in determining the battery energy/power density and cycle–life. However, new aspects must be considered nowadays, apart from higher energy/power density, such as safety and the availability of raw materials in the short- and long term. At present, there are three most-known types of positive materials; olivine materials (e.g. $LiFePO_4$), spinel materials (e.g. $LiMn_2O_4$), and layered materials (e.g. $LiNi_xCo_yMn_2O_2$). These types of cathode materials are being broadly used in LIBs, predominantly for new energy vehicles [62, 195].

5.1. Layered $LiNi_xMn_yCo_{1-x-y}O_2$ cathode materials (NMC)

The co–substitution of Ni and Mn at the Co sites in $LiCoO_2$ to synthetize $LiNi_xMn_yCo_{1-x-y}O_2$ cathode materials have provided advantages, such as higher capacities, lower costs, less problematic cobalt used and better thermal stabilities compared to conventional layer–structured $LiCoO_2$ (LCO) and olivine–structured LFP cathode materials [196, 197].

Each metal ion in the cathode materials (NMC materials) has an important role to play. Ni is an electron supplier, Mn maintains the structure and improves the thermal stability, and Co provides the order of the layered structure. Even though a large effort has been made to study NMC materials, not a single optimal composition has been found. Increasing the Ni content increases the initial discharge capacity; however, the capacity retention reduces drastically during the cycling. Increasing the Mn content reduces the discharge capacity on NMC materials [198]. Furthermore, increasing Co content reduces considerably the capacity loss during cycling, however, the material cost increases significantly, as well as increases limitations in cobalt supply. This section presents the $LiNi_xMn_yCo_{1-x-y}O_2$ cathode materials in three different categories depending on the Nickel content as shown in Table 13.

Table 13. $LiNi_xMn_yCo_{1-x-y}O_2$ cathode materials categories

Category	Cathode material
Conventional ternary layered cathode materials [198-200]	$LiNi_xMn_yCo_zO_2$ (where x <0.5, x + y + z = 1): which include $LiNi_{1/3}Mn_{1/3}Co_{1/3}O_2$, $LiNi_{0.4}Mn_{0.4}Co_{0.2}O_2$, $LiNi_{0.4}Mn_{0.2}Co_{0.4}O_2$, and $LiNi_{0.5}Mn_{0.3}Co_{0.2}O_2$
Nickel–rich layered cathode materials [201, 202]	$LiNi_{0.6}Mn_{0.2}Co_{0.2}O_2$, $LiNi_{0.75}Mn_{0.15}Co_{0.15}O_2$, $LiNi_{0.8}Mn_{0.1}Co_{0.1}O_2$, $LiNi_{0.85}Mn_{0.075}Co_{0.075}O_2$

The detailed chemical and electrochemical properties of the NMC cathode materials are shown in Table 14.

Table 14.   Comparison of layered LiNi$_x$Mn$_y$Co$_z$O$_2$ positive materials

Sample	Chemical formula	Specific capacity (mAh·g^{-1})	Average potential (V)
NMC111	LiNi$_{1/3}$Mn$_{1/3}$Co$_{1/3}$O$_2$	~ 150	3.65
NMC 424	LiNi$_{0.4}$Mn$_{0.2}$Co$_{0.4}$O$_2$	~ 170	3.65
NMC 532	LiNi$_{0.5}$Mn$_{0.3}$Co$_{0.2}$O$_2$	~ 160	3.66
NMC 622	LiNi$_{0.6}$Mn$_{0.2}$Co$_{0.2}$O$_2$	~ 170	3.65
NMC 811	LiNi$_{0.8}$Mn$_{0.1}$Co$_{0.1}$O$_2$	~ 190	3.65
NCA	LiNi$_{0.8}$Mn$_{0.05}$Co$_{0.15}$O$_2$	~ 190	3.65

5.1.1. Conventional ternary cathode materials

The most important characteristics of cathode materials to meet LIBs requirements are high energy/power density, superior rate capability, and long lifespan. Layer–structured ternary NMC cathode materials have been extensively studied for high-performance cathodes due to their lower toxicity, larger capacity, and higher energy density than layer–structured LCO or olivine–structured LFP materials [203]. The first developed NMC material was Li(Ni$_{0.33}$Mn$_{0.33}$Co$_{0.33}$)O$_2$ (NMC111), this formulation had an equal transition metal (TM) content. NMC111 reaches a specific capacity not sufficient (~150 mAh·g^{-1}) for enhancing the energy density of LIBs. Afterwards, LiNi$_{0.4}$Mn$_{0.4}$Co$_{0.2}$O$_2$ (NMC442), and LiNi$_{0.5}$Mn$_{0.3}$Co$_{0.2}$O$_2$ (NMC532) cathode materials were developed, these new formulations showed relatively lower cost, higher energy density, higher thermal stability, and higher specific capacity 160–170 mAh·g^{-1} than NMC111, [204, 205]. These abovementioned NMC cathode materials showed some disadvantages, such as relatively low electronic conductivities, which limited their rate capability and cycle performance, as well as poor structural stability, which could lead to increase cell resistance and cell capacity fading, as well as thermal runaway at high temperatures. These issues could be attributed to the low conductivity, and the instability of layer structure during the cycling process, which are dependent on the physicochemical properties (e.g. structure, morphology, particle–size distribution, surface area and density) of materials. The synthesis method has also a direct effect on the physicochemical properties [195, 206]. Constant efforts have been made to improve cathode material properties such as energy/power density, cycle life and safety [203].

The general strategies made to tackling abovementioned issues can be classified into three categories,

Doping with a small volume of other metals elements, doping is the simplest and most effective technique to improve performance and keep the structural and thermal stabilities of NMC materials. A small amount of metal elements such as Na, Al, Mg and many others have been introduced into the layered NMC cathode materials [207]. This technique is related to: a) the introduction of the electrochemically inactive element into the structure, b) prevention of undesired phase transition from the layered to the rock–salt structure, and c) promotion of the lithium-ion transport. Due to their low cost, Na, Mg and Al are among the most attractive dopants. Na–doped NMC523 materials showed superior electrochemical performance by increasing the Li^+ diffusion coefficient. Al–doped NMC523 exhibited a stable electrochemical performance with a capacity fading of 0.02% per cycle compared to undoped NMC523 (capacity fading of 0.07%), [208]. Furthermore, after electrochemical cycling the Al–doped NMC523 exhibited lower charge transfer resistance and Al could modify the surface structure of the cathode by reacting with the electrolyte. In terms of the structural stability, the integration of Al into the NMC material prevented the formation of oxygen during the delithiation process. The suppressed oxygen inhibited the nickel migration from the metal site to the lithium site, stabilizing the cathode structure [197, 209]. ***Anion doping*** is another well-known type of doping to improve the electrochemical of cathode materials for Li–ion batteries. However, undesirable side reactions occur leading to an unsatisfactory overall performance. Doping a small amount of fluorine could improve the stability of the NMC structure.

For example, $Li_{1.2-x}Ni_{0.13}Mn_{0.54}Co_{0.13}O_{2-x}F_x$ (x=0.08) exhibited about 95% capacity retention as compared to 62% for $Li_{1.2}Ni_{0.13}Mn_{0.54}Co_{0.13}O_2$ after 100 cycles [202, 210].

Surface coating with metal oxides and metal fluorides, this is a feasible and simple strategy to address the issues of layer–structured ternary $LiNi_xMn_yCo_{y1-x-y}O_2$ cathode materials. The process of coating aims to form a barrier to avoid side (parasitic) reactions between the electrode and electrolyte, leading to suppressed TM dissolution, oxygen loss, phase transformation and safety issues. Therefore, by the adequate selection of coating material, it is possible to manipulate the ionic/electronic conductivities and structural/thermal stabilities. Three types of coating synthesis routes are core–shell structure coating, ultrathin film coating and rough coating. Their general processes, advantages and disadvantages area shown in Table 15 [211].

Table 15. Summarization and comparison of core-shell coating, ultrathin film coating and rough coating

Type	Method	Advantages	Disadvantages
Core-shell	Two – step, co-precipitation	Core: high capacity, shell: high stability	Thickness too high, complex preparation, structural mismatch, increased mechanical stress, formation of cracks
Ultrathin film	ALD, CVD	Uniform, continuous, nanoscale, tunable thickness, precise control	Limited sources, impeded conductivity
Rough	Co-precipitation, hydrothermal, solvothermal, spray drying, sol-gel, ball milling	Simple preparation, easy of scale up	Not continuous, not uniform

These surface coatings aim to protect cathode materials from dissolving into the electrolyte and stabilize layered structures. Li_2TiO_3 was used as a novel coating material to modify $Li(Li_{0.2}Ni_{0.19}Mn_{0.51}Co_{0.10})O_2$ cathode materials. Adding 3% of Li_2TiO_3 exhibited high-rate capability of 169.9 $mAh \cdot g^{-1}$ at 2C, showing a stable cycling [212]. The host structure was stabilized, protecting the electrode surface from F^- ion attack and preventing side reactions on the electrode surface.

Furthermore, electrochemical impedance spectroscopy tests revealed that Li_2TiO_3 suppress the impedance of the host electrode. Therefore, choosing the proper coating material and method is crucial to enhance cathode material coulombic efficiencies, charge/discharge process and the capacity retention. Ideally, a coating layer should be covering AM uniformly with a controlled coating thickness. However, considering the real application in industry, co-precipitation (rough coating) is the best choice for scaling up this approach at low cost. Improving ionic/electronic conductivities and thermal stability were new targets to reach, however, complex synthesis procedures and higher costs seem to be critical issues to be considered. Furthermore, the scaling up from laboratory to industrial level will come with its own numerous problems. Regarding the safety issue, the coating must work without problems under mechanical strain and other conditions influencing its structure, like over–charge, over–discharge, high/low temperatures, etc. To sum it up, an ideal coating should provide high ionic and electronic conductivity, be electrochemically inert, structurally stable, and provide stable electrochemical performance [213].

Optimizing the preparation method, in addition to the aforementioned methods, optimizing the preparation techniques and using various raw materials are often employed to enhance the properties of NMC positive electrode materials. The structures and morphology are influenced by various factors, including electrochemical reaction processes and material synthesis. NMC materials can be synthesized through methods such as co-precipitation, sol–gel, and hydrothermal processes. The co-precipitation method is the most commonly used, but ideal conditions needed (pH value, precipitant concentration, ammonia molar ratio, stirring speed, and reaction time) are complex, making it challenging to obtain materials with homogeneous and consistent shapes [214]. Generally, positive materials prepared with various raw materials exhibit varying rate discharge characteristics. For instance, Yang et al. demonstrated that the morphology, tap density, and rate cycling performance of NMC111 are significantly affected by various lithium raw materials, such as $LiOH \cdot H_2O$, Li_2CO_3, $CH_3COOLi \cdot 2H_2O$, and $LiNO_3$ [215]. Their study found that spherical NMC111 synthesized using continuous carbonate co-precipitation retained 97.5% and 92% of its initial capacity after 100 cycles at 1C and 5C, respectively, with $LiOH \cdot H_2O$ enhancing tap density (up to 2.32 $g \cdot cm^{-3}$) and Li_2CO_3 improving rate performance. Thus, selecting different raw materials can yield materials with higher capacity and better rate characteristics.

Calcination temperature is a crucial factor affecting the performance of NMC positive materials. For example, Kong prepared quasi-spherical NMC532 using a continuous hydroxide co-precipitation method and calcined a mixture of precursors and Li_2CO_3 at 750°C, 850°C, and 950°C for 10 hours in air. The sample calcined at 850°C demonstrated excellent electrochemical performance, with an initial discharge capacity of 193.4 $mAh \cdot g^{-1}$ and a coulombic efficiency of 85.4% at a current density of 20 $mAh \cdot g^{-1}$. It also exhibited good rate capability and cycle performance, highlighting the importance of selecting suitable calcination temperatures, which affect the size and morphology of the materials [209]. In general, nano-sized positive materials provide better electrochemical performance than micro-sized ones because their nano-/micro-hierarchical architectures can shorten the lithium cation diffusion path and minimize unwanted anti-site cation mixing, improving Li^+ diffusion kinetics. For instance, Kang et al. synthesized nano-sized NMC111 with a nanofiber morphology using an electro-spinning method, achieving high charge and initial discharge capacities of 217.9 $mAh \cdot g^{-1}$ and 172.8 $mAh \cdot g^{-1}$, respectively. Similarly, Chen et al. used a sacrificial template method to produce hierarchical nano-/microsphere $LiNi_{1/3}Mn_{1/3}Co_{1/3}O_2$ (PNM-NMC111) with significantly improved electrochemical performance compared to

conventional bulk-NMC materials. Their cell delivered high specific reversible capacities and retained 90.3% capacity after 50 cycles. Li et al. synthesized NMC nanoplates with exposed active facets, showing high-capacity retention at 0.1C with 89.4% after 50 cycles. However, while nano-sized electrode materials offer benefits in kinetics and capacity, they often suffer from low thermodynamic stability and high surface energy. Hierarchical micro/nanomaterials can circumvent these issues, combining the advantages of both nano-sized building blocks and micro-sized assemblies. For example, Zhao et al. synthesized $LiNi_{0.5}Mn_{0.3}Co_{0.2}O_2$ with a hollow microsphere structure using $Co_{0.4}Mn_{0.6}CO_3$ as a self-template and a simple impregnation process. This material displayed high discharge capacity, superior rate capability, and better cycling stability, along with good processability in commercial production due to its nano-microsphere structure and narrow grain-size distribution.

Despite remarkable progress in doping, surface coating, and optimizing preparation methods for ternary layered materials like NMC111, their relatively low specific capacities demand the development of new cathode materials with higher specific capacities to increase LIB energy density [216].

5.1.2. Lithium–rich layered cathode materials

Lithium-rich layered positive materials (denoted as $xLi_2MnO_3 \cdot (1-x)Li(Ni, Mn, Co)O_2$ or $Li_{1+x}(Ni, Mn, Co)_{1-x}O_2$) generally offer higher capacities for LIB energy density, exceeding 250 $mAh \cdot g^{-1}$. The Li/M ratio and TM distribution significantly influence the electrochemical performance of these materials. However, challenges such as high surface residual lithium, high irreversible capacity, and low electrochemical reaction kinetics persist. Recent research has focused on addressing these issues to improve the performance of lithium-rich layered positive materials [217].

Surface residual lithium, one major issue is the presence of residual lithium compounds like LiOH and Li_2CO_3, which can destabilize the positive electrode slurry due to the gelation of PVdF binders. These compounds also generate gases at high cell voltages, reducing coulombic efficiency and causing cell swelling. Residual lithium compounds lead to increased side reactions between the electrode and electrolyte during cycling, raising polarization and interfacial resistance, and damaging the electrode surface structure [218]. To mitigate these effects, researchers have used additives during material synthesis. For example, Aida et al. employed ammonium meta tungstate $((NH_4)_6H_2W_{12}O_{40} \cdot xH_2O$, AMT) as an additive in the co-precipitation method to synthesize LIB positive materials. The AMT-modified materials

demonstrated significantly improved rate performance, particularly at high discharge rates, by reducing residual lithium compounds.

Other compounds such as BPO_4, $LiAlO_2$, and H_3PO_4 have also been used to reduce residual lithium. BPO_4, for instance, encapsulates $Li_{1.16}(Ni_{0.25}Mn_{0.75})_{0.84}O_2$ particles and forms a Li-doped $Li_xBPO_{4+x/2}$ (LBP) nanolayer using residual Li_2CO_3 as the Li^+ source. This layer reduces surface residual lithium, enhancing the structural stability of the electrode material and significantly reducing capacity and voltage fade during cycling. Electrochemical performance studies of materials like 2-LBP@LNMO showed discharge capacities of 181 and $117 \cdot mAh \cdot g^{-1}$ at 2C and 5C, respectively, with retention capabilities of 80.2% and 61.2% at 0.5C. EIS analysis confirmed that the LBP coating lowered the solid electrolyte interface resistance compared to pristine LNMO, demonstrating the coating's effectiveness in improving electrochemical performance [219].

Irreversible Capacity Loss, the second challenge for lithium-rich layered materials, is irreversible capacity loss. These materials can deliver capacities over 250 $mAh \cdot g^{-1}$, but often lose 40–100 $mAh \cdot g^{-1}$ in initial cycles and have low discharge rate performance. This issue arises because oxygen is released from the lattice during the first charge, creating vacancies filled by TM ions, altering the structure [220]. To address this, researchers have optimized synthesis, used surface modifications, and applied nano-coatings [206]. Carbon surface modification is effective and simple. Deng used poly(vinylpyrrolidone) (PVP) as a carbon source to modify $Li(Li_{0.2}Ni_{0.13}Mn_{0.54}Co_{0.13})O_2$, improving its capacity and discharge rate. These changes showed better cycle stability with a retention rate of 86% after 70 cycles.

Coating lithium-rich layered oxides with materials like Li_2ZrO_3 has improved performance. A thin Li_2ZrO_3 layer on LNMO enhances reversible capacity, reduces side reactions, and prevents TM dissolution, improving lithium cation conductivity and AM structural stability. Zr^{4+} doping with Li_2ZrO_3 coating also reduces voltage fade and enhances layered structure stability. Wu et al. created ultrathin spinel membrane-encapsulated layered lithium-rich (USMLLR) cathode material that improves capacity and rate capability, and stabilizes capacity, showing that surface coatings can significantly improve electrochemical performance [221, 222].

Electrochemical Reaction Kinetics, the third significant issue with lithium-rich layered positive materials is their poor electrochemical reaction kinetics. Lithium cations need to diffuse along specific crystal planes within the 2D percolating network, known as the classic

1-TM channel. However, the lithium-rich component has low electron conductivity and a poor lithium diffusion coefficient, resulting in considerable electrode polarization. Additionally, interfacial resistance increases with ongoing side reactions during cycling. Consequently, due to sluggish kinetics, the practical capacity of Li-rich cathodes rapidly decreases at high current rates [220]. Intrinsic charge transfer kinetics in these materials are complex and differ from conventional layered cathode materials. Studies using EIS and galvanostatic intermittent titration technique (GITT) have shown that the Li^+ diffusion coefficient (D_{Li}) is about 10^{-14} $cm^2 \cdot s^{-1}$ in the smoothly sloping voltage profile below 4.4 V *vs*. Li/Li^+ during charging. However, this coefficient drops sharply to 10^{-19} $cm^2 \cdot s^{-1}$ at the voltage plateau above 4.4 V *vs*. Li/Li^+ [223-225].

During discharging, D_{Li} is 10^{-14} $cm^2 \cdot s^{-1}$ between 4.4 and 3.8 V *vs*. Li/Li^+, then decreases to 10^{-16} $cm^2 \cdot s^{-1}$ between 3.0 and 3.6 V *vs*. Li/Li^+. To address these issues, metal-ion doping and surface modifications through coatings, such as Li_2SiO_3, AlF_3, and Li_2ZrO_3, have been employed to enhance electrochemical performance. Li_2SiO_3 not only matches the Li-rich electrode crystal structure but also provides a pathway with low energy barriers for Li^+ diffusion, leading to improved electrochemical performance and stability [203, 226].

Despite extensive use of chemical doping to enhance the electrochemical performance of Li-rich layered oxide cathodes, the correlation between electrochemical kinetics and the local structure and chemistry post-doping remains not fully understood. A comprehensive understanding of the local structure and chemistry is crucial for elucidating the mechanism and behavior of chemical doping, thus improving the rate performance of lithium-rich layered positive electrode materials. Research by Ding et al. demonstrated a gradient doping strategy using dopants like Si^{4+} and Sn^{4+} to enhance electrochemical kinetics. The experimental results showed that such substitutions decreased the TMO_2 layer thickness and increased interlayer spacing, enhancing Li^+ diffusivity and rate performance in Si/Sn doped materials [226].

Another strategy to improve reaction kinetics involves fabricating nanostructured cathode materials with well-defined morphologies, such as porous structures and hollow spheres. These nanostructures shorten the lithium cation diffusion length and improve particle contact with the electrolyte. Furthermore, the electrode material could tolerate the volume change (expansion/contraction) that might occur during lithiation/delithiation. For instance, hollow spherical particles synthesized by co-precipitation followed by calcination showed significant enhancements in Li^+ diffusion coefficients and reduced the charge transfer resistance [227]. Additionally, creating integrated hierarchical spinel layers through pH modulation can further

stabilize the structure during charge-discharge cycles. The improvement of the cycling stability, rate capability, and performance at low temperature are significantly noticeable. Materials like graphene and carbon nanotubes (CNTs) have also been used to increase electronic conductivity and stabilize the electrode–electrolyte interface during the repeated lithiation/delithiation process [226], leading to superior performance in terms of specific capacities, rate capability, and Li^+ diffusion coefficients.

Voltage fading, the commercialization of lithium-rich NMC is significantly hindered by voltage drop during cycling and limited power rates due to sluggish kinetics of anionic redox species. This voltage fade is primarily linked to a phase transition from the layered structure to the spinel phase, driven by the migration of TM cations into lithium cation layers. During electrochemical activation, lithium and oxygen are irreversibly removed from the Li_2MnO_3 component, creating Li^+ vacancies and causing TM cation migration. This inherent voltage decay in Li-rich Mn-based layered cathode materials is challenging to eliminate without compromising other electrochemical properties. To address this, various strategies such as concentration gradients, surface grafting, coatings, and doping have been proposed globally. For example, achieving an optimal precursor concentration ratio has demonstrated improved performance, suggesting a connection between voltage fade and anionic redox activity. Studies show that with cycling, materials suffer from Li/M intersite mixing and spinel-like nanodomain formation, which, despite stabilizing voltage fade, lead to a significant voltage drop [228, 229].

Doping and surface modifications are also explored to suppress voltage fade. Suitable coating layers can enhance Li^+ transportation, reduce electrolyte corrosion, and improve rate performance and cycling stability. Migration and doping decrease energy barriers, facilitate quick Li^+ insertion and extraction by enlarging interplanar spacing, and stabilize the layered structure. Reduced cation mixing due to migration further enhances rate capability. For instance, surface modifications with Li_2SiO_3 and Li_2ZrO_3 coatings on LMNO electrodes significantly improved cycling performance and capacity retention. These coatings stabilize the cathode structure, prevent direct contact with the electrolyte, and mitigate oxygen loss, thereby enhancing overall performance.

Collectively, these advancements highlight the potential of lithium-rich layered positive materials as high-energy density cathodes, although commercialization challenges remain due to residual lithium compounds, irreversible capacity loss, and sluggish anionic redox kinetics. Ongoing research into concentration gradients, surface modifications, and doping continues to offer promising solutions for large-scale practical applications of these materials [217-219].

5.1.3. Nickel–rich cathode materials

Recently, the scope of LIB applications has expanded from small mobile devices to larger uses such as electric vehicles and home or even grid-scale energy storage systems. This growth has driven demand for LIB systems with higher energy and power density, faster charge rates, greater safety, and lower costs. Nickel-rich layered $LiNi_xMn_yCo_zO_2$ (where x > 0.5, x + y + z = 1) cathodes have emerged as promising candidates for these applications, particularly in electric vehicles. These Ni-rich oxides are valued for their high capacity (180 – 210 mAh·g^{-1} above a charge of 4.5 V vs. Li/Li$^+$), relatively low cost, and environmental friendliness [209, 230].

Despite their advantages, Ni-rich cathodes face challenges such as poor capacity retention and insufficient thermal stability, which worsen with increasing nickel content (x between 0.6 and 0.9). Capacity retention issues stem from side reactions between tetravalent nickel ions (Ni^{4+}) and the electrolyte, and phase transitions from the layered to rock-salt structure (NiO) at the particle's surface. These issues lead to significant declines in lithiation kinetics at the electrode–electrolyte interface [231]. Thermal stability problems arise from oxygen release from the crystal lattice in highly delithiated states, posing safety risks. Addressing these issues is crucial for meeting industry demands for high-performance LIBs [210, 232].

Surface residual lithium, surface chemistry plays a critical role in the performance of Ni-rich cathode materials. Residual lithium compounds from synthesis can degrade stability by forming undesirable surface species like Li_2CO_3, LiOH, and NiO. These compounds react with air and moisture, causing nickel ions to convert to a lower oxidation state (Ni^{2+}), forming an inert rock-salt NiO phase or a cation-mixing layer. Maintaining a controlled environment with low moisture and CO_2 levels during storage can mitigate these effects but increase production costs. Developing strategies to restore the inherent characteristics of Ni-rich materials and improve their electrochemical performance is essential [233].

Surface modifications have shown promise in enhancing the stability and performance of Ni-rich cathodes. Techniques like creating an artificial cathode-electrolyte interphase (CEI) layer have demonstrated high structural and thermal stability, even at elevated temperatures [234, 235]. These methods help address issues like electrolyte decomposition and thick SEI layer formation, which increase interfacial resistance and capacity loss.

Interfacial stability remains a significant challenge for Ni-rich layered compounds. High charge voltages lead to severe reactions with the electrolyte, forming thick CEI layers and increasing interfacial resistance and causing various problems including capacity loss, structure

deterioration, and surface side reactions that accelerate the capacity fade [236]. Structural degradation, including phase transitions and microcrack formation, further intensifies these issues [234]. Efforts to improve interfacial stability include electrode doping with materials like MoO_3, Al_2O_3, CeO_2, and ZrO_2, and designing heterostructural shells around the Ni-rich core [237]. These strategies aim to protect the materials and reduce Li^+/Ni^{2+} mixing during cycling. A surface coating of nano – sized SiO_2 powder applied on Ni–rich $LiNi_{0.6}Mn_{0.2}Co_{0.2}O_2$ demonstrated a good HF scavenging, reducing the electrode degradation, improve the thermal stability, also offered the benefit of lower cost, improving electrochemical and physicochemical characteristics of NMC622 cathode [238].

Issues with Ni–rich materials, thermal instability is a major concern for Ni-rich materials, as it can lead to safety hazards like oxygen release and thermal runaway [209, 210]. The onset temperature for oxygen release decreases with higher nickel content, increasing the risk of flammable electrolyte ignition. Surface coatings and doping can help mitigate these risks by suppressing electrolyte decomposition and forming more stable surfaces [230, 239]. Additionally, managing micro strain and preventing cracks in primary particles are critical for maintaining cycling stability, especially at high temperatures. Further research and engineering are needed to address these challenges and enhance the overall performance of Ni-rich layered oxides for LIBs [198].

5.1.4. Challenges for enhancing layered–type cathode materials

Lithium and/or nickel-rich layered TM oxides are highlighted as the most promising candidates for next-generation LIBs due to their large reversible capacity and high operating voltage. Consequently, these materials have garnered extensive attention. Despite significant progress in understanding the mechanisms and causes of voltage fading in lithium-rich layered positive electrode AMs, cost-effective solutions for practical applications are still lacking. Efforts to implement these findings in Li-rich NMC materials are ongoing, with particle engineering approaches like core–shell, single crystals, and gradient-concentration configurations showing some success. However, significant challenges remain before these materials can be practically applied, including long-term stability of surface peroxo species and the interplay between cationic and anionic redox processes. Intensive research is required to address these issues and unlock the full potential of Li-rich NMC materials.

Nickel-rich layered positive materials are promising, capable of delivering sustained capacities over 185 mAh·g^{-1}, making them ideal for applications such as electric vehicles.

Increasing the nickel content can yield capacities up to 200 mAh·g^{-1}, but this requires coating with a Mn-rich NMC phase for stability. Despite their application potential, Ni-rich layered oxides face challenges related to surface chemical instability, leading to capacity and power losses due to side reactions in both air and electrolyte. Moreover, structural instability in the highly de-lithiated state poses safety concerns, such as oxygen release and thermal runaway.

Addressing these challenges through continued research is essential for the practical application of lithium and nickel-rich layered positive materials. By overcoming issues like surface instability and understanding the kinetics of redox processes, researchers can significantly improve the integrated properties of these materials. Future studies are expected to pave the way for large-scale applications, enhancing the performance and safety of lithium-rich layered cathode materials, particularly in high-demand applications such as EVs.

5.2. Olivine LFP cathode materials

Olivine-type positive electrode materials like LFP, known for their lithium insertion/extraction reversibility, have been extensively researched since Goodenough et al. first identified them as suitable for LIBs in 1997 [25, 205]. LFP has since found widespread application in electronic devices, EVs, and power grids due to its flat voltage profile, high cycling and thermal stability, low material cost, abundant supply, and better environmental compatibility compared to other cathode materials shown in Table 16 [240, 241].

Table 16. Comparison of the properties of different cathodes in 18 650 cells

Property	LiAl$_{0.05}$Co$_{0.15}$Ni$_{0.8}$O$_2$	LiCoO$_2$	LiFePO$_4$
Average potential (V)	3.65	3.84	3.22
Theoretical capacity (mAh·g^{-1})	265	274	170
True density (g·cm^{-3})	4.73	5.05	3.60
Conductivity (S·cm^{-1})	-	10^{-3}	10^{-9}
Diffusivity (cm^2·s^{-1})	10^{-8}	10^{-8}	10^{-13} to 10^{-16}
Specific energy (Wh·kg^{-1})	219.8	193.3	162.9
Energy density (Wh·L^{-1})	598.9	557.8	415.0
Materials cost (US $)	1.628	1.82	1.22

However, its drawbacks include relatively low electronic conductivity, challenging lithium cation diffusion, and low tap density, which negatively impact its gravimetric and volumetric energy density. To address these issues and enhance their performance for large-scale applications like electric vehicles, various methods such as surface coating, doping, and synthesis optimization have been developed to improve the electronic and ionic conductivity of LFP cathode materials [242].

5.2.1. Strategies for improving electronic conductivity

Surface coating techniques have been studied as a method to improve the dispersion and thermal stability of AM particles, enhance the electronic conductivity of LFP, and enhance the physical, chemical, and mechanical properties of LFP cathode materials [243].

Carbon coating is particularly effective; by mixing battery materials with carbon precursors and applying high-temperature thermal treatments, the conductivity of the battery material can be significantly improved. This method is both simple and feasible for large-scale industrial production [244, 245]. CNTs and graphene have also been used to create a 3D conductive network within the electrode, which further enhances conductivity and electrochemical performance. Graphene, in particular, has shown promise as a CM. Its layered structure and excellent electronic conductivity create a more effective conductive framework compared to traditional carbon black. Studies have demonstrated that LFP electrodes using graphene can achieve higher discharge capacities and better rate performance. Additionally, incorporating graphene into the electrode can form a nanoscale three-dimensional network that improves electron conductivity and restricts the growth of LFP crystalloids [226]. Therefore, graphene is not only a promising CM, but also provide high-rate performance through a simple and viable method [246].

5.2.2. Strategies for improving lithium cation diffusivity

Improving lithium cation diffusivity in LFP is critical for enhancing battery performance, particularly for fast-charging applications in electric vehicles [199]. One effective approach is ***reducing the particle size of LFP.*** Smaller particles shorten ion diffusion pathways, leading to better rate capability. For instance, carbon-coated and core-shelled LFP materials with nano-sized particles have shown significant improvements in discharge capacity, attributed to increased lithium cation diffusion [247, 248].

Another method involves ***suppressing antisite defects,*** where iron occupies lithium sites, blocking diffusion pathways. Solvent selection during synthesis can control these defects [245]. For example, using ethanol as a solvent in a solvothermal process has produced LFP with fewer antisite defects, enhancing its electrochemical performance. Doping with various ions can also improve both electronic and ionic conductivity, further boosting the rate capability and cycling performance of LFP. When Ni and Zn were used to dope LFP, it showed notable improvements in performance [249, 250].

LFP morphology plays an important role in improving the kinetics of the lithium extraction/insertion process. The one-dimensional lithium diffusion suggests that the synthesis of thin and well-dispersed LFP with a large surface area would enhance high-rate performance [246, 251]. Therefore, synthesis of large surface area forms such as nanowires, nanoparticles, nanosheets, and core-shell structures allow fast lithium cation and electron transportation, enabling high electrochemical performance.

5.2.3. Strategies for improving low-temperature performance

LFP-based LIBs typically exhibit poor discharge rate performance at low temperatures due to low electronic and ionic conductivity. To address this, researchers have explored various preparation techniques. For instance, using a ferrous phosphate precursor and combining liquid co-precipitation with a polyol process has produced LFP/C with improved low-temperature performance [252, 253]. These materials demonstrated good electrochemical properties, with minimal capacity fading, less than 3%, even at sub-zero temperatures. This is attributed to the highly crystalline structured nano–sized LFP/C particles and the uniform carbon coating.

Combining ionic and electronic conductor coatings allows faster lithium cation diffusion [244]. It can also enhance the rate performance and low-temperature performance. Coating LFP with materials like Li_3PO_4 or $CePO_4$ allows for faster lithium cation diffusion, and when combined with a carbon coating, results in hybrid coatings that improve both rate performance and low-temperature characteristics. This approach has led to materials with high reversible specific capacities of ~100 $mAh·g^{-1}$ even at temperatures such as –20°C, though optimizing the ratio and method of hybrid coating remains a challenge. Additionally, improving the particle size distribution of LFP can enhance its performance at low temperatures. Techniques that produce highly crystalline, uniformly coated nano-sized particles showed significant improvements in low-temperature electrochemical properties. These methods help to optimize the material's structure, reducing defects and improving conductivity, which are crucial for better performance in cold environments [240, 254].

5.2.4. Strategies for enhancing tap density (for higher volumetric energy density)

High tap density in (which means high volumetric energy density) in LFP materials in LIBs is critical for their large-scale industrial application in electric vehicles [255]. Traditional LFP materials have relatively low tap densities (1.0 $g·cm^{-3}$), requiring larger battery volumes compared to materials such as LCO (2.2 $g·cm^{-3}$) for the same discharge capacity. To address

this, researchers have explored various synthesis methods to increase tap density while maintaining the morphology and size distribution of LFP particles [256].

One approach is ***synthesizing porous LFP microspheres with interconnected open pores.*** These structures facilitate fast lithium cation diffusion by reducing diffusion length. Carbon-coated LFP microspheres with high tap densities have been synthesized using methods like coprecipitation and hydrothermal processes. These materials achieve tap densities ranging from 1.0 to 1.5 g·cm^{-3}, which is significantly higher than common LFP electrode AMs [247]. These electrodes can achieve densities of up to 1.5 g·cm^{-3}, offering higher volumetric energy density. However, reducing particle size to improve rate performance can adversely affect tap density. Balancing size reduction while maintaining high tap density is crucial, as smaller particles tend to have higher surface areas, leading to unwanted side reactions and poor cycling performance. Recent advancements have shown that controlling the morphology and size distribution of LFP particles can lead to high tap densities without compromising performance. For example, a two-step drying process has produced LFP/C composites with tap densities as high as 1.8 g·cm^{-3}, significantly enhancing specific capacity and energy density. Table 17 shows examples of differences in the preparation method, morphology and tap density [245, 257, 258].

Table 17.   Comparison between the tap densities of LiFePO$_4$/C

Method	Morphology	Tap density (g·cm^{-3})
Co-precipitation	Spherical	1.0
Solvothermal	Flower-like	1.2
Hydrothermal	Microsphere	1.2
Carbothermal reduction	Micro/nano spherical	1.3

5.2.5. Summary of olivine LFP positive materials

LFP has emerged as a promising material for LIBs, particularly in EVs, due to its safety, cost-effectiveness, and specific capacity. However, several challenges remain, such as improving rate capability, capacity density, cycle life, and low-temperature performance. Various strategies have been explored to address these issues, focusing on enhancing electronic and ionic conductivity, optimizing particle size, and synthesis techniques.

Carbon coating and doping are key methods for increasing electronic conductivity. While carbon coating enhances conductivity between particles, doping with cations and anions can significantly improve intrinsic conductivity, despite ongoing debates about the precise mechanisms. Downsizing particles is essential for improving ionic conductivity, but balancing this with maintaining high tap density is challenging**.**

Understanding the kinetics of phase transformation and surface chemistry is crucial for achieving high-rate performance and volumetric energy density. Improving *low-temperature performance* involves optimizing material preparation to produce highly crystalline, uniformly coated, nano-sized particles.

Novel electrolyte formulations may also enhance performance in cold environments. For large-scale production, developing reliable, low-cost synthesis methods is vital to prepare LFP cathode materials with high-rate performance. With continued research and development, LFP has the potential to become widely used in LIBs for electric vehicles, meeting stringent technical requirements and industry demands. The production of LFP in China in 2023 has been at >1.6 millions of tons, far exceeding that of various NMCs.

5.3.   Olivine LiMn$_{1-x}$Fe$_x$PO$_4$ (LMFP) cathode materials

Olivine LFP, known for its orthorhombic structure, offers a promising alternative for LIB cathodes due to its low toxicity of ferrous ions, and stability of phosphate ions [25].

Despite its theoretical capacity of 170 mAh·g^{-1}, its voltage of about 3.5 V *vs*. Li/Li$^+$ is lower than desired for high-performance applications. Thus, it has been turned to element-doped compounds such as LiMnPO$_4$ (LMP) and LMFP, which offer higher voltage platforms around 4 V *vs*. Li/Li$^+$, making them suitable for next-generation batteries [259].

The shift towards LMP is driven by its higher redox potential of 4.1 V *vs*. Li/Li$^+$. Although LMFP batteries can achieve a capacity of 171 mAh·g^{-1} at low current densities, their performance drops significantly at higher currents due to slow lithium cation diffusivity. This can be attributed to the slow diffusivity of lithium cations in MnPO$_4$ and the misfit in the lattice parameters between the LMP phase and the MnPO$_4$ [226, 240]. LMP phase works with poor electrical and ionic conductivity, and the Jahn-Teller effect from Mn$^{2+/3+}$. This effect would lead to the meta stability of the delithiated phase, and a rapid capacity degradation compared to LFP [260]. These challenges require further improvements through methods like carbon coating, cation doping, and nanosizing to enhance its electrochemical performance.

5.3.1. Carbon coating

Carbon coating is a widely adopted strategy to enhance the electronic and ionic conductivity of LMP–based materials. Carbon used for this purpose can be pyrolyzed amorphous carbon from organic sources or graphitic carbon like graphene and CNTs [261]. Pyrolyzed carbon forms a uniform layer on nanoparticles, facilitating lithium cation access, but has lower conductivity compared to graphitic carbon. For instance, graphene, known for its

superior electronic conductivity, has been used to modify olivine materials by the ball milling method or adding graphene oxide directly into solvothermal reactants [224].

Studies have shown that composites like $LiMn_{0.85}Fe_{0.15}PO_4/C$, synthesized using methods such as ultrasonic pyrolysis and ball milling demonstrate enhanced discharge capacities [240]. $LiMn_{0.5}Fe_{0.5}PO_4/C$ nano-plates synthesized by a simple solvothermal method has resulted in excellent cycling performance [224, 262]. Furthermore, dual doping with pyrolyzed carbon and reduced graphene oxide ($LiMn_{0.9}Fe_{0.1}PO_4$, LMFP/C/rGO) has been found to provide superior electrochemical performance, maintaining around 95% of the initial capacity after 140 cycles at 0.2C rate [263]. This improvement is attributed to the synergy between uniformly coated pyrolyzed carbon and the high conductivity of graphene [264].

5.3.2. Cation doping

Cation doping, particularly substituting Mn^{2+} with Fe^{2+}, is a common approach to boost the electrochemical activity of LMFP. Although excessive $Fe^{2+}+$ substitution can lower the energy density due to its lower redox potential, optimal doping levels can enhance rate capability and stability [260].

Multi-element doping at the Mn site, involving elements like Mg, Co, and Ni, has shown to improve rate capabilities and cycling stability [226]. These enhancements are due to improved kinetics and reduced lattice mismatches, aiding lithium cation diffusion. Further studies are needed to understand the relationship between doping compositions and defect behaviors, which can significantly influence the performance of LMP materials.

5.3.3. Nanosizing of the LMFP materials

Various synthesis methods have been explored to synthesize nano-LMFP [265]. Each method has its advantages and challenges, such as the high-temperature requirements of hydrothermal synthesis or the difficulty in achieving stoichiometric ratios with co-precipitation. Nanosizing improves electrochemical performance by reducing diffusion distances for lithium cations and electrons [260]. For instance, using PEG 4000 as a template in the rheological phase reaction method produces $LiMn_{0.5}Fe_{0.5}PO_4/C$ nanorods with uniform carbon coating and enhanced electrochemical performance of 162, 133, 108, 95, and 78 mAh·g^{-1} at 0.1, 1, 5, 10, and 20 C rates respectively. Such composites retain high capacities even at fast discharge rates. The improved performance is attributed to the smaller crystal sizes, which shorten lithium cation diffusion paths, highlighting the benefits of nanosizing in enhancing electrochemical performances [260].

5.3.4. Summary of LMFP cathode materials

Despite significant advancements in the development of LMFP as cathode materials for high-energy and high-power LIBs, challenges remain. Poor electronic conductivity and lithium cation diffusion coefficients limit their rate capability. Strategies like cation/anion doping, carbon coating, and particle morphology control have shown promise in overcoming these issues, yet more research is needed.

For large-scale commercial applications, improving specific capacity, rate performance, cycle life, and thermal stability through cost-effective and environmentally friendly synthesis methods is crucial. The development of LMFP-based full batteries will be the key to their feasibility for electric vehicles, hybrid electric vehicles (HEVs), and large-scale storage systems, requiring ongoing efforts to address fundamental and technological challenges.

5.4. Spinel $LiMn_2O_4$ cathode materials

$LiMn_2O_4$ is an attractive cathode material for LIBs due to its low cost, suitability for high current applications, good low-temperature performance, and environmental compatibility [266]. Ball milling is considered as an efficient method for synthesizing this material [267]. However, its capacity deteriorates at elevated temperatures above 55°C, which poses a significant challenge for practical applications. The primary degradation mechanisms include Mn^{2+} dissolution in the electrolyte through the disproportionation reaction of $2Mn^{3+} => Mn^{2+} + Mn^{4+}$; electrolyte decomposition at high voltages, and irreversible structural changes due to the Jahn-Teller effect [268]. To address these issues, various technical improvements have been explored. Doping with TMs like Al, Mg, Ni, Co, and Cr can stabilize the structure and enhance performance at high temperatures, though excessive doping can reduce capacity. Coating with metal oxides such as Al_2O_3, Fe_2O_3, Y_2O_3 and TiO_2 helps to reduce side reactions with the electrolyte, though it can impede lithium cation intercalation [269, 270]. Effective coating materials and processes are essential to balance stability and ion transfer, with Li_2MnO_3 showing promise as a stabilizing layer that reduces Mn^{3+} dissolution and improves cycle life.

Researchers have investigated various positive materials, such as $LiNi_{0.5}Mn_{0.5}O_2$, $LiNi_{1/3}Co_{1/3}Mn_{1/3}O_2$, $LiNi_xMn_{2-x}O_4$, and $LiNi_{0.5}Mn_{1.5}O_4$, as surface coating layers for $LiMn_2O_4$ to address its degradation issues [267]. Surface coating has emerged as a viable method to enhance the stability of lithium manganese oxide ($LiMn_2O_4$) electrodes. Among the manganese compounds, Li_2MnO_3 is noteworthy for its layered structure, providing a two-dimensional

pathway for lithium cation intercalation/de-intercalation while remaining electrochemically inert below 4.5 V *vs*. Li/Li$^+$ [271]. This makes Li$_2$MnO$_3$ an effective stabilizing coating layer for other positive electrode materials, shielding them from direct electrolyte exposure without hindering lithium cation movement.

Peng et al. demonstrated a straightforward method to create LiMn$_2$O$_4$@Li$_2$MnO$_3$ composites with varying coating contents [272]. Their study revealed that a sample with a 3 wt.% Li$_2$MnO$_3$ coating exhibited superior electrochemical performance compared to uncoated LiMn$_2$O$_4$, delivering a discharge capacity of 110 mAh·g^{-1} at 1C, with capacity retentions of 94.17% after 500 cycles at 25°C and 89.75% after 200 cycles at 55°C. This Li$_2$MnO$_3$ layer effectively acted as a barrier, reducing direct contact between the AM and the electrolyte, enhancing stability through thermal treatment, and suppressing the disproportionation reaction ($2Mn^{3+} => Mn^{2+} + Mn^{4+}$) and Mn^{2+} dissolution into the electrolyte.

Additionally, kinetic analysis is crucial for improving LiMn$_2$O$_4$ performance and reducing deterioration. Slow lithium cation diffusion in micron-scale electrode powders limits the charging speed of LIBs. Researchers found that using nanoporous LiMn$_2$O$_4$ powders with smaller crystallite sizes (10, 20, 40, and 70 nm) shortened diffusion paths, speeding up charging times [270]. Smaller crystallite sizes resulted in lower capacity but faster charge/discharge rates, longer cycle life, and higher capacitive contributions. The 40 nm sample emerged as the most promising for practical applications, retaining around 75% capacity after 2000 cycles, suggesting a critical size threshold above which performance deteriorates significantly [269, 273].

Crain et al. studied the effects of ball-milling time on the electrochemical behavior of LiMn$_2$O$_4$ electrodes, composed of a mix of nano- and micrometric particles. They found that nanoparticles facilitate surface-localized lithium insertion/extraction, enhancing charge/discharge rates, while micrometric particles stabilize the nanoparticles, preventing segregation and excessive electrolyte reactions. This balance improves electrode cyclability and performance. Despite these advancements, the thermal stability of LiMn$_2$O$_4$ materials remains a significant challenge, particularly at high temperatures. Future research must focus on further improving the stability and performance of LiMn$_2$O$_4$ in these conditions to ensure the practicality and longevity of these materials in real-world applications. Continued exploration of suitable coating materials and processes, as well as an in-depth understanding of kinetic behaviors, will be essential for the ongoing enhancement of LIB technologies [272].

5.5. Green and sustainable perspective on cathode materials

Layered metal oxides with the generic formula of $LiMO_2$, comprising various metals such as Ni, Mn, Co, and Al ($LiNi_{1-x-y-z}Mn_xCo_yAl_zO_2$, abbreviated as NMC or NCA), represent the current state-of-the-art cathode materials in most LIB cells. These materials exhibit key properties such as practical specific capacity (140–210 mAh·g^{-1}), redox potential (~3.7 V *vs* Li/Li$^+$), material density (4.5–5.1 g·cm^{-3}), and rate capability, outperforming other viable cathode material candidates [196, 226]. Li/Mn-rich layered oxide cathodes ($Li_{1+x}M_{1-x}O_2$, where x = 0.15–0.20 and M = Ni, Mn, Co, abbreviated as LMR-NMC) offer high initial practical capacities (200–300 mAh·g^{-1}), [130, 213, 274], but face challenges like insufficient cycle life, lower rate capability, lower redox potential and lower material density compared to NMC. An overview of various commercial and alternative cathode materials, including their sustainability and technological maturity, is provided in Figure 5.
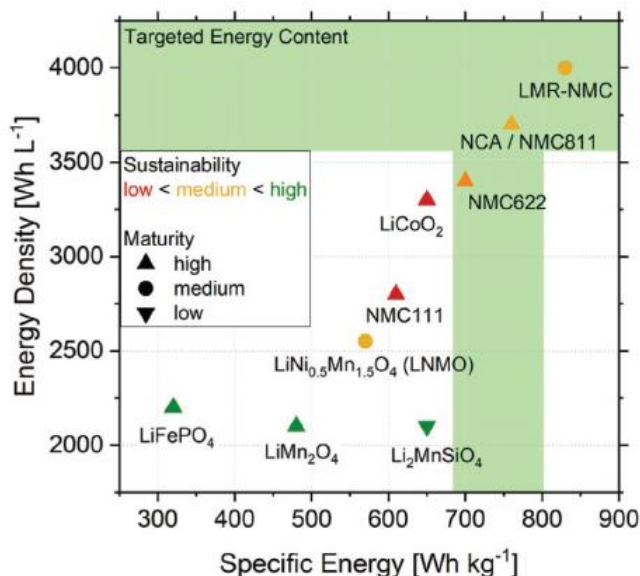
Figure 5. Energy density vs. specific energy for cathode materials for LIBs. Energy data and targeted energy content (indicated by green bands) taken from ref. [9]

Critical raw materials for LIBs, such as Co, and Ni, are predominantly associated with the cathode material. Co and Ni are classified as carcinogenic, mutagenic, and toxic to reproduction (CMR) [9]. Co is a major cost driver and raises significant moral and environmental concerns due to questionable mining conditions in central Africa [9]. Despite the critical nature of Cobalt (Co), LCO, which relies exclusively on Co as the redox-active TM, remains widely used for small-sized batteries in portable consumer electronics (<50 Wh, e.g., smartphones, tablet computers). This is primarily due to its high material density (5.1 g·cm^{-3}), good rate capability, and cycle life. The absolute Co demand for small-sized batteries is

relatively low, often justifying the higher cost for a more compact battery. Despite their widespread use and high Co content, most used cells are not currently recycled [48].

The demand for LIBs with higher energy densities and the high cost of Co have led to increasing Ni and decreasing Co contents in layered cathodes, such as transitioning from NMC111 to NMC811. Manufacturers are introducing NMC811 and NCA with Ni contents > 90% into their batteries, although this high-Ni approach improves energy content at lower costs but reduces cycle life and safety [199, 275].

To enhance the long-term cycling stability of layered cathode materials, the synthesis of single crystal materials has been intensively explored recently. Unlike polycrystalline cathodes, typically synthesized via a coprecipitation route, single crystal cathode materials are prepared in a salt flux, consisting of larger particles with lower specific surface areas [276]. This reduced surface area decreases the tendency for parasitic reactions, such as electrolyte oxidation or gas release, thereby extending cycle life compared to polycrystalline materials. Although single crystal cathodes exhibit slightly lower capacities [275], they could play a significant role in long-life battery applications. Considering potential raw material scarcity, Co-free cathode chemistries like the high-voltage spinel $LiNi_{0.5}Mn_{1.5}O_4$ (LNMO) and certain Li/Mn-rich oxide compositions are gaining attention as alternatives to current cathode materials [277]. Element availability is particularly crucial for larger-scale applications like electromobility (20–100 kWh) or grid storage, where extensive amounts of raw materials are required.

Phospho-olivine-type cathode materials like LFP or LMFP are considered ecofriendly since they consist solely of abundant elements [1, 169]. The high structural stability of the polyanionic phosphate network and the relatively low operational voltage window, which prevents unwanted parasitic reactions of the battery electrolyte, allow long cycle and shelf life for LFP-based LIBs. However, they do not meet the requirements of the automotive industry in terms of energy content at the material level (min. 680 $Wh \cdot kg^{-1}$ and 3600 $Wh \cdot L^{-1}$, green bands in Figure 5) and are thus preferably used in stationary energy storage systems as well as electric buses and other heavy-duty automotive applications, such as trucks. Their long cycle life and low raw material costs, however, could lead to a low total cost of ownership (TCO) for LMFP-based batteries compared to other high-energy chemistries, especially since their currently high production cost is expected to decrease in the coming years. The isostructural analogues $LiMPO_4$ with M = Co, Ni, which involve Co or Ni as redox-active metals, promise higher energy densities due to their higher redox plateau at a similar capacity. However, this material class possess limited practical feasibility due to their very low electronic conductivity and insufficient compatibility with current electrolytes [240, 278].

6. ELECTRODES – ANODE MATERIALS

The increasing demand for LIBs with higher energy and power density has made the development of high-performance LIBs more urgent. The anode, one of the key components (along with the cathode, and electrolyte), plays a crucial role in determining LIB performance. Current commercial anode materials include carbonaceous materials (such as NG, SG and amorphous carbon), lithium titanate (LTO), and silicon (Si)-based materials (such as nano silicon carbon materials, SiO_x, and amorphous silicon alloy). This section presents the performance of anode materials under extreme conditions, such as low temperatures, in comparison to their performance at room temperature [279]. It is worth to highlight that improving electrolyte properties alone is insufficient, as changes in the electrode materials, such as reduced electron and Li^+ conductivity due to excessive passivation films (CEI and SEI), also contribute to low-temperature degradation. Thus, understanding anode performance at such conditions is essential to address the influence of each component.

An overview of the known anode materials categories is shown in Figure 6, [225].
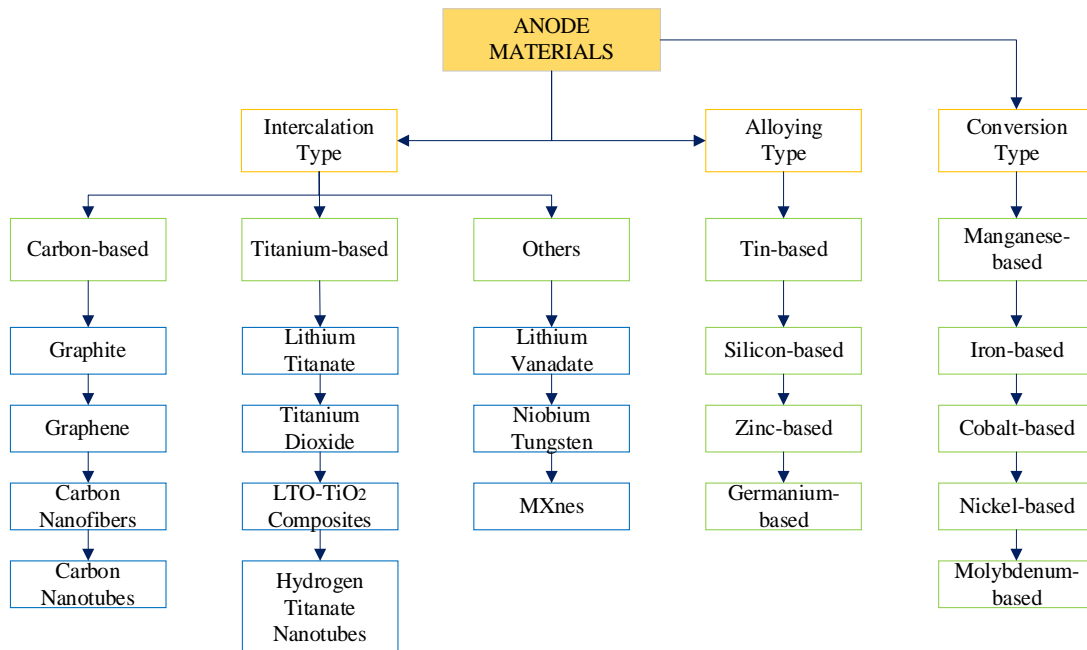
Figure 6. Summary of studied anode materials for LIBs

The lithiation and delithiation processes at the anode involve surface processes, which include Li^+ kinetics within the SEI and charge transfer mechanisms on the anode surface, and volume processes governed by diffusion coefficients. At extreme conditions, both surface and volume processes are adversely affected, resulting in increased polarization, poor capacity, and a higher risk of dangerous lithium plating. Beyond the commonly used graphite anode

materials, numerous materials and composites have been developed. These anode materials offer higher gravimetric and areal specific capacities and operate at higher voltages *vs.* Li/Li$^+$.

6.1. Intercalation-type anodes

Anode materials, such as graphite, reversibly store lithium through an intercalation/deintercalation mechanism. During the lithiation and delithiation processes, lithium cations are inserted into and extracted from the host structure, respectively, resulting in minimal volume changes without altering the basic structure of the material. Consequently, intercalation-type anodes exhibit excellent cycling stability and high-rate capability. This intercalation/deintercalation process can be represented by the following reaction:

$$MO_x + yLi^+ + ye^- \leftrightarrow Li_yMO_x \tag{6.1}$$
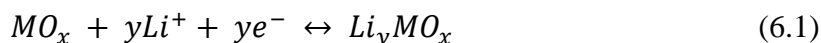
where M represents metal. Common intercalation-type anode materials include carbon-based materials like graphite, graphene, CNTS, CNFs, and titanium-based materials such as lithium titanate and titanium dioxide [280].

Carbon-based materials are widely used as anode materials in commercial LIBs, offering high specific capacity, good coulombic efficiency, and long cycle life [281]. In addition to the prevalent carbon anode, graphite, and other carbon materials with various microstructures, textures, crystallinities, and morphologies have been developed. Nanosized carbon materials, such as graphene, CNTs, and (CNFs are alternative electrode materials that could provide enhanced electrochemical performance.

6.1.1. Carbon-based materials: graphite

Graphite is the most common anode material due to its low cost, abundance, and low operating voltage. It has been widely used since the first commercial LIB with a graphite anode. During lithiation, lithium cations intercalate into the spaces between graphene layers, forming a Li-rich phase with a theoretical specific and volumetric capacity of 372 mAh·g^{-1} and 850 mAh·cm^{-3} [155, 282], respectively.

However, graphite performs poorly at low temperatures due to increased resistance in the passivation layer, bulk electrode, and charge transfer at the electrode/electrolyte interface, alongside decreased lithium diffusion rates. This leads to high polarization, approaching the Li deposition potential before intercalation completes, raising safety concerns due to lithium metal deposition and dendrite formation, which can cause short circuits [283].

Zhang et al. [284] investigated the performance of graphite electrodes in electrochemical cells at low temperatures. They found that when both lithiation and delithiation were conducted at −20°C, the retained delithiation capacity was only 12% of the capacity at room temperature. However, when lithiation was performed at room temperature, 92% of the capacity was retained.

Wang et al. [285] explored the low-temperature behavior of graphite and mesocarbon microbeads (MCMB) electrodes using GITT and EIS. They observed that the limited lithium insertion into graphite at −30°C was due to its higher polarization compared to the equilibrium plateau potential for the lithium-rich phase. Additionally, the study revealed that the SEI film resistance was 27 times higher, and the electrolyte resistivity was 10 times higher at −30°C compared to 25°C, leading to significant polarization and limited lithium insertion at low temperatures.

To enhance the low-temperature performance of graphite anodes, researchers have explored the addition of metal powders or coating the graphite surface with a thin metal layer. Mancini et al. [286] investigated the effects of mixing copper powder with partially oxidized graphite or coating its surface with a thin copper layer. They found that both methods improved the low-temperature electrochemical performance of graphite anodes by reducing charge transfer resistance. Cyclic voltammetry revealed that the surface copper layer was more effective than powder in decreasing overall polarization.

Graphite-tin composites, created either by adding tin powder or coating with a thin Sn layer, were studied by Nobili et al. [287] Both strategies provided good cycling stability at room temperature and significant improvements at low temperatures.

Gunawardhana et al. [225] proposed using chemical vapor deposition (CVD) to apply a carbon coating on the surface of graphite anodes to prevent lithium deposition at temperatures below 0°C. Their study showed that at the range of 10-15% carbon coating effectively suppressed lithium deposition on NG during cycling at −10°C. This was due to the formation of an effective SEI layer that facilitated lithium intercalation and C_6Li formation, suggesting that surface modification by carbon coating can enhance both performance and safety of graphite anodes in low-temperature conditions [288].

Zhao et al. [288] suggested an expansion modification to improve the low-temperature performance of mesocarbon microbeads (MCMB). By increasing the interlayer distance, they facilitated lithium cation insertion kinetics, achieving a capacity of around 100 mAh·g^{-1} at −40°C for expanded MCMB, compared to almost no capacity for pristine MCMB. The superior

performance of expanded MCMB was attributed to smaller charge transfer resistance and better lithium diffusion kinetics due to the increased interlayer distance.

Park et al. [288] examined the effects of various degrees of graphitization, rhombohedral phase content, and surface areas on the low-temperature electrochemical performance of graphite. They found that with higher degrees of graphitization the electrodes were more affected by the drop of temperature. Increased lithium deposition was observed on rhombohedral graphite due to accumulation at the edge planes. Additionally, spherical graphite with a high surface area provided an increased pathway for lithium intercalation and decreased lithium deposition, indicating that particle shape and surface area play crucial roles during the battery performance.

Marinaro group [289] developed a composite of copper nanoparticles supported on Super-P carbon to improve the low-temperature performance of graphite anodes. Graphite electrodes with this Cu/Super-P composite retained significantly higher capacities during cycling at −30°C compared to those with pristine Super-P. The addition of copper particles enhanced interfacial charge transfer kinetics and reduced DC-electrical resistance, leading to improved capacity retention at low temperatures. Similarly, Yaqub et al. [290] found that electrodes with higher copper content in the Cu/Super-P composite delivered higher capacities at −32°C compared to those with pristine Super-P. Their full-cell tests showed over 50% capacity retention at various C-rates, highlighting the effectiveness of copper in enhancing low-temperature performance.

6.1.2. Carbon-based materials: graphene

Graphene, due to its unique structure, has shown potential for enhanced low-temperature performance in LIBs. Multilayer crystalline graphene (GRAL) can intercalate and de-intercalate lithium cations similarly to graphite but offers superior low-temperature performance due to smaller particle size and thickness, which enhance lithium diffusion. GRAL electrodes have delivered significantly higher capacities at low temperatures compared to graphite [291].

For example, under low-temperature cycling at 0.05 A·g^{-1} and 0.1 A·g^{-1}, GRAL achieved capacities of 224 mAh·g^{-1} and 160 mAh·g^{-1} at −20°C and 112 mAh·g^{-1} and 64·mAh·g^{-1} at −30°C after 45 cycles, respectively. The superior low-temperature performance can be attributed to the small particle size and thickness, which improves lithium diffusion into the carbonaceous matrix.

Another innovative approach involves using a surface-controlled charge storage mechanism by developing free-standing electrodes of 3D crumpled graphene particles within a few-walled carbon nanotube (FWNT) matrix [281].

This configuration has shown impressive low-temperature performance, delivered high capacities and maintained stability even at very low temperatures. For instance, such electrodes delivered 215 mAh·g^{-1} at -20°C, 135 mAh·g^{-1} at -40°C and 48 mAh·g^{-1} at -60°C, with excellent rate capability and cycling stability. This performance is attributed to the transition from a diffusion-controlled to a surface capacitive current-controlled charge storage mechanism as temperature decreases, demonstrating graphene's potential for low-temperature applications.

6.1.3. Carbon-based materials: carbon nanofibers (CNFs)

Carbon nanocomposites that include metal catalysts like iron carbide (Fe_3C) can enhance the reversible capacity of carbon anodes by reducing some SEI components. Li's group [292] developed a homogeneous hybrid material incorporating iron metal into a composite of Fe_3C CNFs (Fe/Fe_3C-CNFs). They tested the electrochemical performance of the Fe/Fe_3C-CNF anode at -15°C, achieving 270 mAh·g^{-1} under 400 mAh·g^{-1} and 380·mAh·g^{-1} under 200 mA·g^{-1} after 50 cycles. These findings suggest that the presence of Fe can significantly enhance the low-temperature performance of CNFs by increasing conductivity and reducing charge transfer resistance.

Electrodes containing Cu powder in graphite or Super P, and those coated with a Sn layer, can deliver around 150 mAh·g^{-1} at -20°C. At extremely low temperatures of -40°C and -60°C, galvanostatic cycling tests have been performed only on structure-controlled crumpled graphene anodes, which deliver approximately 140 mAh·g^{-1} and 50 mAh·g^{-1}, respectively, at a low C-rate ($<$C/20). In terms of areal specific capacity, values exceeding 1 mAh·cm^{-2} are maintained down to -10°C, while at -30°C, graphite anodes coated with a Sn layer or mixed with Cu/Super-P composite can provide nearly 0.5 mAh·cm^{-2}.

In conclusion, the main challenges of carbon-based anodes at low temperatures include very high charge transfer resistance and low lithium cation diffusion, particularly during the lithiation process. These issues, combined with their low lithiation potential versus Li/Li$^+$, lead to high polarization at low temperatures, which significantly hampers the full lithiation of the anode. Graphene-based materials, owing to their layered structure, may offer enhanced conductivity and improved lithium diffusion coefficients. However, their complex preparation methods pose scalability issues, limiting their mass loadings and making them less suitable for commercial applications due to their insufficient areal specific capacities [293].

6.1.4. Titanium–based materials: lithium titanate (LTO)

Spinel lithium titanate ($Li_4Ti_5O_{12}$ or LTO) is a notable anode material with a theoretical capacity of 175 mAh·g^{-1} and a stable operating voltage of 1.55 V *vs.* Li/Li$^+$. This voltage is advantageous for low-temperature LIBs because it is above the reduction potential of commonly used electrolyte solvents, preventing the formation of a SEI, and it minimizes the risk of lithium plating at low temperatures.

Additionally, LTO is a zero-strain lithium insertion host, exhibiting minimal volume change (0.1–0.2%) during charge/discharge cycles, which ensures structural stability and long cycle life. However, LTO's capacity is lower than that of graphite, and its near-insulating electronic conductivity (10^{-13} S·cm^{-1}) hampers its electrochemical kinetics [294].

Allen et al. [295] examined the impact of particle size on the low-temperature electrochemical performance of $Li_4Ti_5O_{12}$ anodes. Discharge capacities for 350-nm LTO were about 152, 148, 135, 115, and 80 mAh·g^{-1} at 20°C, 0°C, -10°C, -20°C, and -30°C, respectively, whereas 700-nm LTO showed capacities of 163, 135, 92, 60, and 35 mAh·g^{-1} under similar conditions. This suggests that smaller particle sizes improve low-rate, low-temperature performance due to shorter diffusion lengths and more lithium insertion sites. However, at higher rates of 1C to 5C, the 700-nm LTO outperformed the 350-nm LTO, due to fewer interparticle contacts.

Phjalainen et al. [225] also studied the influence of LTO particle size on high C-rate and low-temperature performance using high (LTO-SP) and light (LTO-LP) grinding during milling. At 0.1C from 20°C to -20°C, both electrodes showed similar capacities. However, at 1C, the LTO-SP electrode delivered 109 mAh·g^{-1} at -20°C, higher than the 83 mAh·g^{-1} of LTO-LP, due to the surface effect and higher reaction voltage of surface sites.

Yuan et al. [296] developed pristine and carbon-coated $Li_4Ti_5O_{12}$ ($Li_4Ti_5O_{12}$/C) electrodes using a cellulose-assisted combustion technique. The carbon coating, being amorphous, highly porous, and about 5-nm thick, significantly reduced charge transfer resistance. At -20°C, the carbon-coated LTO delivered higher discharge capacities of 119·mAh·g^{-1} at 1C and 41 mAh·g^{-1} at 10C, compared to 108 mAh·g^{-1} and 31 mAh·g^{-1} for pristine LTO, respectively. This indicates that carbon coating enhances LTO performance at low temperatures and high rates.

Liang et al. [272] created a peapod-like nano-sized $Li_4Ti_5O_{12}$-Carbon composite with LTO nanoparticles encapsulated in carbon fiber/tubes. This composite showed excellent cycling stability and rate capability, retaining 152 mAh·g^{-1} after 5000 cycles at 10C and

delivering 125 mAh·g^{-1} at 90C. At -25°C, it retained 157 mAh·g^{-1} after 500 cycles at 10C and had a discharge capacity of 122 mAh·g^{-1} at 30C, highlighting the benefits of uniform carbon coating and synergistic effects between the AM core and carbon-fiber shell. Zhang et al. [297] used a dry method surface fluorination strategy with NH$_4$F to enhance the low-temperature performance of commercial LTO. The fluorinated LTO (F-LTO) delivered a stable discharge capacity of 130 mAh·g^{-1} at -10°C and 100 mAh·g^{-1} at -20°C at 1C, retaining 82.6% and 63.3% of room-temperature capacity, respectively. This is attributed to a larger specific surface area, faster lithium cation transfer, and enhanced electronic conductivity due to Ti^{3+} presence.

Wang et al. [298] modified LTO with NF$_3$ gas fluorination. The fluorinated LTO (F-LTO) exhibited better electrochemical performance than pristine LTO, delivering 65 mAh·g^{-1} at -20°C after 100 cycles at 1C. This enhancement is likely due to Ti^{3+} presence, which improves electrode kinetics by reducing polarization and increasing lithium cation diffusion coefficient. Zou's group [299] employed a strategy of heteroatoms doping to improve LTO's electronic conductivity. They fabricated Li$_{3.9}$Cr$_{0.3}$Ti$_{4.8}$O$_{12}$ nanofibers with an in-situ surface coating of Li$_2$CrO$_4$, enhancing interparticle and intraparticle conductivities. The LCTO-NF structure retained a stable discharge capacity of around 130 mAh·g^{-1} at -10°C after 100 cycles at 1C. In 2019, Ho's group [290] embedded Li$_4$Ti$_5$O$_{12}$ nanoparticles in a hierarchical macropore-mesoporous shell carbon network (LTO/HCMS-C). This nanocomposite demonstrated excellent long-term stability at high currents and low temperatures, retaining 76% of capacity at -10°C and 40% at -20°C after 1000 cycles at 10C.

6.1.5. Titanium–based materials: titanium dioxide (TiO$_2$)

Titanium dioxide (TiO$_2$) offers a theoretical capacity of 335 mAh·g^{-1} with a working potential between 1.5–1.8 V $vs.$ Li/Li$^+$. Among its polymorphs, rutile TiO$_2$ is the most stable but can only accommodate minimal lithium at room temperature. Decreasing particle size significantly enhances lithium reactivity [300]. Marinaro et al. found that using a broader potential window improved the low-temperature performance of nanosized rutile TiO$_2$, delivering 77 mAh·g^{-1} at −40°C when cycled at C/5, which is over 20% of its room temperature capacity (324 mAh·g^{-1}) [301].

Mancini et al. explored the impact of various binders on anatase TiO$_2$ anodes. Using sodium carboxymethyl cellulose (CMC, sodium salt is Na-CMC) instead of PVdF resulted in similar performance but with lower initial irreversible capacity loss and higher capacity at high rates. TiO$_2$/CMC electrodes also showed lower polarization and overall impedance, suggesting that environmentally friendly and cost-effective binders can be used without sacrificing

performance. These findings highlight the importance of particle size and binder selection in enhancing the electrochemical performance of TiO_2-based anodes at low temperatures [286].

6.1.6. Titanium-based materials: LTO/TiO₂ composites

The low-temperature performance of $Li_4Ti_5O_{12}$ (LTO) combined with rutile TiO_2 (LTO-RTO) has been investigated, showing significant improvements over pure LTO. Huang et al. [302] demonstrated that an LTO-RTO composite retained higher discharge capacities at −40°C compared to pristine LTO, indicating reduced structural changes and lower activation energy at low temperatures. This improvement is attributed to the composite's enhanced crystal structure stability and better lithium cation diffusion paths.

Further development by the same group involved hierarchical porous LTO-anatase TiO_2 (HP LTO-TO) microspheres, which showed impressive low-temperature performance. These microspheres, synthesized through hydrothermal methods, maintained substantial capacities at temperatures as low as −40°C and displayed excellent rate capability and cycling stability at −20°C. The enhanced performance is due to the abundant dual-phase interfaces and grain boundaries, which reduce activation energy. These studies emphasize the potential of LTO/TiO₂ composites for low-temperature applications. By leveraging the structural and electrochemical advantages of both materials, these composites can deliver high performance and stability, making them suitable for advanced LIB technologies.

6.1.7. Titanium-based materials: hydrogen titanate nanotubes (HTNTs)

Nanostructured electrodes derived from hydrogen titanate nanotubes and nanowires have been developed and characterized by Li et al. [290]. The titanate nanotubes demonstrated stable capacities of around 100 mAh·g⁻¹ at 340 mA·g⁻¹ and 60 mAh·g⁻¹ at 680 mA·g⁻¹ at −25°C. In contrast, the titanate nanowires retained only about 40 mAh·g⁻¹ at 55 mA·g⁻¹ and 15 mAh·g⁻¹ at 170 mA·g⁻¹. This difference in performance is attributed to variations in diameter and specific surface area between the nanotubes and nanowires.

Rutile TiO_2 and composites like 3-LTO-RTO and HP LTO-TO deliver 75–90 mAh·g⁻¹ at −40°C. At −30°C, LTO/HCMS-C and LTO Cu/Super-P composites provide the highest capacities, around 120 mAh·g⁻¹, and maintain high-rate capability up to 5C. NS-LTO-C electrodes excel at low temperatures, delivering over 120 mAh·g⁻¹ at 30C at −25°C. While the areal specific capacity of titanium-based anodes is generally lower than that of graphite, NS-LTO-C anodes with a high mass loading of 12 mg·cm⁻² can achieve around 2 mAh·cm⁻² at a 1C rate down to −25°C.

Despite having lower gravimetric specific capacity compared to carbon-based materials, titanium-based materials offer significant advantages such as a high lithiation potential (>1.5 V *vs*. Li/Li$^+$) and structural stability during cycling. Research efforts primarily focus on enhancing their electronic conductivity through strategies like particle size reduction, metal particle addition, and material doping. The most promising results come from composites combining LTO with carbon-based materials or TiO_2, capable of operating at low temperatures with exceptional high-rate capability, for instance, under 30C at −25°C and 5C at −40°C. Thus, although titanium-based materials may have lower energy densities due to their high operating voltage and low specific capacity, they are promising alternatives for high-power applications, particularly for delivering high currents at low temperatures with long cycling stability

6.1.8. Intercalation–type materials: MXenes

MXenes, a class of 2D TM carbides and nitrides, have gained attention as potential anode materials due to their theoretical capacity of around 448 mAh·g^{-1} and enhanced high-rate performance. The general formula is $M_{n+1}X_nT_x$ (1 ⩽ n ⩽ 3), where M denotes the TM (e.g. Ti, V, Mo, Sc, Nb), X denotes carbon and/or nitrogen and T_x represents functional groups of surface termination (usually O, OH and/or F). With wider interlayer spacing compared to graphite, MXenes facilitate quick lithium cation intercalation and exhibit pseudocapacitive behavior [303]. Wang et al. [54] improved MXene ($Ti_3C_2T_x$) performance at low temperatures by substituting O for F termination, resulting in higher capacity retention and improved cycling stability due to enhanced lithium cation diffusion and structural integrity.

To address the issue of nanosheet restacking in pure $Ti_3C_2T_x$ MXenes, Zhao's group introduced Fe^{3+} to stabilize the structure, preventing repulsion and enhancing capacity. This modification activated –O/–OH groups in MXene interlayers, leading to more active layers and lower diffusion barriers. The Fe^{3+}–stabilized $Ti_3C_2T_x$ exhibited significantly higher specific capacities at low temperatures compared to pure MXene [303, 304]. These advancements highlight the potential of MXenes as high-performance anode materials for low-temperature applications. By optimizing surface terminations and structural stabilization, MXenes can achieve superior electrochemical properties, making them promising candidates for next-generation LIBs.

6.1.9. Intercalation-type materials: lithium vanadate (LVO)

Lithium vanadate (Li_3VO_4, LVO) is a potential anode material with a low Li intercalation potential (0.5–1.0 V *vs.* Li/Li$^+$) and a capacity comparable to graphite. However, its low

electronic conductivity limits its performance. To address this, Liang's group [290] developed well-crystalline, in-situ carbon-coated Li_3VO_4 (Li_3VO_4/C) anodes. These anodes showed improved electrochemical performance at low temperatures, delivering higher capacities at various current rates and maintaining stability over multiple cycles. The carbon coating on Li_3VO_4/C anodes significantly reduced charge transfer resistance and increased lithium diffusion coefficients, enhancing low-temperature performance. At $-20°C$, these anodes delivered stable capacities of 120 mAh·g^{-1} at 0.2C and 20 mAh·g^{-1} at 15C. The development of Li_3VO_4/C anodes demonstrates the potential of surface engineering to enhance the performance of lithium vanadate. By addressing conductivity issues through carbon coating, these anodes can achieve better low-temperature capabilities, making them viable alternatives for advanced battery technologies.

6.1.10. Intercalation-type materials: niobium tungsten oxide (NbWO)

Niobium tungsten oxides (NbWO) stand out for their high intercalation potential of $1.57-1.70$ V *vs*. Li/Li$^+$, similar to lithium titanium oxide (LTO), while offering additional benefits such as more redox electron pairs, enhanced safety, and greater specific capacity. Particularly, $Nb_{16}W_5O_{55}$ can undergo four redox reactions, achieving a theoretical capacity of 343 mAh·g^{-1} with minimal expansion of 5.5% during lithium intercalation. Research by Ma's team [290, 305] revealed that $Nb_{16}W_5O_{55}$ anodes maintained stable capacities of over 150 mAh·g^{-1} at 0°C and 100 mAh·g^{-1} at $-20°C$ after 400 cycles at 100 mA·g^{-1}. This stability is attributed to micromorphology and crystal structure remaining largely unaffected by temperature changes during cycling.

6.2.   Alloying–type anode materials

Anode materials such as silicon and tin store lithium through an alloying/dealloying mechanism, reacting with lithium to form various lithium-based alloys.

This process can be represented by the reaction (6.2):

$$M + xLi^+ + xe^- \leftrightarrow Li_xM \tag{6.2}$$

where M is a metalloid or an alloyed element. Materials like silicon, tin, germanium, and zinc, [279, 306] which utilize this mechanism, offer extremely high specific capacities at low operating potentials. For instance, capacity of around 4200 mAh·g^{-1} for silicon is achievable through a following reaction (6.3):

$$Si + 4.4Li^+ + 4.4e^- \leftrightarrow Li_{4.4}Si \tag{6.3}$$
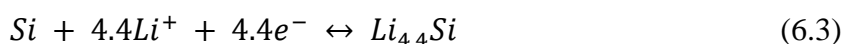
This reaction occurs at <1.0 V *vs*. Li/Li$^+$. However, all alloying-type anode materials undergo significant volume changes, for instance tin and silicon up to about 300%, due to phase transitions during lithiation and delithiation [307].

This severe mechanical stress leads to the formation of cracks and pulverization of the material, adversely affecting the cycling stability and kinetics of these alloying-type materials. To enhance their mechanical stability, several strategies have been proposed, including the development of nanostructured materials and composites [308] that can buffer these large volume changes during cycling.

6.2.1. Tin-based materials (Sn)

Metallic tin (Sn) has gained significant attention as an alloying-type anode material, capable of forming Li$_{4.4}$Sn with a theoretical capacity of 994 mAh·g^{-1} [308]. However, it faces severe capacity fade due to mechanical stress from volume changes of up to 300% during alloying and de-alloying.

To address these issues, Nobili et al. [225] developed a composite anode with nanosized tin particles embedded in electrically conductive porous multichannel carbon microtubes (Sn-PMCMT). This anode demonstrated enhanced mechanical stability and capacity retention using a charge capacity-limited protocol during activation. Sn-PMCMT delivered 190, 100, and 45 mAh·g^{-1} at C/4, C/2, and 1C, respectively, at −20°C. Encapsulation of tin by the PMCMT matrix effectively buffered volume variations and mechanical stresses during the Li-Sn reversible alloying process.

Yan et al. [309] developed a Sn/C composite with nano-Sn embedded in expanded graphite (Sn/EG). The uniformly distributed nano-Sn particles within the expanded graphite layers showed electrochemical performance at −20°C, with capacity retention of 200·mAh·g^{-1} at 0.1C and 130 mAh·g^{-1} at 0.2C, representing 30% and 20% of the room temperature capacity, respectively. The improved performance of Sn/EG was attributed to enhanced electronic conductivity, lower overpotential, and shortened lithium cation diffusion length in the 2D graphene/nano-Sn structure.

Yamauchi et al. [310] proposed the use of metal oxide with an amorphous structure to mitigate capacity degradation and limited cycle life due to mechanical stresses. They developed a tin-phosphate glass anode (Glassy SnO-P$_2$O$_5$, GPSO), which transformed into a nanocomposite with metallic crystals embedded in an amorphous lithium phosphate matrix after the first charge. The SnO-P$_2$O$_5$ system underwent an initial irreversible precipitation of

metallic tin followed by reversible lithiation of the tin crystals. The GPSO cells showed discharge capacities of about 450 mAh·g^{-1} at $-5°C$ after 50 cycles at a 0.2C rate, with the lithium phosphate matrix helping to suppress volume changes during cycling.

In 2021, Tan's group [311] developed pure SnO_2 anodes with good cycling stability, particularly at subzero temperatures. SnO_2, which offers high theoretical gravimetric and volumetric capacities (1494 mAh·g^{-1}, 10223 mAh·cm^{-3}), stores lithium cations through a two-step process involving a conversion reaction at around 1.2 V vs. Li/Li$^+$ and an alloying reaction at 0.5 V vs. Li/Li$^+$. SnO_2 anodes exhibited serious capacity fade at room temperature, retaining only 63% after 100 cycles at 200 mA·g^{-1}. However, they showed enhanced capacity retention at subzero temperatures, maintaining 96.9%, 90.2%, and 86.6% of the initial capacity after 100 cycles at $-10°C$, $-20°C$, and $-30°C$, respectively. This improved performance at low temperatures was attributed to the intrinsic properties of Sn, such as its low recrystallization temperature and the β-Sn to α-Sn allotropic transformation occurring at low temperatures.

6.2.2. Silicon-based materials

Silicon-based materials, with high specific capacity, low cost, environmental friendliness, and abundant reserves, are potential anode materials for next-generation high-energy-density LIBs. The most explored Si-based anodes include silicon, silicon alloys, and silicon oxides. Silicon offers a high theoretical specific capacity of 3580 mAh·g^{-1} and low voltage potential (<0.5 V vs. Li/Li$^+$) but suffers from significant volume expansion (nearly 400%), leading to particle pulverization and AM peeling, thus reducing cycling lifespan. SiO_x (x = 0 to 2) anodes, with reversible capacities of 1500–2000 mAh·g^{-1}, exhibit less volume variation (200%) [312, 313]. Despite lower theoretical capacity, byproducts like inert irreversible lithium oxide (Li_2O) and lithium silicate salts (Li_4SiO_4) formed during initial lithium cation intercalation can act as buffers against volume change, enhancing cycling performance. However, SiO_x still faces severe volume effects compared to other anodes, significant Li$^+$ consumption by the SEI layer leading to low Coulombic efficiency, and low intrinsic conductivity coupled with incompatibility with some electrolytes, affecting electrochemical properties. To address these issues, researchers have been developing modified SiO_x anodes to improve cycling performance and coulombic efficiency [314].

SOX have been developed for LIB anodes. The optimal composite structure, in terms of silicon domain size and Si-to-O ratio, achieved a capacity of 1562 mAh·g^{-1} at a 0.06C rate, with 80% ICE and 88% capacity retention after 100 cycles at a 1C rate [315].

The carbon matrix in the composite enhances electrical conductivity and buffers mechanical stress, improving overall performance and durability. These attributes make SOX a promising candidate for next-generation high-performance LIBs, offering a balanced combination of capacity, stability, and efficiency [316].

6.2.3. Germanium-based materials

Germanium, despite having a lower theoretical gravimetric capacity of $1624 \cdot mAh \cdot g^{-1}$ compared to silicon, exhibits significant advantages such as a higher lithium insertion voltage (<0.5 V *vs*. Li/Li$^+$) and electrical conductivity [317, 318] that is two orders of magnitude greater. However, similar to other high-capacity alloying materials, germanium anodes suffer from a substantial volume expansion exceeding 350% during lithiation, which leads to cracking and pulverization, thereby limiting their cycle life. Choi et al. [319] addressed this issue by developing anodes made of mesoporous germanium (Ge) particles. These mesoporous structures, with their high surface area and large void spaces, helped to mitigate the volume changes. When tested at -20°C under a current rate of 0.5C, these anodes achieved $566 \cdot mAh \cdot g^{-1}$ after 50 cycles and could recover to 1264 mAh·g^{-1} at 25°C, maintaining 86% of the initial room temperature capacity. Furthermore, a full cell with a LFP cathode exhibited an 80% capacity retention at 0.5C after 50 cycles at -20°C, highlighting the benefits of the mesoporous structure such as volume changes and reducing side reactions.

6.2.4. Zinc-based materials

Zinc anodes, offering a theoretical capacity of 409 mAh·g^{-1}, possess almost double the volumetric capacity of graphite and operate at a low voltage of 0.4 V *vs*. Li/Li$^+$ [320]. However, pure zinc anodes experience poor cycling performance due to significant volume changes during lithiation, leading to pulverization. To address this, Varzi's group [309] developed carbon- and binder-free Zn-rich porous Cu-Zn alloys, investigating the influence of alloy composition on low-temperature performance. During lithiation, these Cu-Zn composites undergo a reversible conversion of ZnO to Zn below 0.8 V *vs*. Li/Li$^+$ and alloying to LiZn below 0.2 V *vs*. Li/Li$^+$. At -10°C, the best performing $Cu_{18}Zn_{82}$ composition delivered 238, 167, and 52 mAh·g^{-1} under current densities of 0.05, 1, and 5 A·g^{-1}, respectively. Additionally, its capacity remained stable above 100 mAh·g^{-1} after 160 cycles at 0.1 A·g^{-1}. These results are attributed to the porous sponge-like morphology and the copper network, which facilitate electronic conduction.

Zinc sulfide (ZnS) emerges as a promising anode material due to its high theoretical specific capacity of 962 mAh·g^{-1}, natural abundance, low cost, and environmental friendliness [321]. However, its poor electrical conductivity and significant volume variations during cycling limit its performance. He et al. [322] synthesized ZnS/C composite materials with varying carbon content and compared their low-temperature performance with commercial MCMB anodes. The ZnS/C (9.3 wt% C) anode performed best, delivering 268 mAh·g^{-1} at 0°C and 207 mAh·g^{-1} at -20°C, which corresponds to 74.4% and 57.5% of the room temperature capacity after 50 cycles at 400 mA·g^{-1}. In contrast, MCMB anodes displayed specific capacities lower than 100 mAh·g^{-1} at subzero temperatures. The improved performance of ZnS/C anodes is attributed to the uniform dispersion of ZnS nanoparticles in a conductive carbon coating.

Zinc stannate (Zn_2SnO_4) offers a high theoretical specific capacity (1231 mAh·g^{-1}), high electrical conductivity, and low cost, but large volume changes during cycling result in capacity fading. Gao's group [323] developed a Co-doped Zn_2SnO_4-graphene-carbon (Co-ZTOG-C) nanocomposite, where Co doping enhances the ionic and electronic conductivities, and the graphene-carbon matrix reduces volume expansion. The Co-ZTO-G-C electrode exhibited specific capacities of 695 mAh·g^{-1} at room temperature and 196 mAh·g^{-1} initially at -25°C, which dropped to about 50 mAh·g^{-1} after 50 cycles at 0.1C. Despite the capacity decrease at higher current densities, capacity recovery was observed when the current density was lowered, demonstrating that Co doping improves low-temperature capacity, although its effectiveness diminishes after 20 cycles due to structural degradation of Zn_2SnO_4.

6.3. Conversion-type anodes

Many TM oxides, including CoO and Fe_2O_3/Fe_3O_4, store lithium via the conversion reaction mechanism. During lithiation, these oxides are transformed into metallic clusters within a Li_2O matrix as shown in the reaction:

$$M_xO_y + 2yLi^+ + + 2ye^- \leftrightarrow yLi_2O + xM \tag{6.4}$$
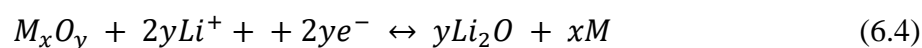
where M is a metal. Extensive research has been conducted on TM oxides, sulfides, selenides, fluorides, nitrides, and phosphides as conversion-type anode materials [324]. These anodes exhibit higher specific capacities and safety compared to graphite due to their higher potential vs Li/Li$^+$. However, they face challenges such as poor electronic and ionic conductivity and significant volume expansion with over 200%. Some metals obtained during the conversion reaction, after the reduction, like Sn–, Sb–, or Zn–based compounds can further interact with Li$^+$ and undergo an alloying reaction, which is called mixed conversion-alloying mechanism.

6.3.1. Manganese-based materials

Manganese monoxide (MnO) is a promising candidate for anode materials due to its relatively high theoretical specific capacity of 755 mAh·g^{-1}, moderate discharge potential of 0.5–0.6 V *vs*. Li/Li$^+$, natural abundance, and environmental friendliness [290]. However, MnO encounters significant challenges, such as poor electronic conductivity and large volume expansion, which result in poor rate capability and rapid capacity fading.

To address these issues, Tian et al. [325] developed MnO@Graphite composite anodes where MnO nanoparticles are anchored on graphite layers. This composite demonstrated a specific capacity of 295 mAh·g^{-1} at 100 mA·g^{-1} and −25°C in the first cycle and 456 mAh·g^{-1} after 320 cycles, showing superior low-temperature performance due to the structural integrity of the electrode, as well as hybrid pseudocapacitance contributions.

In 2020, Xue's group [326] created a nanocomposite consisting of MnO nanoparticles embedded in flake graphite (FG) and coated with a thin N-doped carbon layer (N-C), forming a plum-pudding-like structure (MnO@N-C/FG). This anode initially exhibited 382 mAh·g^{-1} and maintained 354 mAh·g^{-1} after 25 cycles at −20°C with a current density of 100 mA·g^{-1}. The impressive low-temperature performance of this composite is attributed to the FG skeleton providing mechanical support, the short ion pathways in the well-connected 3D structure, and the fast electron transfer kinetics enabled by the N-C conductive network.

Manganese ferrite (MnFe$_2$O$_4$) is another spinel ferrite material with a high theoretical capacity of 928 mAh·g^{-1} and a slightly higher potential of around 0.7 V *vs*. Li/Li$^+$ [327]. Du et al. [328] synthesized MnO@MnFe$_2$O$_4$@rGO nanocomposite anodes with a core-shell structure of MnO (core) and MnFe$_2$O$_4$ (MFO shell) nanoparticles anchored on reduced graphene oxide (rGO). The pristine MnO@3MFO, with a 1:3 molar ratio of MnO to MnFe$_2$O$_4$, initially showed a severe capacity fade from 1493 mAh·g^{-1} to 368 mAh·g^{-1} after 10 cycles. However, nanocomposites with 20–30 wt% rGO retained 579 mAh·g^{-1} after 200 cycles at 200·mA·g^{-1}. Cycling at −20°C, the MnO@3MFO@rGO electrode delivered more than 200 mAh·g^{-1} at 200 mA·g^{-1} (0.4C) and 300 mAh·g^{-1} at 50 mA·g^{-1} (0.1C).

6.3.2. Iron-based materials

Ferric oxide, or hematite (Fe$_2$O$_3$), possesses a high theoretical specific capacity of 1007·mAh·g^{-1} and reacts with metallic lithium to form Li$_2$O at a potential of around 0.7–0.8 V *vs*. Li/Li$^+$ [329]. Zou et al. [330] developed composites of silver-incorporated CNFs with Fe$_2$O$_3$ nanoparticles (Ag-Fe$_2$O$_3$/CNFs) and examined their performance at low

temperatures. Under current densities of 200 and 600 mA·g^{-1} at −5°C, Ag-Fe$_2$O$_3$/CNFs anodes delivered a capacity of 560 mAh·g^{-1} after 65 cycles, significantly outperforming the 260 mAh·g^{-1} of electrodes without silver. The incorporation of highly conductive silver in the composite enhanced low temperature cycling stability by decreasing total resistance.

Magnetite (Fe$_3$O$_4$) is another iron oxide with a theoretical specific capacity of 926·mAh·g^{-1} [331]. In 2019, Chen's group [332] developed a metal oxide@heterogeneous-doped carbon composite by synthesizing two-dimensional Fe$_3$O$_4$ nanorods, approximately 300 nm in length, coated with an N-doped carbon matrix (Fe$_3$O$_4$@NCm). The Fe$_3$O$_4$@NCm electrode showed a capacity of 760 mAh·g^{-1} after 900 cycles at a high current density of 1000 mA·g^{-1}. Additionally, rate capability tests demonstrated their ability to handle higher currents, maintaining a specific discharge capacity of around 400·mAh·g^{-1} at 2000 mA·g^{-1}. These promising results are attributed to the composite's high pseudo-capacitance, the carbon matrix enhancing conductivity and buffering volume changes, and the N-doping that increases the electronegativity of carbon atoms, providing more active sites for lithium cations.

Both Fe$_2$O$_3$ and Fe$_3$O$_4$ demonstrate significant potential as anode materials for LIBs due to their high specific capacities and effective performance at low temperatures.

6.3.3. Molybdenum-based materials

Two-dimensional molybdenum disulfide (MoS$_2$) has attracted attention as an alternative anode material due to its layered structure similar to graphite, but with a higher theoretical capacity of 670 mAh·g^{-1} and low cost. The lithiation process of MoS$_2$ involves two steps: the intercalation of Li$^+$ into MoS$_2$ interlayer spaces at 1.0–1.1 V *vs*. Li/Li$^+$ to form Li$_x$MoS$_2$, and the conversion of Li$_x$MoS$_2$ into Li$_2$S and metallic Mo at 0.5–0.6 V *vs*. Li/Li$^+$.

However, structural deterioration during cycling and low intrinsic electrical conductivity hinders its electrochemical performance. To address these issues, Teng et al. [333] developed a nanostructure where MoS$_2$ sheets are perpendicularly connected with graphene. While pure MoS$_2$ showed an initial discharge capacity of 693 mAh·g^{-1}, which quickly dropped to about 200 mAh·g^{-1} after 20 cycles, the MoS$_2$/graphene (MoS$_2$/G) composite demonstrated an initial capacity of 896 mAh·g^{-1}. This capacity increased to 1077 mAh·g^{-1} after 150 cycles at 100·mA·g^{-1}. At 500 mA·g^{-1}, it maintained a stable specific capacity of 350 mAh·g^{-1} after 40 cycles. The superior performance of MoS$_2$/G is attributed to the synergistic effect of graphene and MoS$_2$ nanocrystals, which prevents the restacking of graphene sheets and agglomeration of MoS$_2$ nanosheets, providing active sites for lithium reactions. In 2020, Liu's group [334] prepared a MoS$_2$/carbon (MoS$_2$/C) hybrid with thin MoS$_2$ nanosheets uniformly intermixed

with carbon layers. During rate capability tests at −20°C, the MoS$_2$/C anodes withstood high current densities up to 3 A·g^{-1}, delivering more than 140 mAh·g^{-1}. The improved capacity and rate performance at low temperatures are attributed to the high lithium cation diffusion coefficient, due to the enlarged MoS$_2$ layer spacing, and enhanced conductivity provided by the carbon layers. Overall, both the MoS$_2$/G and MoS$_2$/C composites show significant potential as anode materials for LIBs due to their enhanced electrochemical performance.

6.3.4. Cobalt-based materials

Cobalt-based materials, Co$_3$O$_4$ is a conversion-type anode material that undergoes a complete phase transition to metallic cobalt during lithiation, offering a high theoretical capacity of 890 mAh·g^{-1} and a lithiation potential of 1.1 V *vs.* Li/Li$^+$ [335]. In 2020, Tan's group [336] developed a hierarchically structured Co$_3$O$_4$@graphene composite (Co$_3$O$_4$@G) to enhance the structural stability and charge transfer capability of Co$_3$O$_4$ nanoparticles. When cycled at low temperatures, Co$_3$O$_4$@G anodes showed 79% capacity retention after 50 cycles at −20°C under 0.2 A·g^{-1}. Cobalt sulfides are also emerging as promising anodes due to their high theoretical capacity, unique crystal structure, and low cost. However, they suffer from severe capacity fading. To address this, researchers have incorporated carbon materials such as amorphous carbon or rGO. Lu et al. [337] synthesized amorphous carbon-decorated and graphene-anchored hollow Co$_9$S$_8$ nanoparticles and evaluated their electrochemical performance at low temperatures. This composite anode maintained a stable room temperature capacity of around 700 mAh·g^{-1} with a low capacity fading of 0.15% per cycle.

6.3.5. Nickel-based materials

NiO is a promising anode material with a high theoretical capacity of 718 mAh·g^{-1} and a high crystal density, resulting in almost six times higher volumetric energy density than graphite [338]. However, its poor low-temperature performance is attributed to low conductivity, slow electrode kinetics, and severe aggregation and volume changes between NiO nanoparticles, leading to rapid capacity fade. To address these issues, Bai's group [339] developed an *in-situ* nitrogen-doped carbon encapsulated 2D nickel oxide nanosheets (NiO@C-N NSs) composite and examined its electrochemical performance at temperatures down to −40°C and current densities up to 10·A·g^{-1}. The NiO@C-N NSs anodes delivered more than 400, 250, and 100 mAh·g^{-1} at −40°C under current densities of 0.05, 0.1, and 0.2 A·g^{-1}, respectively. This superior wide-temperature rate capability is due to the pseudocapacitive behavior of the NiO@C-N NSs, which increases with higher current rates.

6.4. Comparison of anode materials

Recent advancements in the enhancement of intercalation-type, alloying-type, and conversion-type anode materials have been shown previously and it is shown in Table 18, [340]. Most research focuses on boosting the electronic and ionic conductivity of anode materials, which enhances their electrochemical performance, as it is primarily hindered by significantly increased charge transfer resistance and decreased lithium cation diffusion coefficient, especially during lithiation.

Table 18.   Research on active anode material, theoretical capacity, advantages [341]

Active anode material	Theoretical capacity $(mAh \cdot g^{-1})$	Advantages	Common issues
Insertion/de – insertion materials A. Carbonaceous a. Hard carbons b. CNTs c. Graphene	200 – 600 1116 1780/1116	Good working potential Low cost Good safety	Low coulombic efficiency High voltage hysteresis High irreversible capacity
Insertion/de – insertion materials B. Titanium oxides a. $LiTi_4O_5$ b. TiO_2	175 330	Extreme safety Good cycle life Low cost High power capability	Very low capacity Low energy density
Alloy/de-alloy materials a. Silicon b. Germanium c. Tin d. Antimony e. Tin oxide f. SiO	4212 1624 993 660 790 1600	Higher specific capacities High energy density Good safety	Large irreversible capacity Huge capacity fading Poor cycling
Conversion materials a. Metal oxides (Fe_2O_3, Fe_3O_4, CoO, Co_3O_4, Mn_xO_y, Cu_2O/CuO, NiO, Cr_2O_3, RuO_2, MoO_2/MoO_3, etc.)	500 – 1200	High capacity High energy Low cost Environmentally compatibility High specific capacity Low operation potential and Low polarization than counter oxides	Low coulombic efficiency Unstable SEI formation Large potential hysteresis Poor cycle life High cost of production
Conversion materials b. Metal phosphides/sulfides/nitrides (MX_y; M ¼ Fe, Mn, Ni, Cu, Co, etc. and X ¼ P, S, N)	500 – 1800	High capacity High energy Low cost Environmentally compatibility High specific capacity Low operation potential and Low polarization than counter oxides	Low coulombic efficiency Unstable SEI formation Large potential hysteresis Poor cycle life High cost of production

Besides the commonly used carbon-based materials, titanium-based materials like LTO are gaining attention due to their high working potential, ensuring safety against lithium plating, and high-rate capability, making them ideal for high-power applications.

Alloying-type materials such as silicon–based and germanium provide the highest specific capacities even at extremely low temperatures.

Conversion-type anode materials are promising alternatives offering higher energy than intercalation-type and higher power than alloying-type materials, though many are less environmentally friendly and abundant.

Beyond high specific capacity and high-rate capability needed for high-energy and high-power applications, respectively, the long-term cycling stability of anode materials during low-temperature operation is crucial for practical use. At temperatures between $-5°C$ and $-15°C$, MXene delivers around 140 $mAh \cdot g^{-1}$ after 300 cycles at approximately C/2 rate, while the Co_3O_4@Graphene composite retains 400 $mAh \cdot g^{-1}$ after 400 cycles at a high current rate of 1C. LTO/HCMS-C exhibits long-term stability and high-rate capability, delivering over 40 $mAh \cdot g^{-1}$ after 1000 cycles at high current rate of 10C. MnO@graphite has been cycled for over 300 cycles, delivering almost 450 $mAh \cdot g^{-1}$ at approximately C/5 rate.

An exceptional specific capacity of almost 750 $mAh \cdot g^{-1}$ is retained by Fe_3O_4@NCm-60 anodes after 900 cycles at a high current rate of 1C. After 1000 cycles, MXene $Ti_3C_2T_x(O)$ retains almost 200 $mAh \cdot g^{-1}$ at approximately C/4 rate.

At temperatures lower than $-25°C$, no anode materials have been cycled for over 100 cycles. Specifically, between $-25°C$ and $-35°C$, a graphitic compound of KS-15 in a mixture of copper particles and Super-P has achieved nearly 150 $mAh \cdot g^{-1}$ after 100 cycles at a current rate of C/5. SnO_2 anodes have shown promising results, retaining a specific capacity of over 400 $mAh \cdot g^{-1}$ after the same number of cycles at a C/4 rate. Below $-35°C$, the extensively cycled materials are the GeO_x@Mxene composite, delivering around 340 $mAh \cdot g^{-1}$ at a C/5 rate, and crumbled graphene, CG-1000, which retains over 150 $mAh \cdot g^{-1}$ but at a much lower current (<C/20).

In summary, various materials have been cycled across a wide range of temperatures, with intercalation-type titanium-based materials delivering mostly 50–150 $mAh \cdot g^{-1}$ and carbon-based materials around 150–200 $mAh \cdot g^{-1}$. Alloying-type and conversion-type anodes retain 300–800 $\cdot mAh \cdot g^{-1}$. Higher current rates are primarily provided by titanium-based materials, while conversion-type materials follow with slightly lower current rates but higher specific capacities.

6.5. Synthetic graphite – green and sustainable perspective on anode materials

Carbonaceous materials, especially graphitic carbons, are considered the state-of-the-art anode materials in LIBs [342]. They exhibit exceptional electrochemical properties, including a low and stable operating potential close to but distinct from lithium metal, a relatively high specific capacity of 372 mAh·g^{-1}, and long-lasting performance in well-composed carbonate-based electrolytes. Additionally, these materials offer low voltage hysteresis and high energy efficiency [343]. Over the past few decades, advancements in anode materials have significantly enhanced the energy density of LIBs, transitioning from coke-based anodes to hard carbons and eventually to graphite. Graphitic carbons are categorized into SGs (synthetic graphites) and NGs (natural graphites). The production of graphitic carbons starts with the pretreatment of carbon precursors for SGs or mining and processing of graphite ore for NGs, followed by graphitization, further processing, and finally particle refinement [288, 344, 345], as shown in Figure 7, [9, 315].
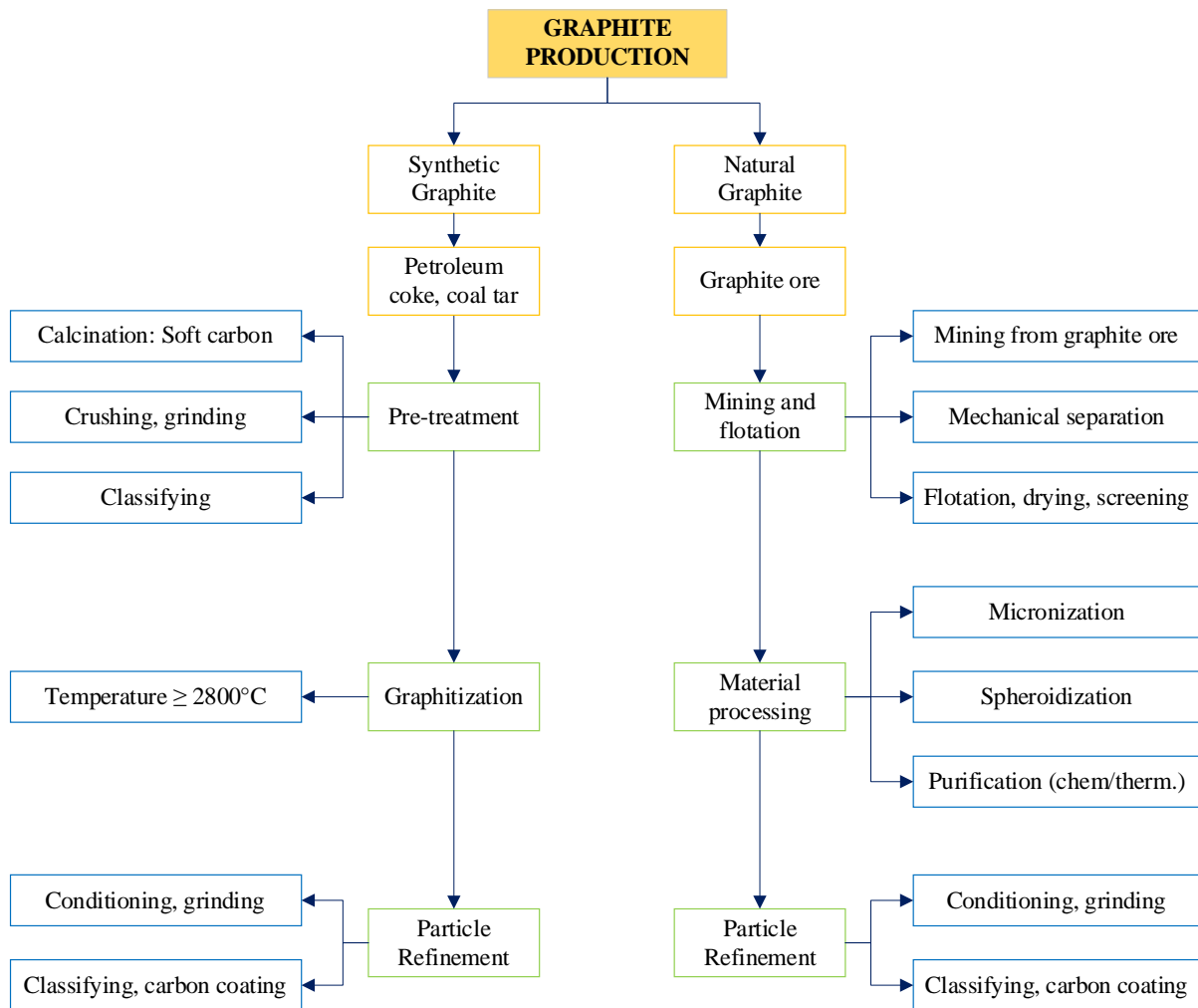

Figure 7.   Natural and synthetic graphite production for anode materials for LIBs.

Despite the lower cost of graphite compared to advanced cathode materials, there are substantial cost differences between SGs ($12–13 per kg) and NGs ($4–8 per kg). This cost discrepancy is mainly due to the energy-intensive production of SGs and the abundant supply of NGs, particularly from China [9]. Currently, NGs (~35%) and SGs (~56%) hold the major market share for commercial LIB anode materials, with SGs being preferred for electric vehicle batteries due to their high purity, consistent quality, essential for meeting battery lifetime requirements [346], as well as they have no abundance issues, they are price speculation-proof and there are rarely supply line difficulties, unlike NGs.

SG–based materials are classified into primary and secondary types. Secondary SGs, often a byproduct of electrode manufacturing for the steel or aluminum industry [97], vary in quality based on production batches. Primary SGs, however, are specifically prepared for battery applications with well-defined properties (such as ash content, density, particle size).

Synthetic Graphite (SG) production: SG is typically created from petroleum coke, often blended with coal-tar pitch, through high-temperature treatments ranging from 2500 to 3000°C. Initially, the precursor material undergoes calcination at 800-1200°C, transforming it into soft carbon. This material is then mechanically treated to adjust particle size, shape, and morphology, followed by particle classification. Soft carbon can be used directly in battery applications or further processed into graphitic carbon. The crucial, cost-intensive step in SG production is graphitization at temperatures above 2800°C, which can take days to weeks including cooling phases. Final mechanical refinement (which includes grinding, classifying, carbon coating) of the graphite particles optimizes their design for specific requirements such as particle size, specific surface area, and surface morphology [26, 345, 347].

Reducing graphitization costs and energy: One strategy to reduce the high energy consumption and cost associated with graphitization (10–12 kWh·kg^{-1}) involves using certain metal additives, such as $FeCl_3$ or $Ni(NO_3)_2$ [348], which lower the required temperatures.

For instance, Gomez-Martin et al. found that adding iron (Fe) catalysts significantly increased the graphitization degree of biomass-derived carbons, enabling high reversible specific capacity at lower pyrolysis temperatures.

NG production: NG forms from organic material deposits subjected to high temperatures and pressures over long periods. Economically viable deposits contain up to 20% graphite and are considered critical raw materials by the EU and the US, with the largest deposits in China.

NG production involves mining graphite ores through drilling or explosives, followed by a series of processing steps like crushing, milling, screening, flotation, and leaching to purify the graphite flakes. The processes of micronization and spheroidization are essential steps in achieving high-purity levels of graphite materials, often requiring further wet-chemical, thermal, or thermochemical treatments to reach purities of 99.0% or higher. This can be accomplished through acid leaching using acids such as hydrofluoric acid (HF), hydrochloric acid (HCl), and oxidizing acids like sulfuric (H_2SO_4), nitric acid (HNO_3) or mixtures.

Among these methods, acid leaching is particularly effective in removing silicate impurities. Additionally, heat treatments above 2000°C and thermochemical roasting, which involves thermal treatment with caustic soda at ~250–1000°C, followed by water washing and acid leaching, are also employed for NG purification. Despite its industrial use, particularly in China, the roasting process poses significant **environmental challenges**, including pollution from wastewater. Consequently, research is ongoing to develop more environmentally friendly and energy-efficient purification techniques, such as microwave treatment, capable of producing graphite with purities up to 99.99% [27]. In response to environmental concerns and the need for sustainable materials in LIBs, there is growing interest in **synthetic carbonaceous anode materials derived from biomass or industrial waste**. Various studies have explored a wide range of biomass precursors, including mushrooms, apple waste, sisal fibers, coffee shells, rice husks, pinecone hulls, banana fibers, cherry stones, tea leaves, coconut shells, and peanut shells. These materials are attractive due to their favorable structures, abundance, low cost, and compatibility with aqueous electrode processing routes. Waste products such as tire rubber, plastic bags, and bamboo chopsticks have also been used as carbon sources [345]. However, challenges remain in ensuring the reproducibility of materials from renewable sources and scaling up production to meet the growing demand for LIB raw materials.

7. BINDERS AND SOLVENTS FOR ELECTRODE FABRICATION

The binder material represents around 2–5% of the total mass of the electrode, and it has an important influence on the performance, cost, environmental impact, and recycling possibility of the battery [299]. Binders interconnect AMs and CMs, adhering electrode materials to current collectors to prevent disintegration from mechanical and chemical stress during charging and discharging. This binding function can be direct (covalent) or indirect (noncovalent). Direct binding involves binders with reactive functional groups, such as alcoholic and carboxylic acid groups, forming strong interparticle bridges with AMs. Indirect binding uses binders like nonfluorinated polymers that mechanically adhere to the surface of AMs. Direct binding typically requires less binder due to stronger adhesion. Furthermore, binders also contribute to the conductivity, and the stabilization of the cell during the SEI layer formation, high thermal, chemical and electrochemical stability [349, 350]. Binders can be classified based on their processability (solvent required for electrode manufacturing), chemical composition (fluorine-free), and natural availability (natural or synthetic). Binders soluble in water or ethanol can be categorized as a green alternative [183]. They can also be categorized as fluorinated (e.g., PVdF, PTFE) or nonfluorinated (e.g., starch, SBR, CMC).

7.1. Fluorinated (PTFE and PVdF) binders

In the 1980s, poly(tetrafluoroethylene) (PTFE) was widely used as a binder in LIBs due to its chemical and thermal resistance and binding properties. However, its fibrillation during the fabrication process hindered homogeneous dispersion and interconnection with electrode materials. Sony Corporation's 1991 discovery of the electrochemical activity of LIBs using carbonaceous anodes and lithium metal oxide cathodes with PVdF binders led to widespread adoption by battery manufacturers [351].

PVdF is the most common binder for electrode fabrication. It has high mechanical strength, electrochemical stability, and adhesion ability. However, despite these advantages, PVdF has limitations such as low cohesive force with current collectors and insulating properties. Moreover, PVdF is a common binder not compatible with aqueous-based electrode manufacturing processes (non-aqueous binder), thus requires to be dissolved in N-methyl-2-pyrrolidone (NMP). NMP is a teratogenic and irritating solvent. It is a toxic, expensive, non-desirable solvent due to its negative impact on the environment, which makes the battery recycling difficult [352]. Additionally, PVdF binders require rigorous humidity control due to their sensitivity to moisture. The high cost of PVdF and NMP, coupled with

environmental risks, poses challenges for future battery technology. Additionally, limitations, such as poor adhesion at elevated temperatures and susceptibility to exothermic reactions with lithium, lead to capacity loss and structural integrity issues in batteries. Thus, alternative binder materials that can overcome drawbacks while maintaining performance and safety are required.

7.2. Fluorine-containing binder failure mechanisms

PVdF binders in LIBs face numerous challenges that contribute to rapid capacity loss, including poor electronic conductivity, large volume expansion, and AM dissolution in the electrolyte. Elevated temperatures intensify these issues, leading to exothermic reactions between PVDF and lithium, which deplete Li^+ ions and form impermeable compounds that block ion transport [353]. Additionally, low melting point and swelling behavior in electrolytes further compromise electrode integrity and battery performance.

Limitations of PVdF become more pronounced at extreme temperatures. At low temperatures, PVdF becomes brittle and loses flexibility, leading to mechanical failure. Its swelling in organic-based electrolytes at high temperatures reduces mechanical properties, causing delamination. Furthermore, the partial coverage of electrode materials during SEI layer formation results in unstable SEI layers and rapid capacity degradation. These issues are more severe in conversion-type electrodes, such as silicon, which experiences significant volume changes during cycling.

These changes lead to poor binding strength, high internal resistance, and capacity loss, demanding the development of more flexible and adhesive binders for future LIBs [354].

7.3. Requirements for binders in future LIBs

An ideal binder for future LIBs must meet several strict requirements to justify its adoption for large-scale (industrial) commercialization. The foremost requirement is chemical stability, particularly in a fully charged state, to prevent any adverse reactions with separators, electrolytes, and electrode materials, which could degrade electrochemical performance. High flexibility and excellent mechanical properties are essential to accommodate the large dimensional changes of electrode materials such as silicon, germanium, and tin, ensuring the electrode architecture intact during charge and discharge cycles [299]. Additionally, the binder must provide strong adhesive strength between AMs and the conductive carbon, as well as adhere the electrode slurry firmly to the metallic current collector to resist delamination during cycling. The presence of reactive functional groups on the polymeric backbone binder enhances adsorption capacity, strengthening adhesion between the binder, AMs, and the current collector.

Effective binders should be used in minimal amounts (less than 5 wt.%) to reduce electrical resistance and increase the AM content, thereby improving the specific energy of the cell [355]. The binder/solvent compatibility is also crucial; well-dispersed binders cover the AMs surface, preventing self-agglomeration and forming an artificial SEI layer.

Electrochemical stability across a wide potential range (0-5 V $vs.$ Li/Li$^+$) is another critical requirement, ensuring the binder does not oxidize or reduce at the cathode or anode sides, respectively [356]. Binders must endure operating conditions, particularly elevated temperatures over 60°C, without losing flexibility or resistance to cracking. Moreover, binders should be freely soluble in solvents for easy processing and should be inexpensive, environmentally benign, and not sensitive to air or moisture [357].

7.4. Aqueous-based polymeric binders

Polymeric binders compatible with the aqueous-based electrode manufacturing processes (aqueous binders) offer several advantages for LIBs. They are low cost, green, and do not require strict processing conditions regarding air and humidity, featuring fast solvent evaporation. These binders do not require more than 5 wt.% content on the cell composition, improving the cell energy density compared to traditional PVdF-based binders. Aqueous binders tend to swell less in carbonate-based electrolytes and are cheaper, making them cost-effective for fabrication. Historically, gelatin was used in the 1990s as an aqueous binder, but recent advances have introduced various polymers, hydrocolloids, and copolymers for graphite anodes, Li-rich metal oxide cathode materials, and high-capacity silicon anodes. Companies like Apple, Everyday Battery, and General Motors have demonstrated the electrochemical performance of these binders. Common aqueous binders include sodium salt of CMC, styrene butadiene rubber (SBR), polyacrylic acid (PAA), chitosan, and alginates. Therefore, these binders are gaining more attention, due to their low cost, availability, good chemical/physical interactions with the electrode materials (Si-based anodes, spinels, layered oxide and sulfur cathodes), high electrochemical performance and stability [314]. demonstrating their potential as environmentally friendly and cost-effective alternatives to traditional binders.

7.5. Carboxymethyl cellulose (CMC)

CMC is a prominent aqueous binder characterized by strong noncovalent and hydrogen bonding interactions. CMC, a linear polymeric derivative of cellulose, is highly soluble in water due to the dissociation of carboxymethyl groups. Typically used in its sodium salt form (Na-

CMC), it exhibits excellent mechanical, adhesive, and emulsifying properties, making it widely used across various industries. CMC effectively disperses graphite particles in an aqueous medium, with its hydrophobic parts adsorbing onto the graphite surface and charged carboxylate groups stabilizing it in water [358, 359].

Studies show that graphite/CMC electrodes demonstrate high specific capacity and stable cycling efficiency, attributed to the formation of a stable LiC_6 phase. Electrodes with higher CMC content (5%) exhibit better capacity retention compared to those with lower CMC content, which often show rapid capacity decay due to insufficient binding. Its ability to form a homogeneous and stable passivation layer is crucial for long-term cycling efficiency. CMC is economically available, hydrophilic, environmentally friendly (biodegradable), and compatible with potential electrode materials to develop green and sustainable energy storage devices [360, 361]. However, among its limitations include stiffness, brittleness, and low elasticity, which can cause cracks and detachment from the current collector during cell fabrication and cycling, affecting its use as an elastomeric binder for high-capacity anodes.

7.6. SBR/CMC elastomer binders

SBR is a synthetic rubber that, when combined with CMC, forms a robust elastomeric binder. SBR provides higher binding ability, mechanical properties, and flexibility compared to PVdF, making it suitable for both anodes and cathodes. A combination of SBR and CMC results in binders with improved wetting, less brittleness, higher elongation rates, and stronger adhesion to current collectors. Despite these advantages, SBR/CMC mixtures may exhibit poor cycling efficiency with larger graphite particles due to insufficient binding ability. Studies indicate that SBR/CMC electrodes exhibit comparable properties at both laboratory and pilot scales, retaining rheology, and electrochemical performance even at higher mass loading [362]. This consistency makes SBR/CMC binders commercially viable. Additionally, the elastomeric SBR/CMC binder demonstrates excellent cycling efficiency for various cathode materials, providing good flexibility and reducing resistance, thereby increasing energy density. The homogeneous coating formed ensures good binding strength and flexibility, sustaining electrode expansion and contraction during cycling, which is crucial for maintaining the electrode structure and the battery performance [314, 356, 363].

7.7. Conventional *vs.* aqueous binders for LIBs

Most binders used in Li-ion and other batteries are fluorine-containing polymers, with PVdF being the most prevalent due to its chemical and electrochemical stability and reasonable

processability. However, PVdF has several drawbacks; a significant issue is its weak binding affinity to electrode components, relying mainly on mechanical interlocking and van der Waals forces. This inadequacy is particularly problematic for high-capacity energy storage, such as silicon-based anodes, which experience significant volume changes during charge and discharge cycles. Additionally, PVdF is electrically insulating and requires CMs for proper electrode function. The processing of PVdF also requires the use of the toxic and expensive solvent N-methyl-2-pyrrolidone (NMP), posing health hazards and increasing costs due to its high boiling point and energy-intensive removal process [364, 365].

Aqueous processable binders address many issues associated with conventional binders. Utilizing water as a solvent, these binders offer numerous advantages, such as significant cost savings, being water vastly cheaper than NMP. Additionally, aqueous binders, often priced between $2 to $5 per kilogram, reduce the overall fabrication costs by eliminating the need for solvent recovery and lowering CO_2 emissions. Water lower boiling point compared to NMP also facilitates faster evaporation during the electrode fabrication process, enhancing efficiency and reducing energy consumption [17]. These factors contribute to a more environmentally friendly and cost-effective manufacturing process for battery electrodes. Moreover, aqueous binders possess properties that enhance the performance and stability of battery cells. The functional groups on these binders form stronger interactions with other components, improving electrode stability and longevity. This enhanced binding strength can potentially reduce the amount of binder needed, allowing for a higher proportion of AM and thus improving the energy density of the batteries. Consequently, aqueous binders not only offer a more sustainable and economical solution but also enhance the overall performance, durability and recycling of LIBs [316, 354].

7.8. Conclusions and future perspectives in binders

Fluorinated polymers, particularly PVdF, are commonly used as binders for conventional electrodes due to their chemical stability. However, PVdF has limitations, such as the need for expensive, hazardous solvents like NMP and relying on weak van der Waals forces for material interaction. In contrast, aqueous binders offer advantages like lower cost, reduced environmental impact, and functional groups (e.g., hydroxyl and carboxyl) that enable stronger interactions with electrode materials. Notable aqueous binders include CMC-SBR combinations, which provide good mechanical properties at a lower cost, while polymers like PAA and alginate offer enhanced adhesion due to their higher carboxyl group content. Additionally, polymers such as polyurethanes and catechol-bearing polymers, although not

fully explored, show promise due to their enhanced adhesion and functionality. Future improvements in aqueous binders may follow two main paths: developing binders from sustainable sources that avoid hazardous or costly treatments, such as natural starches and gums, and incorporating additional functionalities like electrical or ionic conductivity and protection of AMs and electrolytes. These functionalities are typically found in synthesized polymer or copolymer systems. Ideally, the development of aqueous binders should strike a balance between being environmentally friendly, safe, and viable at industrial level. A shift towards sustainable materials that do not require hazardous or expensive treatments is essential. At the same time, enhancing binders with additional functionalities will improve their performance in energy storage applications. Some parameters to be considered for designing binders are shown in Figure 8, [351]. The main target is to create binders that are not only green and safe but also efficient and effective in their practical applications at large scale.
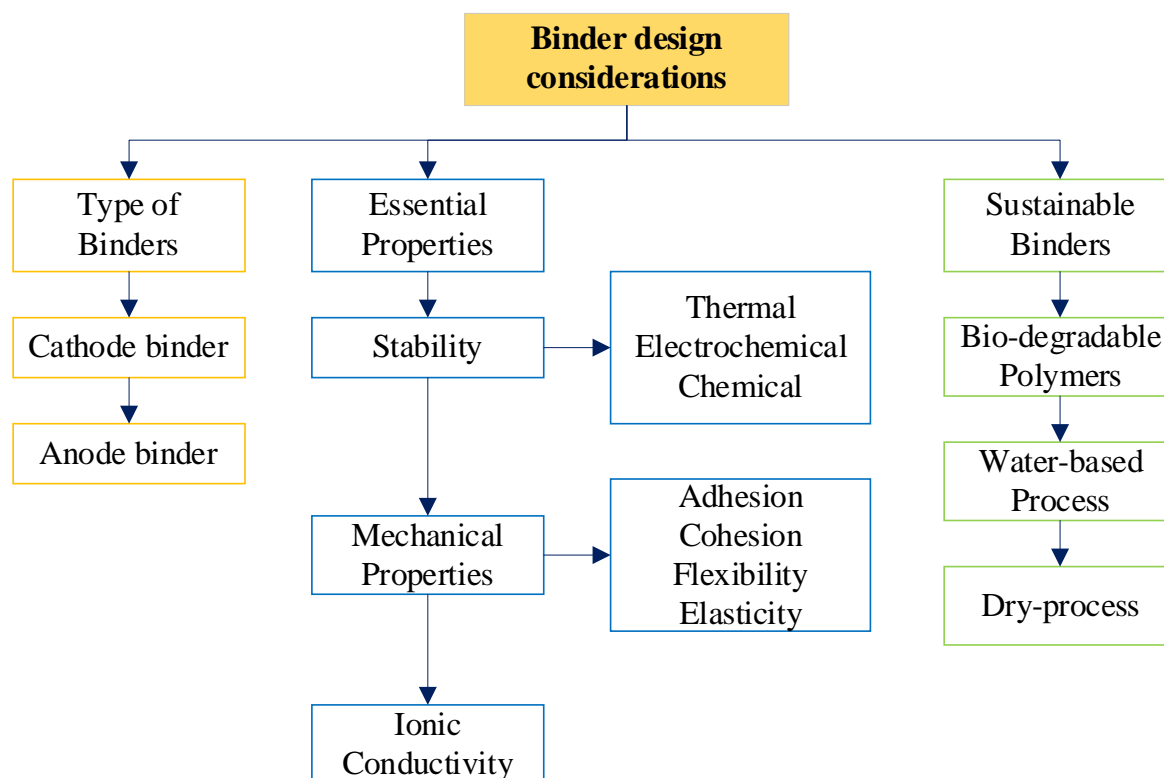

Figure 8. **Type of binders and essential properties for designing**

100

8. DEGRADATIONS MECHANISMS IN LITHIUM-ION BATTERIES

Battery aging can result in capacity fading, power fading, or both, and lifespan over time. Since a battery is composed of various components, the aging of one cell component can deteriorate its performance and affect the operational conditions of other components, accelerating the aging of the entire system, as shown in Figure 9 [366].

Copper current collector	Separator	Aluminum current collector
Copper dissolution Dendrite formation SEI formation and build-up Solvent co-intercalation Graphite exfoliation Copper cracking and contact loss SEI decomposition and precipitation Particle cracking Lithium plating and dendrite formation Re-precipitation of new phases		Aluminum corrosion and contact loss Transition metal dissolution and dendrite formation Structural disordering Binder decomposition Particle micro/cracking Cathodic surface film Internal short circuit Electrolyte decomposition Oxidation of conductive particles Migration of soluble species

Figure 9. Possible degradation mechanisms for the electrodes in a Li-ion cell

8.1.   Classification of degradations mechanisms in LIBs batteries

8.1.1. Chemical degradation mechanisms

Chemical degradation mechanisms primarily arise from electrolyte decomposition and reduction, SEI formation, binder decomposition, solvent co-intercalation, AM dissolution, gas evolution, and lithium loss. The electrolyte can be reduced by the lithiated negative electrode at low potential ranges and/or oxidized by the delithiated cathode at high potentials, with impurities often acting as catalysts for these reactions. The rate of these side reactions depends significantly on temperature and cell voltage, often accelerating at higher temperatures. These side reactions alter the electrode materials, with the redox reaction between the electrode and electrolyte contributing to the formation of an interface layer, which increases cell impedance and leads to capacity fading.

Thus, these effects result from various interacting processes and do not occur in isolation. Long-term chemical degradation of battery materials can adversely affect electrical performance, cell lifespan, and safety by increasing electrical resistance or causing continuity loss, corrosion products or passivating AMs, contaminants reacting with AMs due to loss of cell sealing, and electrolyte loss [367-369].

8.1.2. Mechanical degradation mechanisms

In addition to side reactions, mechanical degradation also contributes significantly to battery aging. Lithium insertion and extraction cause volume expansion and shrinkage, often occurring unevenly. Mechanical degradation mechanisms primarily involve volume changes and the resulting stress in the AM particles of the anode or cathode during lithium insertion (intercalation, conversion reaction, alloying) and extraction (deintercalation, etc.). Tensile stress can lead to cracks in active particles, loss of contact between particles or with the current collector, and isolation. Additionally, cycling-induced stress can alter the pore structure in the separator, reducing lithium cation mobility.

Similar to chemical degradation, mechanical degradation is exacerbated by aging, affecting the structures of the cathode and anode as well as the mechanical properties of other battery components. For instance, it can impact on the modulus of elasticity and hardness of the cathode or the crystallinity of the PVdF binder, [370].

8.2. Degradation modes on the electrodes

Various chemical and mechanical degradation modes exist that commonly affect the main components of LIBs. These degradation modes can negatively impact battery performance and, in severe cases, lead to cell failure, including thermal runaway.

8.2.1. Anode degradation

❖ **Solid electrolyte interphase (SEI) formation**

Researchers have identified changes at the electrolyte/electrode interface as the primary cause of anode aging. These changes result from reactions between the negative electrode and the electrolyte, leading to the decomposition of the reductive electrolyte and the consumption of lithium cations. The decomposition products deposit onto the electrode surface, forming a film known as the SEI. This SEI layer consumes active lithium, increasing electrode impedance and causing capacity and power fading in the cell.

Although SEI formation can occur at both the cathode and anode, it is more significant at the anode due to the low potential during cell charging. The composition and properties of the SEI layer depend on the electrolyte solvents and the anode surface. Numerous studies have investigated the formation of the SEI layer from carbonate solvents such as EC, PC, DEC, and DMC. Initially, the SEI layer formation limits further electrolyte reduction and anode surface

corrosion. However, the SEI continues to grow and stabilize throughout cell life, due to among others, stress-related cracks formation, even though at a slower rate.

This ongoing growth affects the pore size and structure, wettability, contact resistance, and separator porosity, typically accelerating at lower anode potentials [283, 371].

❖ **Lithium plating**

Lithium plating is a hazardous degradation mechanism in LIBs, involving the precipitation of lithium metal on the anode surface when the anode potential drops below 0 V *vs.* Li/Li$^+$. This process consumes active lithium, leading to capacity loss, and the formation of lithium dendrites can cause separator tearing, short circuits, and immediate battery failure.

Lithium plating occurs when the rate of lithium cation intercalation into carbonaceous electrodes is too slow or when lithium cation transport to the electrode surface is very fast. At temperatures below room temperature, lithium cation diffusion into the electrode slows down, requiring overpotential to maintain the current, which can lead to lithium plating. Additionally, cell imbalance (negative to positive electrode capacity ratio; N/P ratio), local electrode polarization, and geometric misfits can also cause lithium plating [372].

❖ **Changes in the AM**

Aging effects within the bulk of the AM are generally minor. The volume changes in graphite or SOX due to lithium cation insertion and extraction can be typically less than 10%, depending on the material composition. Structural changes can lead to mechanical stresses on defects and carbon-carbon bonds, causing structural damage and cracking. AM particle cracking and/or exfoliation, co-intercalation of solvents, electrolyte reduction within the AM, and gas evolution within the AM significantly accelerate electrode degradation, having the strongest influence on AM changes [373].

❖ **Changes in the anode structure**

Loss of electrical or mechanical contact within the anode increases the cell internal resistance and contributes to aging. Volume changes in anode AMs lead to mechanical disintegration throughout the anode structure. Electrode porosity is crucial for anode performance, allowing electrolyte penetration within the anode bulk. Volume changes in AMs negatively impact electrode porosity. Fluorine-containing polymers and copolymers used as binder materials react with the anode, forming LiF, which degrades the mechanical properties of the anode over time. Additionally, the current collector may corrode when reacting with electrolyte components or when the anode potential becomes too positive vs. Li/Li$^+$, resulting

in mechanical or electronic contact loss. Poorly conductive corrosion products cause overpotentials, inhomogeneous currents, and lithium plating [284, 374].

❖ **Conclusion on anode aging**

Table 19 [375, 376], provides an overview of the causes and effects of anode aging and highlights the main factors that enhance or mitigate aging.

In conclusion, the various aging mechanisms for carbonaceous anodes can primarily be attributed to changes at the electrolyte/electrode interface.

Table 19.   Li-ion anode aging-causes, effects, and impacts

Cause	Effect	Results in	Alleviated by	Elevated by
Electrolyte decomposition and SEI formation	Impedance increase Lithium loss	Power fades Capacity fade	Stable SEI (additives) The passage of time reduces the rate	High state of charge High temperature
Gas evolution, solvent co-intercalation, and particle cracking	Lithium loss Graphite exfoliation	Capacity fade	Carbon pre-treatment Additives	Overcharge
Reduced surface area arisen from SEI stabilization	Impedance increase	Power fade	Additives	High state of charge High temperature
Porosity change arisen from volume change of active material particles, SEI stabilization and growth	Overpotentials Impedance increases	Power fade	Additives External pressure	High state of charge High cycling rate
Contact loss caused by the change in volume of active materials	Active material loss	Capacity fade	External pressure	High depth of discharge High cycling rate
Binder decomposition	Mechanical instability Lithium loss	Capacity fade	Appropriate binder selection	high temperature high state of charge
Current collector corrosion	Impedance increase Inhomogeneous current and potential distribution	Power fade	Appropriate choice of current collector	Low state of charge Over discharge
Lithium plating and dendrite formation	Overpotentials Lithium loss	Capacity fade	Narrow operating range of potential	Cell imbalance Geometric misfits Low temperature High cycling rate Low polarization of electrode

8.2.2. Cathode degradation

❖ General characteristics on cathode degradation

The aging mechanisms and control measures for lithium metal oxide cathodes remain a key research area and are not yet fully understood. Various changes in the cathode can affect the longevity of a LIB, including AM aging, degradation of electrode components (such as binders, CMs, or current collectors), oxidation of electrolyte components leading to surface film formation, and reactions between aging products and the anode. These reactions are interdependent and influenced by the specific electrode composition, and cycling conditions.

Capacity loss in positive AMs can be attributed to structural changes during cycling, surface film modifications, and chemical decomposition or dissolution reactions. Figure 10 illustrates these aging mechanisms schematically, [377].
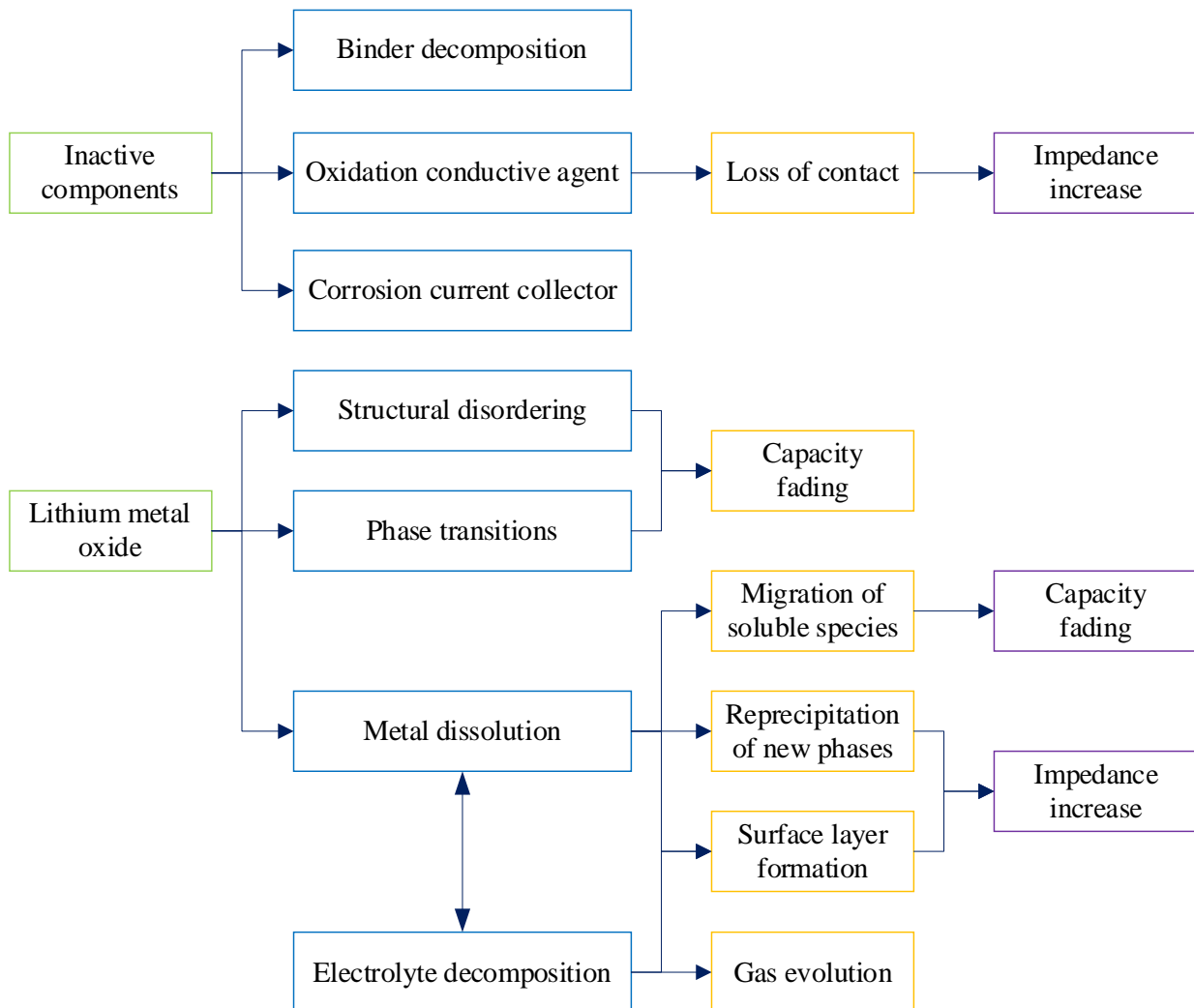

Figure 10. Causes and effects of degradation in the cathode.

Degradation in positive AMs, like in case of the negative electrode, depends on the state of charge (SOC) and cycling conditions. The electrochemical reaction in the cathode involves lithium cation insertion into the metal oxide, which changes the material molar volume, causing mechanical stress and strain in the AM particles and the electrode. This can also lead to phase transitions, crystal lattice distortions, and further mechanical stress.

❖ **Structural changes and mechanical stress**

Degradation mechanisms can be both chemical and mechanical. Mechanically, the process of lithium intercalation/deintercalation causes volume changes, leading to mechanical stress and strain on the AM particles, compromising the electrode structure and the mechanical properties of other battery components. This structural change impacts cathode performance more significantly than a carbonaceous anode. During the lithiation/delithiation process, phase changes in some cathode oxides cause crystal lattice distortion and further mechanical stress, contributing to nanoparticle cracking [378].

❖ **AM dissolution**

AM dissolution primarily affects Mn-based cathodes, especially in spinel structured manganese cathodes at high temperatures and charged states. The dissolution reaction sees Mn^{2+} ions dissolve in the electrolyte, leading to capacity fade due to AM loss and manganese ions migrating to the anode, depositing on its surface or in the SEI layer, which accelerates electrolyte decomposition and charge loss in the lithiated carbon-based anode. Deposition of manganese species on the cathode surface increases electrode impedance [270].

❖ **AM isolation**

AM particle isolation is a major cause of battery degradation. This includes crack formation on the surface, binder fracture, and deterioration of binder adhesion properties. Isolation results from both mechanical degradation of AMs and binders and chemical degradation of binders [370].

8.2.3. Separator degradation

Separator degradation can lead to power loss and eventual cell failure, typically due to lithium dendrite growth in separator pores, electrolyte migration, blockage of separator passageways during cycling, and structural degradation from high temperatures or extensive cycling. High temperatures (130-150°C) soften some of the typical separator films, closing pores and stopping charge/discharge processes by hindering ion transport [379].

This property makes them "shutdown" separators, which can permanently disable the cell during internal temperature spikes. Separator shutdown properties are measured by the impedance increase [367].

Separator materials, although inert and not directly affect electrical output, significantly influence cell performance and safety. Effective separators should have uniform pore structure, low shrinkage, and low resistance. High-resistance separators perform poorly at high discharge rates and prolong battery charging time. Larger pores in the separator can lead to failures during high-potential testing, while very small pores increase resistance and shorten cycle life. Separator materials often face harsh oxidizing and reducing environments from the cathode and anode, respectively. Multi-layer separators (PP/PE/PP) offer better oxidation resistance due to the superior properties of PP in contact with the cathode. Separator resistance, thickness, permeability, porosity, and toughness vary based on cell requirements. Reducing separator thickness increases energy density, however, reduces mechanical strength and electrolyte capacity, leading to potential cell failures [380].

Few studies focus on separator degradation, though it significantly impacts cell resistance and performance. Impedance spectroscopy and thermogravimetric analysis reveal that deposit formation and decomposition increase separator resistance, impeding lithium cation transport and contributing to overall cell impedance rise.

8.2.4. Current collector degradation

Current collectors in LIBs are typically aluminum for positive electrodes and copper for negative electrodes. They distribute current evenly, support electrode materials mechanically, and connect internally to battery leads. These materials, however, are prone to environmental degradation: copper to environmentally assisted cracking (EAC) and aluminum to small holes corrosion, particularly under the highly oxidizing conditions of the charged cathode.

Aluminum and copper corrosion in LIBs is complex, influenced by the organic electrolyte and electrical cycling. Aluminum faces corrosion at the cathode charge potential, filling the available spaces with metal-oxide mixtures. Copper is susceptible to EAC under certain metallurgical conditions, such as large grain size and work hardening.

❖ **Aluminum corrosion**

Studies show aluminum electrochemical behavior in organic electrolytes depends on electrolyte composition and electrode metallurgy. Aluminum is stable in air and neutral water due to a protective oxide layer, which also forms in organic electrolytes with slight oxidants.

However, common electrolytes like alkyl carbonates with lithium salts (e.g. $LiPF_6$) can cause anodic corrosion, forming protective fluoride-containing surface films. Braithwaite et al. found that fluorocarbon-based coatings enhance aluminum resistance to pitting corrosion.

Using XPS and EIS, Braithwaite et al. examined aluminum corrosion in various electrolyte solvents. Localized pitting increased with cycling, more rapidly in EC than PC solvents. Cross-sectional SEM images showed pits filled with aluminum and aluminum oxide mounds, electrically isolating the foil. EIS analysis revealed lower pitting resistance in EC, indicating higher corrosion susceptibility. Higher anodic potential also increased corrosion current, reducing pitting resistance. However, aluminum electrochemical behavior was not significantly affected by cycling number or metallurgical purity [381].

❖ **Copper corrosion**

At moderate potentials, copper current collectors oxidize and dissolve, with copper ions plating onto the anode during recharging, reducing permeability and causing lithium plating, leading to capacity fade and potential internal short circuits. Overcharge accelerates degradation, damaging the anode and promoting lithium plating.

Unlike aluminum, copper is not prone to pitting corrosion at cathodic potentials but can suffer EAC under specific conditions, such as large grain size, work hardening, and zero applied voltage. Braithwaite et al. showed that removing any of these conditions eliminated EAC susceptibility, indicating proper metallurgy can prevent EAC [381].

8.3.   SEI formation, kinetics, and growth

Before the SEI model was introduced in 1979, researchers primarily relied on the Butler-Volmer equation, assuming that direct electron transfer occurred between the electrode and lithium cations in the solution. This model suggested that the rate-determining step (RDS) in lithium batteries was the electron transfer from metal to solution cations. However, it was discovered that a passivating layer formed on the lithium anode, delaying its deposition and dissolution processes. Brummer and Newman concluded that passivating anode limited cycle life, advocating an anode free of this layer to achieve a high-cycle-life [382].

8.3.1. The present, lithium-metal and Li-ion batteries

The SEI is now recognized as essential for the effective operation of lithium and sodium batteries. Proposed by Peled in 1979, the SEI model applies to all alkali metals and alkaline earths in non-aqueous systems. Formed immediately upon metal contact with the solution, the

SEI consists of insoluble and partially soluble reduction products from the electrolyte. The formed layer thickness is defined by the electron-tunneling range and acts as a high electronic resistivity interphase. SEI is crucial for battery safety, power capability, morphology, shelf life, and cycle life, requiring an electrolyte with at least one SEI precursor that reacts quickly with lithium to form an insoluble layer. Techniques such as XPS, SEM, and NMR have been adapted to study SEI properties and structures. An ideal SEI should have high electrical resistance, cation selectivity, mechanical stability, and tolerance to expansion and contraction stresses. Despite advancements, the current SEIs still grow over repeated cycles, indicating the need for further research [383].

8.3.2. SEI formation, kinetics, and growth

When an alkali metal is immersed in an electrolyte, or a negative potential is applied to a carbon or inert electrode, SEI layer formation begins. Various reduction reactions compete at the electrode surface, with products like LiF and Li_2O precipitating on the electrode. The SEI formation potential depends on factors like the type of AM (e.g. type of carbon) and the current density. During the first charge of a LIB, some capacity is lost to form the SEI, known as irreversible capacity loss. This SEI must prevent solvated electron formation, which can cause self-discharge. A stable SEI is necessary to stop these issues, and its continuous growth during cycling indicates a need for rapid formation and healing processes. The SEI formation involves multiple reactions, and choosing appropriate SEI precursors is critical. The SEI grows through processes such as electron conduction and diffusion, with its thickness increasing according to parabolic law [281].

8.3.3. SEI structure

The SEI structure facilitates the transport of ions through mobile-point defects or grain boundaries perpendicular to the anode surface. Initial models described the SEI as multiple layers, with a thin and compact first layer and a potentially more porous second layer that hinders ion transport by filling its pores.

Later, Thevenin and Müller suggested several SEI models, including the PEI (Polymer-Electrolyte-Interphase) model, the SPL (Solid-Polymer-Layer) model, and the CSL (Compact Stratified Layer) model. Aurbach et al. proposed a multi-layered SEI structure based on electrochemical and spectroscopic studies, indicating that both organic and inorganic materials form a mosaic of micro phases on the electrode surface.

The conduction mechanism for lithium cations in the SEI occurs through vacancies and lattice defects, with higher lithium cation concentrations at grain boundaries leading to enhanced conduction compared to the bulk. The equivalent circuit for a mosaic-type SEI electrode includes multiple resistance-capacitance (R-C) elements and Warburg impedance. Typically, the SEI resistance (R_{SEI}) in battery electrolytes ranges from 10 to 1000 $\Omega \cdot cm^2$, while the grain boundary resistance (R_{gb}) at 30°C for a 10 nm SEI is between 10 to 100 $\Omega \cdot cm^2$, requiring their inclusion in the SEI equivalent circuit. Recent studies indicate a generally bilayer structure of the SEI, but it is inherently more complex with heterogeneous compositions like LiF and Li_2CO_3 close to the electrode surface and a porous organic layer extending outward [382, 384].

Research by Balbuena et al. on the polymerization mechanisms of electrolytes shows that SEI growth is influenced by the radical propagation process. Initial stages of SEI nucleation generate radicals that interact with the anode surface or remain in the liquid phase, propagating reactions before the film formation. Radicals can transfer charge to their environment unless the SEI becomes too dense, allowing only small radicals such as lithium atoms to penetrate and induce reactions. Polymerization reactions initiated by open vinylene carbonate or open-EC radical anions with VC molecules are thermodynamically more favorable than those with EC molecules, driving SEI growth through radical propagation [155].

8.3.4. Conclusion and perspectives

The SEI plays a critical role in alkali-metal, alkali-metal ion, and alkaline-earth batteries, with ionic migration through the SEI often being the rate-determining step. The Tafel slope (b) linearly correlates with SEI thickness, which increases parabolically over time under open circuit voltage (OCV) conditions. Future studies of SEI properties in systems such as lithium/sulfur, lithium/air, sodium, sodium-ion, and calcium batteries are in their early stages.

A comprehensive characterization of the SEI processes involves multiple analytical tools, including STM, AFM, XPS, EDS, SEM, XRD, FTIR, NMR, Raman spectroscopy, AC-impedance measurements, and DSC. Molecular dynamics (MD) and density-functional theory (DFT) simulations have enhanced understanding of the relationship between the SEI layer and the electrolyte. Ab-initio molecular dynamics further extends MD capabilities by integrating the Schrödinger wave equation with Newton equations. The SEI forms through parallel and competing reduction reactions, making its composition dependent on various factors.

For LIBs with carbonaceous anodes, reducing the true surface area of carbon, using pure materials, and employing optimal charging protocols can lower irreversible capacity loss. Enhancing SEI properties involves surface modifications like the creation of core-shell-structured carbon composites. Increasing charging rates for rapid SEI formation can result in incomplete and unstable layers, reducing efficiency and safety. Poor electrolyte wetting leads to low-quality SEI layers and premature performance degradation. In lithium/sulfur cells, SEI resistance changes minimally during initial cycles, but capacity fading occurs due to increased R_{SEI} and R_{CT} and decreased diffusion coefficients. Understanding SEI phenomena is crucial for developing safer and more durable batteries, with ongoing research focused on improving SEI properties and creating artificial SEIs to enhance battery longevity and performance.

8.4. Strategies to mitigate degradation

Several strategies to stop or slow down LIBs' degradation have already been implemented in commercial LIBs, such as adding strategic electrolyte additives and applying protective coatings on electrode material surfaces. Additionally, emerging approaches like synthetic optimization to produce materials with graded compositions or shape-controlled materials that expose advantageously reactive facets hold promises for enhancing energy density and increasing the rate capability of future rechargeable batteries. Moving beyond intercalation materials, the significant volume changes, material dissolution, and insufficient energy efficiencies associated with high-capacity battery chemistries (e.g., Li−S, Li−O$_2$, conversion and alloy anodes) have driven efforts to develop conductive composites and/or 3D architectures to address these limitations. While small-scale demonstrations show great promise for achieving higher energy density batteries, converting these fundamental advances to commercial use remains a significant technological challenge. Future applications, such as electric vehicles, demand increased mass loadings of AMs at both the anode and cathode and enhanced utilization of these materials within the cell. These requirements are often overlooked in small-scale demonstrations using low tap density nanomaterials with low mass loading during testing [385].

Continuous innovation and the interplay between materials science and advanced characterization techniques are crucial to transition fundamental advances to commercial applications.

8.5. Battery development strategies for a more sustainable future

As we increasingly shift toward electrical energy in various aspects of our lives, the need for efficient energy storage has driven a growing demand for advanced batteries. This surge in battery production raises concerns about the energy balance and sustainability of both current and future battery technologies. While LIBs are currently the state-of-the-art technology, their production is driven by key performance factors such as energy density, power density, and cost. However, the high energy consumption in their production, the depletion of critical raw materials, and low recycling rates pose significant sustainability challenges, potentially leading to severe environmental impacts and uncertain production conditions in a future dominated by LIBs [386].

This thesis aims to work with more sustainable materials and concepts for LIBs technology where almost all components of a traditional LIB are substituted with greener alternatives that meet many sustainability criteria. However, a fully "green" LIB cell would currently struggle to match the performance of existing LIB cells. This is because the materials used in current LIBs have been carefully selected to meet the high demands of electrochemical processes, whereas greener alternatives often have inherent drawbacks in terms of energy density, cycle life, and cost competitiveness. Nevertheless, improvements in the carbon footprint of LIBs, through ecological advancements in inactive materials and production processes, could enhance sustainability. Additionally, extending battery life, enabling second life applications, and improving material recovery through stringent recycling are crucial for achieving a more sustainable future for LIBs. Enhancing the sustainability of these batteries involves improving their lifetime and recycling.

9. TECHNOLOGY OF LITHIUM-ION CELLS

There are various requirements and characteristics that should be understood on the Li-ion cells for development/design, evaluation, and optimization. Some of them are explained below [387].

9.1. The capacity of LIBs

The irreversible capacity, measured by the loss of capacity during the first or second cycle of a battery, can have multiple causes. For the positive electrode, this loss is often due to lithium de-intercalation during the initial charge, causing a structural modification that is not fully reversible, resulting in some lithium cations being trapped within the electrode particles. For example, LCO typically exhibits an irreversible capacity of 3–5 mAh·g^{-1}, whereas materials with less structural stability like $LiNiO_2$ can experience losses of up to 20–30·mAh·g^{-1}. On the negative electrode side, especially in carbon-based anodes, the initial irreversibility is mainly due to the formation of the SEI from the reduction of the electrolyte on the anode surface. The exact value of this irreversible capacity varies based on the carbon particles shape, size, and crystallinity but usually falls within the range of 20–30 mAh·g^{-1}.

Irreversible capacity can be particularly significant in certain cases, such as when the anode material undergoes amorphization during the first charge or when irreversible chemical reactions occur during the first discharge. Anodes that rely on alloying/de-alloying reactions can exhibit such large irreversible capacities that shift attention to the reversible capacity measured after the first or second cycle. This reversible capacity is critical as it represents the capacity that the battery can consistently deliver throughout its life. Despite the initial losses, the coulombic efficiency of batteries of interest (either commercial or in research) should reach 100% after the first two cycles [388].

In the design and evaluation of batteries, it is crucial to consider the factors contributing to irreversible capacity. For instance, the irreversible loss on the anode due to SEI formation involves Li$^+$ ions that are sourced from the positive electrode during the first charge.

Moreover, for certain anodes, significant irreversible capacity can stem from structural changes or irreversible reactions, necessitating a focus on the sustainable, reversible capacity post-initial cycles. Understanding these dynamics helps in optimizing battery performance and longevity [389].

9.2.   Negative/positive capacity ratio

The N/P ratio, or battery balance, is crucial in battery performance. For instance, consider a negative electrode with an initial capacity of 100 mAh and an irreversible capacity of 10 mAh. This means the formation of the SEI consumes 10 mAh, leaving 90 mAh for subsequent cycles when paired with a Li-metal counter-electrode.

This SEI formation does not limit the half-cell capacity, however, in a full cell, the dynamics change. If in a full cell, the cathode starts with 100 mAh and has a 20 mAh irreversible capacity, its reversible capacity is 80 mAh. The initial charge consumes 10 mAh for SEI formation and 90 mAh for fully charging the anode. During discharge, the negative electrode can only provide 90 mAh, but 20 mAh of this will be trapped due to the cathode irreversible capacity, resulting in a battery capacity of 70 mAh.

Increasing the cathode capacity might seem beneficial, but it can lead to issues like lithium plating. For example, increasing the cathode capacity by 50% results in an initial capacity of 150 mAh and an irreversible capacity of 30 mAh. During the first charge, 100 mAh will be transferred as before, but further charging would cause lithium to accumulate on the anode surface, forming a Li-metal film [390].

This situation poses safety risks due to potential lithium dendrite formation, thus, the capacity of the negative electrode must always be larger than the positive electrode to avoid such issues. Therefore, it is required to increase the negative electrode capacity, although doing so proportionally increases the irreversible capacity, which can still reduce overall battery capacity [391].

Manufacturers optimize the N/P ratio to ensure both safety and capacity. The ideal balance ensures the anode capacity is slightly larger than the cathode, as seen in standard cells like the "18650" where the negative electrode is marginally wider than the positive electrode, fulfilling a N/P ratio of about 1.1. This careful balance is essential for both the efficiency and safety of the battery.

9.3.   Electrode mass loading (areal capacity)

Electrode loading refers to the amount of AM deposited per unit area of the current collector foil, and it is a critical parameter for optimizing battery performance. High loading levels can increase resistance within the electrode layer, limiting the battery rate capability by restricting the electrical current flow. On the contrary, lower loading levels enhance rate

capability but reduce the AM mass, and hence the energy density. To maintain the same capacity with reduced loading, a larger electrode area is required.

To balance this, the electrode loading level is always a compromise, depending on the specific powder used for the electrode, as the effective surface area is influenced by particle size and shape. Reducing the thickness of the metal foil could mitigate the mass penalty, however, practical limitations exist due to the need to handle the foil during manufacturing.

This basic conflict between high power and high energy is a fundamental challenge in LIB design. Manufacturers need to consider adjusting electrode loading to ensure the best performance for the intended application.

By optimizing the mass loading of AM and the thickness of the metal foil (current collector), they can enhance both the energy density and the rate capability of the battery. This optimization process is vital for the development of efficient and high-performing batteries.

EXPERIMENTAL SECTION

CHARACTERIZATION AND STUDY OF THE FLUORINE-FREE

NOVEL ELECTROLYTE

10. EXPERIMENTAL SECTION, MATERIALS AND METHODS

As part of the doctoral project, the electrolyte, anode, and cathode were prepared, and fluorine-containing materials were removed from all battery components. Then, the fluorine-free battery was evaluated and characterized for a better understanding. To enhance understanding and analysis, this research project is divided into three parts.

A. CHARACTERIZATION AND STUDY OF THE FLUORINE-FREE NOVEL ELECTROLYTE

Determination of organic carbonate solvents for the electrolyte preparation and the optimal concentration at various concentration and temperature were found, ionic conductivities and electrochemical stability window at various electrolyte compositions were measured, and lithium passivation was assessed.

10.1. Reagents for electrolyte preparation

Ethylene carbonate (EC), dimethyl carbonate (DMC), ethyl-methyl carbonate (EMC), diethyl carbonate (DEC), and vinylene carbonate (VC) battery grade solvents were purchased from BASF. Lithium hexafluorophosphate ($LiPF_6$, battery grade) and acetonitrile (AN, anhydrous, 99.98%) were procured from Sigma Aldrich. 1 mol·kg^{-1} $LiPF_6$ in EC:DMC (30:70 wt.%) was purchased from E-Lyte Innovations (battery grade).

10.2. Fluorine-free Li-salt and electrolyte preparation

Lithium 1,1,2,3,3-pentacyanopropenide (LiPCP). 1,1,2,3,3-pentacyanopropenide (PCP) is among the most stable carbanions. Its remarkable stability is attributed to the inductive effect of the five electron-withdrawing cyano groups. Consequently, the negative charge is delocalized across the central propenide structure [145, 149, 392, 393]. R. H. Boy reported that no changes in the spectra of PCP were noted up to 11 M perchloric acid or ~85% sulfuric acid, indicating that the free anion may still exist even in this strong acidic environment [394]. Making this salt stable and with no side reactions in contact with air, water and even highly acidic solutions. Furthermore, this novel lithium salt presents high thermal stability up to > 300°C [395].

The LiPCP salt was synthesized in the laboratory at Warsaw University of Technology in a two-step procedure as reported elsewhere [395]. First, a stoichiometric amount of water and excess pyridine is added to tetracyanoethylene to obtain pyridinium

1,1,2,3,3-pentacyanopropenide. Afterwards, tetrahydrofuran (THF) and lithium hydride (LiH) were added as the monovalent metal donor. After filtration and washing with ether at room temperature, LiPCP was obtained. LiPCP salt has a purity above 99% and characterization by nuclear magnetic resonance (NMR) is shown as follows: ^{13}C NMR (125 MHz; acetone–d$_6$) δ/ppm: 135,7 (C1–$\underline{C}$2–C3), 117,0 (2C, C1–$\underline{C}$N/C3–$\underline{C}$N (the side group of the three cyano groups that are on one side of the molecule)), 114,6 (C2–$\underline{C}$N), 113,9 (2C, C1–$\underline{C}$N/C3–$\underline{C}$N (two cyano groups on one side of the molecule)), 57,8 (2C, $\underline{C}$1–C2–$\underline{C}$3).

The fluorine-free electrolyte solutions were prepared in an argon-filled glovebox (LabStar, MBraun, H$_2$O <1 and O$_2$ <10 ppm) by dissolving the LiPCP salt in various solvent mixtures. For solvent screening, electrolyte solutions of 0.8 mol·kg^{-1} LiPCP in EC:DMC (30:70 wt.%), EC:EMC (30:70 wt.%) and EC:DEC (30:70 wt.%) were prepared.

For comparison, the commercial standard, 1 mol·kg^{-1} LiPF$_6$ electrolyte solutions were prepared in the same solvent mixtures. Additionally, for molality screening, solutions from 0.1 to 1.2 mol·kg^{-1} LiPCP in EC:DMC (30:70 wt.%) were prepared.

10.3.   Ionic conductivity measurements

The ionic conductivity of the LiPCP-based electrolytes was obtained by EIS using a VMP3 potentiostat-galvanostat (VMP3, Bio-Logic) in the temperature range of 0°C to 50°C. The measurements were carried out in the frequency range of 500 kHz to 1 Hz with 10 points per decade and signal amplitude of 5 mV. The measurement at each frequency was repeated 6 times. The conductivity micro cells consisted of electrolyte filled between two stainless steel electrodes. Cryostat-thermostat (Haake K75) with a temperature controller (DC50) was used for thermostating the samples.

The conductivity (σ) in mS·cm^{-1} was calculated according to Equation 10.1,

$$\sigma = \frac{k}{R} \qquad (10.3.1)$$

Where k is the cell constant (0.3 − 0.7 cm^{-1} ± 0.3% of precision) for each conductivity microcell, and R is the bulk resistance in ohms (Ω) obtained from the respective Nyquist plot.

10.4.   Linear sweep voltammetry

Linear sweep voltammetry (LSV) was used to evaluate the electrochemical stability window of the following electrolytes: 0.8 mol·kg^{-1} LiPCP in EC:DMC (30:70 wt.%), 0.8 mol·kg^{-1} LiPCP in EC:DMC (30:70 wt.%) + 5 wt.% VC, 0.8 mol·kg^{-1} LiPCP in EC:DMC

(30:70 wt.%) + 5 wt.% VC + 5 wt.% AN, and 0.8 mol·kg^{-1} LiPCP in EC:DMC (30:70 wt.%) + 5 wt.% VC + 10 wt.% AN. The tests were made at room temperature in two-electrode Swagelok-type cell configuration at a scan rate of 0.5 mV·s^{-1}. For the set-up, a Pt disc was used as the working electrode and Li metal disc as the counter and reference electrode.

10.5. Lithium passivation measurements

Lithium passivation was investigated with EIS for the following electrolytes: 0.8 mol·kg^{-1} LiPCP in EC:DMC (30:70 wt.%) + 5 wt.% VC, 0.8 mol·kg^{-1} LiPCP in EC:DMC (30:70 wt.%) + 5 wt.% VC + 10 wt.% AN, and 1.0 mol·kg^{-1} LiPF$_6$ in EC:DMC (30:70 wt.%). The measurements were carried out in the Swagelok-type cells with two lithium electrodes (discs) and Celgard 2400 separator in between of them. For the measurement, a VMP3 potentiostat-galvanostat (Bio-Logic) was used. The measurements were carried out in the frequency range of 500 kHz to 1 Hz with 10 points per decade and signal amplitude of 5 mV, each frequency was repeated 6 times. The impedance spectra were repeatedly measured in the period of 6 h. Impedance spectra were analyzed using RelaxIS 3 software. Table 20 shows the electrolyte compositions used in various experiments through this research.

Table 20.   Electrolyte compositions used in different experiments

Experiment	Electrolyte	Observations
Ionic conductivity measurements	0.1 to 1.2 mol·kg^{-1} LiPCP in EC:DMC (30:70 wt.%)	Screening of compositions at the temperature range of 0°C to 50°C
	0.8 mol·kg^{-1} LiPCP in EC:DMC (30:70 wt.%) EC:EMC (30:70 wt.%) EC:DEC (30:70 wt.%)	Comparison of conductivities of LiPCP and the most commercial electrolyte LiPF$_6$ in various organic carbonate solvents
	1 mol·kg^{-1} LiPF$_6$ in EC:DMC (30:70 wt.%) EC:EMC (30:70 wt.%) EC:DEC (30:70 wt.%)	
Linear sweep voltammetry	0.8 mol·kg^{-1} LiPCP in EC:DMC (30:70 wt.%) 0.8 mol·kg^{-1} LiPCP in EC:DMC (30:70 wt.%) + 5 wt.% VC 0.8 mol·kg^{-1} LiPCP in EC:DMC (30:70 wt.%) + 5 wt.% VC + 5 wt.% AN 0.8 mol·kg^{-1} LiPCP in EC:DMC (30:70 wt.%) + 5 wt.% VC + 10 wt.% AN	Evaluating the electrochemical stability window
Lithium passivation	0.8 mol·kg^{-1} LiPCP in EC:DMC (30:70 wt.%) + 5 wt.% VC 0.8 mol·kg^{-1} LiPCP in EC:DMC (30:70 wt.%) + 5 wt.% VC + 10 wt.% AN 1.0 mol·kg^{-1} LiPF$_6$ in EC:DMC (30:70 wt.%).	Evaluating the lithium effect and effect in the cycling
Galvanostatic charge/discharge cycling	0.8 mol·kg^{-1} LiPCP in EC:DMC (30:70 wt.%) + 5 wt.% VC	This composition was used for the cycling, compatibility and stability evaluation

EXPERIMENTAL SECTION

AQUEOUS-PROCESSED ELECTRODES FABRICATION AT LABORATORY AND PRE-PILOT SCALE

B. ELECTRODES FABRICATION AT LABORATORY AND PRE-PILOT SCALE

Various slurry compositions were prepared at various binder, CMs and AMs ratios, cyclic voltammetry with the optimal electrolyte composition was conducted. For upscaling purposes pH and viscosity of the slurry was evaluated. This research also explored the calendering process, electrode resistance, measured mass loading, and assessed electrode thickness on the chosen electrode optimized formulation for the pouch cells assembly.

10.6.   Chemical reagents for electrode fabrication

The metallic lithium foil was purchased from Honjo Metal. Lithium iron phosphate (LFP, 1.45 wt.% carbon) and lithium iron manganese phosphate (LMFP, 1.5~2.5 wt.% carbon) powdered materials were acquired from MTI and MSE Supplies, respectively. SG (powder, <20 μm, synthetic), and SOX powder material were acquired from MTI Supplies and Sigma Aldrich, respectively. Na-CMC (average M_w of 250,000, degree of substitution equal to 0.9) and SBR (40%) binders were purchased from Sigma Aldrich and Arkema, respectively. Super-P, Ketjenblack and C45 carbon black (TIMCAL SUPER C45) conductive carbons were procured from Alfa Aesar, MSE Supplies, and C-NERGY™, respectively. Carbon coated-aluminum foil (15 μm thickness of aluminum, 1 μm of conductive carbon), aluminum foil (17 μm of thickness), and Copper (18 μm of thickness) were purchased from MSE Supplies and by SCHLENK Metal Foils.

10.7.   Electrode fabrication

10.7.1. Electrode fabrication for coin cells (laboratory scale)

LFP, LMFP, SG and SOX were used independently as the AM. CMC was employed as the binder. Super-P and Ketjenblack conductive carbon black were used independently as the CM for electrode preparation. The components were mixed following various AM:CM:binder ratios (as indicated where appropriate throughout the manuscript) by using magnetic stirring (IKA, type RH Basic Magnetic Stirrer) at 500 rpm for 24 h, and distilled water as the solvent.

The obtained slurry was then cast onto a carbon coated-aluminum foil by using blade coater (Doctor Blade, ZEHNTNER Testing Instruments, ZAA 2300 and ZEHNTNER film applicator ZUA 2000). All electrodes were first dried at 80°C for 2 hours, subsequently, they were vacuum dried at 120°C overnight (Memmert VO 400).

10.7.2. Electrode fabrication and characterization for pouch cells

LFP preparation

LFP was used as the AM. CMC and SBR were employed as the binder. Ketjenblack conductive carbon black was used as the CM for the cathode preparation, and distilled water was used as the solvent. The components were mixed following 92:6:1:1 (AM:CM:CMC:SBR) ratio by a homogenizer (DISPERMAT® CV3-PLUS, Figure 11) varying the mixing speed at 300, 500 and 1500 rpm for 4.5 h at 23°C. The obtained slurry with a solid content of 42 wt.% was then cast onto a carbon coated-aluminum foil by using a blade coater (K Control Coater with a micrometer adjustable applicator) at speed of 1.5 mm/s.

Figure 11. DISPERMAT CV-PLUS dissolver, source: Dispermat official website

Synthetic graphite preparation

SG was used as the AM. CMC and SBR were employed as the binder. Conductive carbon black C-45 was used as the CM for the anode preparation, and distilled water was used as the solvent. The components were mixed following a 95:2:1:2 (AM:CM:CMC:SBR) ratio by a homogenizer (DISPERMAT® CV-PLUS dissolver, Figure 11) varying the mixing speed at 500 and 1500 rpm for 2 h at room temperature. The obtained slurry with a solid content of 37 wt.% was then cast onto a copper foil by using blade coater (K Control Coater with a micrometer adjustable applicator) at speed of 1.5 mm/s.

Silicon oxide composite preparation

SOX was used as the AM. CMC and SBR were employed as the binder. Conductive carbon black C-45 was used as the CM for the anode preparation, and distilled water was used

as the solvent. The components were mixed following a 92:6:1:1 (AM:CM:CMC:SBR) ratio by a homogenizer (DISPERMAT® CV-PLUS dissolver, Figure 11) varying the mixing speed at 300, 1000 and 1500 rpm for 4.5 h at 21°C. The obtained slurry with a solid content of 49 wt.% was then cast onto a copper foil by using blade coater (K Control Coater with a micrometer adjustable applicator) at speed of 1.5 mm/s.

The blade height was adjusted to achieve the desired loading on all electrodes. All electrodes were first dried at room temperature for 2 h and subsequently at 80°C in a safety drying oven (BINDER FDL 115, GmbH) overnight.

pH measurements

The pH value was evaluated at 22°C using a pH-meter (Basic 20, CRISON Instruments) throughout the slurry preparation at each stage for both electrodes. Following the pH measurement, the slurry was immediately transferred into the coating device.

Rheological measurements

The rheological measurements were carried out at 23°C for the LFP, SG and SOX using a rheometer (HAAKE RheoWin, Thermo Fisher Scientific) with the 25 mm diameter parallel plate measuring system (PP25). The gap between plates was fixed at 1 mm for all measurements. Viscosity and shear stress versus the shear rate were obtained with a rotational test. The storage and loss modulus (G', G") versus the shear strain were measured under amplitude sweeps at a constant angular frequency of 10 rad/s.

Thickness and AM loading on the electrode measurements

The mass (analytic balance Metler Toledo XA 204, Delta range) and thickness (Digital depth gauge 547 series, MITUTOYO, micrometer) of the punched electrodes at 12 mm were measured after the calendering process, tools used are shown in Figure 12.
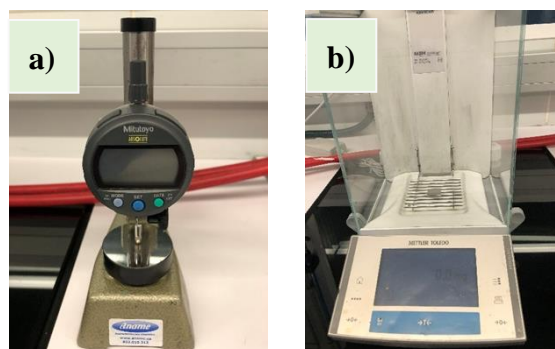
Figure 12. (a) Micrometer and (b) analitycal balance for punched electrodes after calendering measurements

Drying process for electrodes for pouch cells

All electrodes were first dried at room temperature (22°C) for ~2 hours, subsequently, they were dried at 80°C overnight (BINDER drying oven).

Calendering process

The electrodes were then calendered using a R&D calender (Calendering Machine, Figure 13) at a line speed of 0.4 m/min for anodes and 4.40 m/min for cathodes electrodes with the rolls heated at 80°C. Although a porosity of 20% for LFP and 10% for SG and SOX was targeted, since the calendering was performed on sheets of 9 cm × 15 cm using the average value of the thickness and coating weight with the target porosity at the local level where the pouch cell electrodes were cut, the final porosities resulted in approximately values of 15% for LFP, 10% for SG and 10% for SOX.

Figure 13. Calendering equipment, source: Group of prototyping from CIC EnergiGUNE

Conductivity / electrode resistance measurement

The Composite volume resistivity ($\Omega \cdot cm$) was measured using a multipoint probe setup (HIOKI, RM2612, Figure 14). Measurements were performed at three locations for each sample. The samples thickness without current collectors varied from 20-120 μm, the current collector resistivity was considered $1.7 \cdot 10^{-6}$ (Ω cm) for copper and $2.7 \cdot 10^{-6}$ (Ω cm) for aluminum, measurements were carried out at room temperature.
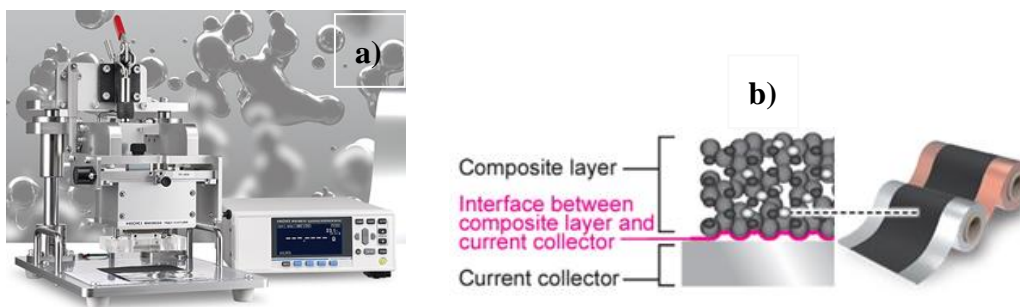
Figure 14. a) electrode resistance meter and b) cross-sectional view of an electrode sheet

10.8. Cyclic voltammetry

To evaluate the electrode/electrolyte compatibility, cyclic voltammetry (CV) measurements were conducted in a potentiostat-galvanostat (VMP3, Bio-Logic). LFP and LMFP electrodes of 11 mm in diameter were punched and assembled in two-electrode Swagelok-type cell configuration using a disc of Li metal as counter electrode. Celgard 2400 microporous polypropylene was used as separator, 0.8 mol·kg^{-1} LiPCP in EC:DMC (30:70·wt. %) was used as the electrolyte and 1 mol·kg^{-1} LiPF$_6$ in EC:DMC (30:70 wt. %) as the commercial reference electrolyte. The scan rate was set at 0.5 mV·s^{-1} in the 2.5–3.9 V $vs.$ Li$^+$/Li for LFP cathode, and 2.5 – 4.5 V $vs.$ Li$^+$/Li potential limits for LMFP cathode.

10.9. Coin cells assembly and electrochemical characterization

For galvanostatic cycling, LFP and LMFP electrodes of 15 mm in diameter were punched and assembled in CR2032 coin-cells, using a Li metal disc as negative electrode and Celgard 2400 as separator.

The electrolyte solution was 0.8 mol·kg^{-1} LiPCP in EC:DMC (30:70 wt. %) + 5 wt.% VC. The tests were performed in a SOLLICH potentiostat-galvanostat (SOLLICH 2061 MPG&T, Multichannel Potentiostat–Galvanostat & Battery Tester) in the 2.5–3.9 V $vs.$ Li$^+$/Li potential range for the LFP cathode and 2.4–4.2 V $vs.$ Li$^+$/Li for the LMFP cathode.

The protocol consisted of one formation cycle at C/25 (where C = 170 mAh·g^{-1} for LFP and 160 mAh·g^{-1} for LMFP) followed by C/10 cycling. In addition, the rate capability of the LFP and LMFP cathodes with the LiPCP-based electrolyte was screened. To this purpose, one cycle at C/25, 5 cycles at C/20, C/10, C/5, C/2, and 1C were performed. The specific capacity of each half– and full cells were calculated based on the mass loading of the cathode materials.

10.10. Pouch cells assembly and electrochemical characterization

This experimental section outlines the assembly, configuration, and testing of two- and three-electrode pouch cells, focusing on their design specifications, fabrication processes, and electrochemical performance as shown in Figure 15.

In the two-electrode pouch cell configuration, the setup included a negative electrode made of SG or SOX with dimensions of 39 mm x 65 mm, providing an area of 21.8 cm². The positive electrode was composed of LFP, measuring 37.5 mm x 64 mm, with an area of 20.25·cm². A Celgard 2325 separator was used to cover both electrodes. The cell was filled with 900 µl of 0.8 m LiPCP dissolved in a mixture of ethylene carbonate (EC) and dimethyl carbonate (DMC) at a 30:70 weight ratio, with the addition of 5 wt.% vinylene carbonate (VC) to enhance performance.
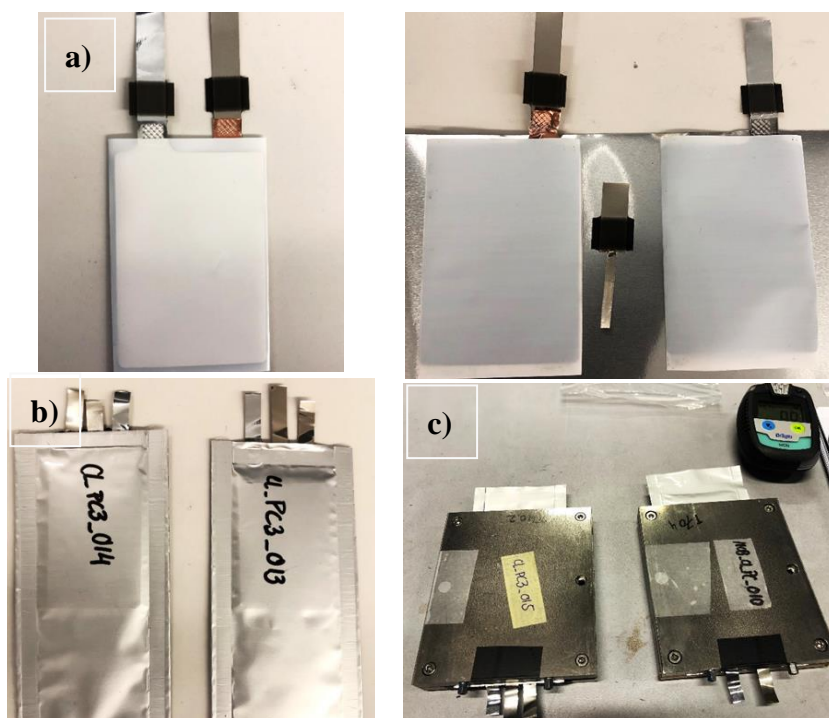
Figure 15. Pouch cells assembly a) two-electrodes configuration, b) three-electrode configuration, c) three-electrodes pouch cells for 24-h resting before cycling, and d) three- and two-electrodes pouch cells configurations between steel plates, torque of 0.8 and 1.0 Nm, respectively, pouch cells ready for cycling.

The three-electrode pouch cell configuration was similar but included a lithium wire placed between the electrodes for enhanced performance. It had a negative electrode of SG or SOX, also measuring 39 mm x 65 mm (area: 21.8 cm²), and a positive electrode of LFP, with dimensions of 37.5 mm x 64 mm (area: 20.25 cm²).

A Celgard 2325 separator covered both electrodes. This configuration used 1000 µl of 0.8 m LiPCP in the same EC:DMC (30:70·wt.%) solution with 5 wt.% VC.

The pouch cell fabrication process began with pre-assembly steps such as side sealing and welding nickel, aluminum, and, in the case of the three-electrode cells, lithium wire to the system. These steps are critical for continuing with the following steps. After partial sealing and full welding, the cells were dried in a vacuum oven at 120°C overnight. Following this, the electrolyte was filled, and the cells were vacuum-sealed. They were then kept at room temperature for 24 hours to ensure proper electrolyte wettability before cycling. The equipments used for sealing, welding, and filling the electrolyte was provided by SOLITH (Sovema Group, supported by Schuler Group).

The pouch cells were cycled between 2.5 and 3.9 V *vs*. Li/Li$^+$ using a BT-lab system at 25°C within a BINDER MK720 safety chamber. The initial formation cycle used a charging and discharging rate of C/25. Further electrochemical characterization was conducted at a C/10 rate. The specific capacity of full–cells on pouch cells configurations were calculated based on the mass loading of the cathode materials.

A total of six full pouch cells were designed and assembled with an average capacity of approximately 2 mAh/cm^2. Additionally, two full pouch cells were assembled for reference surface characterization, using the same 0.8 mol·kg^{-1} LiPCP in EC/DMC (30:70 wt.%) + 5·wt.% VC. The detailed configuration of each cell is presented in Table 21.

Table 21.   Pouch cells assembly and design for further electrochemical characterization

Pouch cell CODE	Cathode	Anode	N/P Ratio	Experiment program	Cell configuration
CL_PC_002	LFP	SG	1.15	No cycling, 24 hours wettability	G + LFP, 2 electrodes
CL_PC_003	LFP	SOX	1.12	No cycling, 24 hours wettability	Si + LFP, 2 electrodes
CL_PC_006	LFP	SG	1.43	1 cycle C/25 69 cycles C/10	G + LFP, 2 electrodes
CL_PC_011	LFP	SOX	1.21	1 cycle C/25 69 cycles C/10	Si + LFP, 2 electrodes
CL_PC3_014	LFP	SOX	1.21	1 cycle C/25 3 cycles 3/10	Si, 3 electrodes
CL_PC_012	LFP	SOX	1.18	Half-charge, C/25	Si, half charge 2 electrodes
CL_PC3_016	LFP	SG	1.23	1 cycle C/25 3 cycles 3/10	G, 3 electrodes
CL_PC_018	LFP	SG	1.17	Half-charge, C/25	G, half charge 2 electrodes

C. SURFACE CHARACTERIZATION OF OPTIMIZED ELECTRODES

The surface morphology of the electrodes used in coin cells was examined using Scanning Electron Microscopy (SEM, FEI Quanta 200 FEG, Thermo Fisher). This SEM analysis offered comprehensive insights into the structural properties of the electrodes before their incorporation into the cell assembly. In addition, electrode sheets were assessed both prior to cycling and after the calendering process.

For the electrodes at the pouch cell size, surface characterization was performed using the Thermo Scientific Apreo 2 Scanning Electron Microscope (SEM). This analysis, conducted both before and after the cycling process, assessed changes in surface roughness, topography, and the presence of cracks. Additionally, the study examined the distribution of electrode components to evaluate any alterations due to cycling, providing valuable insights into the performance and durability of the electrodes in larger cell applications.

RESULTS AND DISCUSSION

CHARACTERIZATION AND STUDY OF THE FLUORINE-FREE

NOVEL ELECTROLYTE

11. RESULTS AND DISCUSSION

This section presents the core outcomes of this research, detailing the data collected, analyzed, and interpreted in accordance with the objectives set forth in the study. The findings are systematically organized to align with the research purposes, providing a comprehensive view of the data gathered. By clearly interpreting the data, this section aims to explain the contribution of the research to the field and set the stage for subsequent conclusions.

A. CHARACTERIZATION AND STUDY OF THE FLUORINE-FREE NOVEL ELECTROLYTE FOR COIN CELLS ASSEMBLY

11.1. Electrolyte characterization – ionic conductivity and LSV

The initial phase of electrolyte optimization involved identifying the most effective organic carbonate solvent mixture for the LiPCP salt. The solvents considered were EC, DMC, DEC, and EMC. Ionic conductivity measurements were conducted to achieve this goal. For comparison purposes, mixtures of solvents containing $LiPF_6$ were prepared. Figure 16a presents the ionic conductivity of LiPCP at varying temperatures and molal concentrations ranging from 0.1 to 1.2 $mol \cdot kg^{-1}$ in EC:DMC (30:70 wt.%). At 20°C, the highest conductivity for LiPCP was observed at 0.8 $mol \cdot kg^{-1}$, with a value of 9.6 $mS \cdot cm^{-1}$. Table A.1 shows that the conductivity of LiPCP solutions meets the minimum conductivity requirements for LIBs, typically between 5 and 10 $mS \cdot cm^{-1}$ [35]. Notably, the optimal concentration for LiPCP is lower (0.8 $mol \cdot kg^{-1}$) than that for $LiPF_6$ (1.0 $mol \cdot kg^{-1}$), which is advantageous economically and ecologically, as it requires less salt. This suggests that LiPCP is competitive with conventional $LiPF_6$-based electrolytes due to its high mobility at a lower concentration and satisfactory ionic conductivity.

Figure 16b shows the ionic conductivity of LiPCP and $LiPF_6$ in various organic carbonate solvents and at various temperatures. Solutions of 0.8 $mol \cdot kg^{-1}$ of LiPCP in EC:DMC (30:70 wt.%), EC:DEC (30:70 wt.%), EC:EMC (30:70 wt.%) and 1.0 $mol \cdot kg^{-1}$ of $LiPF_6$ in EC:DMC (30:70 wt.%), EC:DEC (30:70 wt.%), EC:EMC (30:70 wt.%) were investigated. The highest conductivities of LiPCP and $LiPF_6$ were achieved with the mixture of EC:DMC. At the temperature of 20°C, LiPCP in EC:DMC has a conductivity of 9.6 $mS \cdot cm^{-1}$ and $LiPF_6$ in EC:DMC has a conductivity of 12.3 $mS \cdot cm^{-1}$, the difference between them was of ca. 28% in favor of $LiPF_6$ solution.

The behavior of LiPCP and LiPF$_6$ in various solvent mixtures showed a similar trend: both achieved the highest conductivity with EC:DMC and the lowest with EC:DEC. This trend can be attributed to the lower viscosity of DMC compared to DEC, which has the highest viscosity among the three tested linear carbonate solvents. As a result, the mixture of LiPCP in EC:DMC was selected as the baseline electrolyte for further research. The conductivity values for each electrolyte, and the percentage differences between the LiPF$_6$ and LiPCP salt-containing electrolytes, are detailed in Table A.2 and Table A.3, respectively.
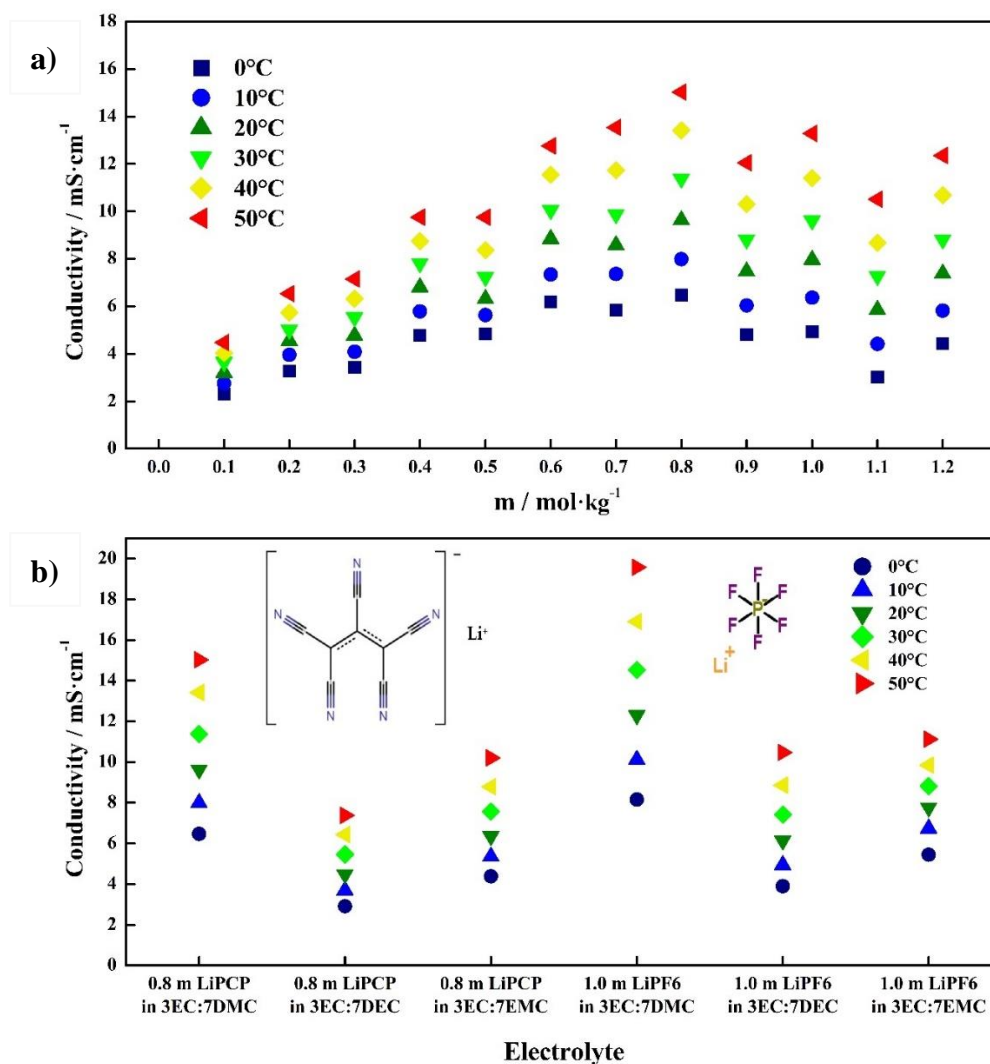
Figure 16. a) Ionic conductivity of LiPCP and LiPF$_6$ in various organic carbonates solvents mixtures from 0 to 50°C. b) Ionic conductivity of LiPCP in EC:DMC (30:70 wt.%) at concentrations in the range of 0.1 – 1.2 mol·kg^{-1} from 0 to 50°C.

Additionally, the electrochemical stability of the baseline LiPCP electrolyte (0.8·mol·kg^{-1} LiPCP in EC:DMC (30:70 wt.%)) was assessed using linear sweep voltammetry (LSV).

Quantum chemistry calculations typically classify anodic stability based on anion structure and functional groups, although the concentration of Li$^+$ ions and the solvent composition also affect anion stability [80]. Therefore, it is crucial to examine the impact of various additives, such as VC and AN, on the electrolyte's electrochemical stability
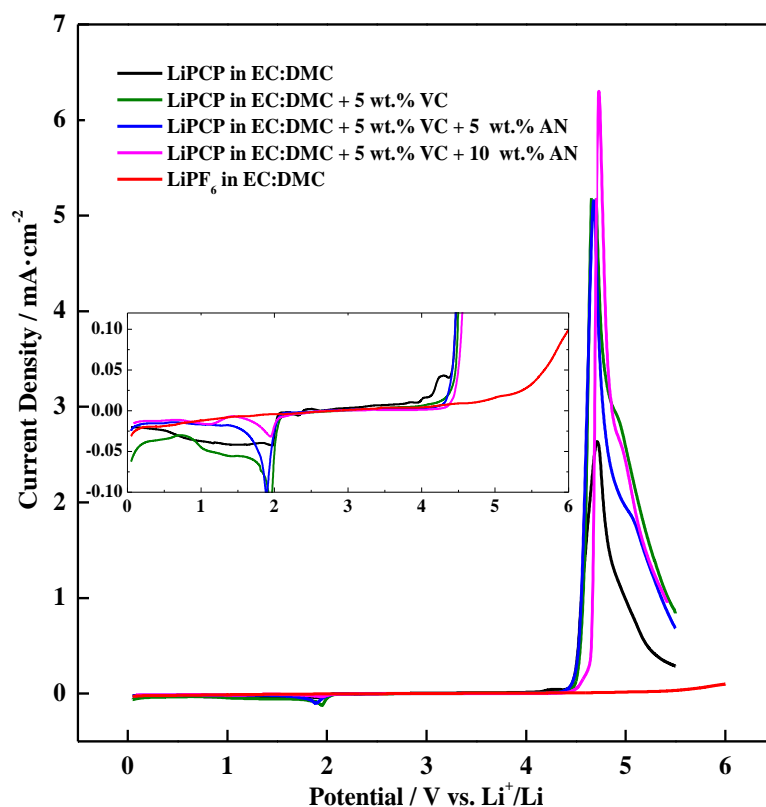
Figure 17. Linear sweep voltammetry (LSV) of 0.8 mol·kg^{-1} LiPCP-based electrolytes without additives and with various electrolyte additive concentrations, with the Pt disc as the working electrode and Li metal disc as the reference electrode in a Swagelok-cell system, at a scan rate of 0.5 mV·s^{-1}. For comparison purposes, data on a LiPF$_6$ electrolyte is included. The inset shows the zoomed area.

Figure 17 displays voltammograms of the electrolyte without additives, with 5 wt.% of VC, and with 5 wt.% of VC plus either 5 wt.% or 10 wt.% of AN. The electrolyte without additives exhibited the lowest stability, limited to 4.0 V *vs*. Li$^+$/Li. By adding 5 wt.% of VC, the stability window increased to 4.4 V *vs*. Li$^+$/Li, and the addition of 10 wt.% AN further extended this window to 4.45 V *vs*. Li$^+$/Li.

A reduction was observed in the nitrile-based electrolyte around 2 V *vs*. Li/Li$^+$, though the origin of this reduction is unclear. It might involve anion decomposition on the electrode surface or the decomposition of solvents/electrolyte additives, resulting in unpredictable reactions/products. Thus, the experimentally determined electrolyte stability, measured in

a Li/Pt system, should be regarded as a reference for electrolyte stability in cells with electrode AMs. The findings suggest that the stability window of the tested electrolytes is adequate for cobalt-free commercial electrodes such as LFP and may also allow for use with LMFP.

11.2. Lithium passivation

The results observed for the samples during the stability measurements are influenced by processes occurring at both the anode and cathode, presenting challenges when comparing data from samples with various electrolytes. Understanding those challenges is important for proper evaluation of used additives. In these cases, the variation in resistance of the passivation layer on the lithium electrode can overshadow effects on the cathode side. To assess this impact, lithium passivation tests were conducted.

Figure 18 presents the charge transfer resistance (R_{ct}), and passive layer resistance (R_p) derived from impedance spectra fitting (Figure S.1).
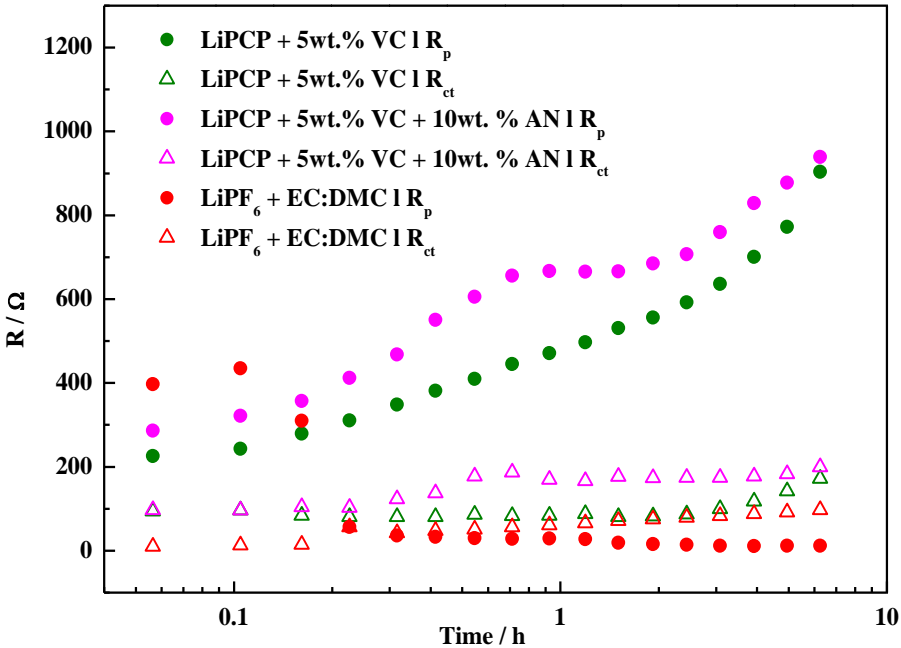
Figure 18. Passive layer resistances (R_p) and charge transfer resistances (R_{ct}) for Li|electrolyte|Li cells with three different electrolytes

For lithium electrodes in LiPCP-based electrolytes, R_p increased over 6 hours from approximately 200 $\Omega \cdot cm^2$ to 1000 $\Omega \cdot cm^2$. Conversely, for the sample with $LiPF_6$, which started with similar resistance, R_p decreased within the first hour to below 100 $\Omega \cdot cm^2$, indicating the dissolution of a native passivation layer on lithium and the formation of a new one with much lower resistance.

The R_{ct} values were similar across all samples, rising to around 100 $\Omega \cdot cm^2$ for the LiPF$_6$ sample and 200 $\Omega \cdot cm^2$ for the LiPCP samples. The LiPCP + 5 wt.% VC + 10 wt.% AN sample showed slightly higher resistance compared to the analogous sample without AN, likely due to the reactivity of AN with metallic lithium [396]. However, it was also demonstrated that the presence of VC enables the formation of a stable SEI for AN-containing electrolytes [397].

The higher resistance observed in LiPCP-containing samples may result in increased polarization of the cells during cycling, independent of the performance of the electrolyte or cathode material.

11.3. Cathodes fabrication, and cyclic voltammetry in Swagelok–cells

To explore sustainable cobalt-free electrode materials, this study selected LFP and LMFP as cathode materials to examine the reversibility of the electrolyte/electrode interaction. Cyclic Voltammetry (CV) measurements were conducted for this purpose. Based on previous LSV results, the chosen electrolyte was $0.8 \cdot mol \cdot kg^{-1}$ LiPCP in a solvent mixture of EC:DMC (30:70 wt.%) with 5 wt.% VC, which provides an adequate stability window for both LFP and LMFP electrodes. In the case of the LFP material, various aqueous-processed electrode formulations were evaluated using CV, as detailed in Table 22.

Table 22. **Weight compositions (LFP, Super P and CMC binder) and key results of various LFP-based cathodes used in cyclic voltammetry experiments**

Code	AM / wt.%, LFP	CM / wt.%, Super P	Binder / wt.%, CMC	Oxidation Peak / V	Reduction Peak / V	ΔV / V	Discharge peak current density / mA·cm^{-2}
LFP1	85	10	5	3.94	3.21	0.73	0.33
LFP2	87	10	3	3.88	3.23	0.65	1.08
LFP3	88	10	2	3.84	3.23	0.61	0.13
LFP4	87.5	10	2.5	3.94	3.14	0.80	0.85
LFP5	90	8	2	3.91	3.24	0.68	0.80
LFP6	90	7.5	2.5	3.90	3.24	0.65	0.61
LFP7	90	7	3	3.91	3.26	0.65	0.47
LFP8	80	17	3	3.91	3.21	0.71	0.83
LFP9	83	14	3	3.92	3.17	0.75	0.25
LFP10	85	12	3	3.92	3.25	0.67	0.64

Table 22 presents the differences between anodic and cathodic peak potentials (ΔV) for each electrode composition. This difference correlates with the polarization or reversibility of the redox reaction: smaller differences indicate greater reversibility and reduced polarization.

Figure 19a illustrates the reversible redox activity of the aqueous-processed LFP cathode across various compositions using a CMC binder and water as a solvent, with a LiPCP-based electrolyte.

The potential difference between oxidation and reduction peaks serves as a measure of electrochemical kinetics. Samples LFP2, LFP3, LFP6, and LFP7 exhibit the smallest potential differences and peak area ratios. Notably, LFP2 displays the sharpest peaks and highest current density, indicating fast redox kinetics. The potential difference (ΔV) is only 0.65 V, reflecting relatively low polarization. These findings suggest that the composition of LFP2, combined with a LiPCP-based electrolyte, provides better conductivity than other compositions. This improved performance can be attributed to the CMC/binder ratio. When the ratio exceeds 3.3, a higher content of CM in the slurry results in uneven distribution of the AM, leading to agglomeration. Additionally, insufficient binder in the slurry weakens cohesion between AMs and CMs and reduces adhesion to the current collector, impairing performance. Conversely, when the ratio is below 3.3, less CM in the electrode formulations reduces reversibility and increases polarization during cycling.

Considering the positive results for the electrolyte with 10 wt.% AN on the LSV electrolyte evaluation (Figure 17), CV was conducted using this electrolyte composition with the LFP2 slurry ratio for the cathode fabrication (Figure 19b).

No improvement was observed compared to the electrolyte without AN; instead, lower current densities were recorded. The sample with AN exhibited about ten times lower current density and the highest polarization, indicating poor performance.

This high polarization and low current density align with the highest resistance observed in passivation tests. The current drop suggests potential compatibility issues between the AN-containing electrolyte and the cathode. A possible explanation is that AN can easily deprotonate and polymerize upon contact with lithium metal, compromising the stability of the AN-containing half-cell. With the same electrode formulation and $LiPF_6$, a potential difference of 0.38 V was noted. Although the peak area ratio suggests significant irreversible reactions with $LiPF_6$, this sample achieved the highest current density, likely due to the lower resistance of the passivation layer on lithium.
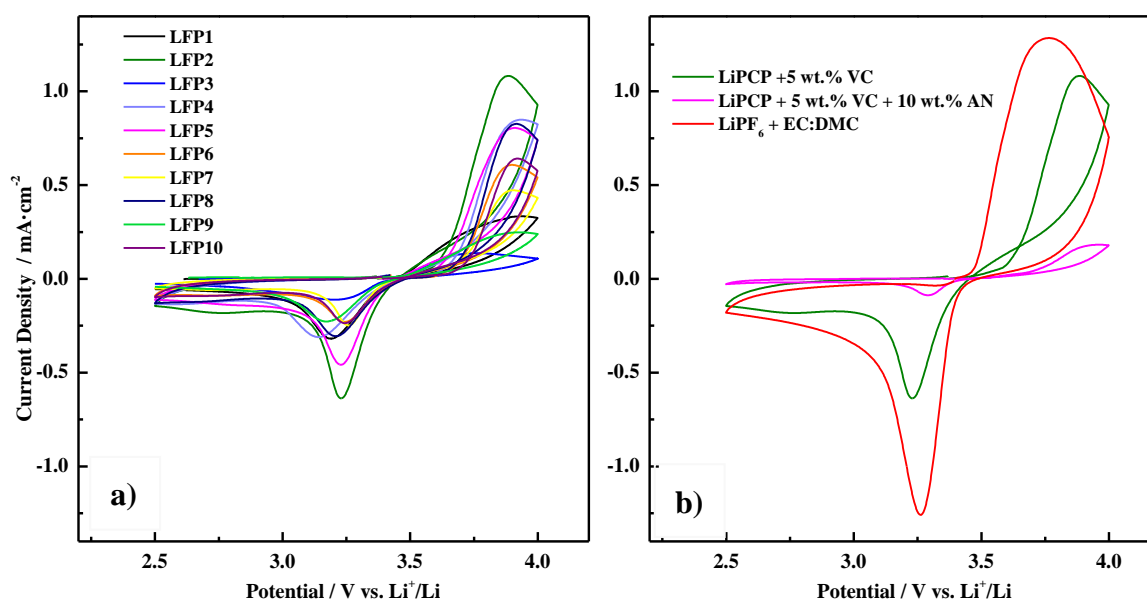
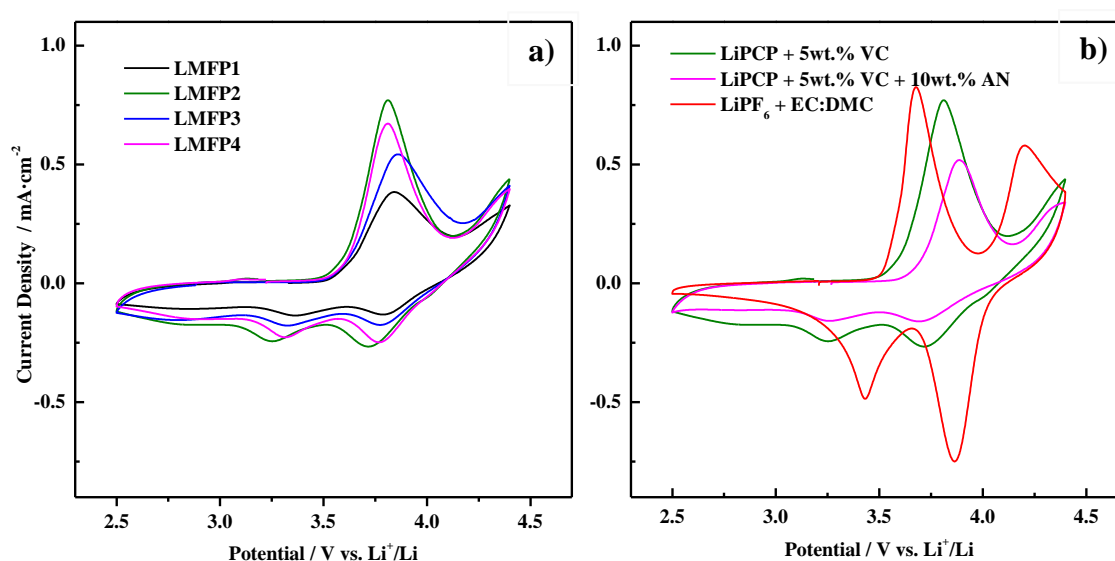**Figure 19.** a) CV voltammograms (1st cycle) of corresponding Li/LFP cells at various LFP compositions with 0.8 mol·kg⁻¹ LiPCP in EC:DMC (30:70 wt.%) and 5 wt.% of VC at a scan rate of 0.5 mV·s⁻¹ at room temperature. b) CV voltammograms (1st cycle) of corresponding Li/LFP2 cells with 0.8 mol·kg⁻¹ LiPCP in EC:DMC (30:70 wt.%) with 5 wt.% VC and with 5wt.% VC plus 10 wt.% AN. For comparison purposes data with reference LiPF₆ electrolyte is shown. Tests were done with a scan rate of 0.5 mV·s⁻¹ at room temperature

Table 23 details the LMFP cathode material at various formulations were evaluated with 0.8·mol·kg⁻¹ LiPCP in a solvent mixture of EC:DMC (30:70 wt.%) with 5 wt.% VC, using cyclic voltammetry. Super P Carbon Black and Ketjenblack EC600JD Carbon Black were selected as CMs. CMC solutions, with concentrations of 1 wt.% and 1.5 wt.%, served as the aqueous binder in the preparation of the slurry for the electrode fabrication.

Table 23. Weight compositions (LiMn$_{0.6}$Fe$_{0.4}$PO$_4$, conductive material and CMC binder) and key results of various LMFP-based cathodes used in cyclic voltammetry

Code	AM / wt.%. LMFP	CM / wt.%	Binder / wt.% CMC	CM Carbon Balck Type	Concentration CMC in solution (wt.%)	Oxidation Peak / V	Reduction Peak / V	ΔV / V	Discharge peak current density / mA·cm⁻²
LMFP1	87	10	3	Super P	1.0	3.83	3.36	0.47	0.38
LMFP2	87	10	3	Ketjenblack EC600JD	1.0	3.81	3.26	0.55	0.77
LMFP3	87	10	3	Super P	1.5	3.86	3.33	0.53	0.54
LMFP4	87	10	3	Ketjenblack EC600JD	1.5	3.81	3.32	0.49	0.67

Due to the LFP powder and aqueous-based binders to be used were stablished, super-P and Ketjenblack conductive additives were considered for the fabrication of cathode materials as the optimization of the electrodes were required to further research and upscaling [398].

Figure 20a presents the voltammograms of the fabricated LMFP cathode material utilizing the LiPCP-based electrolyte. The oxidation and reduction peaks for Fe^{3+}/Fe^{2+} are visible, whereas those for Mn^{3+}/Mn^{2+} are not fully observable due to the potential cut-off.

Figure 20. **a) CV voltammograms (1st cycle) of corresponding Li/LMFP cells at various LMFP compositions with 0.8 mol·kg^{-1} LiPCP in EC:DMC (30:70 wt.%) and 5 wt.% of VC at a scan rate of 0.5 mV·s^{-1} at room temperature. b) CV voltammograms (1st cycle) of Li/LMFP2 cells with 0.8 mol·kg^{-1} LiPCP in EC:DMC (30:70 wt.%) with 5 wt.% of VC and with 5 wt.% VC plus 10 wt.% AN. For comparison purposes, data with LiPF$_6$ electrolyte reference is shown. Tests were done with a scan rate of 0.5 mV·s^{-1} at room temperature**

The potential difference between the anodic and cathodic peaks of Mn and Fe shows a slight shift. For the samples LMFP1, LMFP2, LMFP3, and LMFP4, the potential differences for Fe were 0.47 V, 0.55 V, 0.53 V, and 0.49 V, respectively. LMFP2 exhibited a peak current density of 0.77 mA·cm^{-2}, which is noticeably higher than that of the other samples, indicating more rapid kinetics of the redox processes. Furthermore, the narrower peaks observed in LMFP2 compared to the other LMFP samples suggest lower polarization and significantly improved reversibility. Consequently, LMFP2 demonstrates the fastest Li$^+$ diffusion and the highest reversibility. It is important to note that rapid electrode reaction kinetics and high reversibility should lead to superior cyclability.

This is attributed to the porous nature of Ketjenblack, which enhances electron transport within the electrode, facilitating a more reversible process [399]. LMFP1 and LMFP2 have identical compositions, differing only in the CM, with LMFP2 showing superior performance. A similar trend is observed when comparing LMFP3 and LMFP4, where LMFP4, which uses Ketjenblack, displays a higher and narrower peak than LMFP3. Thus, the effect of CM on the electrode and cell performance is significant.

Figure 20b illustrates the optimized aqueous-processed LMFP2 electrode operating with LiPCP in an EC:DMC (30:70 wt.%) solution containing 5 wt.% VC, alongside a composition of 5 wt.% VC with 10 wt.% AN, and a $LiPF_6$-based electrolyte. The potential differences measured for the oxidation/reduction of Fe were 0.57 V for the 5 wt.% VC sample and 0.64 V for the 5 wt.% VC with 10 wt.% AN content. Similar to an analogous LFP system, the LMFP in 5 wt.% VC with 10 wt.% AN content demonstrated poor cell cyclability and stability.

This behavior is attributed to the reaction of AN with lithium metal during cycling, leading to the highest potential difference, increased polarization, and reduced reversibility. The sample containing $LiPF_6$ exhibited the lowest polarization and the highest current density, which is particularly significant for this cathode due to the limited potential margin over the Mn^{3+}/Mn^{2+} plateau.

11.4. Anodes fabrication, and cyclic voltammetry in Swagelok–cells

The main aim of this research is to develop green and sustainable lithium-ion cells. The main challenge involves not only identifying electrodes that are compatible with a novel fluorine-free electrolyte but also focusing on electrode materials derived from easily available raw materials. SG and SOX are both abundant materials worldwide and were selected as the anode materials to be tested with the novel electrolyte. The anodes were prepared by mixing the AM, Super-P carbon black, and CMC in a weight ratio of 95:3:2 in distilled water. This slurry was then coated onto copper foils, and the electrodes were dried in a vacuum oven for 24 hours. Based on the findings from the cathode materials, these anodes were tested in a $0.8 \cdot mol \cdot kg^{-1}$ LiPCP solution in EC:DMC (30:70 wt.%) with 1 or 5 wt.% of VC at a scan rate of $0.5~mV \cdot s^{-1}$. Figures 21a and 21b demonstrate the compatibility of the novel electrolyte with the proposed anodes (SG and SOX), showing good compatibility throughout various electrolyte additive compositions. The amount of electrolyte additives did not significantly affect cell performance.

Consequently, further research on electrolyte additives interaction with anodes will not be pursued within the scope of this thesis, allowing the focus to shift towards developing a full cell (coin– and pouch–cell configuration).
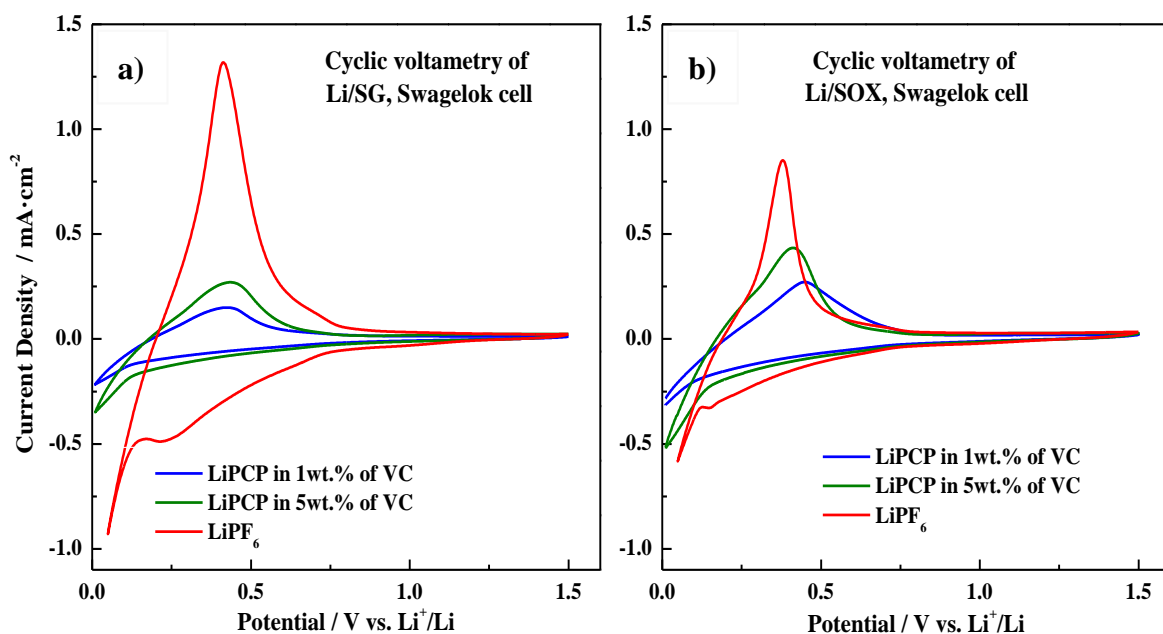
Figure 21. **a) CV voltammograms (4th cycle) of corresponding Li/SG Swagelok cells in 0.8·mol·kg⁻¹ LiPCP in EC:DMC (30:70 wt.%) with 1 and 5 wt.% of VC at a scan rate of 0.5 mV·s⁻¹ at room temperature. b) CV voltammograms (4th cycle) of corresponding Li/SOX Swagelok cells in 0.8 mol·kg⁻¹ LiPCP in EC:DMC (30:70 wt.%) with 1 and 5 wt.% of VC at a scan rate of 0.5 mV·s⁻¹ at room temperature. Both compared with LiPF₆-based electrolyte**

11.5. Determination of cathode materials by rate capability for further research

The performance of the fluorine-free LiPCP electrolyte was evaluated with the aqueous-processed LFP and LMFP electrodes using galvanostatic cycling methods in half-cell coin cells. Encouraged by the results obtained from testing the LMFP material with various concentrations of carbon additives and binder solutions, a similar screening process was applied to the LFP material (see Table 24).

It is important to note that the ratios of the electrode formulation (AM: CM: binder at 87:10:3 by weight ratio) were maintained consistently. The composition referred to as LFPA, also known as LFP2 for cyclic voltammetry, was identified and utilized in these cyclic voltammetry studies.

Table 24. LFP cathode slurry composition for galvanostatic charge/discharge cycling

Code	AM / wt.% LFP	CM / wt.%	Binder/ wt.% CMC	CM Carbon Black Type	Concentration of CMC in solution / wt.%
LFPA	87	10	3	Super P	1.0
LFPB	87	10	3	Ketjenblack EC600JD	1.0
LFPC	87	10	3	Super P	1.5
LFPD	87	10	3	Ketjenblack EC600JD	1.5

Figure 22a demonstrates the performance of cells at various C rates (rate capability) using various aqueous-processed LFP electrode formulations. The LFPA and LFPC formulations showed lower specific capacities, stability, and coulombic efficiencies compared to other LFP samples. Replacing Super P with Ketjenblack in the electrode formulation significantly enhanced cell performance. This substitution resulted in higher initial capacities (125 mAh·g^{-1} for LFPA and LFPC versus 150 mAh·g^{-1} for LFPB and LFPD) and improved overall capacities across various C rates, especially noticeable at high rates such as 1C. Additionally, electrodes containing Ketjenblack (LFPB and LFPD) exhibited more consistent capacity values and achieved higher coulombic efficiency, exceeding 90% at all C-rates for LFPB (Figure 22b).

Ketjenblack appears to enhance electrical contact among AM particles, which is crucial for AM with relatively low conductivity. The initial coulombic efficiency values were 81.4%, 82.1%, 70.4%, and 79.0% for LFPA, LFPB, LFPC, and LFPD, respectively. These relatively low values can be attributed to the instability of the lithium anode and the continuous passivation of the evolving lithium surface. However, they are favorable considering the standard LiPF$_6$-based electrolyte was replaced by a new chemistry. Concerning the concentration of CMC in the binder solution, LFPB (1 wt.%) outperformed LFPD (1.5 wt.%), showing significantly higher coulombic efficiency regardless of the CM used. Thus, it is tentatively suggested that the enhanced stability and capacities of LFPB can be attributed to improved slurry homogenization, resulting from the lower viscosity of the CMC binder solution.

This leads to a more uniform distribution of AMs and CMs, enhancing particle cohesion. Furthermore, the composition improves adhesion between the slurry and the current collector as no delamination is observed, directly affecting cell performance.
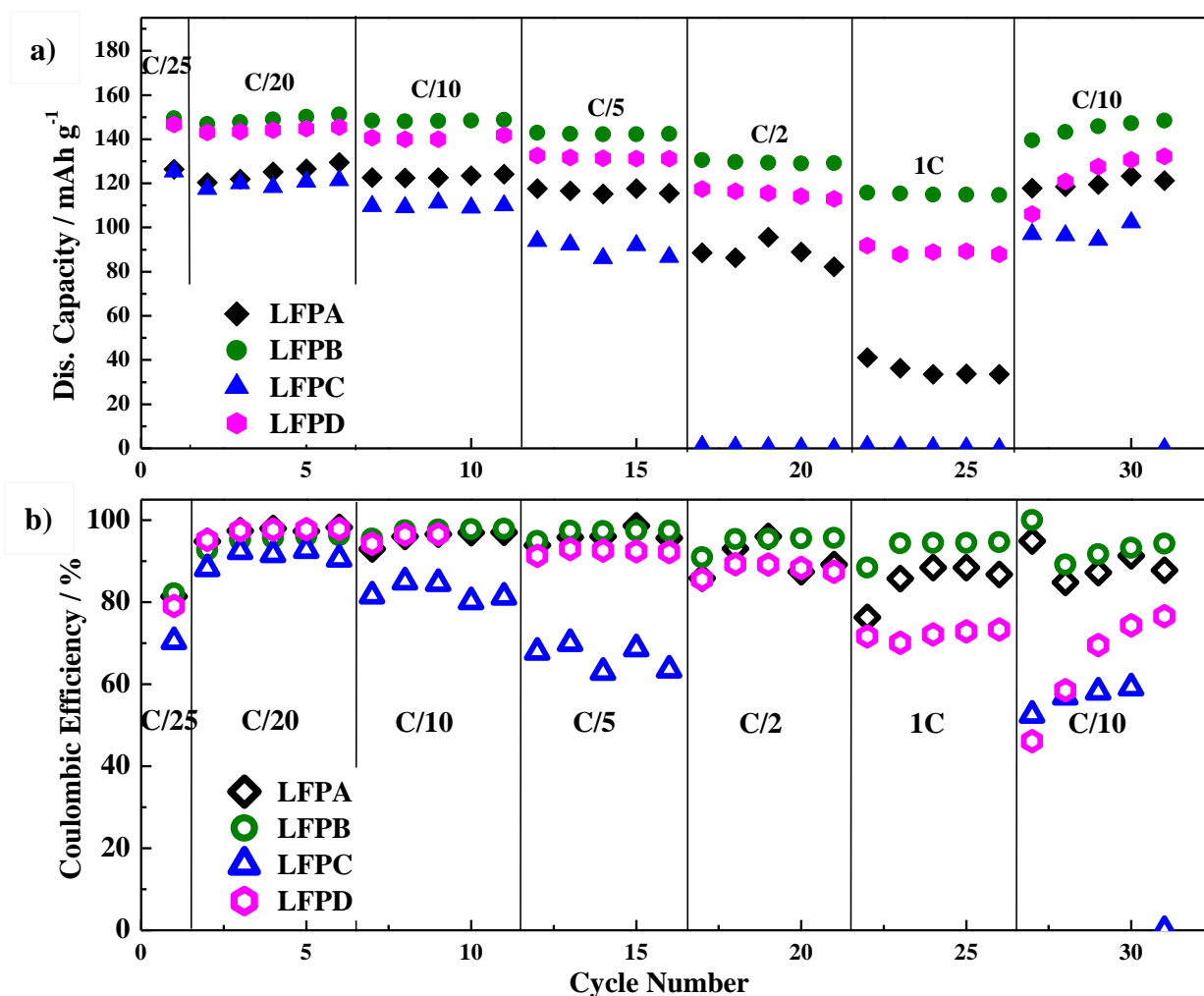
Figure 22. Rate performance of Li/LFP cells with 0.8 mol·kg⁻¹ LiPCP in EC:DMC (30:70·wt.%) and 5 wt.% of VC. Potential range: 2.5 – 3.9 V *vs.* Li⁺/Li. a) Discharge capacities in mAh·g⁻¹. b) Coulombic efficiency in %

A comparison between the best-performing electrode, LFPB, in LiPCP and the standard LiPF$_6$-based electrolyte (Figure 23) yielded interesting results. When assessing the performance of LFPB in both LiPCP and LiPF$_6$ electrolytes, it was observed that the initial discharge capacity was similar (150 mAh·g⁻¹). Interestingly, the initial coulombic efficiency was slightly lower with LiPF$_6$ (72.5% vs. 82.1% for LiPCP). However, in subsequent cycles, the coulombic efficiency remained stable and above 90% for both electrolytes.

Although the overall capacity and coulombic efficiency values were slightly lower with the LiPCP electrolyte, they exhibited less fluctuation compared to the LiPF$_6$ electrolyte.
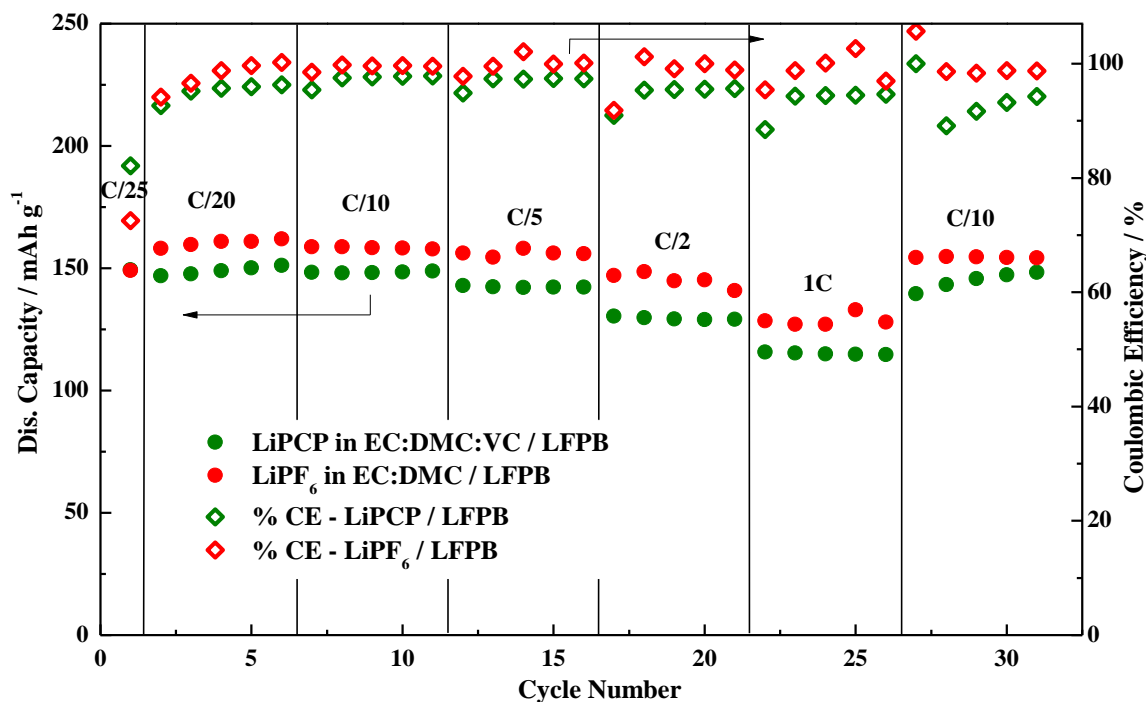
Figure 23. Rate performance and coulombic efficiency of Li/LFP (LFPB) cells with 0.8 mol·kg⁻¹ LiPCP in EC:DMC (30:70 wt.%) and 5 wt.% of VC; and with 1.0 mol·kg⁻¹ LiPF₆ in EC:DMC. Potential range: 2.5 – 3.9 V *vs*. Li⁺/Li

Analyzing the charge-discharge curves (Figures 24 and 25) revealed that both electrolytes with the aqueous-processed LFP cathode material displayed stable behavior, with slightly higher polarization observed in the LiPCP sample.
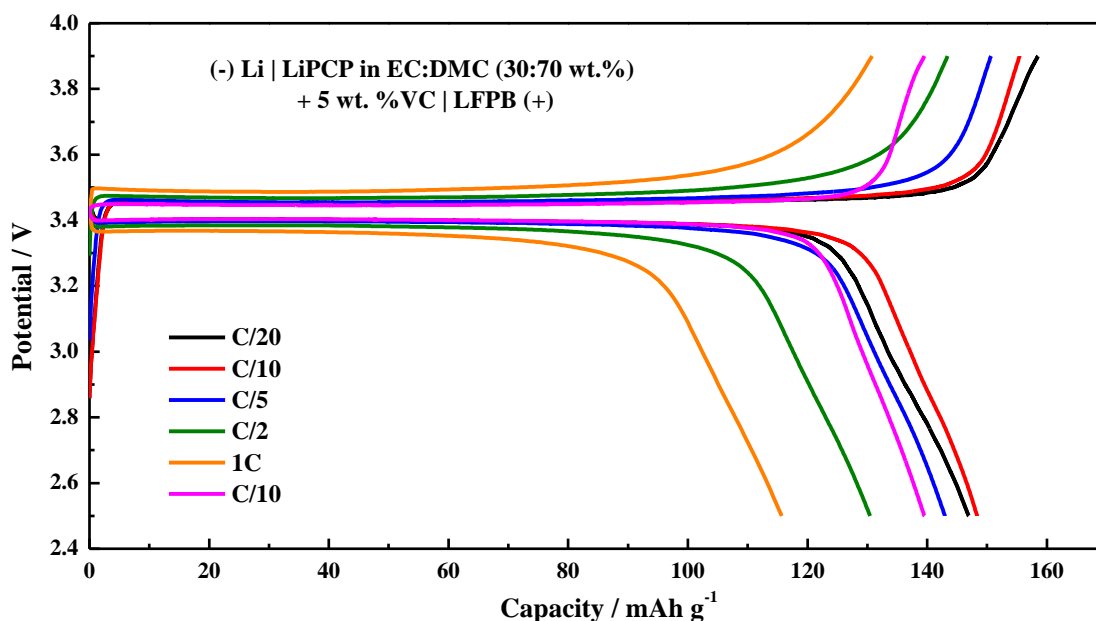
Figure 24. Charge/discharge curves of Li/LFP (LFPB) in coin-cells with 0.8 mol·kg⁻¹ LiPCP in EC:DMC (30:70 wt.%) and 5 wt.% of VC, Potential range: 2.5 – 3.9 V *vs*. Li⁺/Li

The polarization noticed in LiPCP is slightly higher than LiPF$_6$-based electrolyte, however, this polarization did not significantly affect the cell capacity and rate performance, and it can be attributed to the working electrode as this was explained in detail in the 11.2 section. Overall, the LFP electrodes demonstrated compatibility with LiPCP-based electrolytes, providing satisfactory performance.
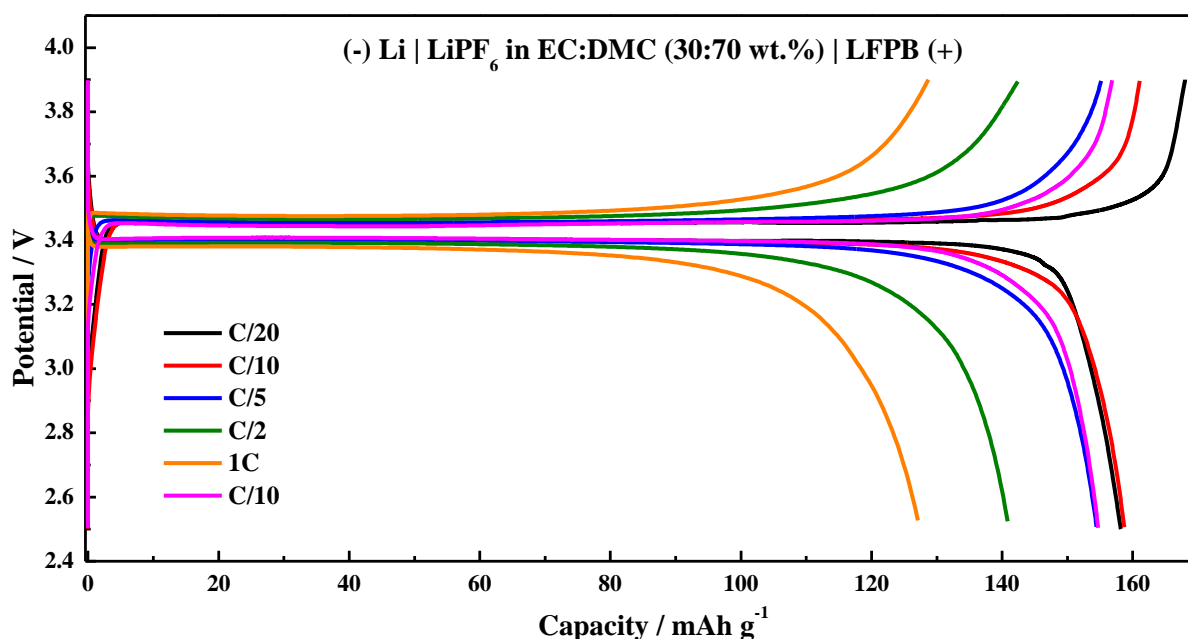
Figure 25. Charge/discharge curves of Li/LFP (LFPB) in coin-cells with 1.0 mol·kg^{-1} LiPF$_6$ in EC:DMC (30:70 wt.%). Potential range: 2.5 – 3.9 V *vs*. Li$^+$/Li

Figure 26a illustrates the performance of Li/LMFP cells at various C-rates using various aqueous-processed LMFP electrode formulations detailed in Table 23. As shown, LMFP2 exhibited the highest initial capacity (140 mAh·g^{-1}) and superior overall capacity across various C-rates. Similar to the results observed with LFP, the use of Ketjenblack as a CM and 1 wt.% CMC in the binder solution produced the best cell performance. This improvement but still inferior capacity can be attributed to the structure of the cathode material, which typically has low electronic conductivity and ionic diffusion.

Despite this, the performance of all cells remained stable at low C-rates but became unstable as the C-rate increased. Additionally, all LMFP samples showed low initial coulombic efficiency values (LMFP1: 73.6%, LMFP2: 48.8%, LMFP3: 56%, and LMFP4: 74%) as seen in Figure 26b. While the LMFP3 sample demonstrated slightly better stability in coulombic efficiency, it came at the expense of capacity.

143

The suboptimal performance of LMFP electrodes in LiPCP electrolytes can be attributed to the electrochemical stability limit of the electrolyte comparing to the cathode material, which restricts full utilization of the electrode capacity, particularly at higher rates. With greater polarization than LiPF$_6$-based electrolytes, cells with LiPCP reach the cut-off potential at lower capacities. Increasing the cut-off potential cannot prevent this issue due to the electrolyte's electrochemical stability limit. Furthermore, the characteristics of manganese and its behavior in an aqueous system may contribute to its tendency to dissolve easily, leading to a rapid capacity loss during the charge-discharge process.
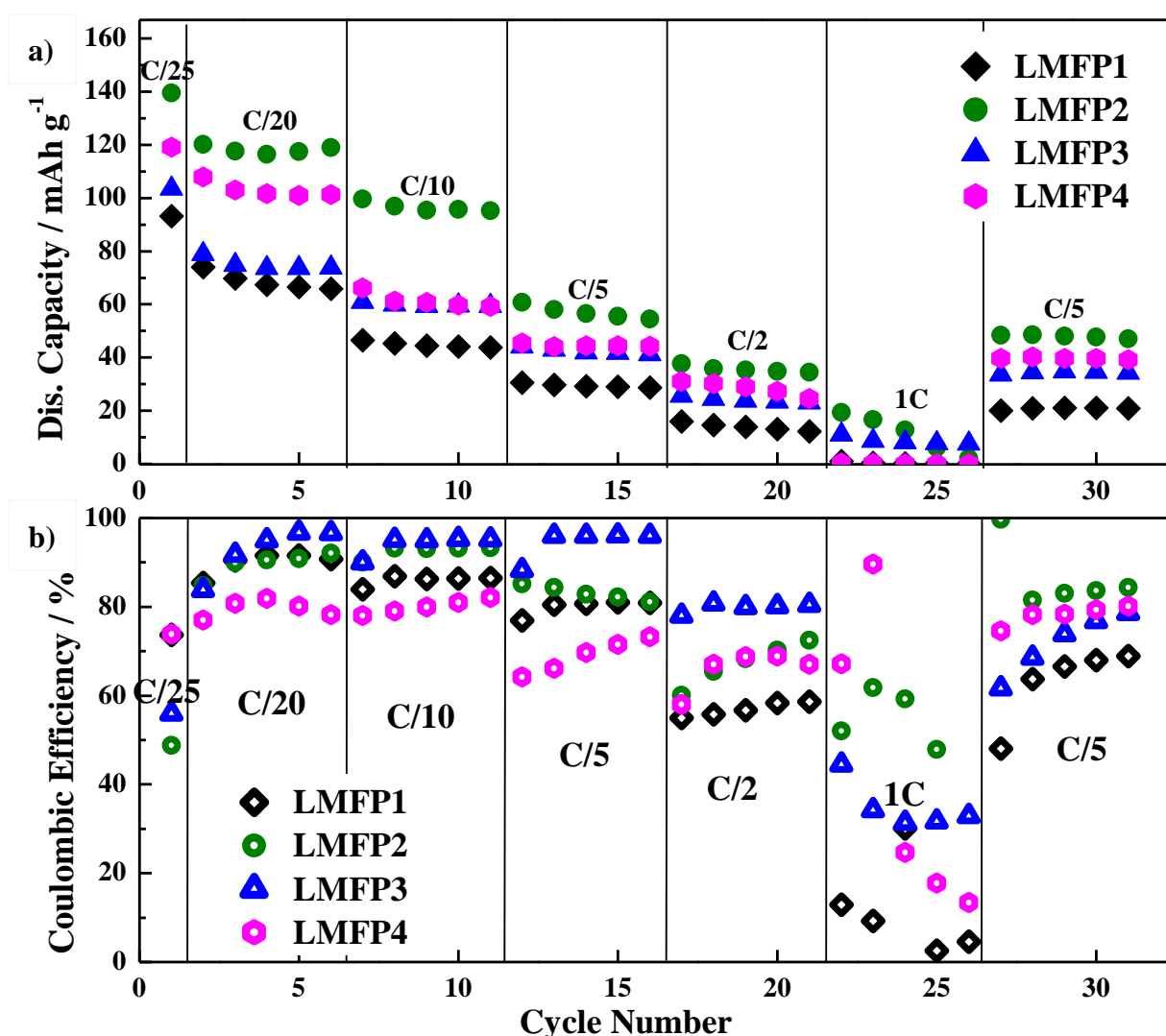
Figure 26. Rate performance of Li/LiMn$_{0.6}$Fe$_{0.4}$PO$_4$ cells with 0.8 mol·kg^{-1} LiPCP in EC:DMC (30:70 wt.%) and 5 wt.% of VC. Potential range: 2.4 – 4.2 V *vs.* Li$^+$/Li. a) Discharge capacities in mAh·g^{-1}. b) Coulombic efficiency in percentage (%)

The performance of the best electrode, LMFP2, was evaluated using LiPCP-based and standard LiPF$_6$-based electrolytes (Figure 27a). The initial discharge capacity and initial

coulombic efficiency for LiPF$_6$ were 125 mAh·g^{-1} and 74.8%, while for LiPCP, they were 139.6·mAh·g^{-1} and 48.8%, respectively (Figure 27b).
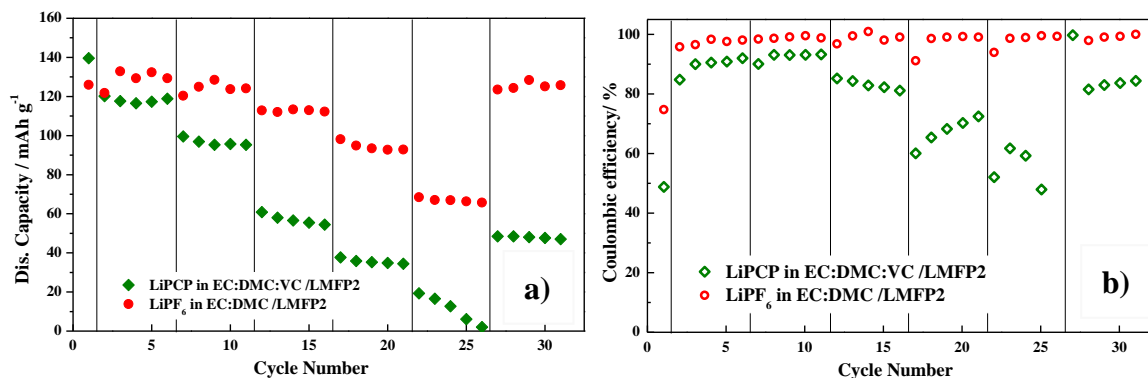
Figure 27. **Rate performance of Li/ LiMn$_{0.6}$Fe$_{0.4}$PO$_4$ (LMFP2) cells with 0.8 mol·kg^{-1} LiPCP in EC:DMC (30:70 wt.%) and 5 wt.% of VC; and with 1.0 mol·kg^{-1} LiPF$_6$ in EC:DMC. Potential range: 2.4 – 4.2 V *vs.* Li$^+$/Li. a) Discharge capacities in mAh·g^{-1}. b) Coulombic efficiency in percentage (%)**

The LiPCP-based electrolyte showed significantly poorer performance compared to the LiPF$_6$-based electrolyte when used with the LMFP aqueous-processed electrode. This discrepancy can be explained by examining the charge-discharge curves (Figures 28 and 29), which reveal progressive polarization that shifts the Mn^{3+}/Mn^{2+} plateau to potential beyond the stability limit of LiPCP.
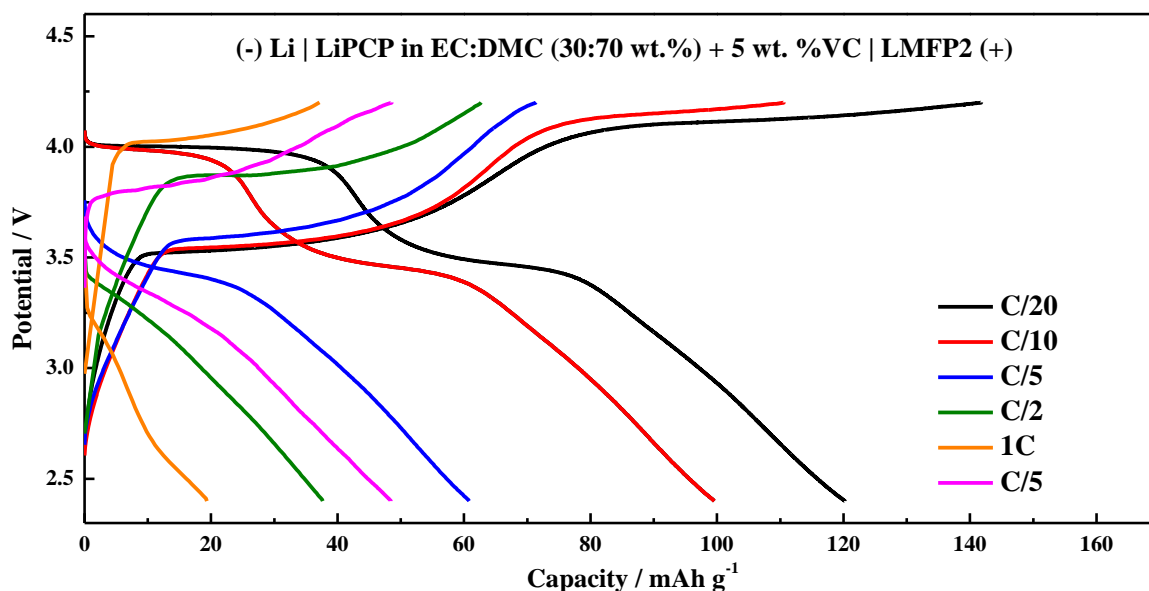
Figure 28. **Charge/discharge curves of Li/ LiMn$_{0.6}$Fe$_{0.4}$PO$_4$ (LMFP2) in coin-cells with 0.8 mol·kg-1 LiPCP in EC:DMC (30:70 wt.%) and 5 wt.% of VC, Potential range: 2.4 – 4.2 V *vs.* Li$^+$/Li**

Additionally, substantial SEI formation during the initial charge accounts for the low initial coulombic efficiency.

Therefore, LMFP working with CMC as a binder and $LiPF_6$ in EC:DMC (30:70 wt.%) as the electrolyte, resulted with significantly reduced polarization and improved coulombic efficiency comparing to LiPCP under the same conditions. The lower polarization of $LiPF_6$ enables the battery to fully harness its capacity within the set potential range, enhancing overall performance and extending the battery lifespan.
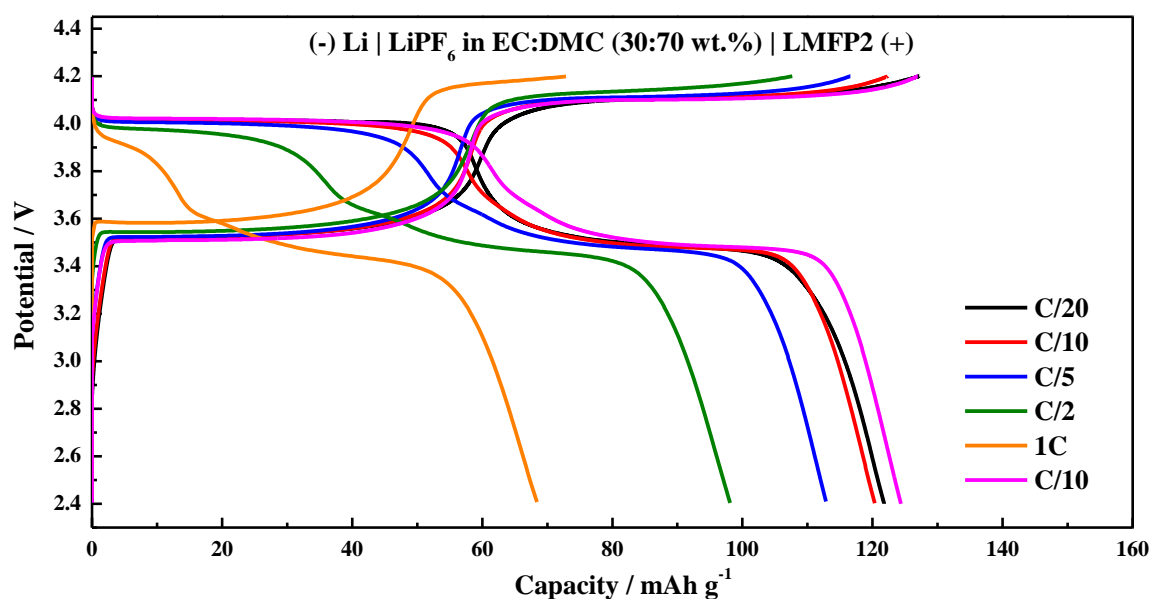
Figure 29. Charge/discharge curves of Li/ $LiMn_{0.6}Fe_{0.4}PO_4$ (LMFP2) in coin-cells with 1.0·mol·kg^{-1} $LiPF_6$ in EC:DMC (30:70 wt.%). Potential range: 2.4 – 4.2 V *vs*. Li+/Li

These findings indicate the need for further optimization of the electrode and electrolyte for this specific LMFP material. Although LiPCP is not inherently incompatible with LMFP, achieving its full potential would require an electrolyte composition that reduces polarization. Furthermore, it is important to note that metallic lithium was used as the anode, which may not be optimal, as suggested by the lithium passivation experiments.

11.6. Determination of the cathode material for upscaling to pouch cells by cycling stability performance

The cycling stability of the optimized **LFPB** (Figure 30) and **LMFP2** (Figure 31) electrodes was assessed using LiPCP-based and standard $LiPF_6$-based electrolytes for over 40 cycles at C/10 cycling. For LFP, the performance of both samples was comparable, with the LiPCP sample showing initially a slightly lower capacity than $LiPF_6$-based electrolyte one (143

vs. 155 mAh·g^{-1}). However, the capacity of the LiPCP sample increased over time, stabilizing after 15 cycles to match that of the LiPF$_6$ electrolyte.

This increase cannot be attributed to parasitic reactions since the coulombic efficiency of the LiPCP sample also rose to approximately 99%. The lower capacity observed previous the 15th cycle may be due to limited wettability, as this cell had only a 4-hour resting period before cycling began.
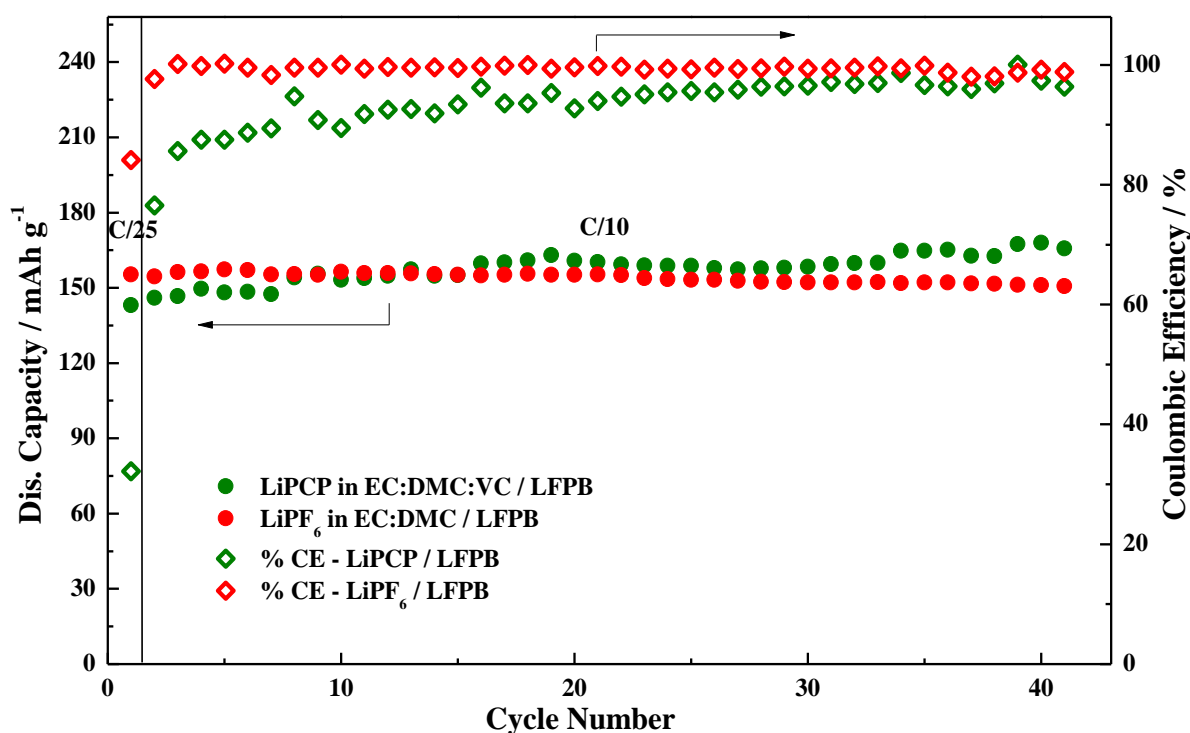
Figure 30. Cycling stability and coulombic efficiency at C/10 of Li/LFP (LFPB) cells with 0.8 mol·kg^{-1} LiPCP in EC:DMC (30:70 wt.%) and 5 wt.% of VC; and with 1.0 mol·kg^{-1} LiPF$_6$ in EC:DMC. Potential range: 2.5–3.9 V *vs.* Li$^+$/Li. The first formation cycle was performed at C/25

In contrast, the LMFP cathode materials showed poorer performance with the LiPCP-based electrolyte. Although capacity remained stable during testing, it fluctuated between 60 and 70 mAh·g^{-1} at a rate of C/10, significantly lower than the stable capacity of approximately 120 mAh·g^{-1} mostly stable, achieved with the LiPF$_6$ electrolyte.

Concerning the coulombic efficiency, LiPCP demonstrated an efficiency higher than 80% after the fifth cycle and remained relatively stable, though it did not surpass 90%. In comparison, LiPF$_6$ exhibited a coulombic efficiency above 95%, maintaining this level of performance throughout the cycling process.

The consistent stability of capacity values for both samples suggests that the issue lies with the electrolyte formulation rather than the electrode, indicating the need for further adjustments, particularly for the LMFP electrodes.
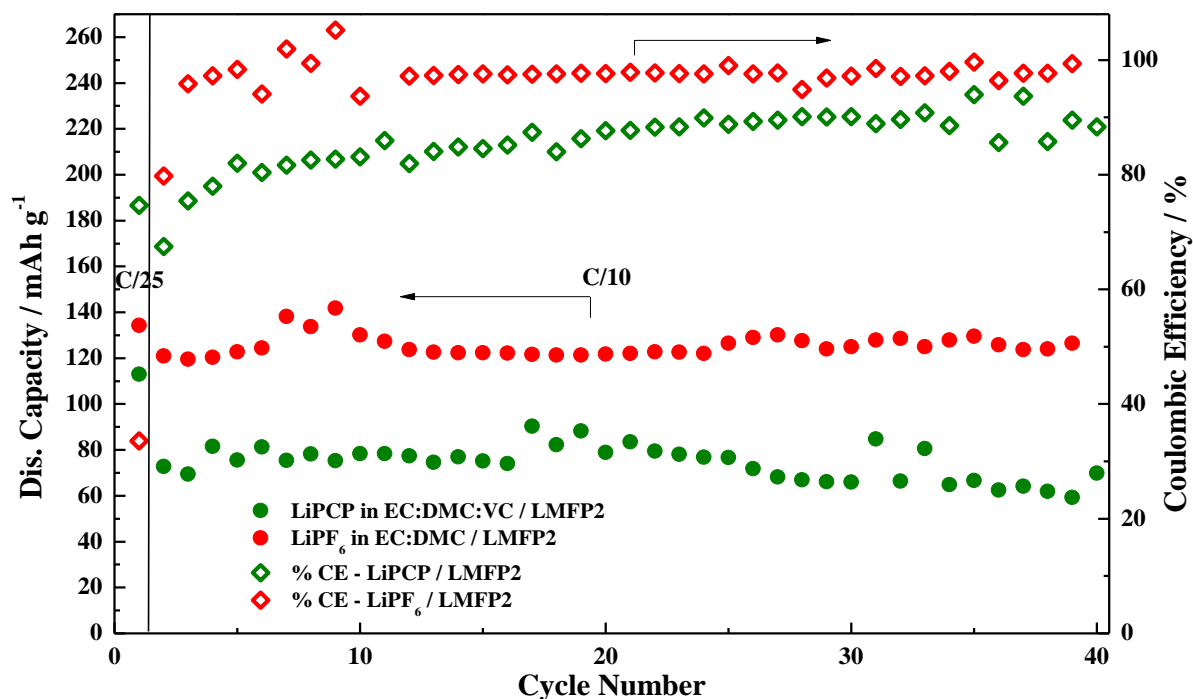
Figure 31. **Cycling stability and coulombic efficiency at C/10 of $Li/LiMn_{0.6}Fe_{0.4}PO_4$ (LMFP2) cells with 0.8 mol·kg^{-1} LiPCP in EC:DMC (30:70 wt.%) and 5 wt.% of VC; and with 1.0 mol·kg^{-1} LiPF$_6$ in EC:DMC. Potential range: 2.4 – 4.2 V *vs.* Li$^+$/Li. The first formation cycle was performed at C/25**

11.7.   Full cell rate capability for LiPCP electrolyte evaluation in coin cells

Figures 30 and 31 present the cycling stability results at a C/10 rate for Li/LFP and Li/LMFP cells, respectively. The results indicate that aqueous-processed LFP electrodes combined with the LiPCP electrolyte exhibit more favorable performance compared to LMFP electrodes. As a result, LFP will be selected for the next phase, which involves assembling full cells using SG and SOX as the anode materials. While LMFP demonstrates acceptable compatibility with LiPCP, further research is needed to optimize both the electrode fabrication and the fluorine-free electrolyte formulation, particularly for LMFP.

Figure 32a illustrates the performance of full-cells at varied C-rates using LFP/SG and LFP/SOX systems. All electrodes were processed using water as the solvent and CMC as the binder, assembled into coin cells, and cycled at 25°C within the potential range of 2.5–3.9·V. Both LiPCP and LiPF$_6$-based electrolytes were employed for comparative analysis.

The initial specific capacities and coulombic efficiencies (CE) at various C-rates, in relation to the full-cell configuration and electrolyte type, are detailed in Table 25.

According to the data presented in Table 25 and Figure 32a and 32b, the specific capacities during cycle formation (C/25) and at C/20 were 111 and 133 mAh·g^{-1} for LiPF$_6$, and 68 and 45 mAh·g^{-1} for LiPCP. This contrasts with the half-cell data (Figure 30), where the initial capacities were 143 mAh·g^{-1} for LiPCP and 155 mAh·g^{-1} for LiPF$_6$. The significant reduction in specific capacity from half-cell to full-cell configurations is particularly pronounced with the LiPCP electrolyte.

Table 25. **Initial specific capacity and %coulombic efficiency of full cells**

	Initial capacity (mAh·g^{-1})				Initial %Coulombic Efficiency			
Electrolyte	LiPF$_6$		LiPCP		LiPF$_6$		LiPCP	
C-rate	LFP/ SG	LFP/ SOX	LFP/ SG	LFP/ SOX	LFP/ SG	LFP/ SOX	LFP/ SG	LFP/ SOX
C/25	111.03	133.08	67.54	44.54	77.36	82.88	58.90	80.83
C/20	116.52	130.73	68.44	46.244	87.14	96.73	81.50	83.83
C/10	97.38	111.90	66.80	49.354	96.58	93.39	92.82	90.48
C/5	93.61	102.33	57.74	47.164	97.75	89.77	83.57	91.09
C/2	87.95	95.19	40.63	34.504	95.77	87.82	65.38	71.11
1C	80.66	89.71	2.67	7.85	94.72	87.22	47.78	37.83
C/5	84.78	94.17	45.75	36.37	99.98	96.58	92.77	95.29

This marked capacity decrease in full cells, especially when using LiPCP, can be attributed to several factors. One primary factor is the formation of the SEI layer during initial cycling. The SEI layer formed in the presence of LiPCP appears to possess higher resistance compared to that formed with LiPF$_6$. This increased resistance likely complicates lithium cation extraction and insertion during the charge and discharge processes, directly impacting the specific capacity and coulombic efficiency. Additionally, the full-cell configuration, which incorporates both the cathode and anode, may intensify these resistive effects, leading to further reductions in capacity, particularly when using LiPCP as the electrolyte.

Importantly, while the initial coulombic efficiencies did not show significant differences between half and full cells for both LiPCP and LiPF$_6$ electrolytes, the specific capacity results emphasize the challenges in optimizing fluorine-free LIBs, particularly in full-cell

149

configurations. This highlights the need for further research into SEI formation, and electrolyte/anode compatibility to improve the performance of fluorine-free cells.

In conclusion, as both LFP/SG and LFP/SOX composite electrodes have shown satisfactory performance, the next research step will focus on advancing this work. This will include further refinement and optimization of both anode and cathode fabrication in aqueous-based processes, specifically for the assembly of pouch cells. Additionally, the electrochemical evaluation of these full cells will be conducted to verify their scalability and potential for application on a larger scale.
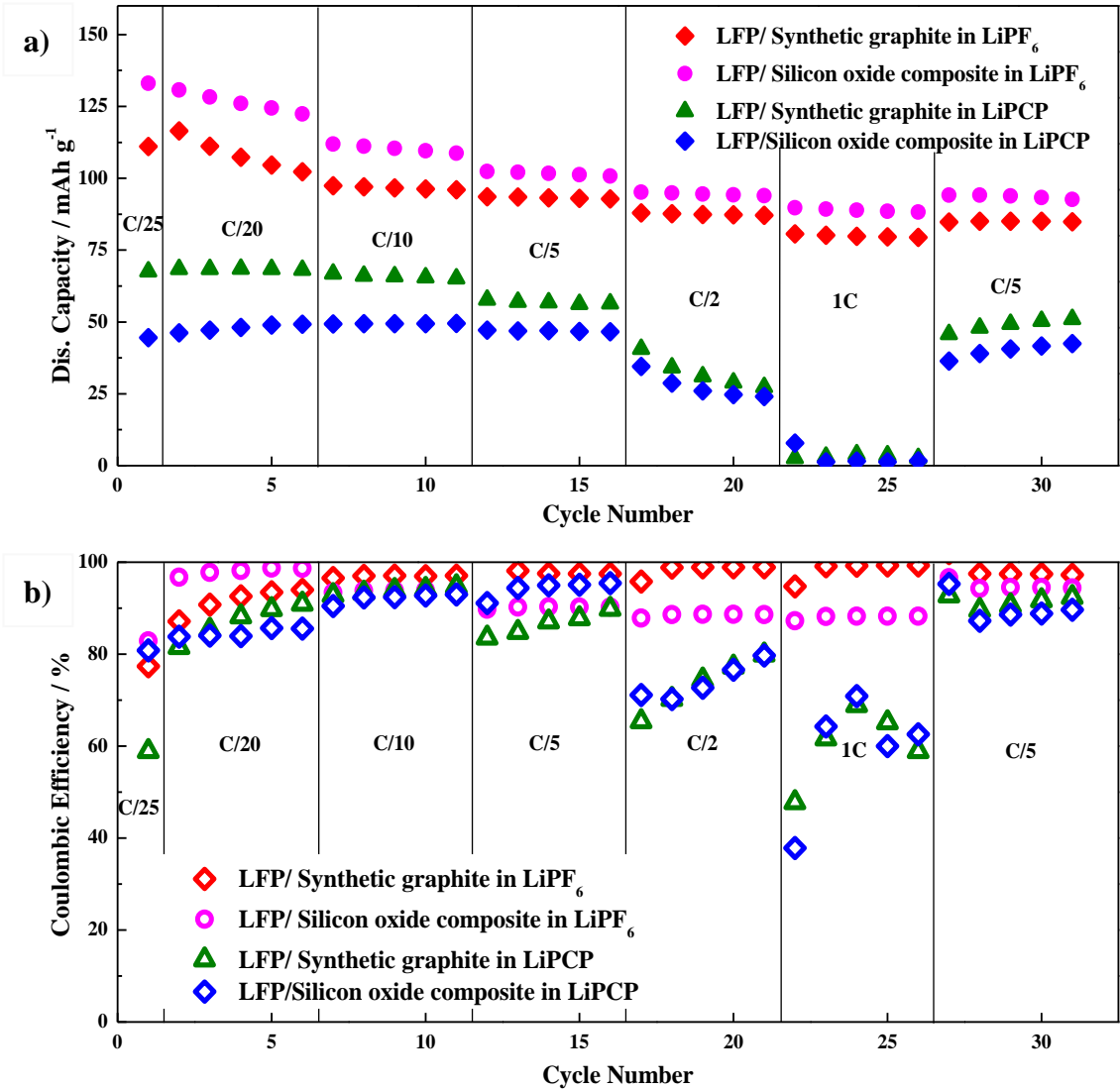
Figure 32. Full cell coin-cell configuration for LFPB/SG and LFPB/SOX with 0.8 mol·kg⁻¹ LiPCP in EC:DMC (30:70 wt.%) and 5 wt.% of VC a) C-rate capability performance and b) coulombic efficiency

RESULTS AND DISCUSSION

ELECTRODES FABRICATION FOR
POUCH CELLS ASSEMBLY

Aqueous-processed electrodes

Lithium iron phosphate (LFP)

Synthetic graphite (SG)

Silicon oxide composite (SOX)

B. ELECTRODES FABRICATION FOR POUCH CELLS ASSEMBLY

11.8. LFP electrode fabrication for pouch cells

The electrode manufacturing process chain is characterized by its complexity and the numerous influencing factors. The initial step involves dispersing the solids in a solvent at 23ºC to obtain a processable, homogeneous slurry with the desired viscosity. In the subsequent step, this slurry is coated upon the current collector at varying thicknesses to achieve a specific mass loading, followed by drying at room temperature for around 2 hours and subsequently at 80ºC overnight and calendering of the electrode sheet. The selection of technology and parameters for mixing, coating, drying, and calendering directly impacts the homogeneity of the slurry, electrode thickness, mechanical stability, and porosity of the electrode layer. This stage is essential, as electrode processing exercises a direct influence on battery performance.

11.8.1. LFP slurry preparation and formulation

The properties of the selected AM and additives, along with the mixing sequences, ingredient concentrations, and ratios, significantly influence electrode performance. The electrode slurry plays a fundamental role in the electrode fabrication process, with its flow behavior being determined by the ratio of raw materials, and the mixing procedure. Additionally, the viscosity function of electrode slurries is critically important to the subsequent coating process [400].

After identifying the optimal electrode slurry composition that demonstrates superior performance with a LiPCP-based electrolyte, as shown in Figure 30, determining the appropriate solid content, the electrode sheet thickness, and viscosity to achieve a mass loading of 2 mAh·cm^{-2} becomes essential. To this end, a total of 10 batches of 10 grams of LFP slurry (designated from LFP S1 through S10) were prepared on a larger scale for pouch cell assembly. LFP S1 and S2 slurry compositions are shown in Tables 26 and 27, both slurries present the same ratio/composition as found optimal at the laboratory scale. The only variation between these S1 and S2 slurries is the mixing time, differing by 50 minutes. It is evident that mixing time has a minimal impact on slurry preparation, as the solid content remains nearly consistent, varying from 33.49 wt.% to 33.53 wt.% for 285 minutes and 240 minutes, respectively. The effect on the slurry viscosity and mass loading are detailed and compared with the rest of the slurries in the following section.

Table 26.   LFP S1 slurry composition, mixing time, thickness and solid content

Slurry composition: LFP_S1		Calculated wt.%	Calculated (g)	Experimental (g)	Experimental wt.%
Binder solution 1			21.74	21.80	
Binder solution 2			0.00		
CM	Ketjenblack (KB)	6.00	0.652	0.65	5.98
Binder 1	CMC (Sigma Aldrich) 1 wt.%	2.00	0.22	0.22	2.01
AM	LFP (MTI)	92.00	10.00	10.00	92.01
Binder 2	SBR (Arkema) 40 wt.%	0.00	0.00	0.00	0.00
Total		100.00	32.61	32.67	100.00
Operating conditions:					
Temperature = 23°C	Solid content = 33.49 wt.%	Total time = 285 (min)		Electrodes sheet thickness, L1 = 80 μm, L2 = 100 μm, L3=150 μm, L4=200 μm	

Table 27.   LFP S2 slurry composition, mixing time, thickness and solid content

Slurry composition: LFP_S2		Calculated wt.%	Calculated (g)	Experimental (g)	Experimental wt.%
Binder solution 1			21.74	21.780	
Binder solution 2			0.00		
CM	Ketjenblack (KB)	6.00	0.6522	0.650	5.98
Binder 1	CMC (Sigma Aldrich) 1 wt.%	2.00	0.22	0.218	2.00
AM	LFP (MTI)	92.00	10.00	10.010	92.02
Binder 2	SBR (Arkema) 40 wt.%	0.00	0.00	0.000	0.00
Total		100	32.61	32.66	100.0
Operating conditions:					
Temperature = 23°C	Solid content = 33.53 wt.%	Total time = 240 (min)		Electrodes sheet thickness, L1 = 100 μm, L2 = 150 μm, L3=200 μm, L4=250 μm	

The solid content of the slurry is crucial for the rheological properties, casting and mass loading of the LFP cathode slurry. Given that solid content defines the slurry rheological properties, a range of 50 to 70 wt.% is typically considered optimal for electrode fabrication. However, this "optimal" solid content was established when using PVdF as the binder and NMP as the solvent. Therefore, identifying an optimal solid content for this aqueous-processed LFP cathode material represents a significant challenge.

Given that LFP S1 and S2 exhibit low solid content, SBR and additional water were considered for the preparation of slurry S3 to increase the solid content, as shown in Table 28. Eight grams of water were added, and a CMC/SBR ratio of 1:1 was chosen to evaluate the

impact of SBR on the solid content and rheology of the slurry. The LFP S3 slurry composition resulted in an increased solid content of 36.48 wt.%, however, this was insufficient to achieve the minimum mass loading required for pouch cell assembly.

Table 28.   LFP S3 slurry composition, mixing time, thickness and solid content

Slurry composition: LFP_S3		Calculated wt.%	Calculated (g)	Experimental (g)	Experimental wt.%
Binder solution 1			10.87	10.90	
Binder solution 2			0.27	0.27	
CM	Ketjenblack (KB)	6.00	0.65	0.65	6.0
Binder 1	CMC (Sigma Aldrich) 1 wt.%	1.00	0.11	0.11	1.0
AM	LFP (MTI)	92.00	10.00	10.02	92.0
Binder 2	SBR (Arkema) 40 wt.%	1.00	0.11	0.11	1.0
Total		100	22.01	22.06	100.0
Operating conditions:					
Temperature = 23°C Water addition = 8 g	Solid content = 36.48 wt.%	Total time = 270 (min)		Electrodes sheet thickness, L1 = 100 μm, L2 = 150 μm, L3=200 μm, L4=250 μm	

Therefore, three strategies were considered to increase the solid content of the slurry: increasing the current CMC binder concentration (1 wt.%), reducing the amount of water added during mixing, or increasing the AM content. Since increasing the binder concentration would significantly reduce the solvent in the slurry, this option was dismissed. Instead, 4 grams of water were added during the preparation of slurry S4, resulting in a solid content of 42.15 wt.% as shown in Table 29. Although this slurry exhibited higher solid content, the electrode casting step was challenging at operational level, and the resulting electrode sheet showed visible cracking on the surface.

Table 29.   LFP S4 slurry composition, mixing time, thickness and solid content

Slurry composition: LFP_S4		Calculated wt.%	Calculated (g)	Experimental (g)	Experimental wt.%
Binder solution 1			10.87	10.90	
Binder solution 2			0.27	0.28	
CM	Ketjenblack (KB)	6.00	0.6522	0.65	6.0
Binder 1	CMC (Sigma Aldrich) 1 wt.%	1.00	0.11	0.11	1.0
AM	LFP (MTI)	92.00	10.00	10.03	92.0
Binder 2	SBR (Arkema) 40 wt.%	1.00	0.11	0.11	1.0
Total		100	22.01	22.08	100.0
Operating conditions:					
Temperature = 23°C Water addition = 4 g	Solid content = 42.15 wt.%	Total time = 270 (min)		Electrodes sheet thickness, L1 = 150 μm, L2 = 200 μm, L3=250 μm	

Consequently, an additional 3 grams of water were added, bringing the total to 7 grams added to the slurry S4. As shown in Table 30, the resulting solid content was 41.55 wt.%, which provided better rheological properties, LFP mass loading for pouch cell assembly, and smooth electrode sheet casting without operational issues.

The effect of solid content on the rheological properties of the slurry for casting (at various coated thickness) and the mass loading achieved in each case are discussed in the following sections.

Table 30.   LFP S5 slurry composition, mixing time, thickness and solid content

Slurry composition: LFP_S5		Calculated wt.%	Calculated (g)	Experimental (g)	Experimental wt.%
Binder solution 1			8.02	8.04	
Binder solution 2			0.20	0.19	
CM	Ketjenblack (KB)	5.00	0.5348	0.54	5.04
Binder 1	CMC (Sigma Aldrich) 1 wt.%	0.75	0.08	0.08	0.75
AM	LFP (MTI)	93.50	10.00	10.02	93.50
Binder 2	SBR (Arkema) 40 wt.%	0.75	0.08	0.076	0.71
Total		100	18.92	18.95	100.0
Operating conditions:					
Temperature = 23°C Water addition = 7 g	Solid content = 41.55 wt.%	Total time = 270 (min)		Electrodes sheet thickness, L1 = 150 μm, L2 = 200 μm, L3=250 μm	

11.8.2. Rheological properties, LFP slurry

Figures 33 (a) and (b) clearly demonstrate the impact of solid content on the flow properties of the slurry. Slurries with a solid content of 33.5 wt.% exhibit good fluidity (CMC only), but this fluidity diminishes as the solid content exceeds 40 wt.%, when SBR is added to the slurry formulation. When the solid content further increases to approximately 41.5 wt.%, the slurries display poor flow properties and take on a soft consistency. Overall, the fluidity of the slurry decreases with increasing solid content, with this decrease becoming more pronounced at higher solid content levels.

CMC serves multiple functions in slurry, depending on its concentration, and plays a significant role in influencing slurry dispersibility. In this study, the CMC concentration in the solution was maintained at 1 wt.%, where CMC primarily acts as a dispersant. The high fluidity observed in the slurry is largely due to the presence of CMC alone, but this behavior changes with the addition of SBR as an additive to the system [401].
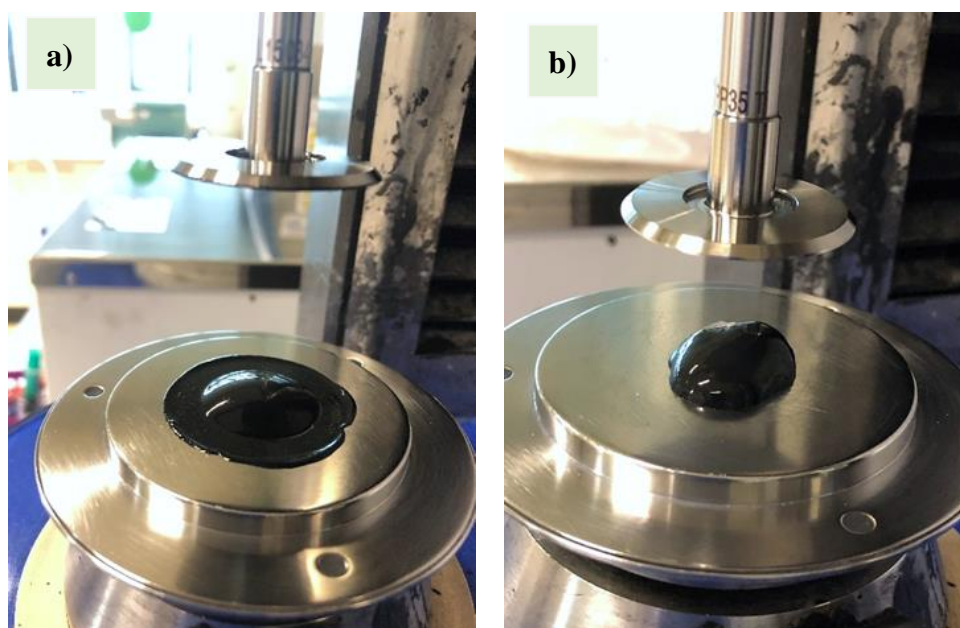
Figure 33. LFP slurries viscosity at a) 33.5 wt.% (S1 – S2) and b) over 40 wt.%

Figures 34(a) and 34(b) illustrate the correlation between viscosity and shear rate for LFP slurries with varying solid contents (from S1 to S10, including the duplicates in 34(a)). Viscosity at low shear rates reflects the stability of the slurry, which indicates its solid sedimentation behavior, while the viscosity at high shear rates determines slurry processability. As observed in the figures, the viscosity of the slurries decreases as the shear rate increases, demonstrating shear-thinning behavior. This indicates that all the slurries prepared with CMC or CMC/SBR are non-Newtonian fluids and contain agglomerates. These agglomerates can be dispersed by applying a lower shear stress, which can be adjusted by modifying the shear rates. Across the entire range of shear rates, moreover, the viscosity of the slurry increases as the solid content rises.

For the slurry with a solid content of 33.5 wt.%, the viscosity is inferior at low shear rates, suggesting poor stability and minimal resistance to sedimentation. In contrast, the slurry with a solid content of 41.5 wt.% exhibits significantly higher viscosity at low shear rates, and as the solid content increases, so does the viscosity at the same shear rate. This observation indicates that the resistance to sedimentation of the solid components improves with higher solid content, enhancing the stability of the slurry.

On the other hand, it can be said that low viscosity at high shear rates is advantageous, as it facilitates more uniform coatings.

156

Consequently, it can be inferred that the slurry with a (low) solid content of 33.5 wt.% would produce a relatively uniform coating, without operational difficulties during casting and no electrodes cracking, whereas the slurry with a (higher) solid content of 41.5 wt.% may result in a less uniform coating. Therefore, at higher solid content such as the slurry LFP S4, operational difficulties will be caused, and a poor surface electrode will be obtained as shown in the surface characterization section.
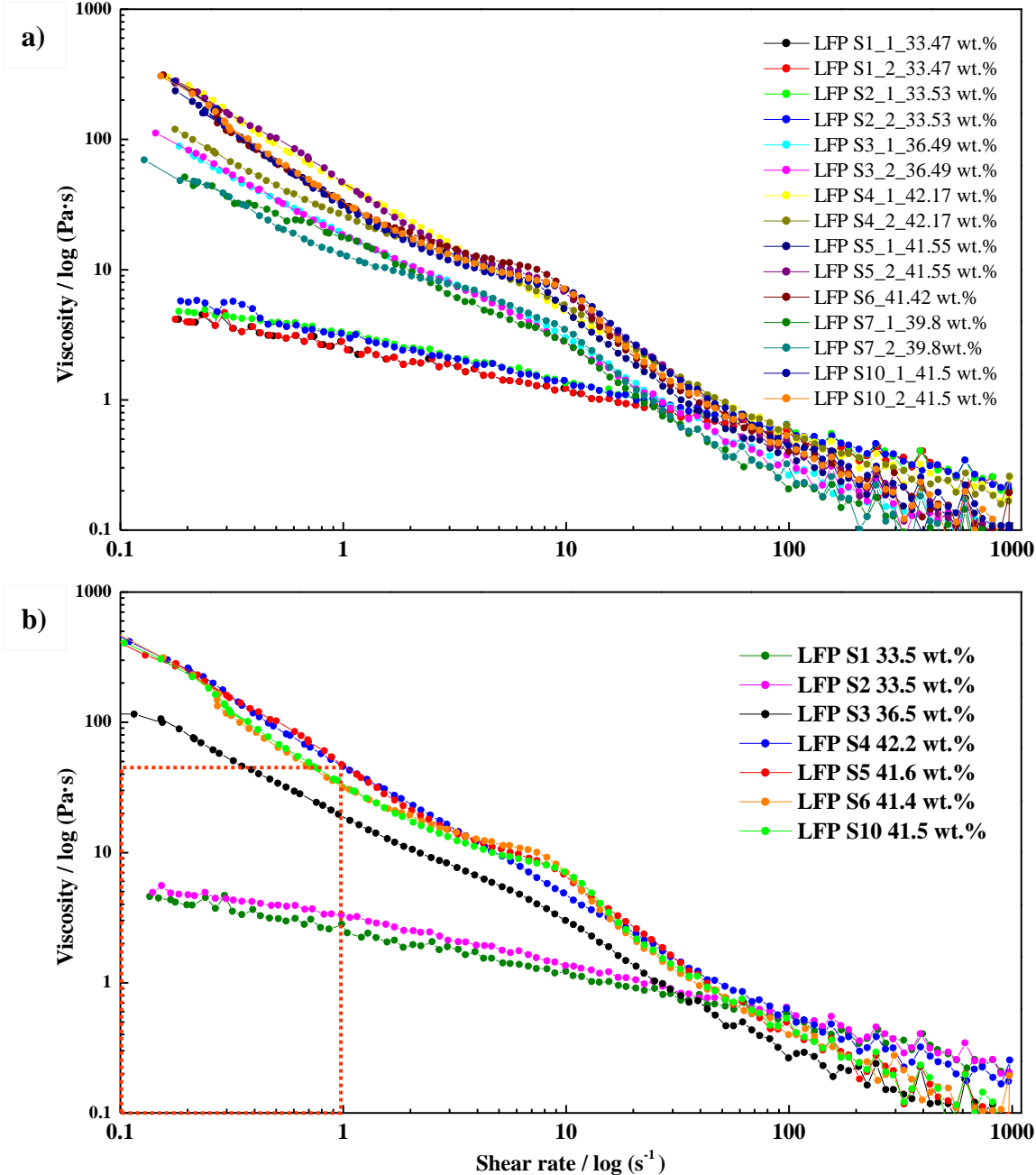
Figure 34. LFP slurry viscosity *versus* shear rate at a) various slurry compositions with duplicate samples and b) LFP S5 slurry viscosity comparison with the rest of the slurries

Furthermore, it is important to consider a range of viscosities when preparing slurries for pouch cell assembly, particularly before casting it onto a current collector. Table 31 presents the appropriate viscosity range for cathode materials that should be taken into account before casting. If the slurry viscosity falls below the minimum threshold, adjustments must be made to increase the viscosity of the cathode material slurry. This consideration applies specifically to cathode materials, as anode materials do not experience difficulty in achieving the minimum mass loading required due to their high specific capacity.

Given that this study involves casting the slurries onto the current collector using a Dr Blade, a slurry with a viscosity range of 40-50 Pa·s is needed. It is worth highlighting that the slurry prepared has 40 Pa·s viscosity as an average at 1 s^{-1} as seen in Figure 34b.

Table 31. **Viscosity range of values for preparation of cathode materials electrodes [402]**

Shear rate (1/s)	Viscosity (Pa s)	Characteristic
1	40 – 50	Dr. Blade
10	2 – 5	Pilot scale
100	~ 1	Industrial scale

According to Figures 34(a) and 34(b), viscosity increases with rising solid content at a fixed shear rate. When the solid content is 33.5 wt.% (LFP S1 and S2, Figure 35), the shear stress of the slurry increases with the shear rate. When the solid content is slightly higher, at 36.5 wt.% (LFP S3, Figure 35), the curve reaches a plateau, when change is not significant. At solid contents above 40 wt.%, this plateau shifts, and higher shear stress is observed. This behavior corresponds to the increase in viscosity at low shear rates as solid content increases, as shown in Figures 34(a) and 34(b). The relatively constant shear stress with varying shear rates suggests the presence of a yield stress in the slurry. This yield stress indicates that a network structure exists within the slurry, and a structural transformation occurs as the slurry transitions from a networked to a liquid-like system.

This transition is due to the breaking of particle connections, which can be explained by the presence of SBR as a binder, as shear rates below 500 rpm are required when SBR is added to the system due to its effect on the SBR bonds at higher RPM. As shown in Figure 35, the shear stress does not increase proportionally with shear rate for the slurries with SBR content. This suggests that the breakdown of the slurry structure is gradual rather than instantaneous, corresponding to a transitional region and a sharp transition point at higher shear rates.

Defining the onset of this transition as the yield point, the stress at this point occurs at shear rates over 100 s⁻¹, and this yield stress represents the minimum stress required to induce flow in the slurry. As the solid content increases, so does the shear stress, keeping the platform at lower shear rates.
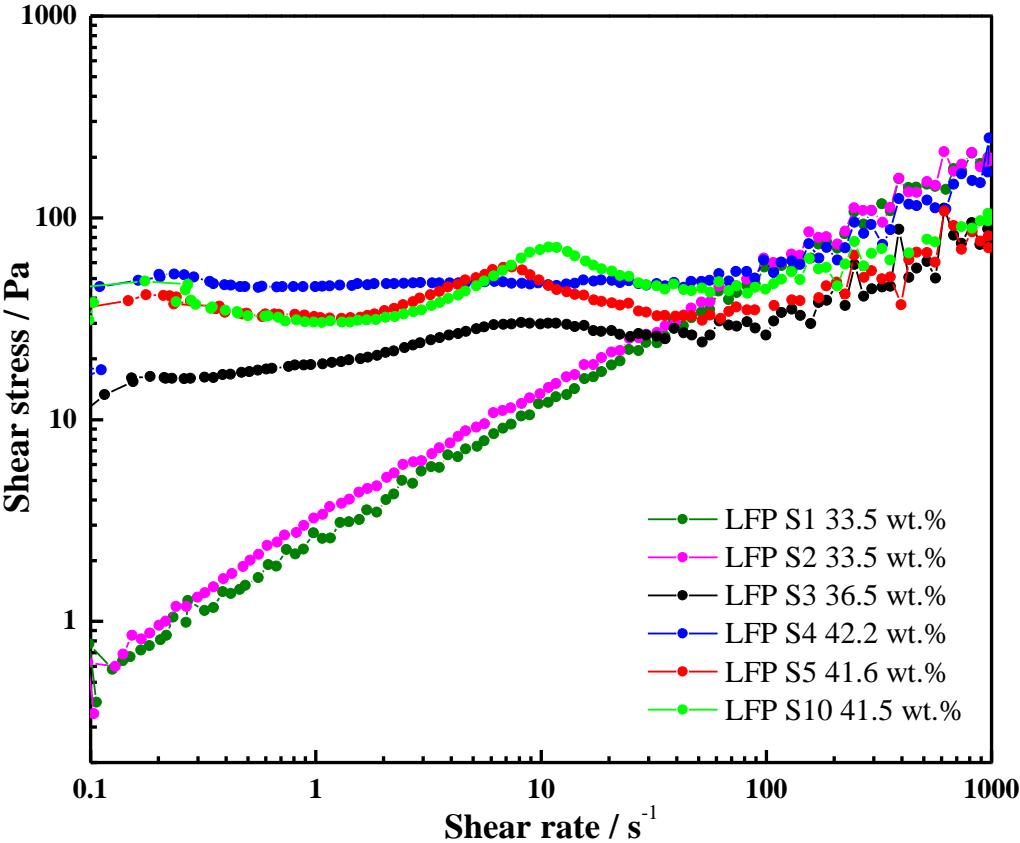
Figure 35. Shear stress vs. shear rate of LFP slurries under various solid content

11.8.3. Determination of thickness and areal capacity, LFP electrode

In LIBs, reducing the electrode thickness decreases the length of the conductive pathways, thereby lowering internal resistance. This makes reducing electrode thickness an effective strategy for enhancing the power output of LIBs. However, this reduction also impacts the cathode material areal capacity, as thinner electrodes result in lower capacity. To balance this, capacity and thickness, a minimum areal capacity of 2 mAh·cm⁻² was set for the cathode for subsequently pouch cell assembly. To achieve this target capacity, while minimizing the negative effects of increased thickness, parameters such as the solid content in the slurry during mixing and the electrode thickness during casting were adjusted accordingly.

During the preparation of LFP slurries, various solid contents were tested, and the resulting thickness and mass loading were measured to find the optimal areal capacity with the thinnest possible electrode. The results are summarized in Tables 32, 33, 34, and 35, which present the experimental thicknesses obtained from slurries with various solid contents cast at various theoretical thicknesses. Only LFP electrodes with an areal capacity of at least $2 \cdot mAh \cdot cm^{-2}$ at the specified thicknesses were considered for further analysis; samples with lower capacities were excluded from subsequent measurements.

Table 32. **LFP slurries S1 and S2 at various thicknesses and areal capacity obtained**

LFP S1 – S2	S1-L1	S1-L2	S1-L3	S1-L4	S2-L1	S2-L2	S2-L3	S2-L4
Theoretical thickness (wet), (μm)	80	100	150	200	100	150	200	250
Loading thickness (dry), (μm)	15.0	22.8	54.5	61.3	19.4	23.4	67.6	84.2
Average weight (mg) (D = 12 mm = 1.131 cm^2)	7.23	8.25	12.17	14.13	7.92	9.42	16.05	17.40
Electrode loading (mg/cm^2)	2.06	2.96	6.43	8.16	2.67	4.00	9.86	11.05
AM content (%)	92	92	92	92	92	92	92	92
AM loading (mg/cm^2)	1.89	2.73	5.91	7.50	2.46	3.68	9.07	10.17
AM loading (mAh/cm^2)	0.32	0.46	1.00	1.28	0.42	0.63	1.54	1.73

Table 33. **LFP slurries S3 and S4 at various thicknesses and areal capacity obtained**

LFP S3 – S4	S3-L1	S3-L2	S3-L3	S3-L4	S4-L1	S4-L2	S4-L3
Theoretical thickness (wet), (μm)	100	150	200	250	150	200	250
Loading thickness (dry), (μm)	3.25	52.4	65.0	78.3	72.5	86.0	108.3
Average weight (mg) (D = 12 mm = 1.131 cm^2)	6.42	13.00	12.18	15.80	14.78	17.40	20.33
Electrode loading (mg/cm^2)	1.34	7.16	6.43	9.64	8.73	11.05	13.65
AM content (%)	92	92	92	92	92	92	92
AM loading (mg/cm^2)	1.24	6.59	5.92	8.87	8.03	10.17	12.55
AM loading (mAh/cm^2)	0.21	1.12	1.01	1.51	1.37	1.73	2.13

Table 34. **LFP slurries S5, S6, and S7 at various thicknesses and areal capacity obtained**

LFP S5 – S6 – S7	S5-L1	S5-L2	S5-L3	S6-L1	S6-L2	S6-L3	S7-L1	S7-L2
Theoretical thickness (wet), (μm)	150	200	250	200	200	200	200	200
Loading thickness (dry), (μm)	58.8	99.7	120.0	97.8	103.8	103.5	58.3	61.5
Average weight (mg) (D = 12 mm = 1.131 cm^2)	14.15	19.13	22.23	16.53	18.40	19.07	14.18	14.38
Electrode loading (mg/cm^2)	8.18	12.59	15.33	10.28	11.94	12.53	8.20	8.38
AM content (%)	93.5	93.5	93.5	93.5	93.5	93.5	93.5	93.5
AM loading (mg/cm^2)	7.65	11.77	14.33	9.61	11.16	11.71	7.67	7.83
AM loading (mAh/cm^2)	1.30	2.00	2.44	1.63	1.90	1.99	1.30	1.33

Table 35.   LFP slurries S8, S9, and S10 at various thicknesses and areal capacity obtained

LFP S7 – S8 – S9 – S10	S7-L3	S8-L1	S8-L2	S9-L1	S9-L2	S9-L3	S10-L1	S10-L2
Theoretical thickness (wet), (µm)	200	200	200	200	200	200	200	200
Loading thickness (dry), (µm)	79.3	79.5	84.3	93.0	109.0	91.0	127.3	128.3
Average weight (mg) (D = 12 mm = 1.131 cm^2)	14.50	15.95	16.93	17.28	19.63	17.08	20.53	19.65
Electrode loading (mg/cm^2)	8.49	9.77	10.63	10.94	13.02	10.77	13.82	13.04
AM content (%)	93.5	93.5	93.5	93.5	93.5	93.5	93.5	93.5
AM loading (mg/ cm^2)	7.94	9.14	9.94	10.23	12.17	10.07	12.92	12.19
AM loading (mAh/cm^2)	1.35	1.55	1.69	1.74	2.07	1.71	2.20	2.07

Figure 36 presents a summary of the results derived from Tables 32, 33, 34, and 35.

As illustrated in Figure 36, at low solid contents (LFP S1, S2, and S3), electrode thicknesses ranging from 80 to 250 µm did not achieve the minimum required value, with the highest areal capacity recorded at 1.73 mAh·cm^{-2}. Consequently, slurries with higher solid content were prepared, where the LFP S4 slurry achieved 2.13 mAh·cm^{-2} at 250 µm. However, as previously discussed, operational difficulties occurred during the casting stage, resulting in non-homogeneous slurry distribution and visible cracking after the initial drying step at room temperature.

In contrast, the LFP S5 slurry, with a solid content of 41.6 wt.% (slightly lower than LFP S4), did not encounter such operational difficulties during the casting stage. The slurry distribution on the current collector was generally homogeneous, achieving the minimum required areal capacities of 2.00 and 2.44 mAh·cm^{-2} at 200 and 250 µm, respectively. This allowed for the possibility of fabricating a thinner electrode, which could reduce internal resistance and thereby enhance electrode performance.

Given that the LFP S5 slurry formulation met the required areal capacity, slurries from S5 to S10 (excluding S7 and S8) were prepared under the same conditions. Electrode sheets with an areal capacity of 2 mAh·cm^{-2} were selected for further research.

It is crucial to note that a higher solid content in the slurry under these conditions does not necessarily correspond to a higher areal electrode capacity. For example, the LFP S4 unlike LFP S5 slurry did not achieve the minimum required capacity at 200 µm due to the non-homogeneous distribution of the slurry on the current collector.

Samples were taken from four different corners of the electrode sheet, and the thickness and mass of each sample measured at these points varied significantly, resulting in low and unreliable values since the average value obtained was not representative.

Additionally, it is important to consider that not all electrode sheets had the same thickness, even though they were prepared with the same LFP S5 slurry formulation and cast at 250 µm. These discrepancies can be attributed to the manual calibration of doctor blade, as the calibration was constant across various electrode sheets, potentially introducing considerable error from one casted electrode to another.
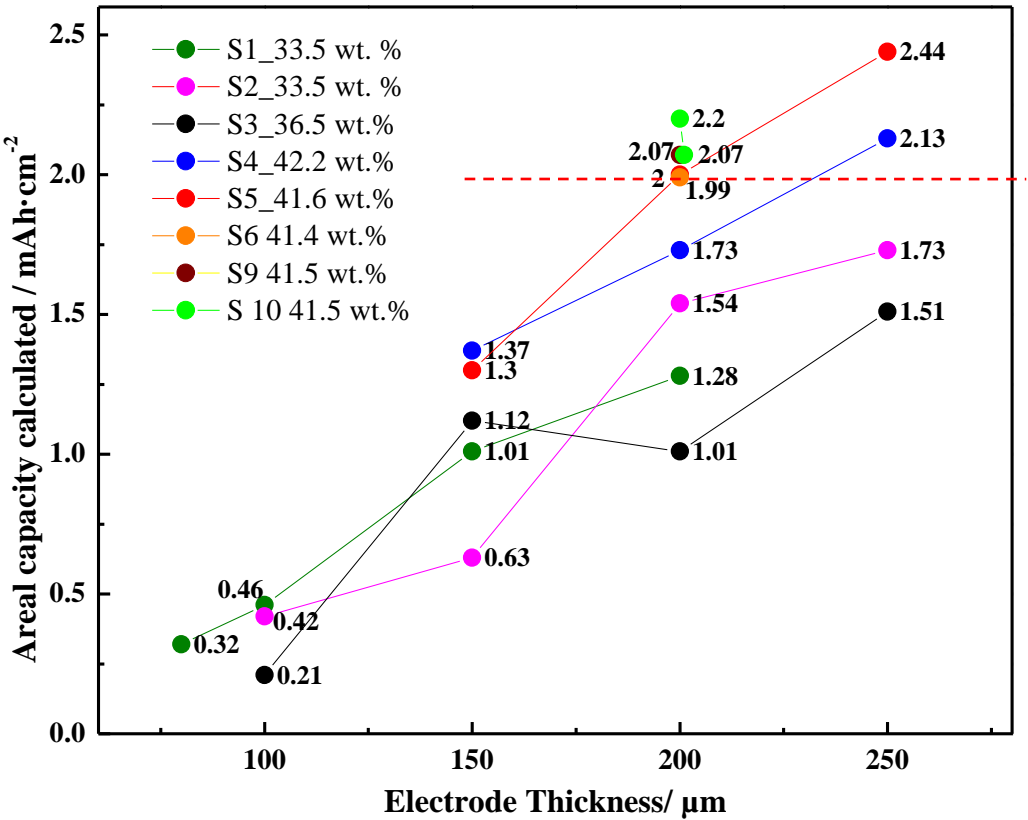
Figure 36. LFP mass loading at various solid content (wt.%) in the LFP slurry, and various thicknesses of electrodes sheets

11.8.4. Scanning electron microscope characterization of aqueous-processed LFP

Key parameters such as solid content, viscosity, and electrode thickness are critical in the fabrication of electrodes. However, surface characterization is an essential tool that determines whether these parameters have been optimally set or require further adjustment before proceeding to cell fabrication.

Techniques like scanning electron microscopy (SEM) are particularly valuable in this context, as they provide detailed insights into the surface morphology and microstructure of the electrodes. By revealing features such as particle distribution, porosity, and the presence of defects such as cracks on the electrodes surface. Thus, the surface characterization was not merely a supplementary step but a vital component of this research process, ensuring the reliability and effectiveness of the electrodes for the life span and cell performance.

Figure 37 presents the surface electrode sheets of the LFP slurry S1, with thicknesses equal to L1 = 80 µm, L2 = 100 µm, L3=150 µm, L4=200 µm.
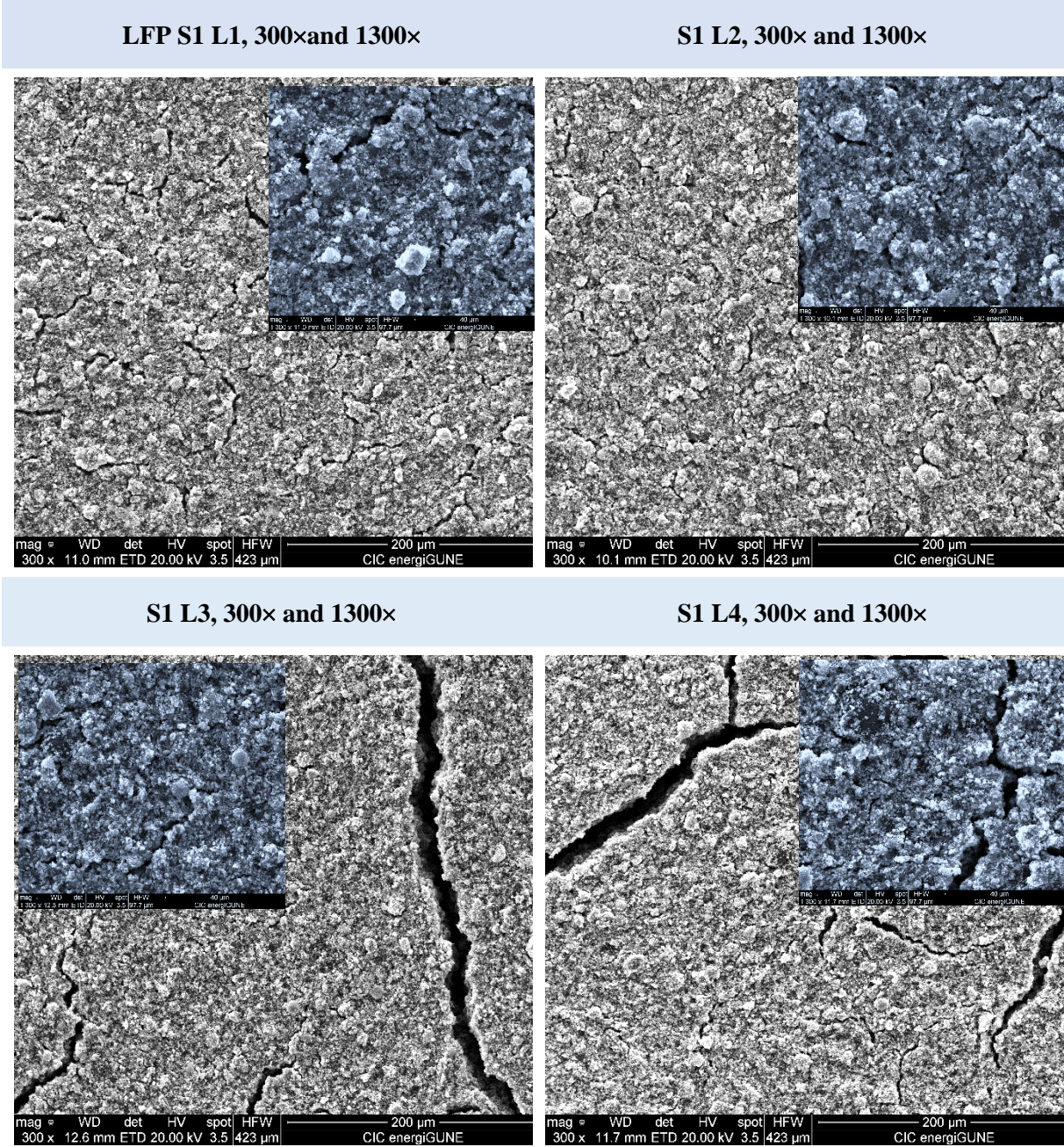
Figure 37. Surface characteristics of slurry LFP S1 at various thicknesses

Figure 38 presents the surface electrode sheets of the LFP slurry S2, with thicknesses equal to L1 = 100 µm, L2 = 150 µm, L3=200 µm, L4=250 µm.
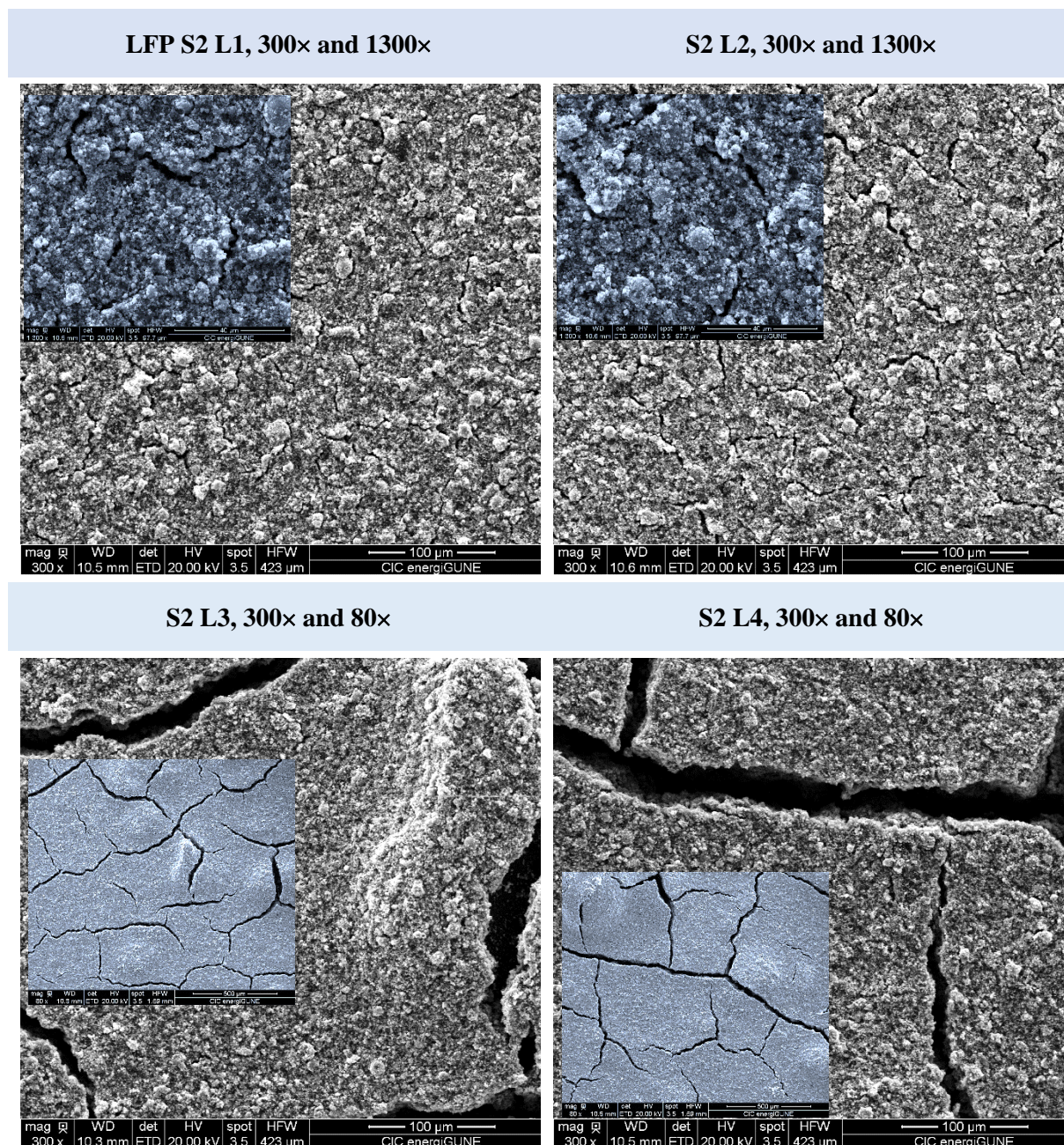
Figure 38. Surface characteristics of slurry LFP S2 at various thicknesses

The electrode surfaces resulting from the LFP S1 and S2 slurries were observed to be similar, which can be attributed to both slurries having the same solid content of 33.5 wt.% and given that the only variable varied during slurry preparation was the mixing time.

Figures 37 and 38 illustrate the influence of electrode thickness on the final electrode structure after the drying process.

At thicknesses of 80, 100, and 150 μm, and at a magnification of 150×, no cracks are visible on the electrode surface. However, when the magnification is increased to 1300×, small cracks become apparent. In contracts, for electrodes with thicknesses of 100, 150, and 200 μm cracks are more prominent with not need of magnification. This observation indicates that even with a lower solid content in the slurry, a uniform and smooth electrode surface is not guaranteed.

The formation of cracks, particularly at increased thicknesses, can be explained by the non-uniform drying of the electrode slurry, which leads to differential shrinkage. This phenomenon is well-documented in literature, where capillary forces during the drying process cause stress within the electrode structure, leading to crack formation. The thicker the electrode, the more prone it is to these stresses, as the interior of the electrode dries at a different rate compared to the surface. Additionally, the solid content plays a critical role in determining the viscosity and drying behavior of the slurry. While a lower solid content might reduce the likelihood of large cracks, it does not necessarily ensure a perfectly smooth surface, as the particle distribution and binder network also significantly influence the electrode final morphology.

Figure 39 presents the surface electrode sheets of the LFP slurry S3, with thicknesses equal to L3=200 μm, L4=250 μm and solid content of 36.5 wt.%.
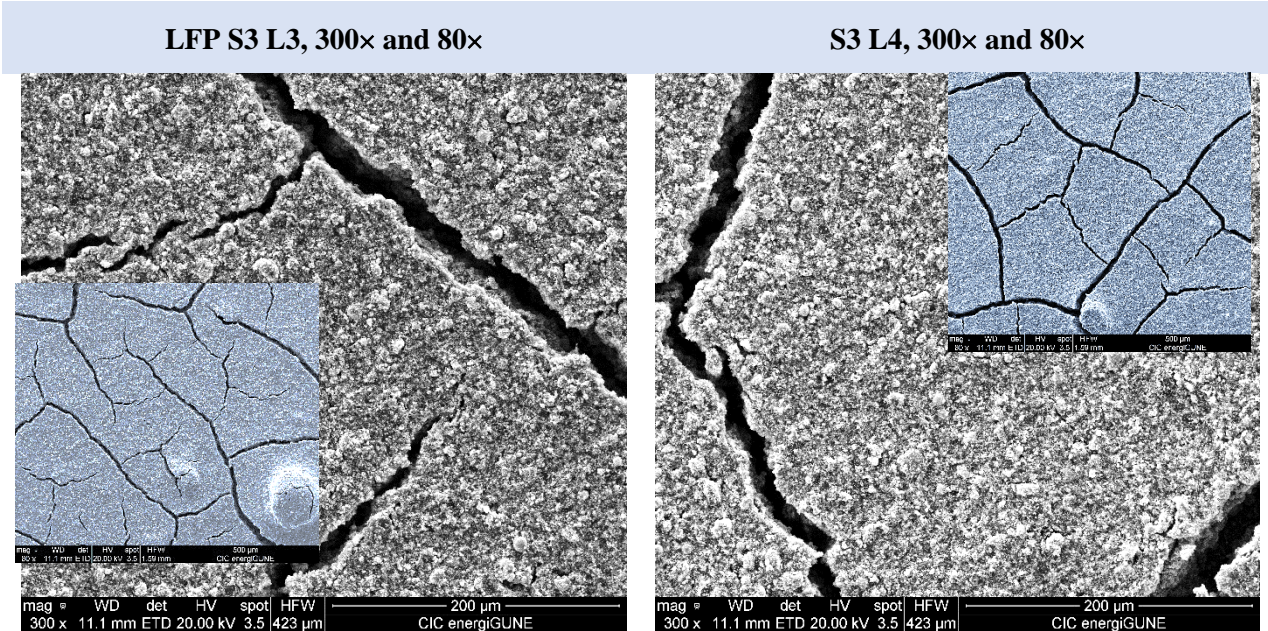
Figure 39. Surface characteristics of slurry LFP S3 at various thicknesses

Figure 40 presents the surface electrode sheets of the LFP slurry S4, with thicknesses equal to L2 = 200 µm, L3=250 µm and solid content of 42.2 wt.%.
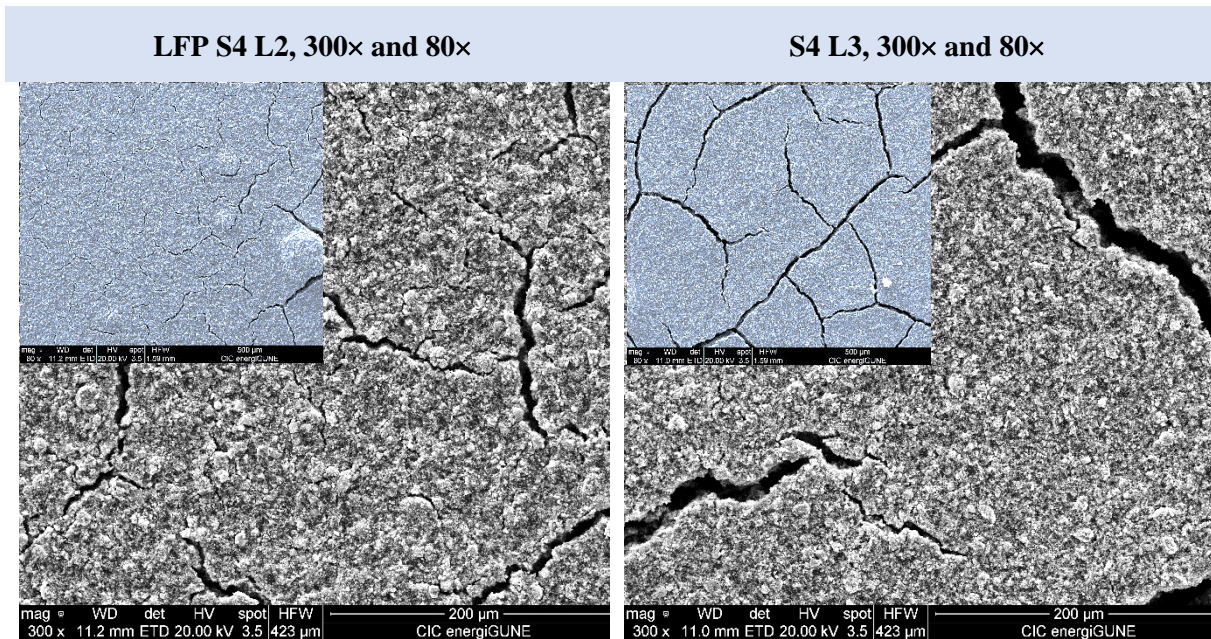
Figure 40. Surface characteristics of slurry LFP S4 at various thicknesses

Figures 39 and 40 present the electrode morphology at higher solid content. The increase in cracks on the electrode surface of LFP as the solid content increases is primarily due to the greater stress induced during the drying process. When the solid content is higher, the slurry becomes more viscous, leading to a denser packing of AM particles. This higher viscosity can cause non-homogeneous mixing of the materials, making the slurry more prone to cracking as it dries due to uneven distribution and stress accumulation within the electrode structure. Additionally, during drying, the removal of water is causing the particles to draw closer together, resulting in increased capillary forces and differential shrinkage within the electrode. This generates internal stresses that manifest as cracks, especially as the drying is uneven across the electrode thickness.

Cracks in lithium-ion cell electrodes can significantly degrade performance by disrupting electrical conductivity, creating uneven lithium cation diffusion, and increasing the risk of degradation. These cracks can lead to higher internal resistance, accelerated capacity fading, and mechanical instability as the cell undergoes repeated charge and discharge cycles. The exposure of AM to the electrolyte through cracks can also trigger unwanted side reactions, further contributing to the deterioration of the electrode effectiveness and the overall lifespan of the cell.

Figure 41 presents the surface electrode sheets of the LFP slurry S5, with thicknesses equal to L1 = 150 μm, L2 = 200 μm, L3=250 μm and solid content of 41.6 wt.%.
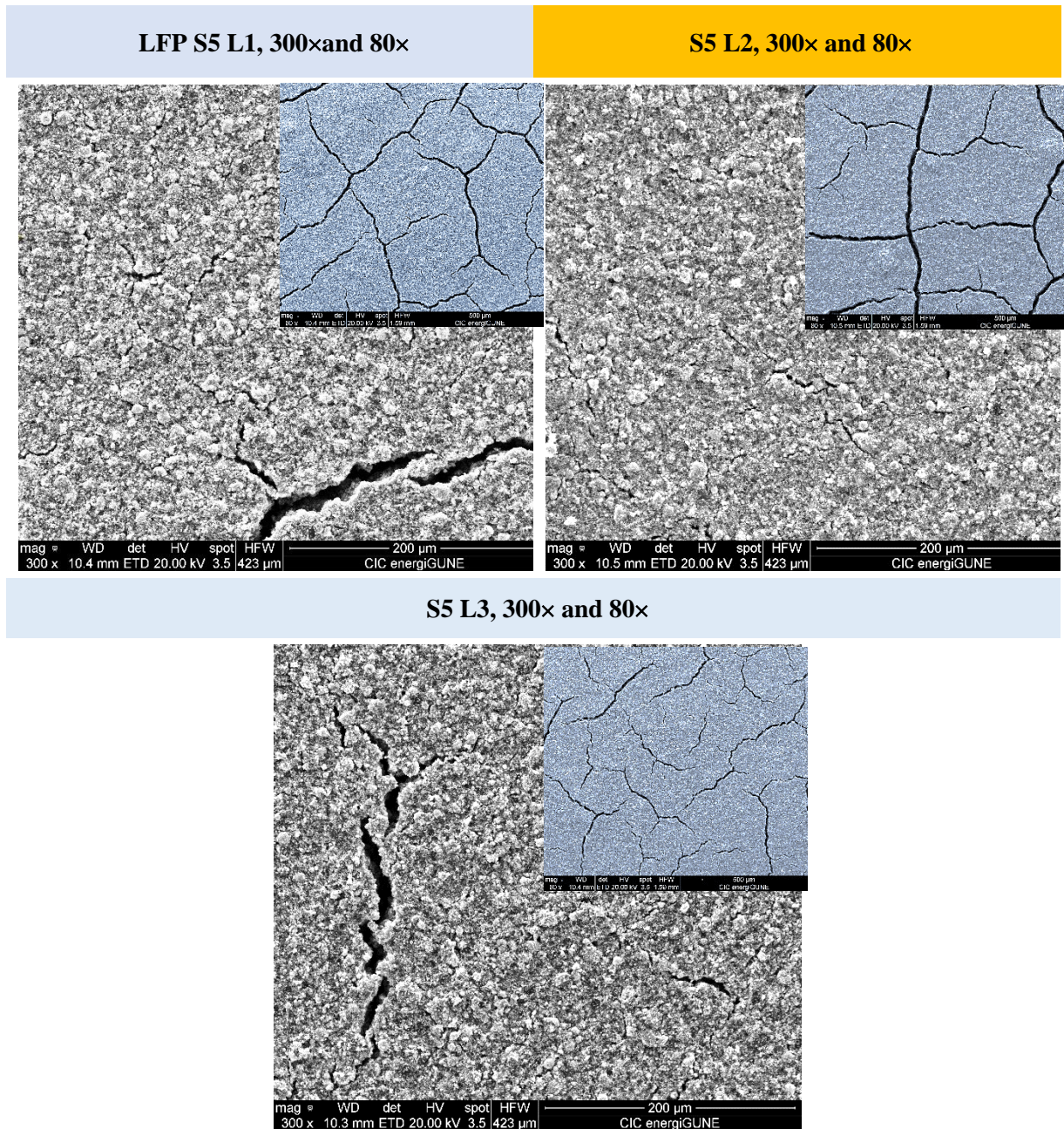
Figure 41. Surface characteristics of slurry LFP S5 at various thicknesses

The electrode surface of the LFP slurry (S5) exhibits a superior quality compared to the other electrodes prepared at various slurry formulations. It has notably fewer cracks, and there are no visible agglomerates, unlike those observed in the slurry samples S3 and S4. Considering the previously studied parameters such as solid content, viscosity, and the surface characteristics, LFP S5 has been selected for further research.

One key reason for this choice is that the cracks present on the surface of the LFP S5 electrode are fewer, and the channels formed by these cracks are thinner, making them more amenable to improvement during the calendering process. Although the formation of a perfectly smooth and crack-free surface is not the primary goal for aqueous-processed electrodes at this stage, the reduced presence of cracks in LFP S5 is a positive indicator.

In aqueous-processed electrode systems that utilize CMC and SBR as binders, cracks are a common issue, especially at higher solid content and electrode thickness. CMC and SBR are essential for providing mechanical stability and flexibility to the electrode. However, at higher solid contents, the increased particle packing density can lead to stress within the electrode during drying, which often results in cracking. Similarly, with thicker electrodes, the internal stress during solvent evaporation can cause cracks to propagate more easily.

Further research and optimization, particularly in the calendering process, are necessary to address the remaining surface crack issues and enhance the overall quality of the electrode.

11.8.5. Calendering process of LFP electrodes

The next step for the electrode sheets, which had an areal capacity of 2 mAh·cm^{-2} or higher, was the calendering process. Following the mixing, coating, and drying stages, the porous coating undergoes mechanical compaction, which decreases the porosity and enhances the volumetric energy density by reducing the coating's thickness (Figure 42). Calendering is a crucial step in the production of electrodes for LIBs because it defines the final microstructure of the electrode [403, 404].
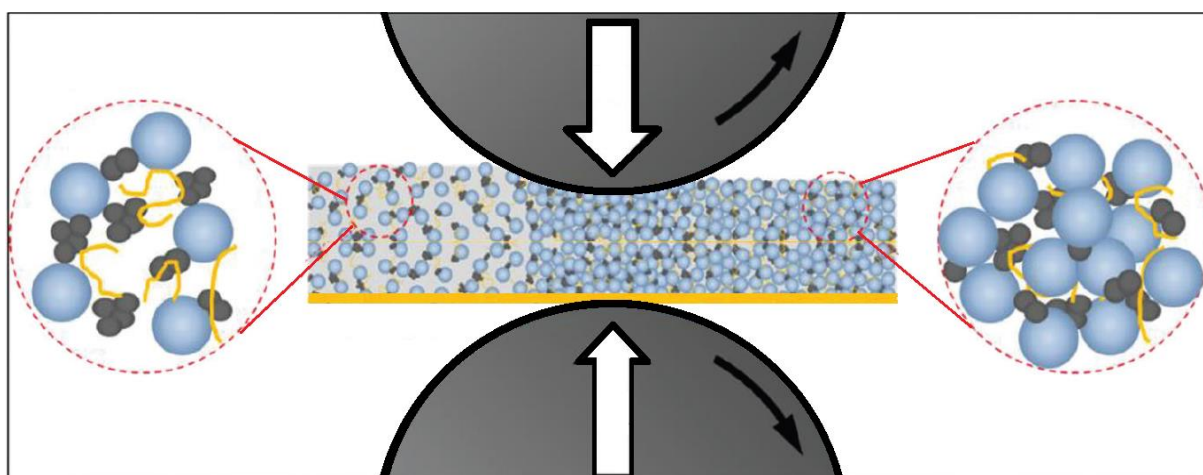
Figure 42. Calendering process with details on rollers, initial and final thickness, [405]

To enhance the surface and bulk uniformity of the electrodes, the calendering process typically involves passing the electrode through a gap between two heated rollers. The applied force compacts the electrode, and the heating reduces the required force, which in turn minimizes the rebound (spring back) of the electrode and reduces shear stress between the current collector and the coating.

For electrodes made with LFP formulations (S5, S6, and S10), a thickness reduction between 10% and 30% was established as the standard for the calendering process.

The electrode sheet, which consists of a current collector foil (copper for anodes and aluminum for cathodes) coated with the slurry prepared is passed through the gap between the rollers. To control the process, the gap was set smaller than the electrode thickness depending on the percentage aimed at being reduced. This step has a significant impact on the electrode electrochemical performance because it significantly alters the pore structure of the coating.

Table 36.   Percentage of thickness reduced after calendering process

LFP Calendering	S5 – L2	S5 – L2	S5 – L2	S6 _L2	S10_L1
Current collector foil thickness (μm)	17	17	17	17	17
% Calendered (theoretical)	10%	20%	25%	15%	15%
Initial thickness (μm)	99.67	99.67	99.67	93.00	128.33
Thickness after calendering (μm)	83.67	63.75	54.50	79.00	106.50
% Thickness reduction	16.05	36.04	45.32	15.05	17.01

To understand the impact of reduced electrode thickness after calendering on cell performance, a reduction of 10%, 20%, and 25% from the initial thickness was targeted and the LFP density was calculated. Measurements of the initial and final thickness were taken, and the differences are presented in Table 36.

The calendering process required specific parameters, including roller speed, temperature, and the gap between the rollers. For this study, the temperature was set to 80°C, the roller speed for the LFP cathode was adjusted to 4 m/min, and the gap between the rollers was varied based on the intended thickness reduction.

Two key observations were made during the LFP calendering process. First, the electrode sheet did not retain uniform thickness across the current collector, resulting in one side being slightly thinner or thicker than the other. This led to a greater reduction in thickness than initially calculated, as shown in Table 37.

Second, when the thickness was reduced by 30% or more, the coating on the current collector began to crack and delaminate, with fragments of the electrode falling off. Therefore, to prevent surface cracking, the thickness reduction should be kept below 25%.

Table 37.   LFP electrode density before and after the calendering process

LFP slurry	LFP S5 L2				S6 L3		S10 L1		S10 L2	
%Thickness targeted	0%	10%	20%	25%	0 %	15%	0 %	15 %	0 %	15 %
%Experimental Thickness reduced	0	16.05	36.04	45.32	0	15.05	0	17.01	0	17.01
LFP density before/after calendering (g/cm³)	1.26	1.50	1.97	2.31	1.13	1.25	1.05	1.62	1.15	1.62

Regarding the density of LFP after calendering, it was found to increase proportionally with the reduction in thickness. Although there is no established standard for LFP density, a value of 2.0 ± 0.1 g·cm^{-3} for electrodes processed with PVdF is generally considered suitable for commercialization (MTI Corp.). Therefore, densities ranging from 1.5 to 2.0 g·cm^{-3} are deemed acceptable in this research for assembling pouch cells. As shown in Figure 43, the electrodes chosen for calendering achieved an average density suitable for cell assembly.
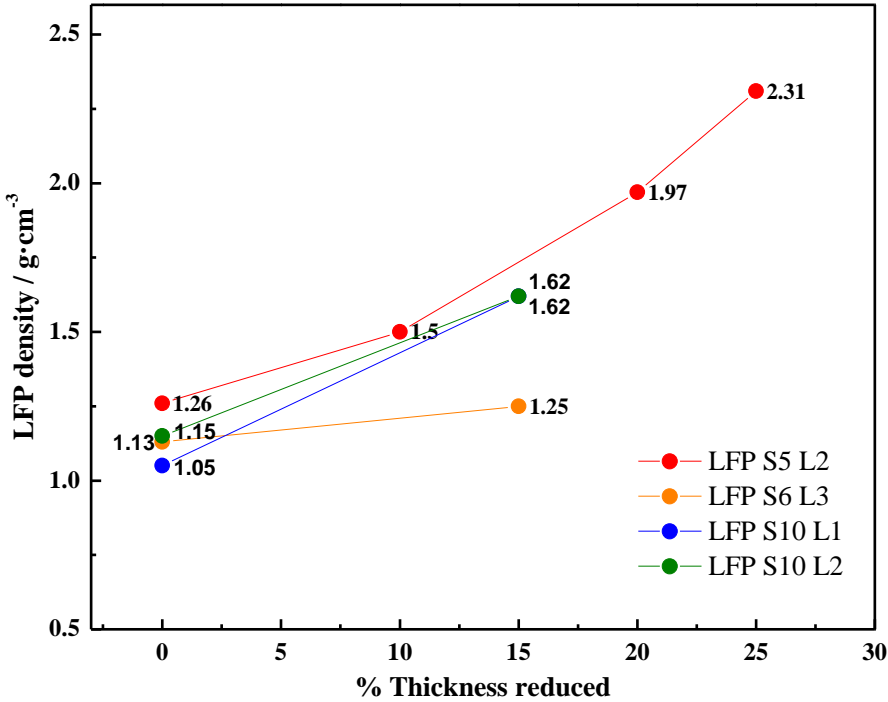
Figure 43. LFP electrode density before and after the calendering process

It is important to highlight that, if the porosity is high, it can enhance ion transport by allowing better electrolyte penetration, which improves the rate capability and enables faster charging and discharging.

However, this also reduces the amount of AM and CMs, leading to lower electrical conductivity and higher internal resistance. Additionally, high porosity can compromise the mechanical stability of the electrode, causing particles fractures, cracking, or delamination during cycling, and can increase electrolyte consumption due to a larger surface area.

In contrast, if the porosity is too low, the dense structure can obstruct the lithium cation transport, slowing down lithium cation diffusion through the electrolyte, which reduces the battery rate capability and increases polarization. Although low porosity improves the electrode mechanical strength and electrical conductivity by providing a more robust conductive network, the restricted ion movement can lead to higher overpotentials, reduced capacity, and poorer overall performance under high current.

Moderate compaction can reduce irreversible capacity loss and lower ohmic contact resistance, while it also reduces electrochemical impedance [404]. Thus, the range of densities from 1.5 to 2.0 $g \cdot cm^{-3}$ are confirmed as acceptable for the assembly of fluorine-free Li-ion pouch cells [258].

Finally, to gain a clearer understanding of the effects of calendering, galvanostatic cycling tests at C/25 and C/20 were performed, and a surface characterization of the calendered electrode was conducted.

11.8.6. Surface characterization after calendering process, LFP cathode material

Figure 44 illustrates the enhancement of the electrode surface following the calendering process. The improvement is evident even after a 10% thickness reduction, which was experimentally determined to be 16%. Based on these findings and considering the established limit of 25% thickness reduction, along with its impact on electrode density, a thickness reduction of 15–20% can be confirmed as a viable option for further research.

Given that the electrode density range has been established based on current results and the characteristics of a commercially available electrode using PVdF and NMP, the next step before pouch cell assembly is to conduct galvanostatic cycling. This will help determine the effect of electrode density on overall cell performance.
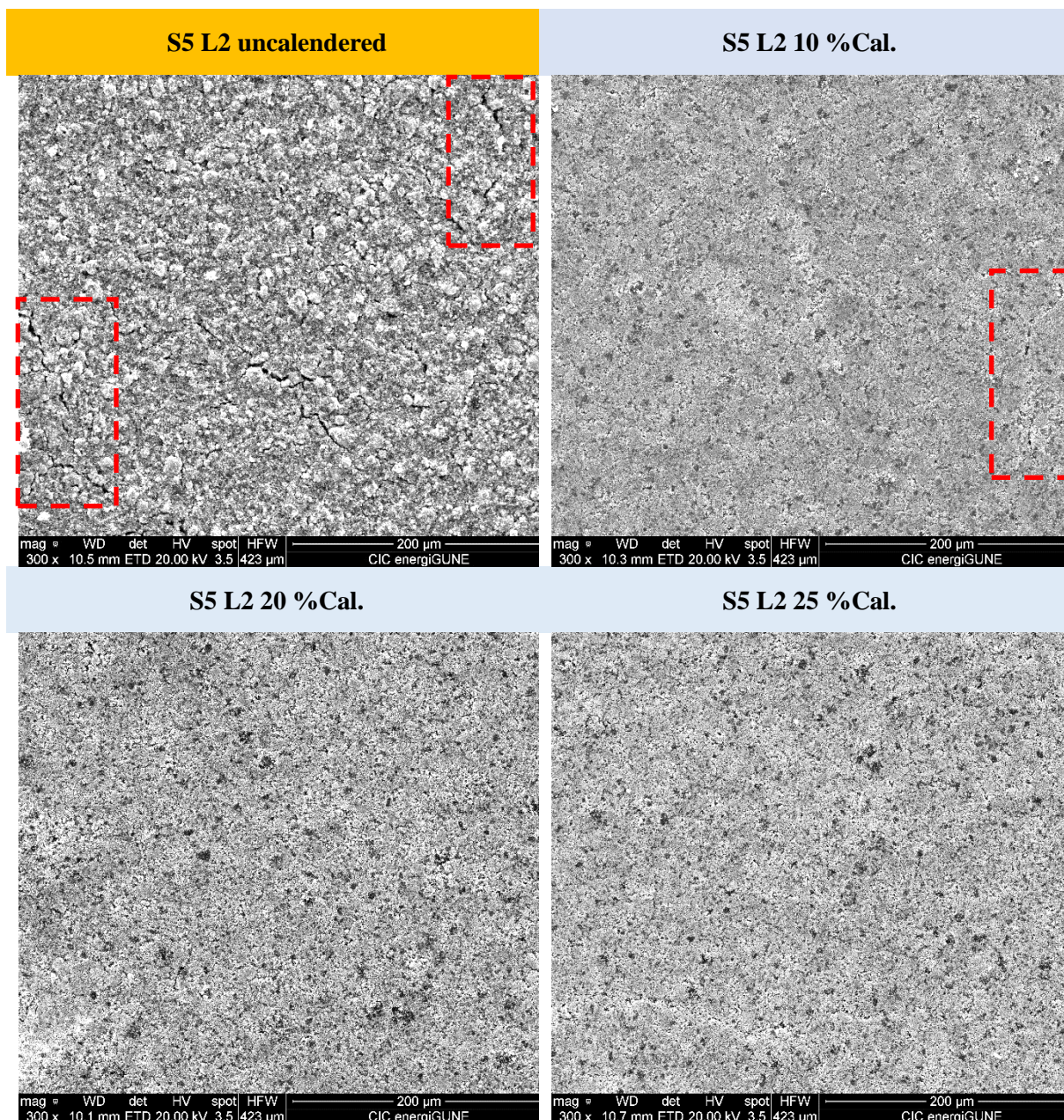
Figure 44.   Surface characteristics before and after calendering, LFP S5

11.8.7. Galvanostatic cycling after calendering process on the electrodes

Figure 45 illustrates the impact of calendering on the coulombic efficiency by galvanostatic cycling performance at C/25 and C/20. A clear improvement in specific capacity is observed when comparing non-calendered electrodes to those that have undergone calendering. Notably, the electrode calendered at 10% (equivalent to 16% experimentally) exhibited the highest specific capacity at C/25 and similar to the rest at C/20.

Additionally, although the discharge capacities do not show significant differences, with variations not exceeding 6.5%, the charge curve reveals more pronounced distinctions.

The uncalendered electrodes exhibit the lowest coulombic efficiency at C/25 with a CE of 82.4%, whereas the electrodes calendered at 10% (16% experimentally) achieve the highest efficiency with 93.5%. Furthermore, all the calendered electrodes demonstrate a coulombic efficiency of over 98% at C/20, in contrast to the uncalendered electrode, which only reaches 95.5%, notably lower than the calendered counterparts.
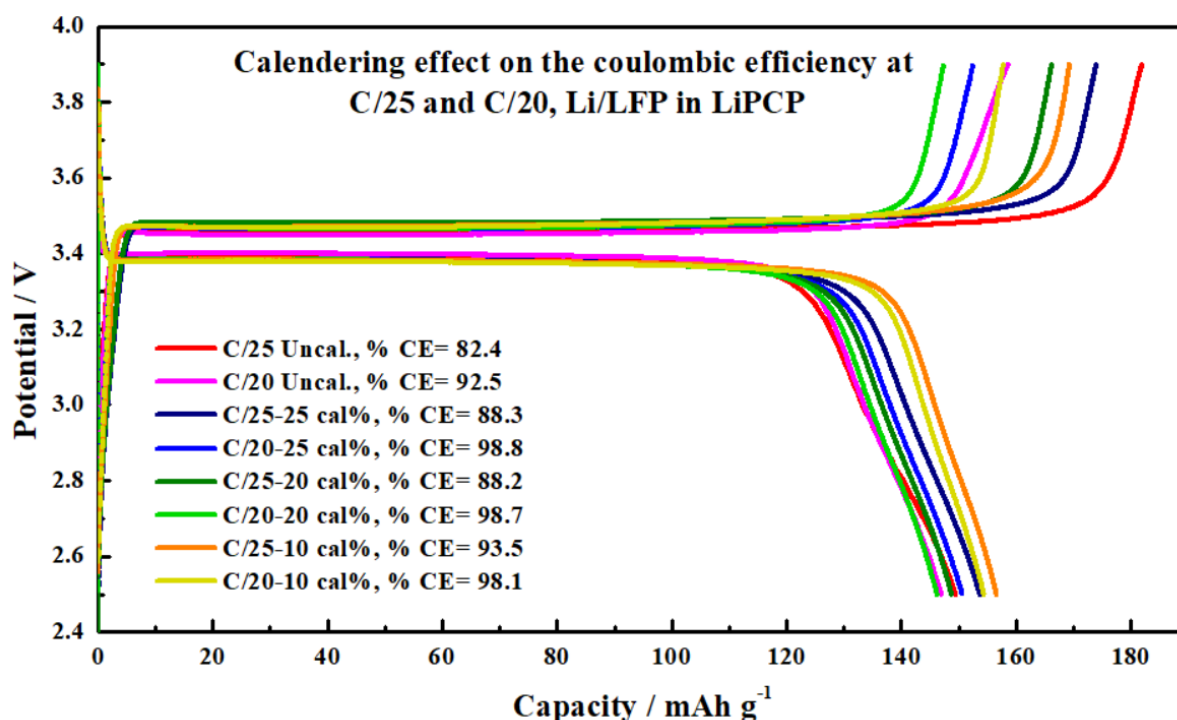
Figure 45. Evaluation of the calendering effect on the coulombic efficiency on the first cycle of C/25 and C/20 by galvanostatic cycling

While this improvement may seem not very significant when considering the results obtained with half-cells, the impact could be more pronounced in full-cell configurations. The 16% reduction in electrode thickness through calendering enhances the electrode density, improves electronic and ionic conductivity, and reduce internal resistance, all of which contribute to better overall cell performance, suggesting that higher reductions might not be significantly beneficial for cell performance.

Consequently, based on these results, along with surface electrode characterization and galvanostatic cycling data, a thickness reduction target of 15–20% will be adopted moving forward, as this range has demonstrated a beneficial impact on the electrode performance.

11.8.8. LFP electrode sheet resistance evaluation before and after calendering

Figure 46 illustrates how electrode conductivity in LIBs varies with electrode thickness and the solid content of the slurry (See Tables A.3. and A.4. for detailed data). Both factors, solid content and thickness, play a crucial role in determining electrode conductivity.

Slurry S1 and S2, with a similar solid content of 33.5 wt.%, exhibited the lowest electrode conductivity, which decreased further as the electrode thickness increased. This reduced conductivity is likely due to the lower concentration of AM in S1 compared to the other slurries. In contrast, Slurry S3 showed a significant increase in conductivity, which can be attributed to its higher AM content.

Generally, a higher solid content in the slurry enhances both electronic and ionic conductivity by increasing the concentration of AMs, thereby improving overall battery performance. However, excessively high solid content can lead to poor dispersion of CMs, which in turn reduces conductivity, as observed with Slurry LFP S4.

For Slurries S5 through S10, the conductivity is lower than that of S1 and S3 but appear more stable and consistent, making it more feasible to replicate.
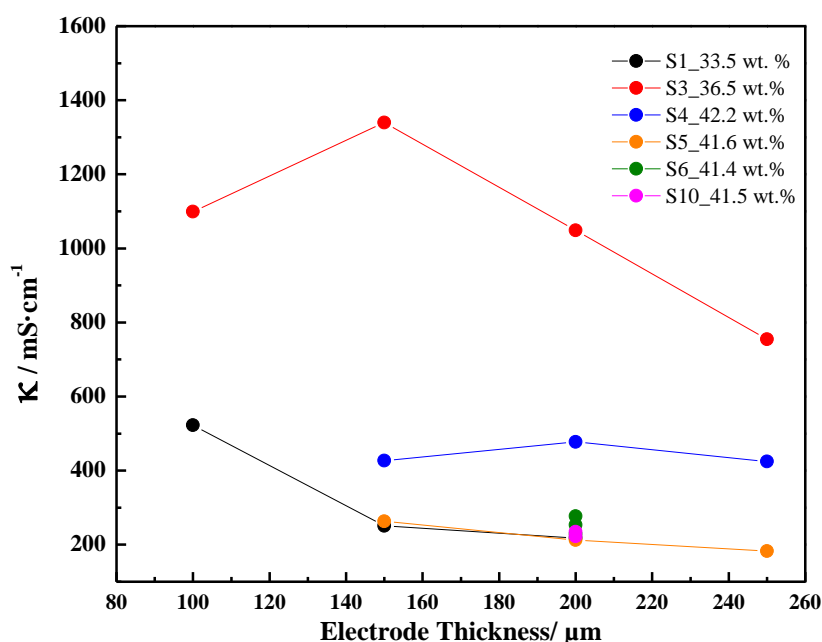
Figure 46. Electrode conductivity evaluation at various electrode thicknesses

Thicker electrodes can store more energy, leading to higher battery capacity. However, this also increases internal resistance due to the longer ion transport paths, which can slow down charge and discharge rates and potentially cause uneven lithium plating.

Additionally, some inconsistencies in the conductivity of Slurries S3 and S4 at various thicknesses were observed. This could be due to the non-uniform distribution of the slurry on the current collector, as shown in the surface characterization in Figures 39 and 40.

Figure 47 illustrates how calendering impacts electrode conductivity. The data shows that calendering enhances electrode conductivity. This improvement is primarily due to the increased particle-to-particle contact within the AMs and CMs, which allows for more efficient electron transport. Moreover, the reduction in porosity that occurs during calendering contributes to better electrical connectivity across the electrode, thereby decreasing internal resistance and improving overall performance.
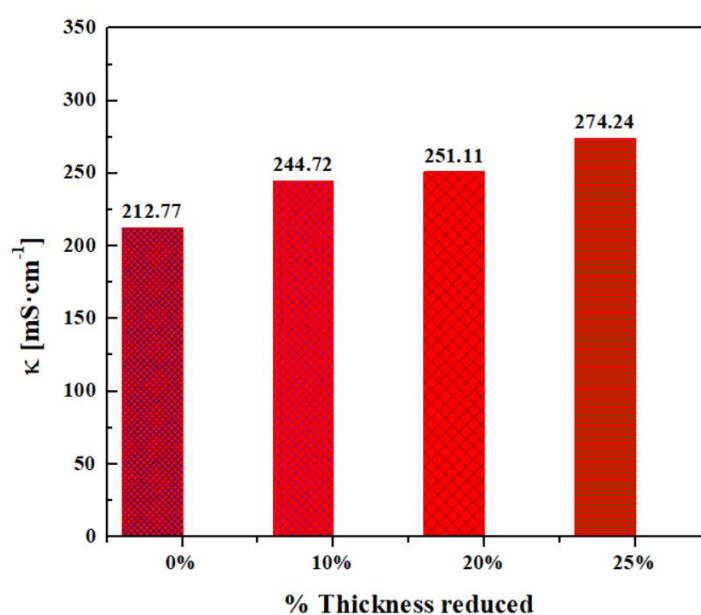
Figure 47. Conductivities of LFP S5 after calendering at various thicknesses reductions

11.8.9. pH measurements on LFP slurry preparation for electrode fabrication

The pH value of slurries used in electrode fabrication is a critical parameter that can significantly influence the performance, stability, and manufacturability of electrodes. The optimal pH range varies depending on the specific materials used for the anode and cathode.

To determine an appropriate average pH value for the cathode, it is necessary to consider the presence of aluminum as the current collector and water as the solvent. Aluminum corrosion resistance depends on a protective oxide film, which remains stable in aqueous media when the pH is between approximately 4.0 and 9.0. However, for safety reasons, a pH range of 7 to 9 was targeted for the final slurry before the casting stage.

During slurry preparation, 2 ml samples were taken at the end of each stage to assess the impact of each material (binder, AM, and CM) in the slurry, as detailed in Table 38. The pH of CMC at a 1 wt.% concentration (A1) and SBR at a 40 wt.% concentration (A2) was measured independently. Both exhibited a pH ranging from 6.8 to 8.3. The minor variations in these results can be attributed to environmental temperature changes, which were deemed insignificant, so no further adjustments were made to the binder solutions.

Table 38.   pH measurement at 22 ºC, at various stages of the LFP slurry preparation

N°	Stage measurement	LFP_ S1	LFP_ S2	LFP_ S3	LFP_ S5	Stage description
A1	CMC (1%)	7.14	6.87	6.82	7.05	CMC solution
A2	SBR (40%)	-	-	8.05	8.26	SBR solution
KB	CMC + KB	9.79	10.28	10.18	10.15	CMC with KetjenBlack-CB after 90 min of mixing
AM_o	$CMC + KB + LFP_o$	8.71	8.72	8.65	8.38	CMC, KetjenBlack-CB with LFP after 10 min of mixing
AM_f	$CMC + KB + LFP_f$	8.50	8.52	8.50	8.12	CMC, KetjenBlack-CB with LFP after 90 min of mixing
F	$CMC + KB + LFP_f + SBR$	-	-	8.55	8.41	Final slurry for casting

The first step in slurry preparation involved adding Ketjenblack as the CM. To ensure a homogeneous distribution of carbon particles with the binder, the mixture was stirred for 90 minutes at 1500 rpm. After this stage, the pH was measured and found to be 10.1 (KB), which is higher than the pH of the binder solution alone. This increase can be attributed to Ketjenblack high pH, ranging from 9.0 to 10.5. Since this stage was not final, no further changes were made at this point.

Upon adding the AM, LFP in this case, the pH decreased to 8.6 after 10 minutes of mixing (AM_o) and to 8.4 after 90 minutes of mixing (AM_f). This pH level is within the acceptable range for further research.

Additionally, since SBR was incorporated to increase the solid content in the slurry, the pH was measured 30 minutes after adding this second binder additive (F), and the results

remained within the acceptable range, with a final slurry pH in the range of 8.4 to 8.6 before the casting stage.

Figure 48 summarizes the results obtained at the various stages outlined in Table 38.
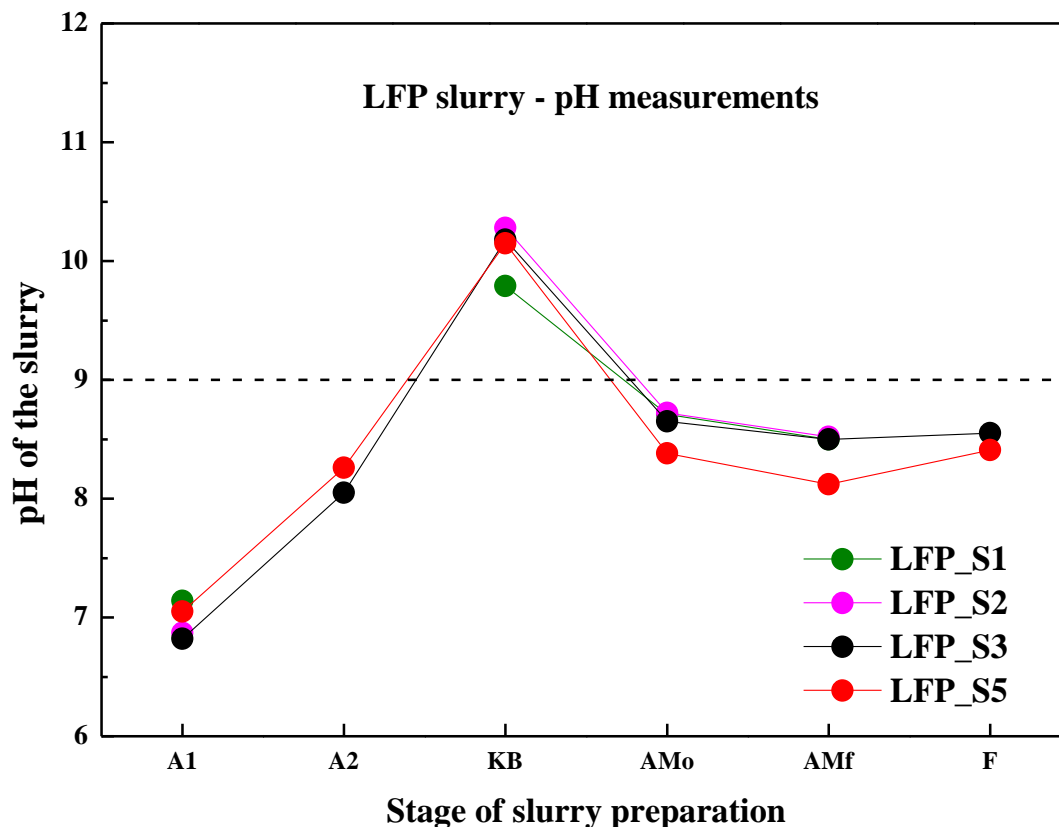
Figure 48. pH value at various LFP slurry stages during electrode preparation

As the pH value of the slurry remained within the acceptable range, no further studies, such as the addition of acids or bases, were conducted during slurry preparation.

11.9. SG electrode fabrication for pouch cells

This section focuses on the fabrication of SG as the anode material for fluorine-free Li-ion cells. The fabrication stages considered here are similar to those used for LFP cathode preparation, as described previously. Specifically, this section details the following steps: slurry mixing at room temperature, rheological property analysis, electrode thickness measurement and its influence on areal capacity, the calendering process, conductivity assessment before and after calendering, pH measurements during slurry preparation, and surface characterization before and after calendering.

11.9.1. SG slurry formulation

The SG slurry was prepared at room temperature using a formulation similar to that used in laboratory coin cell assembly. However, owing to the requirement for higher viscosity, SBR was added as an additive. The mixing process followed the same procedure as for the LFP slurry preparation. Initially, a 1 wt.% CMC solution was blended with C45 CM in a homogenizer at 1500 rpm for 45 minutes. After this, the AM (SG) was incorporated and mixed at the same speed and time period. Finally, SBR was incorporated into the system. Since SBR is prone to degradation under high shear rates, the mixing speed was reduced to 500 rpm in 30 minutes. Properties such as solid content, mixing time, and thickness of slurry casted on the current collector are shown in Tables 39, 40, and 41.

Table 39.   SG S1 slurry composition, mixing time, thickness and solid content

Slurry composition: SG S1		Calculated wt.%	Calculated (g)	Experimental (g)	Experimental %
Binder solution 1			10.53	10.550	
Binder solution 2			0.53	0.520	
CM	C45 (TIMCAL C-NERGY™ SUPER C45)	2.00	0.2105	0.210	1.98
Binder 1	CMC (Sigma Aldrich)	1.00	0.11	0.106	0.99
AM	SG (Sigma-Aldrich)	95.00	10.00	10.100	95.07
Binder 2	SBR (Arkema) 40%	2.00	0.21	0.208	1.96
Total		100.00	21.58	21.69	100.0
Operating conditions:					
Temperature = Room temperature	Solid content = 37.3 wt.% Water added = 7.13 g	Total time = 120 (min)		Electrodes sheet thickness, L1 = 100 μm, L2 = 150 μm, L3=200 μm	

Table 40.   SG S2 slurry composition, mixing time, thickness and solid content

Slurry composition: SG S2		Calculated %	Calculated (g)	Experimental (g)	Experimental %
Binder solution 1			10.53	10.63	
Binder solution 2			0.53	0.53	
CM	C45 (TIMCAL C-NERGY™ SUPER C45)	2.00	0.2105	0.21	1.99
Binder 1	CMC (Sigma Aldrich)	1.00	0.11	0.11	1.01
AM	SG (Sigma-Aldrich)	95.00	10.00	10.03	95.00
Binder 2	SBR (Arkema) 40%	2.00	0.21	0.21	2.01
Total		100.00	21.58	21.72	100.0
Operating conditions:					
Temperature = Room temperature	Solid content = 37.1 wt.% Water added = 7.08 g	Total time = 120 (min)		Electrodes sheet thickness, L1 = 150 μm (3 sheets)	

Table 41.   SG S3 slurry composition, mixing time, thickness and solid content

Slurry composition: SG S3		Calculated %	Calculated (g)	Experimental (g)	Experimental %
Binder solution 1			10,53	10,570	
Binder solution 2			0,53	0,530	
CM	C45 (TIMCAL C-NERGY™ SUPER C45)	2,00	0,2105	0,210	1,99
Binder 1	CMC (Sigma Aldrich)	1,00	0,11	0,106	1,00
AM	SG (Sigma-Aldrich)	95,00	10,00	10,010	94,99
Binder 2	SBR (Arkema) 40%	2,00	0,21	0,212	2,01
Total		100,00	21,58	21,64	100,0
Operating conditions:					
Temperature = Room temperature	Solid content = 37,2 wt.% Water added = 7.03 g	Total time = 120 (min)		Electrodes sheet thickness, L1 = 150 µm (3 sheets)	

Initially, a high solid content similar to that used in LFP electrode fabrication was targeted. The first slurry, coded as SG-SX, had a solid content of 40.1 wt.% and exhibited acceptable viscosity for electrode casting using a Dr. Blade. However, it was not possible to spread the slurry uniformly during casting. This implies that the thickened mixture lost flowability, which is crucial for achieving a uniform cast layer.

In contrast to LFP, SG does not require specific minimum values for solid content or rheological properties. However, it is important to achieve properties compatible with the LFP electrode prepared earlier, such as areal capacities over 2 mAh·cm^{-2}. Thus, three SG slurries were prepared. Since no operational issues emerged during slurry preparation and casting, the same formulation was used for all three slurries, resulting in an average solid content of 37.2·wt.% and no further formulation changes were made. The study then proceeded to analyze the rheological properties.

11.9.2. Rheological properties, SG slurry

Figure 49 shows the viscosity of the SX and S1-S3 formulations. The data clearly illustrates that a small difference of just 3 wt.% in solid content has a significant impact on viscosity, with a change from 1150 mPa·s to 200 mPa·s at a shear rate of 1·s^{-1}. This dramatic decrease in viscosity may explain the operational issues encountered, which were likely caused by the initially high viscosity.
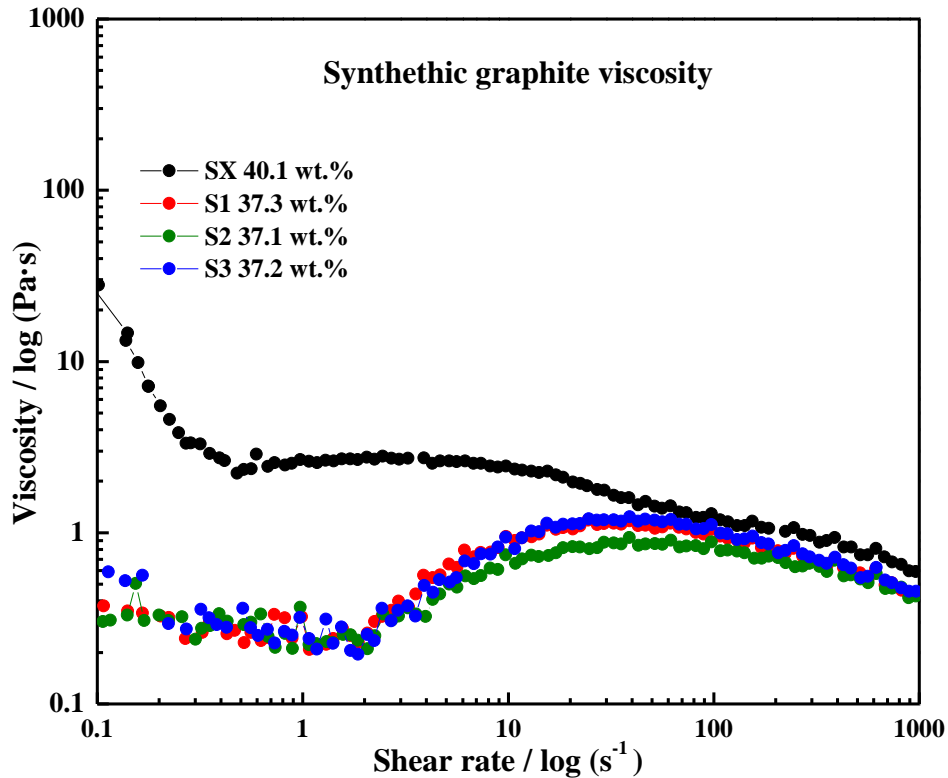
Figure 49. SG slurry viscosity versus shear rate with the duplicate samples

The operational problems encountered, even at relatively high viscosity, can be attributed to the tendency of SG particles to aggregate due to their hydrophobic nature, forming a gel-like structure in an aqueous slurry. Both CMC and SBR are used to promote dispersion by adsorbing onto the graphite surface. In the graphite/CMC/SBR slurry, the microstructure remained unchanged with the addition of SBR because SBR could not adsorb onto the graphite surface due to the presence of CMC. However, the SBR may have affected the dispersion of graphite particles because of the low CMC concentration, leading to the operational problems observed during the casting process.

The rheology of SG slurry for electrode fabrication exhibits a complex behavior where viscosity changes with shear rate.

Initially, at low shear rates, the slurry has slightly high viscosity due to a network structure formed by graphite particles, which creates resistance to flow. As the shear rate increases, this network structure begins to break down, resulting in a decrease in viscosity, a phenomenon known as shear thinning. However, at even higher shear rates, the viscosity starts to increase again, which can occur due to particle alignment with the flow direction or shear thickening, where particles interact more strongly and form clusters that resist flow.

This slight increase in viscosity helps stabilize the dispersion of graphite particles, preventing sedimentation and improving the homogeneity of the slurry. However, because the CM concentration is relatively low (1 wt.%), the thickening effect will be moderate, and the slurry may exhibit more pronounced shear thinning behavior as the network structure is less robust, making it easier to break down under shear. This means the slurry might flow more readily under higher shear rates, which could be beneficial for the coating processing in electrode fabrication.

Additionally, CMC and SBR play crucial roles in shaping the rheological behavior of SG slurry. CMC acts as a thickening agent, increasing viscosity, particularly at low shear rates, by enhancing the network structure through interactions with graphite particles. This results in a more stable slurry with improved suspension of the particles. SBR, a binder additive, contributes to the slurry viscoelastic properties, providing flexibility and ensuring that the slurry maintains its form during processing. Together, CMC and SBR help control the slurry viscosity, promoting better dispersion and stability, which are essential for uniform electrode fabrication.

Given that the theoretical capacity of graphite is 372 mAh·g^{-1} and the areal capacity slightly higher than 2.2 mAh·cm^{-2}, thin electrode sheets are required. Thicker layers typically require higher viscosity to maintain stability during casting. Despite the lower viscosity observed, it provided an optimal balance between flowability and stability during the casting process. This allowed for a smooth surface and uniform slurry spreading without issues like sagging or uneven coating. As a result, no further adjustments to solid content, binder concentration, or mixing conditions were necessary.

11.9.3. Determination of thickness and areal capacity, SG electrode

As discussed in the LFP section, reducing electrode thickness in LIBs shortens the conductive pathways, thereby lowering internal resistance. This reduction is an effective strategy for enhancing the power output of LIBs. In this research, the anodes were fabricated considering the parameters established for the LFP cathode. Among these parameters, the N/P ratio is the most critical for designing a Li-ion pouch cell.

The N/P ratio is crucial in determining the performance and lifespan of Li-ion cells. An optimal N/P ratio, typically between 1.1 and 1.18, ensures that the anode has a slightly higher capacity than the cathode. This balance helps prevent lithium plating on the anode during charging, a condition that can lead to cell degradation and safety hazards.

If the N/P ratio significantly exceeds 1.18, the excess anode capacity may result in unused lithium within the cell, reducing its energy density and efficiency. Conversely, if the N/P ratio falls below 1, the anode might become fully lithiated, increasing the risk of lithium plating, which accelerates cell degradation and reduces cycle life and safety. Based on these considerations, the SG electrode areal capacity must reach a minimum of 2.2 mAh·cm^{-2}.

Table 42 presents the areal capacity (mass loading) obtained at various thicknesses during the casting process. Given the minimum capacity requirement of 2.2 mAh·cm^{-2}, a thickness of 150 µm seems ideal for achieving the necessary capacity for cell design and assembly. The SG slurry formulation showed no operational issues during casting, maintaining stability and acceptable flowability. With the thickness determined, no further changes were made, and slurries S2 and S3 were prepared under the same conditions as S1, with the electrode coating thickness at 150·µm.

Table 42.   SG slurry S1 at various thicknesses and areal capacities obtained

SG S1	L1	L2	L3
Theoretical thickness (wet), (µm)	100	150	200
Loading thickness (dry), (µm)	49.2	65.4	97.0
Average weight (mg) (D = 12 mm = 1.131 cm^2)	23.72	25.16	27.53
Electrode loading (mg/cm^2)	5.06	6.33	8.42
AM content (%)	95	95	95
AM loading (mg/cm^2)	4.80	6.01	8.00
AM loading (mAh/cm^2)	1.79	2.24	2.98

Tables 43 and 44 display the characteristics of the electrode sheets produced. Notably, not all sheets reached the required capacity. These differences can be attributed to the manual thickness adjustment of Doctor Blade, which introduces variations that become evident when the electrodes are dry. Additionally, the rheological properties of the slurry allowed for homogeneous spreading across the current collector, resulting in a consistent thickness throughout the electrode. This consistency will simplify the next stage, the calendering process, and make the results more representative.

Table 43.   SG slurry S2 at various thicknesses and areal capacities obtained

SG S2	L1	L2	L3	L4
Theoretical thickness (wet), (µm)	150	150	150	150
Loading thickness (dry), (µm)	75.0	90.3	66.0	59.5
Average weight (mg) (D = 12 mm = 1.131 cm^2)	25.55	27.08	25.07	24.27
Electrode loading (mg/cm^2)	6.68	8.02	6.25	5.54
AM content (%)	95	95	95	95
AM loading (mg/cm^2)	6.34	7.62	5.94	5.26
AM loading (mAh/cm^2)	2.36	2.84	2.21	1.96

SG S3	L1	L2	L3	L4
Theoretical thickness (wet), (μm)	150	150	150	150
Loading thickness (dry), (μm)	64.2	72.2	76.9	76.7
Average weight (mg) (D = 12 mm = 1.131 cm^2)	25.70	25.85	25.87	26.03
Electrode loading (mg/cm^2)	6.81	6.94	6.96	7.10
AM content (%)	95	95	95	95
AM loading (mg/cm^2)	6.47	6.59	6.61	6.75
AM loading (mAh/cm^2)	2.41	2.45	2.46	2.51

Table 44.   SG S3 at various thicknesses and areal capacities obtained

Figure 50 summarizes the areal capacity obtained depending on the solid content in the slurry and the thickness of the electrode sheet dry.
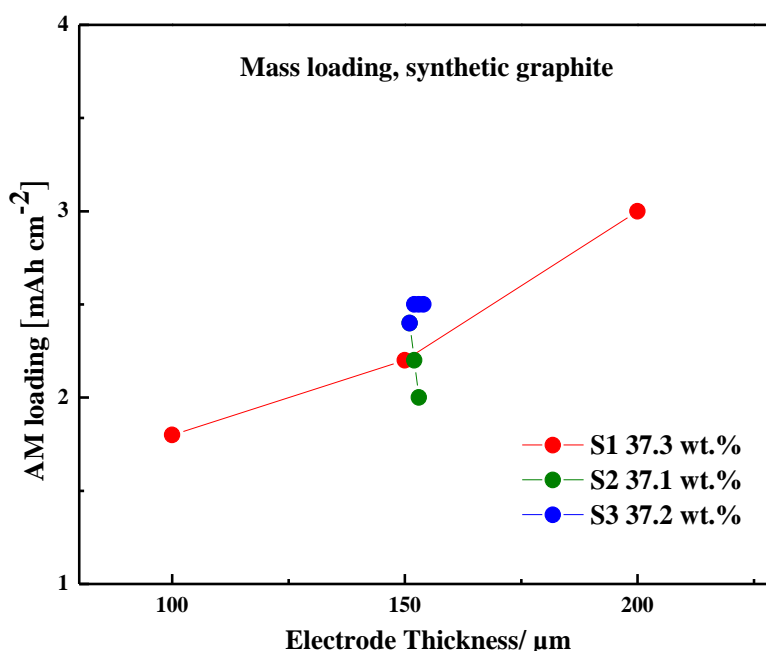
Figure 50. SG mass loading based on the solid content (wt.%) at various thicknesses of electrodes sheets

11.9.4. Scanning electron microscope (SEM) characterization of aqueous-processed SG electrodes, before and after calendering

This section describes the surface characterization of SG before and after calendering. Understanding the shape of the SG powder is crucial for analyzing its surface morphology. The SG used in this research has a flake-like shape, as shown in Figure 51. This shape may contribute to the absence of cracking as an optimum solid content these flakes-shape can ensure the homogeneous distribution of CMs and AMs in the slurry as it is seen in Figure 51.

However, when the solid content exceeds 40 wt.%, the slurry does not distribute evenly to the current collector. This uneven distribution is attributed to the shape of the SG flakes.

As the solid content increases, there is insufficient space for the flakes to spread, leading to agglomeration.
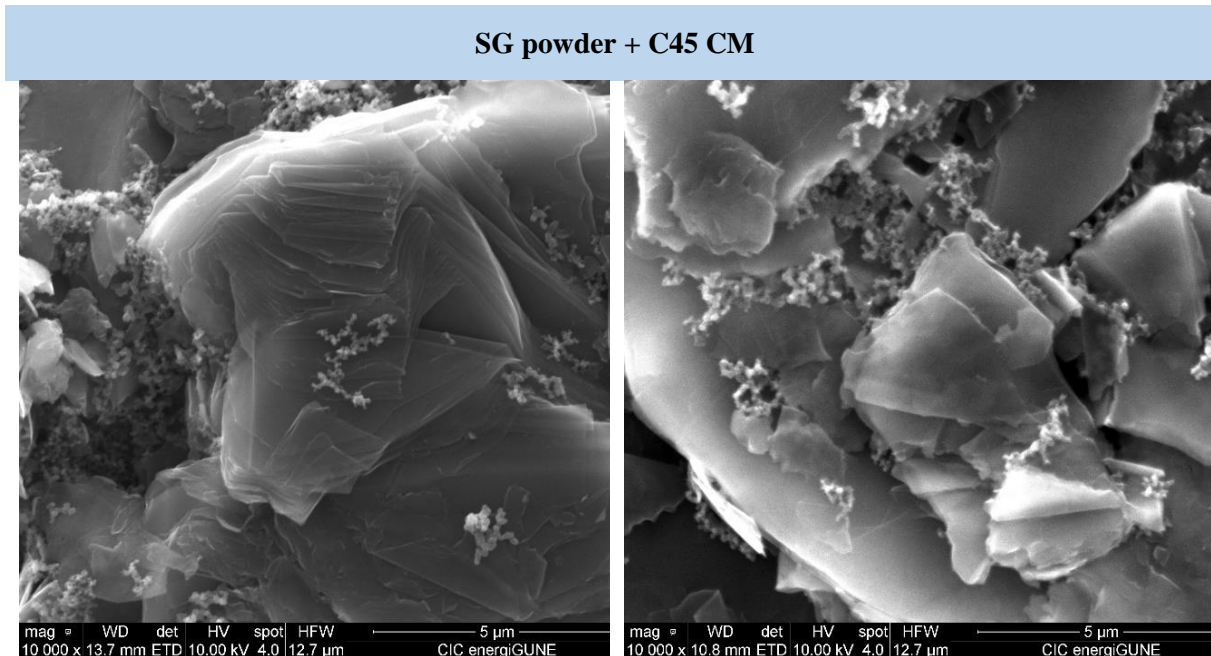
Figure 51. SG powder with C–45 surface characterization

Key parameters such as solid content, viscosity, and electrode thickness, discussed previously, directly affect cell performance. However, surface characterization is essential to determine whether these parameters have been optimally set or require further adjustment before proceeding with cell fabrication.

Similar to the LFP electrode fabrication, Scanning Electron Microscopy (SEM) was used for characterizing the SG electrodes. SEM provides detailed insights into the surface morphology and microstructure of the anode, revealing critical features like particle distribution, porosity, and defects such as cracks on the electrode surface.

This characterization step ensured the electrodes' reliability and effectiveness for cell performance and lifespan.

Figure 52 illustrates the surface of the SG electrode sheets from the S1 slurry, with thicknesses of L1 = 100 µm, L2 = 150 µm, L3 = 200 µm and the electrode S1 L2 calendered at 10% of the initial thickness electrode.

GRAPHITE - S1 L1, 300×	S1 L2, 300×

S1 L3, 300×	S1 L2 10%Cal, 300×
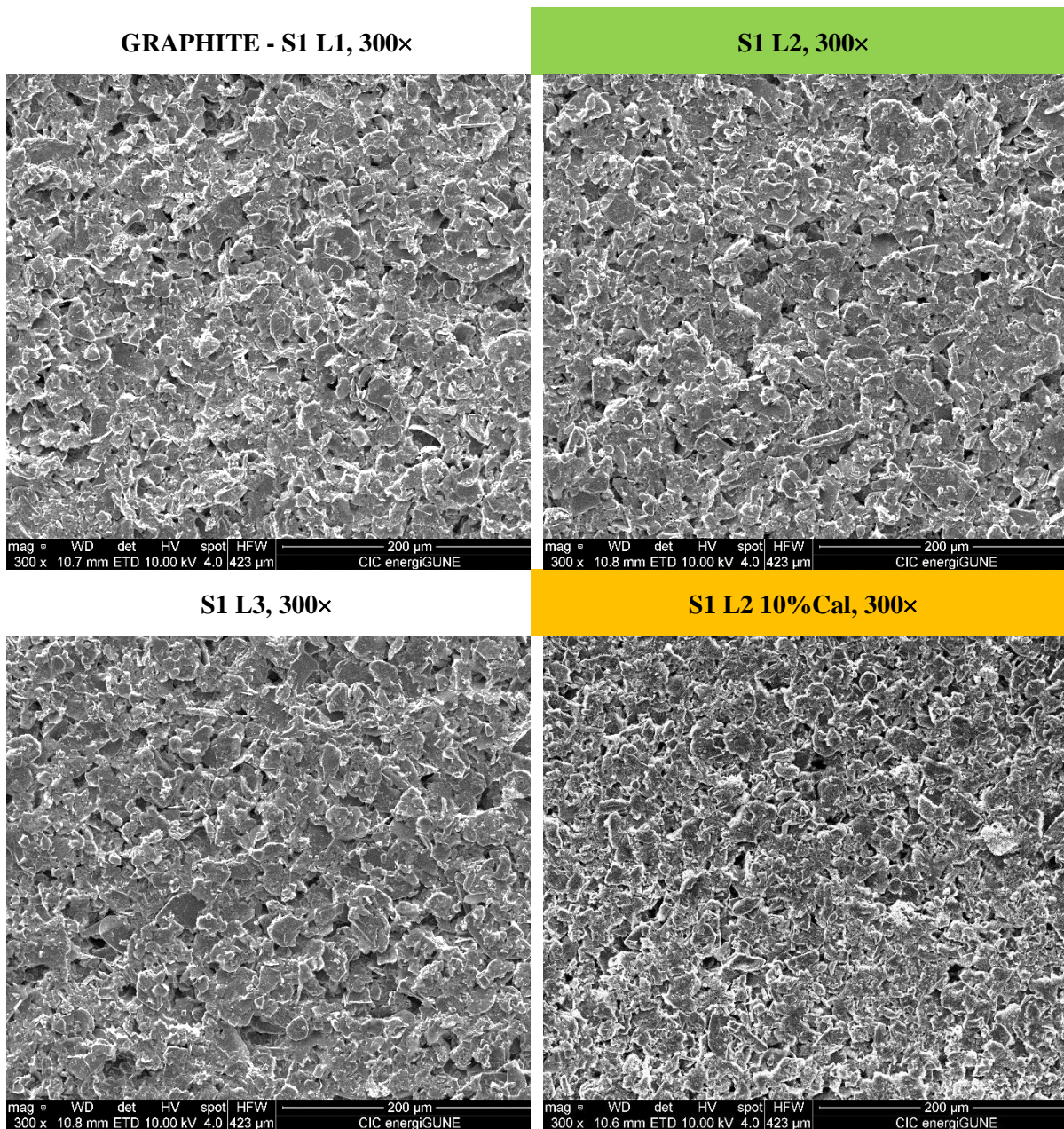
Figure 52. SG surface characteristics before and after calendering

Achieving a homogeneous and well-distributed SG electrode results from cautious adjustments during slurry preparation and coating.

The pH of the slurry was maintained within an optimal range (between 7.0 and 9.0), ensuring proper dispersion of graphite particles in the aqueous medium and preventing aggregation. Proper dispersion was found to be critical for evenly distributing the particles throughout the slurry, leading to a uniform coating on the electrode substrate. Additionally, using a compatible binder, such as CMC and SBR as an additive, which interacts effectively with the graphite particles at an acceptable range of pH, contributes to the electrode homogeneity by ensuring strong adhesion and even distribution of the particles.

Controlling slurry viscosity was also important, as it enables consistent application of the slurry onto the electrode surface, resulting in a smooth, uniform coating without defects like clumps or thin spots. These factors produce a well-distributed SG electrode with enhanced electrical conductivity and mechanical stability. Due to the desirable characteristics obtained under these parameters, no further adjustments were necessary for the SG electrodes fabrication.

11.9.5. Calendering process of SG electrodes

Calendering the SG electrode with a reduction in the range of 10 to 25 wt.% significantly enhances the electrode properties and performance. Overall, calendering with this level of reduction optimizes the balance between electrode thickness, mechanical strength, and electrical performance, leading to higher energy density and improved cell performance. Calendering was applied to the SG electrodes within the range of 10–25 wt.%, as described in Table 45.

Table 45.   Thickness reduced of the SG electrode after calendering

Calendering G S1	S1 _L2	S2_L1	S2_L3	S3_L1	S3_L2
Current collector (CC) foil thickness (μm)	18	18	18	18	18
Initial thickness without CC	62.50	90.25	66.00	64.25	72.25
Thickness after calendering without CC	56.00	55.00	49.50	49.75	57.75
% Thickness reduction	10.4	39.06	25.00	22.57	20.07

The electrode density and the areal capacity were calculated and detailed in Table 46.

Table 46.   SG density and areal capacity before and after calendering

Calendering	S1 L2o	S1 L2	S2 L1o	S2 L1	S2 L3o	S2 L3	S3 L1o	S3 L1	S3 L2o	S3 L2
Average thickness (μm)	80.5	74.0	108.25	73.0	84.0	67.50	82.25	67.75	90.25	75.75
Loading thickness (μm)	62.5	56.0	90.25	55.0	66.0	49.50	64.25	49.75	72.25	57.75
Coating density before/after calendering (g/cm^3)	1.01	1.19	0.74	1.25	0.94	1.28	1.06	1.31	0.96	1.16
Areal capacity / AM loading (mAh/cm^2)	2.24	2.36	2.36	2.43	2.19	2.24	2.41	2.30	2.45	2.37

Figure 53 presents the results of SG coating density and areal capacity before and after calendering. The coating density increased across all samples, exceeding $1.15 \ \text{g} \cdot \text{cm}^{-3}$. While

no optimal electrode density range was established, the primary goal was to achieve a minimum areal capacity of 2.2 mAh·cm^{-2} and ensure a uniform slurry distribution on the current collector, avoiding cracks before cycling the pouch cell.
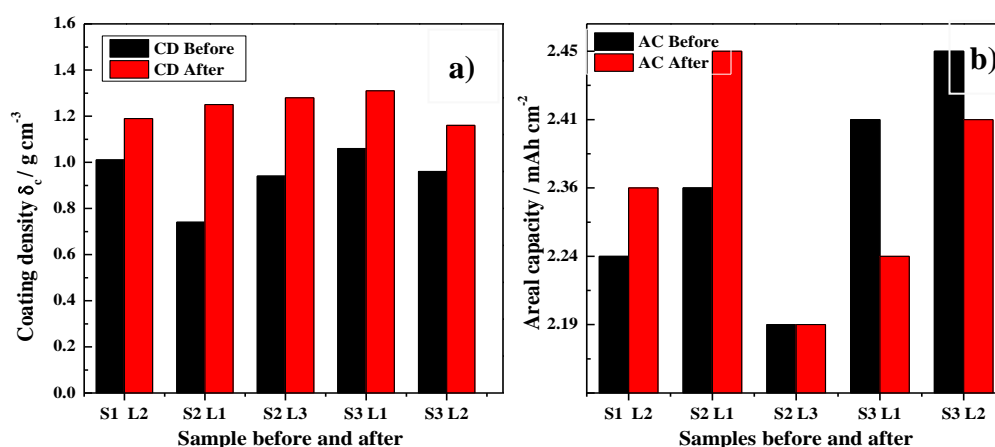
Figure 53. SG electrodes before and after calendering a) coating density and b) areal capacity over 2 mAh·cm^{-2}

However, the areal capacity exhibited unexpected behavior. For the first three samples, which experienced a thickness reduction of 10-30 wt.%, the areal capacity increased after calendering. Conversely, for samples with a thickness reduction of 20–22 wt.%, the areal capacity decreased after calendering. By compressing the electrode, calendering reduces thickness and can increase the concentration of AM per unit area, potentially raising areal capacity. However, excessive calendering can decrease electrode porosity, making it more difficult for the electrolyte to access the AM, thereby reducing lithium cation intercalation and, consequently, areal capacity. Given the lack of consistent behavior in areal capacity before and after calendering, the results for the slurry G S3 may be attributed to equipment-related issues, such as improper calibration.

11.9.6. Resistance evaluation before and after calendering SG electrode sheet

Table 47 and Figure 54 present the influence of the electrode thickness and the calendering stage on the electrode conductivity.

Table 47. Resistivities measured and conductivities calculated of SG at various thicknesses

G S1	$1/\kappa$ ($\Omega \cdot$ cm)	κ (S·cm^{-1})
L1	0.039	25.70
L2 -0%	0.042	23.54
L3	0.043	23.49
L2 -10%	0.039	25.70

The conductivity of SG electrodes increases after the calendering process primarily because calendering compresses the material, increasing its density and reducing porosity. This compaction brings graphite particles closer together, improving their contact and alignment, which facilitates more efficient electron transport. Additionally, calendering reduces microcracks and structural defects, further enhancing the conductivity by providing a more continuous path for electron flow.
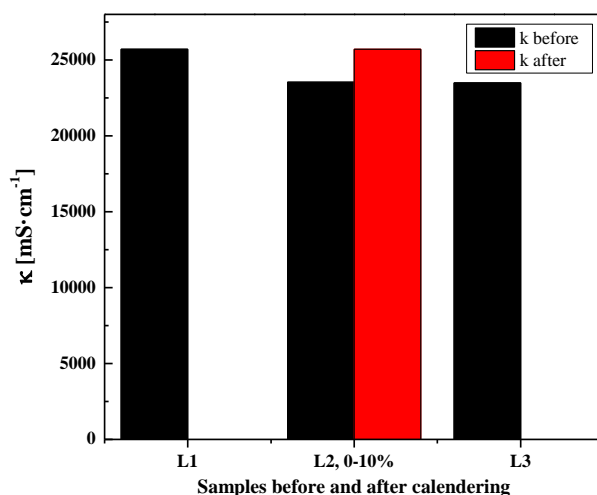
Figure 54. Conductivities of SG electrode at various thicknesses

Furthermore, when the thickness of the electrodes increases, conductivity tends to decrease because the electrons must travel through a longer path, which increases the overall resistance. Thicker electrodes often have higher internal resistance due to the increased likelihood of defects, non-uniform distribution of materials, and potential for less effective particle contact in the deeper layers. This greater resistance results in reduced overall conductivity, as the efficiency of electron transport diminishes with thickness.

11.9.7. pH measurements of anodes (SG and SOX) slurry preparation for electrode fabrication

This parameter is important as all the previous ones, however, for a better understanding this parameter is explained at the end of each section. The pH value of the slurry for anodes is important in the fabrication of aqueous-processed electrodes for LIBs, mainly because it affects the dispersion stability of the AM particles (SG and SOX) and the rheological properties of the slurry. Maintaining the pH within an optimal range, typically between 7.0 and 9.0, ensures that the AM particles remain well-dispersed in the aqueous medium, preventing aggregation or sedimentation.

This is essential because aggregated particles can result in uneven coatings on the electrode, leading to poor electrical conductivity and reduced electrochemical performance. Additionally, a stable pH within this range helps maintain the slurry viscosity, and a uniform electrode coating during the fabrication process.

Table 48.   pH measurements at various stages during SG and SOX slurry preparation

N°	Stage measurement	G_ S1	SOX_ S1	SOX_ S4	Stage description
A1	CMC (1%)	7.28	7.11	7.15	CMC solution
A2	SBR (40%)	7.95	--	7.88	SBR solution
C45	CMC + C45	7.46	7.54	7.51	CMC with C45-CB after 45 min of mixing
F	CMC + C45 + AM$_f$ + (SBR)	8.05	7.59	7.75	Final slurry after casting

Figure 55 represents the data detailed in Table 48, the effect of each material (CMs and AMs, binders) on the pH values at various stages during the SG and SOX preparation.
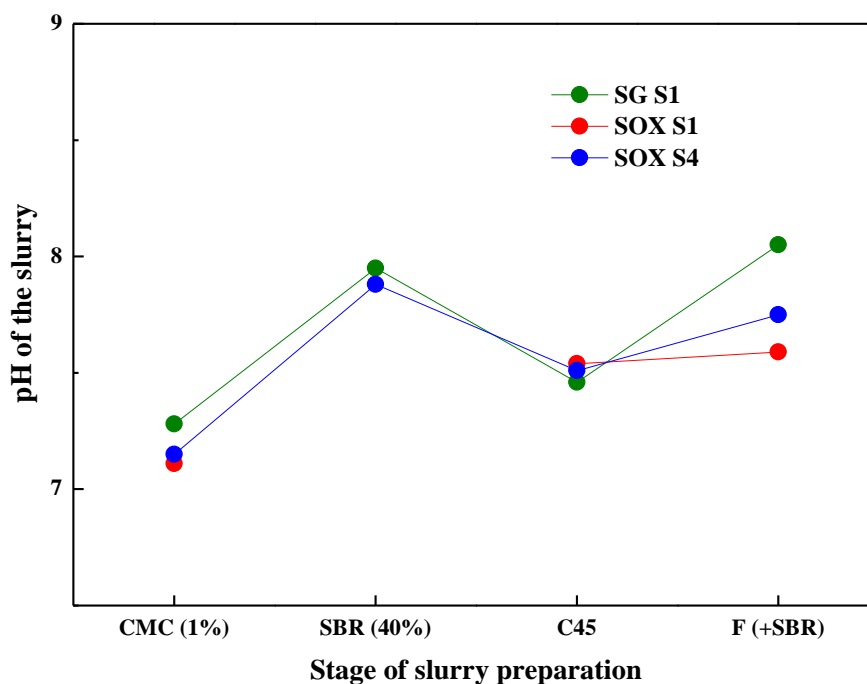
Figure 55. pH value at various SG and SOX composite slurry stages during electrode preparation

Moreover, the pH influences the interaction between the graphite, SOX particles and the binder, usually a water-soluble polymer like CMC. At a pH within the 7.0 to 9.0 range, the functional groups on the binder molecules are adequately ionized, promoting effective binding to the graphite particles.

If the pH deviates outside this range, it could disrupt this interaction, weakening the adhesion between the graphite particles and the binder. This can compromise the mechanical integrity of the electrode, leading to issues such as electrode delamination or cracking during the battery charge-discharge cycles.

Therefore, maintaining the pH within the stable range during slurry preparation is critical for ensuring the long-term performance and reliability of the LIB.

The pH value of anode slurries is often overlooked during battery fabrication, with the focus typically placed on the cathode due to its critical role in overall battery performance. However, controlling and maintaining the pH within a specific range for the anode is crucial for enhancing the entire cell efficiency and lifespan. A well-regulated pH can prevent several detrimental processes that degrade the anode and reduce battery life. For instance, at low potential, copper current collectors are prone to oxidation and dissolution, leading to copper ions migrating and plating onto the anode during recharging. This copper plating diminishes the anode permeability and fosters lithium plating, which is a key factor in capacity fading and the formation of internal short circuits.

Furthermore, improper pH levels can exacerbate the effects of over-discharge, accelerating the degradation of the anode material and promoting lithium plating. This lithium buildup not only degrades the anode but also significantly increases the risk of thermal runaway, a dangerous condition that can lead to battery failure. Therefore, maintaining an appropriate pH range in the anode slurry during the first stage of the electrode fabrication is essential to ensure the stability and safety of the battery, preventing the adverse effects that compromise performance and safety.

11.10. SOX electrode fabrication for pouch cells

This section as the previous ones focuses on the fabrication of SOX electrodes for fluorine-free Li-ion cells. The fabrication stages considered here are similar to those used for LFP and SG, as described previously. Specifically, this section details the following steps: slurry mixing at the temperature of 21°C, rheological property analysis, electrode thickness measurement and its influence on areal capacity, the calendering process, conductivity assessment before and after calendering, pH measurements during slurry preparation were reported in the previous section 11.9.7 (Figure 55), and surface characterization before and after calendering.

11.10.1. SOX slurry formulation

The SOX slurry was prepared at 21°C using a formulation similar to that employed in laboratory coin cell assembly. However, due to the need for higher viscosity, SBR was added as an additional component. The mixing process followed the same procedure as previous slurry formulations, with a few key adjustments.

Initially, a 1 wt.% CMC solution was combined with C45 CM working with a homogenizer, operating at 1500 rpm for 45 minutes. This step ensured a uniform distribution of the CM within the CMC solution. After this, the AM, SOX, was introduced and mixed at a speed of 1000 rpm for 90 minutes. This slower mixing speed facilitated the thorough incorporation of the SOX, promoting homogeneity in the slurry.

Subsequently, for the slurry SOX S4, SBR was added at a reduced speed of 300 rpm and mixed for 90 minutes. The reduction in mixing speed was a necessary precaution because SBR is prone to degradation under high shear rates.

To ensure the slurry consistency and remove any trapped air bubbles in the final slurry (degassing), an additional 60 minutes of mixing at 300 rpm was performed.

Tables 49 and 50 present the properties of the solid content and thickness of the slurry cast on the current collector. Table 49 specifically highlights the slurry prepared with only CMC. This formulation resulted in a low solid content, making the slurry difficult to work with due to its low viscosity.

Table 49. SOX S1 slurry composition, mixing time, thickness and solid content

Slurry composition: SOX S1		Calculated wt.%	Calculated (g)	Experimental (g)	Experimental %
Binder solution 1	1 wt.%		21.74	21.75	
Binder solution 2	40 wt.%		0.00	0.00	
CM	C45 (TIMCAL C-NERGY™ SUPER C45)	6.00	0.652	0.65	5.98
Binder 1	CMC (Sigma Aldrich) 1%	2.00	0.22	0.218	2.00
AM	SOX (MTI)	92.00	10.00	10.01	92.02
Binder 2	SBR (Arkema) 40%	0.00	0.00	0.00	0.00
Total		100.00	32.61	32.63	100.0
Operating conditions:					
Temperature = 21°C	Solid content = 33.6 wt.%	Total time = 195 (min)		Electrodes sheet thickness, L1 = 60 μm, L2 = 80 μm, L3=100 μm	

To address this issue, SBR was added for the slurry SOX S4 towards the end of the slurry preparation process as shown in Table 50, which increased the solid content in the slurry from 33.6 wt.% to 49.2 wt.%. This adjustment improved the slurry workability, making it more suitable for subsequent processes.

Table 50.   **SOX S4 slurry composition, mixing time, thickness and solid content**

Slurry composition: SOX S4		Calculated wt.%	Calculated (g)	Experimental (g)	Experimental %
Binder solution 1	1 wt.%		10.87	10.98	
Binder solution 2	40 wt.%		0.27	0.27	
CM	C45 (TIMCAL C-NERGY™ SUPER C45)	6.00	0.6522	0.65	6.02
Binder 1	CMC (Sigma Aldrich)	1.00	0.11	0.11	1.02
AM	SOX (MTI)	92.00	10.00	10.03	92.96
Binder 2	SBR (Arkema) 40%	1.00	0.11	0.00	0.00
Total		100.00	22.01	22.04	100.0
Operating conditions:					
Temperature = 21°C	Solid content = 49.2 wt.%	Total time = 255 (min)		Electrodes sheet thickness, L1 = 60 μm, L2 = 80 μm	

Both the CMC-only and CMC-SBR composite slurries were successfully cast onto copper current collectors without encountering any operational issues.

After drying the electrode sheets at room temperature and overnight in an oven, no cracking or other defects were observed. Since the slurry demonstrated the desired properties and stability, it was advanced to the next stages of research, including further evaluation for potential use in pouch cells.

11.10.2.   Rheological properties, SOX (SiO$_x$/C)

The rheological properties of the SOX slurries were studied at two different solid contents: 33.6 wt.% (containing only CMC) and 49.2 wt.% (containing a 1:1 ratio of CMC to SBR as shown in Figure 56. Both slurries exhibited similar behavior, with a slight shift towards higher viscosity observed in the slurry with 49.2 wt.% solid content.

Unlike SG, the viscosity of the SOX slurry remains relatively stable across a range of shear rates. This indicates that as the shear rate increases, the viscosity decreases only slightly, and this change is not as pronounced as it is for SG. For example, at a low shear rate of $0.1 \cdot s^{-1}$, the viscosity was measured at 1 Pa·s for the slurry with 33.6 wt.% solid content and increased to 20 Pa·s for the slurry with 49.2 wt.% solid content.

Similarly, at a high shear rate of $1000 \cdot s^{-1}$, the viscosity was 0.25 Pa·s for the 33.6 wt.% slurry and increased to 0.6 Pa·s for the 49.2 wt.% slurry.
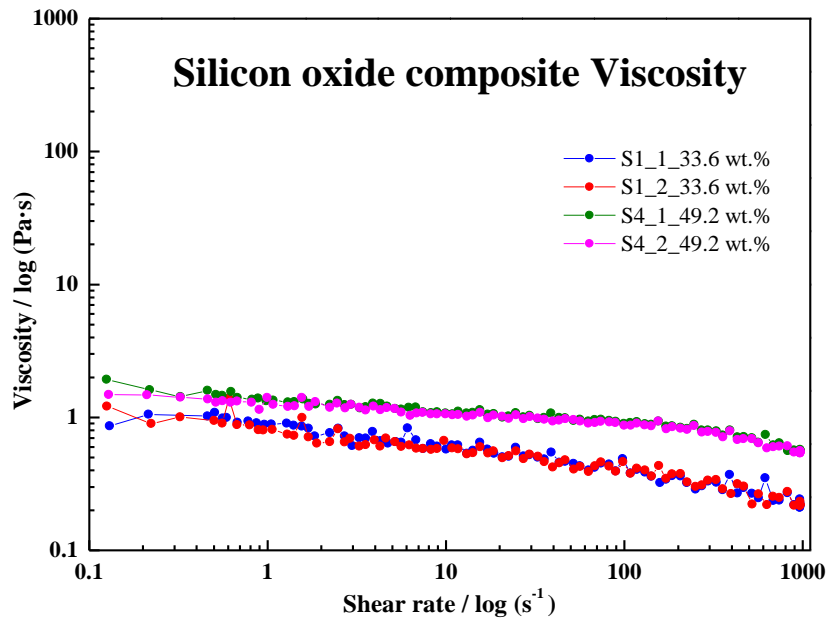
Figure 56. SOX slurry viscosity versus shear rate with their duplicate samples

This relatively stable rheological behavior can be attributed to the physical characteristics of the SOX material, which is predominantly spherical or elliptical in shape. Spherical and elliptical particles tend to flow more easily and maintain consistent interactions under varying shear rates, leading to less dramatic changes in viscosity.

In contrast, materials like SG, which may have more irregular or plate-like (flake-like) particle shapes, can experience significant changes in viscosity as the shear rate changes due to increased inter-particle friction and alignment effects.

The rheological behavior of the SOX slurry is influenced by particle shape, shear rate, and solid content. Therefore, the relatively stable viscosity of SOX contrasts with materials like SG, which often exhibit pronounced shear-thinning due to their more irregular or flake-like particle shapes that lead to increased inter-particle friction and alignment effects under shear. Additionally, the higher solid content (49.2 wt.%) increases viscosity due to the greater number of particle interactions and the presence of SBR, which adds elastic resistance to flow. These factors together result in a slurry that maintains consistent rheological properties, facilitating easier processing and uniform application of the slurry on the copper current collector on the casting stage.

Since this slurry possesses a relatively stable viscosity across the range of shear rates and slight shear-thinning behavior, it can be classified as a pseudoplastic fluid.

Pseudoplastic fluids are characterized by a decrease in viscosity with increasing shear rate, but in the case of the SOX slurry, this effect is relatively mild. The near-constant viscosity, particularly when compared to more pronounced shear-thinning materials like SG or LFP, suggests that the slurry does not undergo significant structural changes or particle alignment under shear, which is typical of pseudoplastic fluids. This type of fluid behavior is beneficial for the coating process, where consistent viscosity under various shear conditions is needed for uniform application on the current collector.

11.10.3. Determination of thickness and areal capacity, SOX electrode

Reducing electrode thickness shortens conductive pathways and lowers internal resistance. In this research, SG and SOX were fabricated with specific parameters designed to match the LFP cathode, with particular attention given to the N/P ratio.

Tables 51 and 52 present the areal capacities of SOX obtained at various thicknesses.

Table 51.   SOX slurry S1 at various thicknesses and areal capacities obtained

SOX S1	L1	L2	L3
Theoretical thickness, wet (μm)	60	80	100
Loading thickness, dry (μm)	25.4	39.2	47.6
Average weight (mg) (D = 12 mm = 1.131 cm^2)	21.26	23.12	23.84
Electrode loading (mg/cm^2)	2.88	4.53	5.16
AM content (%)	92	92	92
AM loading (mg/cm^2)	2.65	4.16	4.75
AM loading (mAh/cm^2)	1.33	2.08	2.38

Table 52.   SOX slurry S4 at various thicknesses and areal capacities obtained

SOX S4	L1	L2	L3
Theoretical thickness, wet (μm)	60	80	80
Loading thickness, dry (μm)	41.5	49.3	50.3
Average weight (mg) (D = 12 mm = 1.131 cm^2)	23.58	24.50	24.73
Electrode loading (mg/cm^2)	4.93	5.75	5.95
AM content (%)	92	92	92
AM loading (mg/cm^2)	4.54	5.29	5.48
AM loading (mAh/cm^2)	2.27	2.64	2.74

The N/P ratio, which ideally falls between 1.1 and 1.18 for commercial electrolytes, is crucial for maintaining a balance between the anode and cathode capacities.

To achieve the optimal N/P ratio, SOX electrode must reach a minimum areal capacity of ~2.2–2.4 mAh cm^{-2}, calculated using a theoretical specific capacity of 500 mAh g^{-1}.

The results show that the binder composition significantly influences the areal capacity of electrodes. At a 60 µm thickness, the areal capacity was 1.33 mAh·cm^{-2} when using only CMC as a binder. However, when a combination of CMC and SBR in a 1:1 ratio was used, the areal capacity at the same thickness increased substantially to 2.27 mAh·cm^{-2}. This trend was also observed at an 80 µm thickness as seen in Figure 57, highlighting the extraordinary impact of binder composition on areal capacity.
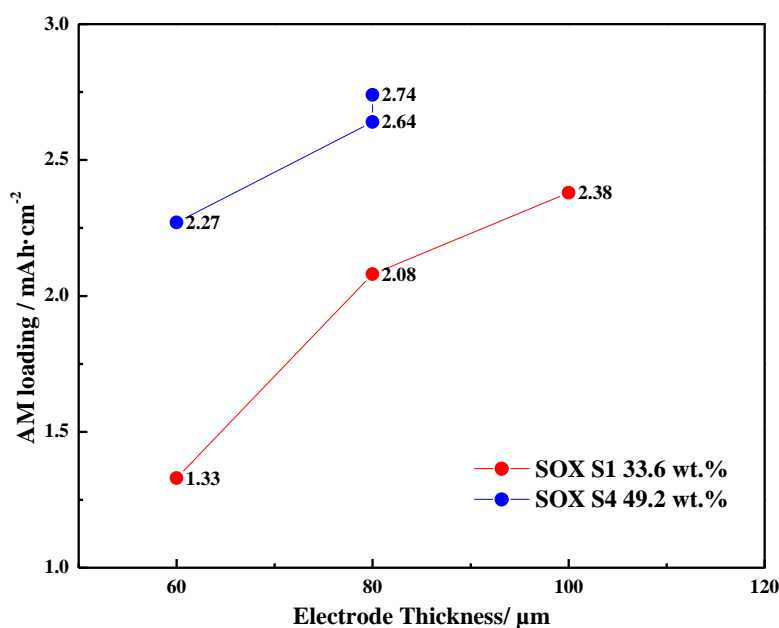
Figure 57. Areal capacity (mass loading) of SOX slurry at various electrode thicknesses and solid content in the slurry

Since the required minimum mass loading of 2.2 mAh·cm^{-2} was achieved, no further changes were required in the SOX slurry preparation stage. Future research will focus on optimizing the electrodes with the selected AM loading to enhance their performance.

11.10.4. Scanning electron microscope (SEM) characterization of aqueous-processed SOX anode, before and after calendering

Figure 58 presents the surface characterization of SOX powder that is mostly rounded, and/or elliptical. Exhibits smooth, well-defined contours with minimal angular features. The particles tend to be uniform in size, with some variations leading to the presence of slightly elongated or elliptical forms.

This morphology is advantageous for processes such as packing density and flowability, where uniform particle shape contributes to consistent performance.
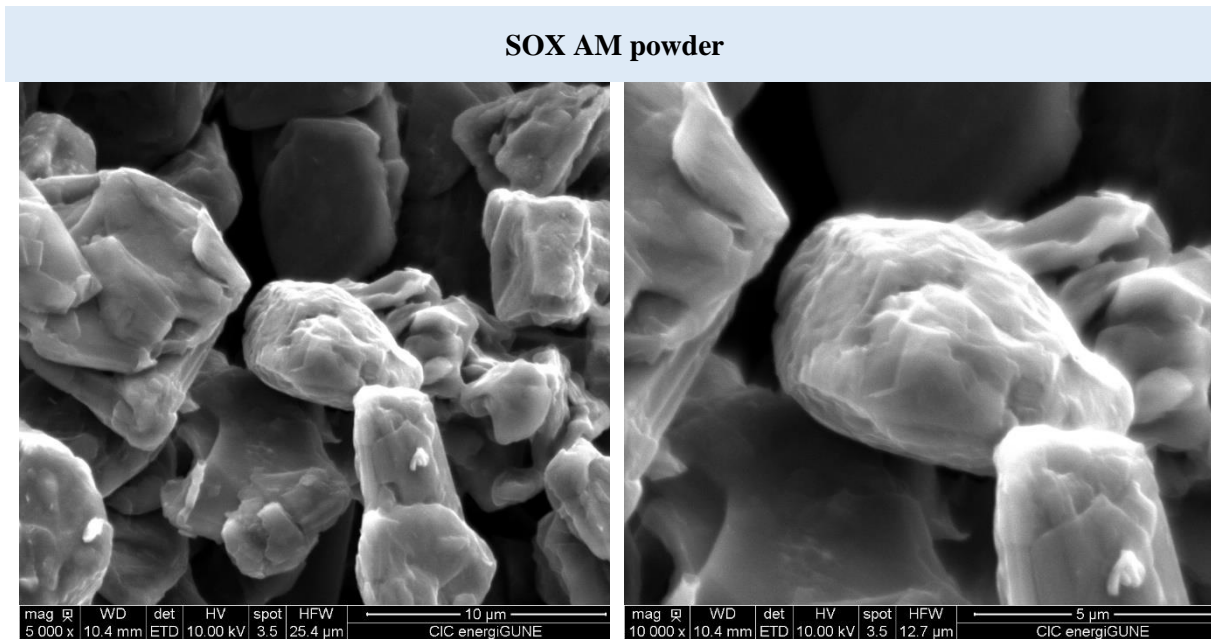
SOX AM powder

Figure 58. SOX AM powder

Figure 59 illustrates the surface of a SOX electrode at 80 µm (L2), 100 µm (L3), and the calendared electrode L2 up to 10% of thickness reduction. These electrode sheets were prepared with CMC as binder, and free from cracks after drying, were typically smooth and uniform. The CMC binder forms a cohesive matrix that evenly distributes the SiO_x particles, resulting in a well-integrated electrode structure. The absence of cracks indicates that the drying process was controlled to prevent stress accumulation in the material, which is crucial for maintaining the mechanical integrity of the electrode. This smooth surface promotes uniform contact with the electrolyte, which is essential for efficient ionic conduction and overall electrode performance.

Moreover, the smoothness and integrity of the surface contribute to the durability and cycling stability of the electrode in applications like LIBs. The even distribution of the binders ensures that the SiO_x particles are well-supported, reducing the likelihood of particle detachment or electrode degradation during repeated charge and discharge cycles. The binder ability to maintain a crack-free surface underlines its effectiveness in accommodating the volume changes associated with SiO_x, which is known for its significant expansion and contraction during lithiation and delithiation processes.

The surface of a SOX electrode, prepared with CMC binder and free from cracks after drying, is smooth and uniform, indicating well-distributed particles and a cohesive matrix. However, a stage of calendering was applied in case of the existence of micro cracking. The calendering process significantly enhances this surface by applying controlled pressure to compact the electrode, reducing its thickness, and improving particle-to-particle contact. This densification not only increases electrical conductivity by minimizing internal resistance but also ensures the surface remains free of fractures or cracks, leading to a more robust and durable electrode. The result is a well-integrated structure that maintains its integrity and the cell performance under various conditions.
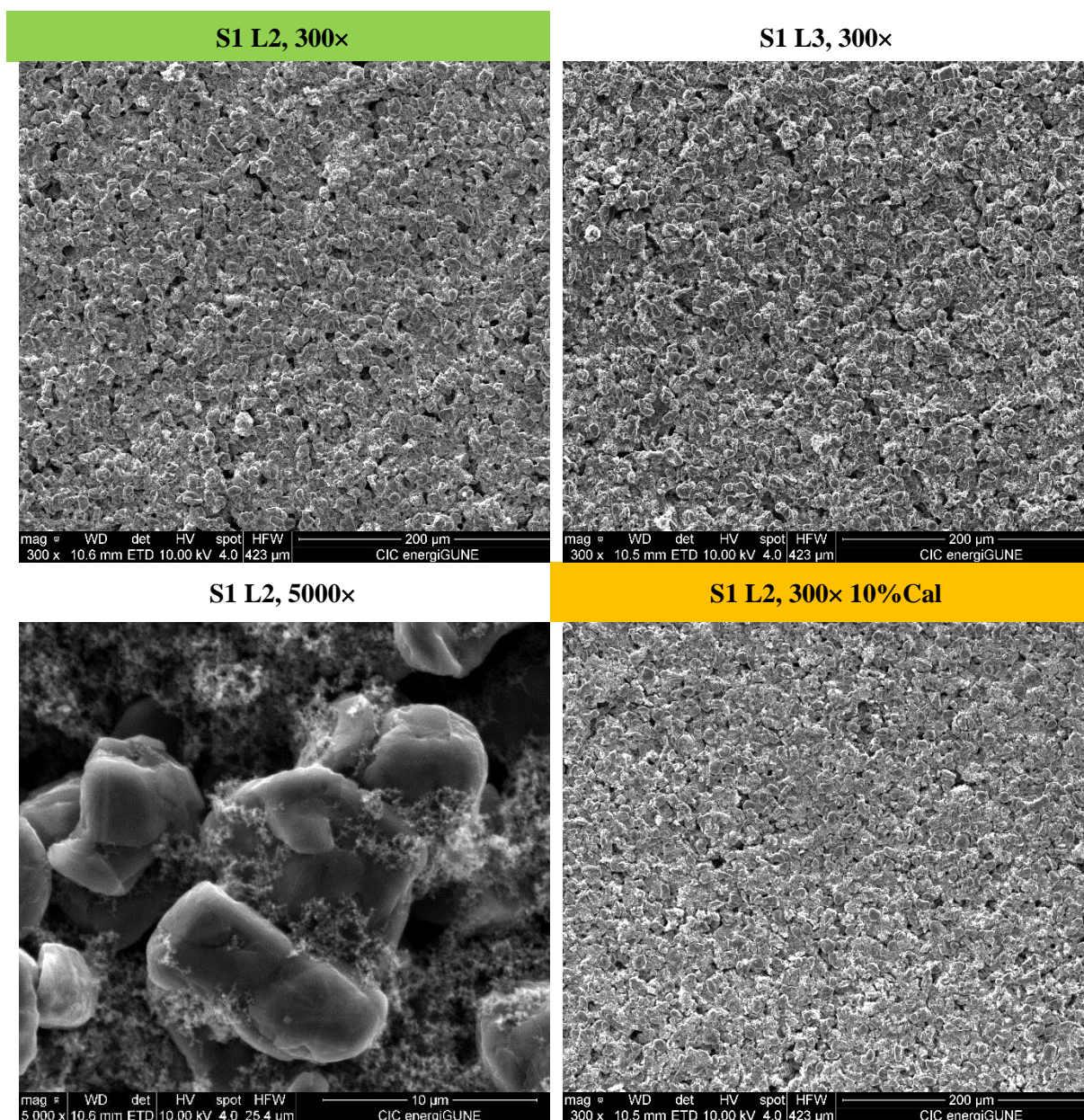
Figure 59. SOX electrode sheets before and after calendering

11.10.5. Calendering process of SOX anode

Tables 53 and 54 show that an areal capacity ~2.2 mAh·cm^{-2} was achieved at specific SOX electrode thicknesses. Consequently, further research was conducted to optimize these values and prepare them for use in pouch cell assembly. Table 53 illustrates the reduction in thickness after the calendering process, which ranged from 10% to 25%.

Table 53.   Thickness reduction after calendering for electrodes S1 and S4

Calendering	S1 _L2	S1_L3	S4 L1	S4 L2
Current collector foil thickness (µm)	18	18	18	18
Initial thickness without CC	39.20	47.60	41.50	49.25
Thickness after calendering without CC	32.00	35.75	37.25	42.25
% Thickness reduction	18.37	24.89	10.24	14.21

Table 54 shows the electrode density obtained after the calendering process. The electrode increase is significant, giving a percentage increase in the range of 10 to 15%.

Table 54.   Coating electrode density before and after calendering, S1 and S4

Calendering SOX	S1 L2o	S1 L2	S1 L3o	S1 L3	S4 L1o	S4 L1	S4 L2o	S4 L2
Initial thickness, wet (µm)	80	80	100	100	60	60	80	80
Loading thickness, dry (µm)	39.2	32.00	47.60	35.75	41.5	37.25	49.25	42.25
Average weight (mg) (D = 12 mm = 1.131 cm^2)	23.12	22.88	23.84	23.28	23.58	23.53	24.50	24.45
Electrode loading (mg/cm^2)	4.53	4.31	5.16	4.66	4.93	4.89	5.75	5.70
AM loading (mg/cm^2)	4.16	3.97	4.91	4.43	4.54	4.49	5.29	5.25
Coating density before/after calendering (g/cm^3)	1.15	1.35	1.08	1.30	1.19	1.31	1.17	1.35

The coating density obtained after the calendering process remained consistent, regardless of the solid content variations (S1 and S4), falling within the range of 1.30 – 1.35 g·cm^{-3}. This consistency can be attributed to the homogeneous slurry distribution on the current collector and during the slurry preparation.

Interestingly, while various thicknesses (60, 80, and 100 µm) and varying slurry formulations (CMC only, and a 1:1 ratio of CMC and SBR) significantly influenced the areal capacity, these parameters did not appear to affect the coating density.

Regardless of these results, calendering plays a crucial role in increasing the density of the SOX. By compressing the electrode material, calendering reduces its thickness, which compacts the AM particles more closely together. This densification enhances the electrode electrical conductivity and mechanical stability, improving the overall battery performance.

However, it is essential to balance this process to avoid excessive compaction, which could negatively impact the electrode porosity and the cell performance as a consequence.

Figure 60 presents the coating density difference before and after calendering,
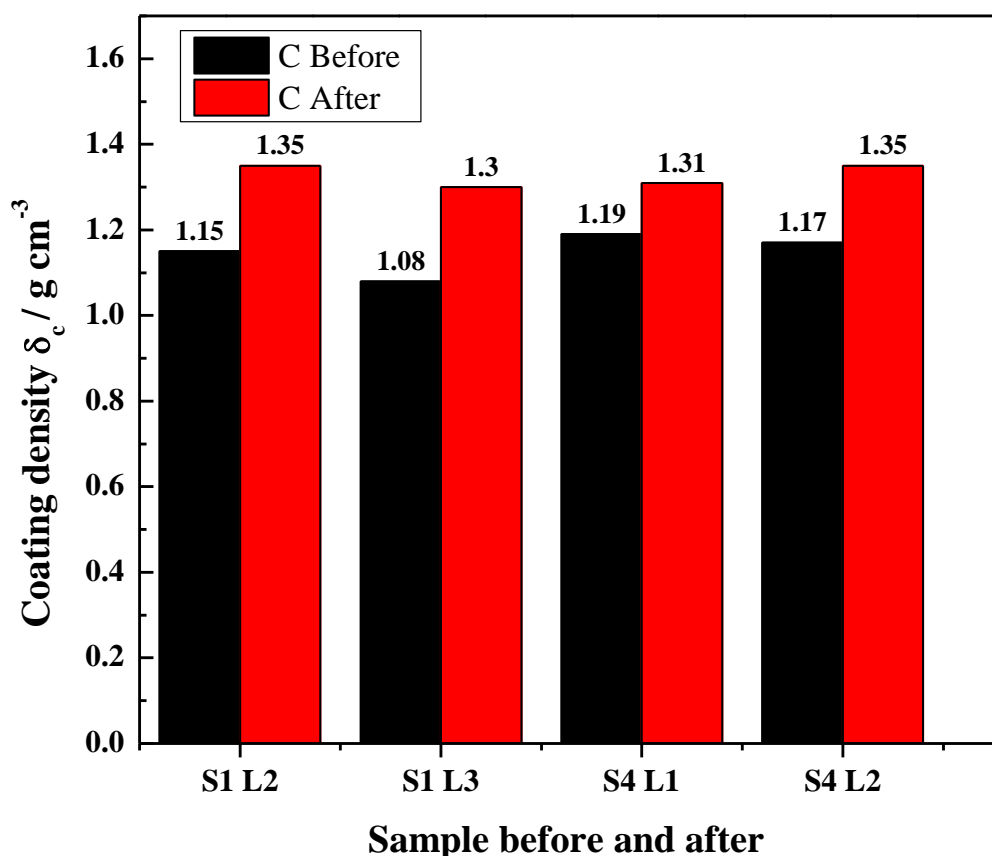
Figure 60. SOX density before and after calendering

The thickness of compression was in the range of 10 to 25% and it was based on findings [404], who observed that excessive compaction of the anode can increase diffusive resistance by reducing porosity, ultimately decreasing its capacity to store lithium cations effectively and leading to a lower areal capacity. Additionally, it found that moderate compaction improves the mechanical properties of the anode [406]. Specifically, it reduces plasticity, which enhances the anode's ability to manage reversible intercalation, thereby improving cycling stability.

11.10.6. Resistance evaluation of SOX anode before and after calendering

Table 55 and Figure 61 present the influence of electrode thickness and the calendering process on the electrode conductivity.

Table 55. Resistivities measured and conductivities calculated of SOX (S1) at various thicknesses

SOX S1	$1/\kappa$ ($\Omega \cdot cm$)	κ ($S \cdot cm^{-1}$)
L1 -60 μm	0.029	33.95
L2 -80 μm	0.044	22.75
L2 – 10%	0.027	37.36
L3 -100 μm	0.046	21.96

The conductivity of SOX electrodes increases after the calendering process primarily because calendering compresses the material (L2 – 10%), increasing its density and reducing porosity. This compaction brings SOX particles closer together, improving their contact and alignment, which facilitates more efficient electron transport. Additionally, calendering reduces microcracks and structural defects.
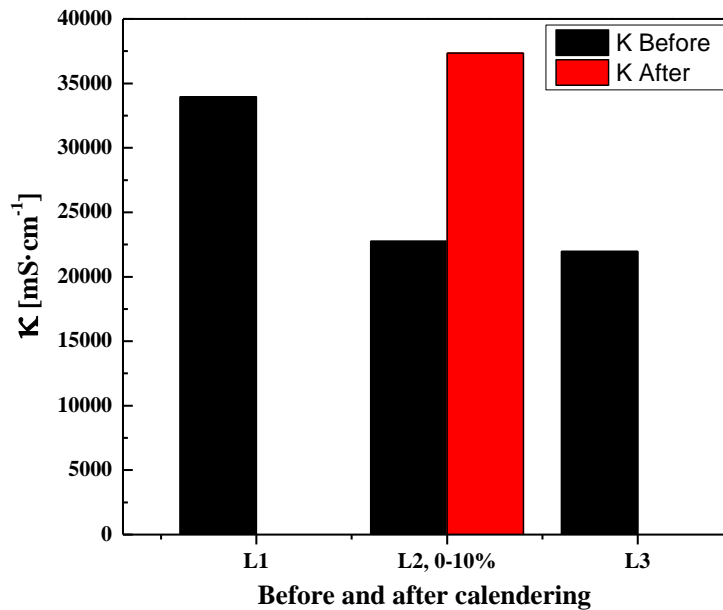
Figure 61. Conductivity of SOX at various thicknesses, before and after calendering

Likewise, when the thickness of the electrodes increases, the conductivity tends to decrease because the electrons must travel through a longer path, which increases the overall resistance. Thicker electrodes often have higher internal resistance due to the increased likelihood of defects, non-uniform distribution of materials, and potential for less effective particle contact in the deeper layers. This greater resistance results in reduced overall conductivity, as the efficiency of electron transport diminishes with thickness.

11.11. Electrochemical characterization of fluorine-free pouch Li-ion cells

This section of the PhD research focuses on the evaluation of specific capacities and coulombic efficiencies for LFP/SG and LFP/SOX coin cells and the effect of the N/P ratio on their performance. The investigation aimed to determine the performance of these aqueous-processed electrode materials with a novel fluorine-free electrolyte, LiPCP. Additionally, the study examined the scalability of these aqueous-processed electrodes, transitioning from coin cells to pouch cells, with optimized electrodes fabricated.

11.11.1. LFP/SG and LFP/SOX, two-electrodes configuration, pouch cells

Figure 32 (shown in section 11.7) illustrates the specific capacity and coulombic efficiency of LFP/SG and LFP/SOX cells tested at various rates. This comparison highlights the performance characteristics of the novel fluorine-free electrolyte, LiPCP, and its compatibility with these materials. The C-rate capability study in coin cells demonstrated promising cycling stability, encouraging further testing, upscaling to pouch cells. The transition from coin cells to pouch cells was a critical step toward validating the scalability of these optimized aqueous-processed electrodes for practical applications.

Figure 62 illustrates the cycling stability of the LFP/SG pouch cell, tested at a C/10 rate in LiPCP electrolyte with a mixture of EC:DMC (30:70 wt.%) and 5 wt.% VC, for two different N/P ratios, showing the influence of this factor on the cell performance.
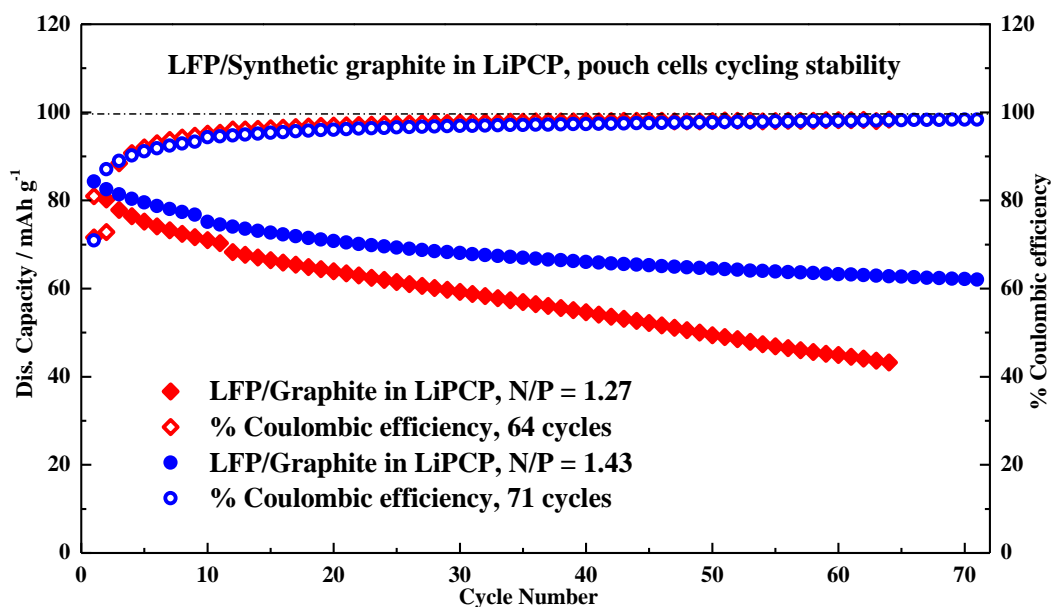
Figure 62. Cycling stability and coulombic efficiency of LFP/SG pouch cell with a N/P ratio equal to 1.27 and 1.43

Effect of N/P ratio on pouch cell performance, the N/P ratio, or the balance between negative (anode) and positive (cathode) electrode capacities, plays a significant role in the performance and stability of Li-ion cells. Previous studies with $LiPF_6$-based electrolytes have established an optimal N/P ratio range between 1.1 and 1.2. However, it was unclear whether this range is applicable to new electrolytes like LiPCP. Therefore, the effect of the N/P ratio on cell performance was examined at higher ratios than the established range.

Initially, an N/P ratio of 1.18 was used to assemble the full cells for the LFP/SG, coin cell configuration. This yielded an average specific capacity of 60 $mAh \cdot g^{-1}$ at a C/10 rate, with a coulombic efficiency around 90%. However, the influence of varying the N/P ratio on cell performance remained unclear. Given the importance of maintaining a ratio greater than 1.0 for systems using graphite anodes, lower ratios were excluded from this research.

The investigation focused on testing two different N/P ratios higher than 1.1. Thus, 1.27 and 1.43 N/P ratios were studied, which exceeded the traditionally accepted range. The performance of the LFP/SG pouch cells with these ratios was recorded, and the results deviated from initial expectations.

At an N/P ratio of 1.27, the cell exhibited a more rapid capacity fading than anticipated. The specific capacity dropped from 71.6 $mAh \cdot g^{-1}$ in the first cycle, with a coulombic efficiency of 81%, to 43.21 $mAh \cdot g^{-1}$ by the 64th cycle, though the coulombic efficiency improved to 98.32%. This decline in capacity indicates a significant deterioration in the cell ability to maintain consistent lithium extraction and insertion during cycling.

In contrast, the N/P ratio of 1.43 demonstrated more favorable results. The initial specific capacity started at 84.36 $mAh \cdot g^{-1}$ with a coulombic efficiency of 70.95%, and after 64 cycles, the capacity stabilized at 62.86 $mAh \cdot g^{-1}$, with a coulombic efficiency of 98.2%. Notably, the coulombic efficiency on both cases improved steadily after the third cycle, eventually exceeding 90%.

The study highlighted two key findings regarding the N/P ratio impact on cell performance. First, at a higher N/P ratio of 1.43, the initial capacity was significantly greater, and even after 64 cycles, the specific capacity remained above 60 $mAh \cdot g^{-1}$. This could be attributed to the properties of the LiPCP electrolyte, which, although it has slightly lower conductivity compared to $LiPF_6$, may require additional time to fully permeate the electrode surfaces, allowing for better lithium extraction and insertion over the charge/discharge cycles.

Second, the larger areal capacity of the anode with the higher N/P ratio likely enhanced lithium transport through the electrodes, leading to the formation of a more stable SEI layer. This may explain why the higher N/P ratio did not negatively affect cell performance. In fact, the study suggests that under these specific conditions, an N/P ratio of 1.43 is acceptable and could offer improved stability compared to lower ratios. These findings challenge the assumption that the ideal N/P ratio range for $LiPF_6$ (1.1 to 1.2) is directly applicable to novel electrolytes. Showing that higher N/P ratios may be better suited for LiPCP-based cells, although further studies are needed to confirm the long-term implications of these results.

Charge/discharge curve analysis

Figures 63 and 64 presents the charge/discharge curves for the two-cell configuration using LFP/SG at N/P ratios of 1.27 and 1.43, respectively. At an N/P ratio of 1.27, the charge/discharge curves show a significant and continuous reduction in capacity with each cycle, supporting the earlier observation of faster capacity fade. In contrast, the curves for the cell with an N/P ratio of 1.43 exhibit more gradual capacity reduction, maintaining a capacity above 60 mAh·g^{-1}, while the coulombic efficiency remains consistently high at over 98%.
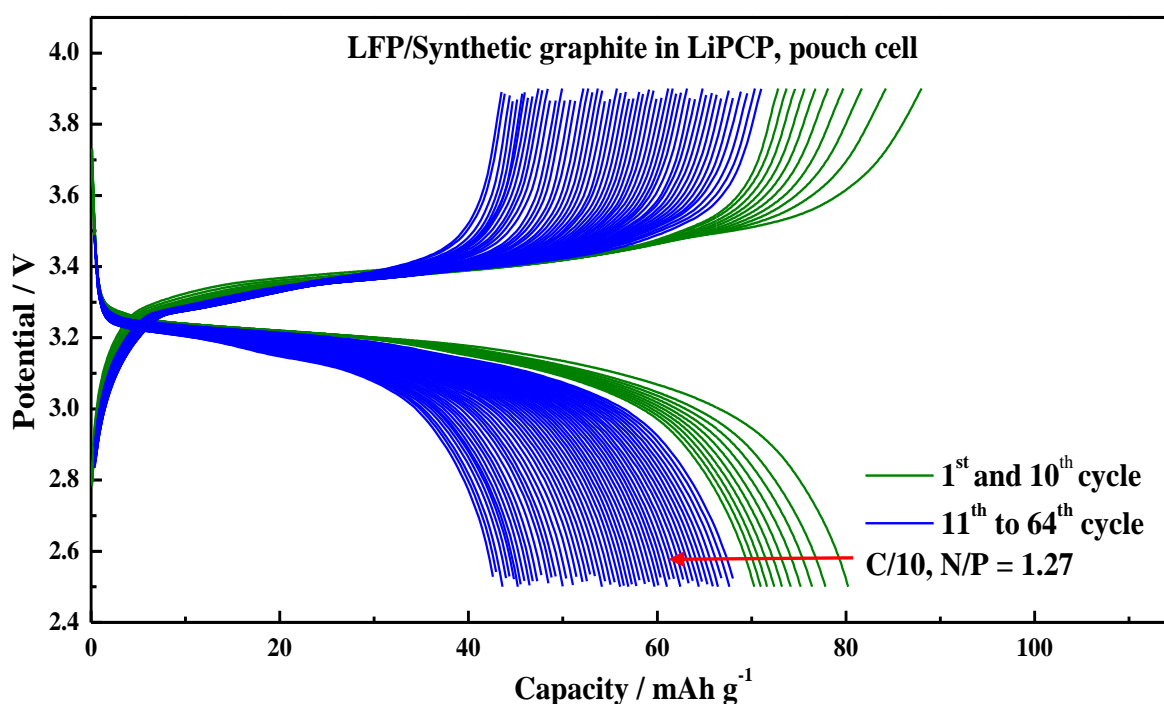
Figure 63. Charge/discharge curves of LFP/SG with an N/P ratio equal to 1.27

These results suggest that while both N/P ratios exhibit some degree of capacity degradation, the higher ratio (1.43) offers better long-term stability and performance.

This could be crucial for the development of more efficient and stable Li-ion cells with fluorine-free electrolytes.
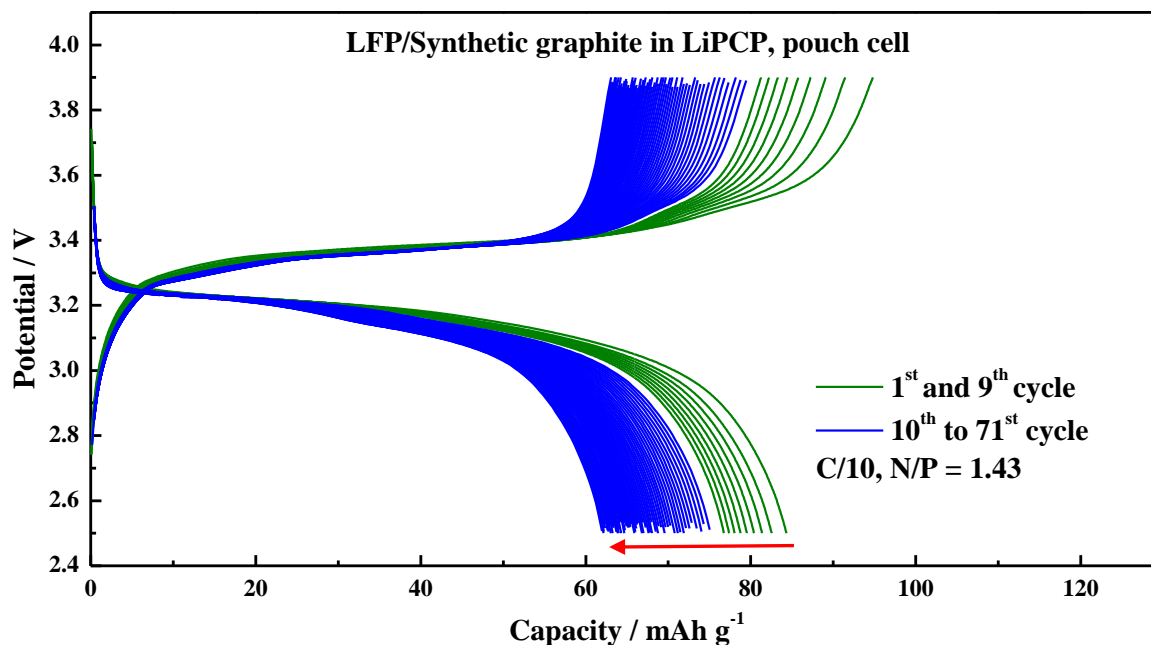
Figure 64.   Charge/discharge curves of LFP/SG with a N/P ratio equal to 1.43

Summarizing, the analysis of the N/P ratio effect on cell performance revealed that ratios outside the conventional range may offer unexpected benefits when using novel electrolytes like LiPCP. While an N/P ratio of 1.27 led to rapid capacity fading, a higher ratio of 1.43 resulted in better capacity retention and higher initial specific capacity.

These findings highlight the need to reconsider the established N/P ratio range when working with new electrolyte formulations, as their physicochemical properties differ from traditional systems such $LiPF_6$.

Future research should explore the optimal N/P ratio for various fluorine-free electrolytes, including the whole fluorine-free Li-ion cell to maximize cell efficiency and stability. This investigation lays the groundwork for further studies aimed at improving Li-ion cell performance through electrolyte and electrode design and fabrication.

This section presents findings on the performance of LFP/SOX cells, expanding the study from coin cells to pouch cells. Figure 32 (Section 11.7) illustrates the cycling stability of the proposed systems at varied rates, using an N/P ratio of 1.12. The cells demonstrated an average specific capacity of 40 mAh·g^{-1}, with an average coulombic efficiency of 90%. These results indicate the compatibility and stability of the LFP/SOX system when working with LiPCP-based electrolyte in coin cells. This lays the foundation for scaling up to pouch cells for further research.

Figure 65 provides insights into the cycling stability of the LFP/SOX pouch cell, tested at a C/10 rate in a LiPCP electrolyte solution consisting of EC:DMC (30:70 wt.%) and 5 wt.% VC. The cells were tested at two slightly different N/P ratios, 1.20 and 1.21, which showed subtle variations in performance. While the difference in the N/P ratios was minor, the impact on capacity fade was noticeable. Cells with an N/P ratio of 1.20 experienced faster degradation, with the specific capacity dropping from 86.8 mAh·g^{-1} (coulombic efficiency of 13%) at the first cycle to 14.3 mAh·g^{-1} (coulombic efficiency of 94%) by the 75th cycle. By the 102nd cycle, the capacity had further declined to 11 mAh·g^{-1} (coulombic efficiency of 94.6%). The coulombic efficiency was higher than 80% after the 5th cycle and higher than 90% after the 20th cycle, but lower than 95%.

In contrast, cells with an N/P ratio of 1.21 exhibited a slower fading capacity. The specific capacity decreased from 73 mAh·g^{-1} (coulombic efficiency of 50.3%) at the first cycle to 22 mAh·g^{-1} (coulombic efficiency of 95%) by the 75th cycle. It is worth noting that both samples underwent the same cycling duration, but the cell with an N/P ratio of 1.20 completed more cycles due to its accelerated degradation. This suggests that while the N/P ratio affects cell performance, the differences in the two ratios are minor, and other factors may be contributing to the observed variations. Therefore, deeper analysis is required to understand this behavior.

Table 43 provides additional data, highlighting specific characteristics of cells CL_PC_007 (N/P = 1.20) and CL_PC_011 (N/P = 1.21). The areal capacity for both the anode and cathode in PC_007 (5.06 and 2.11 mAh·cm^{-2}) was lower than that of PC_011 (5.46 and 2.26 mAh·cm^{-2}). This difference during the cell assembly could significantly influence cycling stability performance. Other than this, all remaining parameters between the cells were identical, implying that the superior performance at a 1.21 N/P ratio can be attributed to the higher areal capacities of the electrodes.
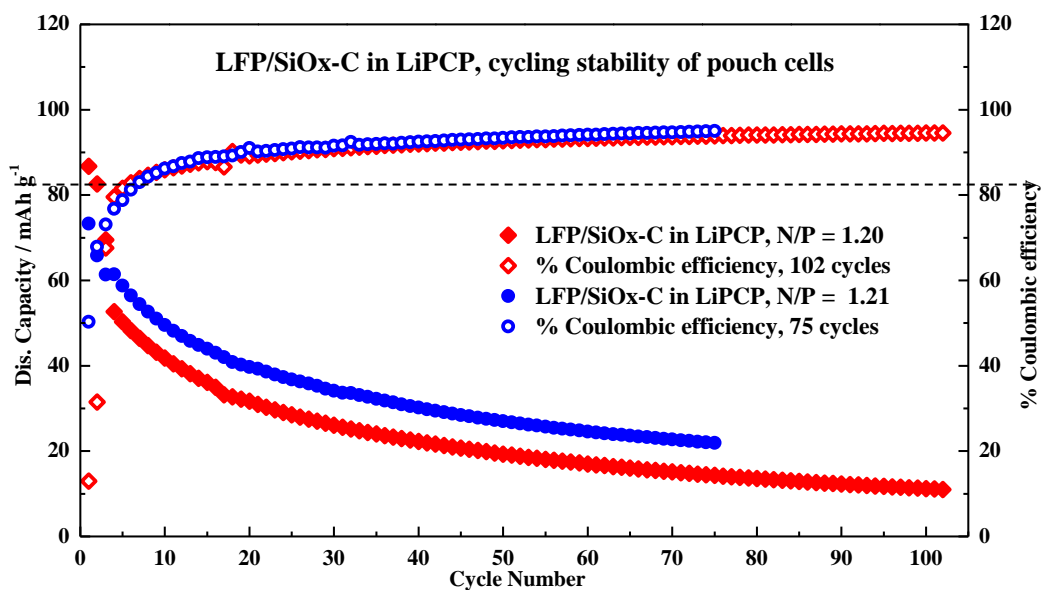
Figure 65. Cycling stability and coulombic efficiency of LFP/SOX pouch cell with a N/P ratio equal to 1.20 and 1.21

Figure 66 presents the charge/discharge curves for the full cell with a 1.21 N/P ratio. The plot reveals rapid capacity fading during the initial cycles, followed by a more gradual decline. This fading can be attributed to the pulverization of the AM, as evidenced by Figure 75, which depicts damage during the lithium extraction/insertion process. Such behavior is commonly expected with the inclusion of silicon in the composite. Despite the uniform and crack-free surface observed on the electrode surface before cycling, further research is required to optimize electrode fabrication and enhance long-term performance.
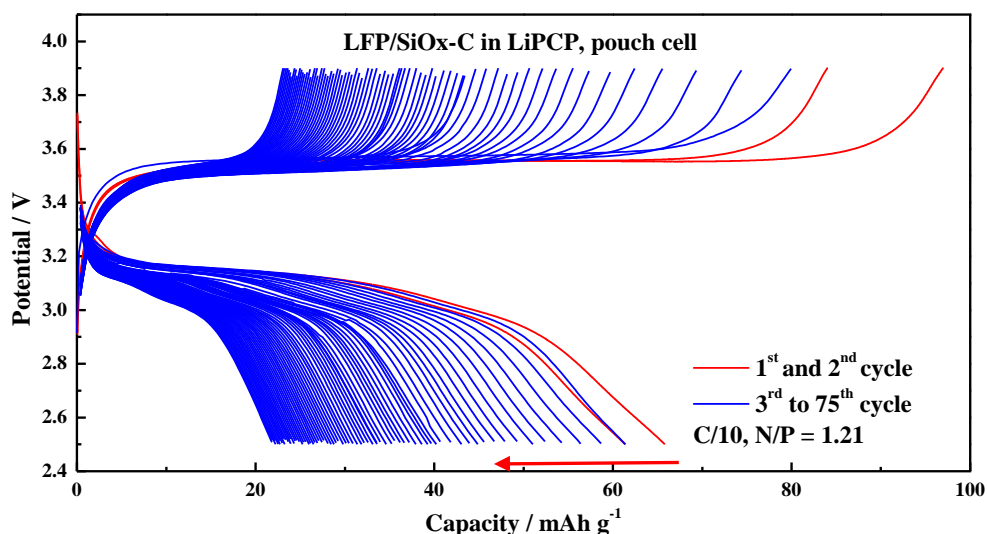
Figure 66. Charge/discharge curves of LFP/SOX with a N/P ratio of 1.21

11.11.2. LFP/SG and LFP/SOX, three-electrodes configuration, pouch cells

The three-electrode cell configuration plays a critical role in the study and optimization of LIBs, providing a precise method to measure the electrochemical performance of individual components, particularly the working and counter electrodes. In this setup, the working electrode (LFP) is paired with a counter electrode (SG), while a lithium metal electrode serves as the reference. The use of a reference electrode allows for independent monitoring of the potential of both the working and counter electrodes, thus enabling more accurate assessments of the electrochemical processes. This approach provides insight into the electrochemical behavior of each electrode without interference from the other, which is essential for understanding degradation mechanisms, optimizing materials, and improving overall cell performance.

Figure 67 presents the first and second cycle at 1.23 and 1.07 N/P ratio of the LFP/SG and lithium metal as reference electrode, pouch cell configuration.
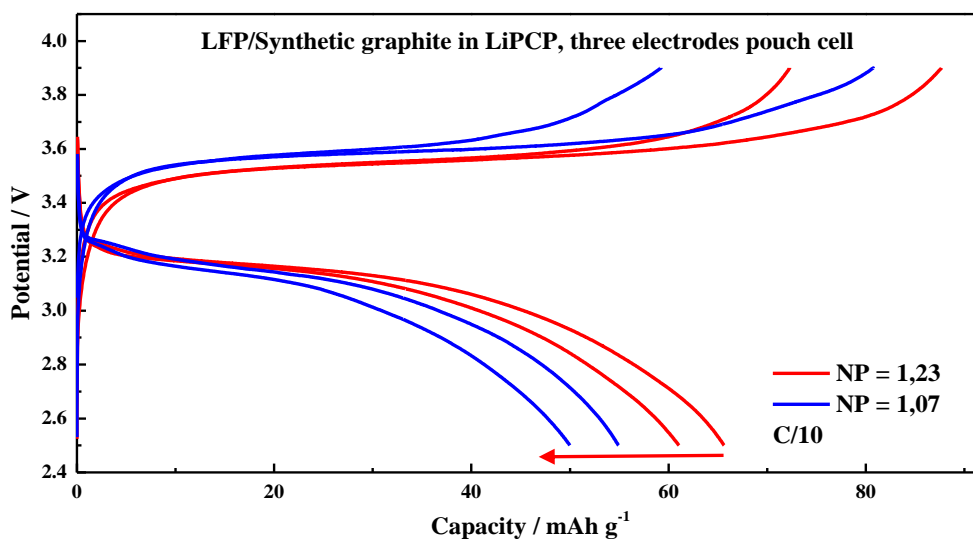
Figure 67. Charge/discharge curves of LFP/SG with a N/P ratio equal to 1.23 and 1.07, three-electrodes configuration, pouch cell

The N/P ratio significantly impacts the performance of Li-ion cells, especially in three-electrode configurations. A balanced N/P ratio ensures that both electrodes operate within their optimal potential ranges, minimizing degradation processes such as lithium plating on the anode or overcharging of the cathode. A low N/P ratio in LIBs leads to overutilization of the negative electrode, increasing the risk of lithium plating, while a high N/P ratio may result in inefficient use of the positive electrode.

Therefore, carefully adjusting the N/P ratio is crucial for optimizing cycling stability and maximizing the specific capacity of both electrodes. However, the ideal N/P ratio for cell assembly is not fixed and can vary depending on factors such as the electrolyte composition. In this study, under the given conditions, an N/P ratio of 1.23 exhibited higher capacities in the initial cycles compared to a ratio of 1.07 (see Figure 67).

Figure 68 presents the potential versus time profile for a three-electrode system, where a potential drop below zero is observed for both N/P ratios. However, this drop is more pronounced at an N/P ratio of 1.07 compared to 1.23 (see Figure 69).
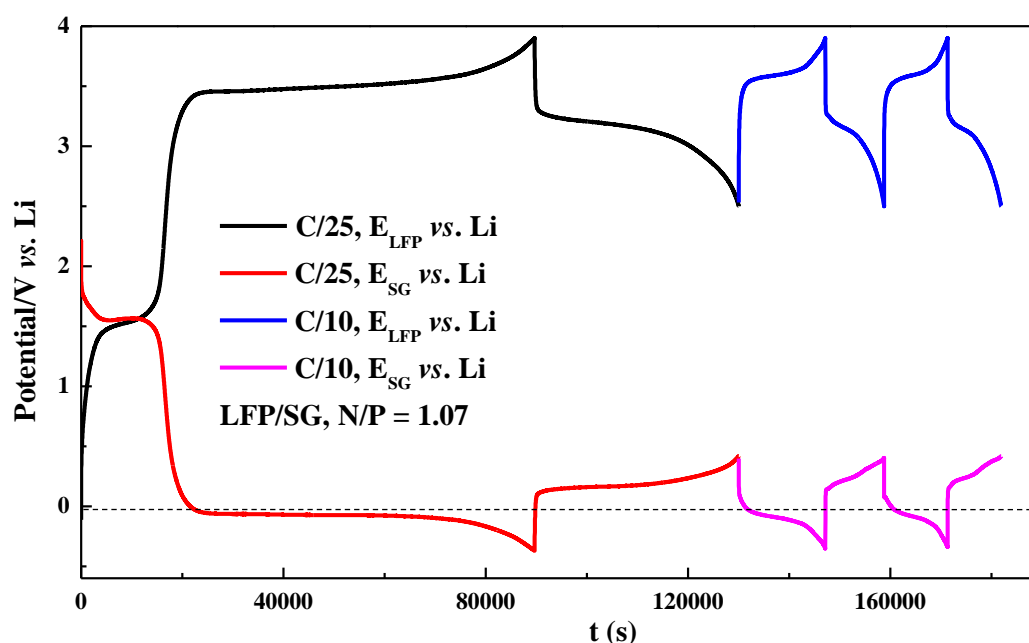
Figure 68. Time (s) vs. potential (v) of LFP/SG with a N/P ratio equal to 1.07, three-electrodes configuration, pouch cell

When the potential of the counter electrode (SG) drops below zero, it implies excessive polarization, bringing the electrode close to the reduction potential of the electrolyte. This suggests that lithium intercalation is occurring, but it also raises the risk of lithium deposition on the graphite surface, especially if the electrolyte is unstable at these low potentials. Lithium plating can lead to several issues, including dendrite formation, which poses safety risks like short circuits and significantly degrades the cell performance over time.

The N/P ratio plays a critical role in mitigating the risks associated with potentials dropping below zero. As shown in Figure 68, the cell configuration with an N/P ratio of 1.07 exhibited a potential below zero for nearly the entire discharge process, indicating severe overutilization of the negative electrode.

208

Figure 69 illustrates the performance of the same cell configuration with a slightly higher N/P ratio of 1.23. While the potential still dipped below zero, it occurred later in the discharge process and was less severe than with the lower N/P ratio. This highlights the importance of fine-tuning the N/P ratio to prevent excessive polarization and lithium plating.
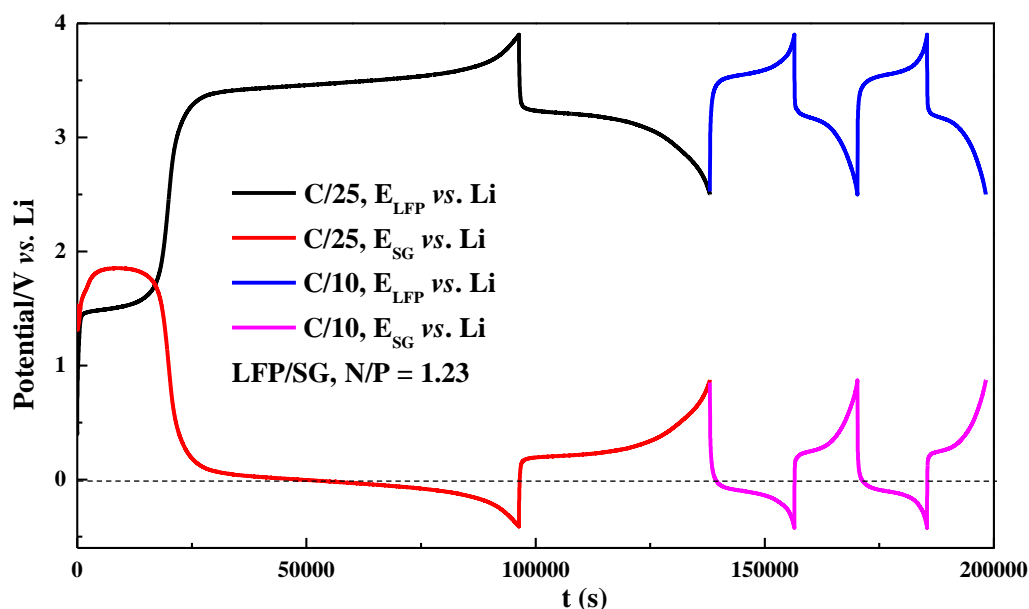
Figure 69. Time (s) vs. potential (v) of LFP/SG with a N/P ratio equal to 1.23, three-electrodes configuration, pouch cell

The behavior of individual electrodes in a three-electrode cell configuration provides valuable insight into battery performance, allowing researchers to optimize both the cell (components of the battery) design and operating conditions. When the counter electrode potential falls below zero, the risk of lithium plating and its associated negative consequences increases, which can compromise cell safety and lifespan. The N/P ratio, therefore, becomes a key factor in maintaining electrochemical balance between the electrodes and preventing performance degradation over time. Therefore, based on the obtained results higher values than 1.2 of N/P ratio must be studied for the improvement of the fluorine-free Li-ion cell.

Finally, the choice of electrolyte and binder, such as the fluorine-free electrolyte (LiPCP) and CMC-based binders used in this study affect how well the electrode-electrolyte interface can withstand the stresses of cycling, particularly under conditions where the potential may drop below zero. Together, these variables—N/P ratio, electrolyte and electrode formulation play an essential role in determining the long-term efficiency and viability of LIBs, making them crucial factors for advancing research and improving battery technologies towards industrial scale and applications.

Figure 70 illustrates the first and second charge/discharge profiles of a fluorine-free Li-ion cell configuration, where LFP serves as the working electrode, a SOX as the counter electrode, and lithium metal as the reference electrode. This system features an N/P ratio of 1.17. The charge curves are not smooth, which can be attributed to the assembly process of the pouch cell. Specifically, two metallic plates were positioned above and below the pouch cell during cycling, tightened with a torque of 0.8 N·m. This setup negatively impacted the cell performance. Notably, once these plates were removed, this irregular behavior disappeared, as seen in the LFP/SG cell shown in Figure 67.
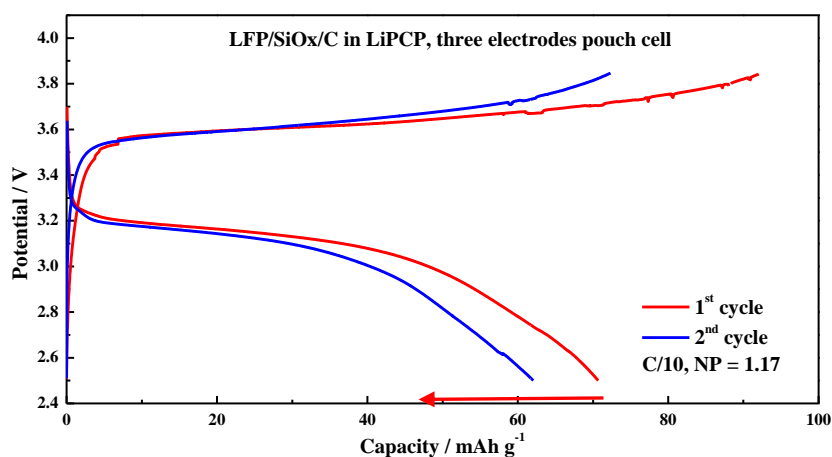
Figure 70. **Charge/discharge curves of LFP/SOX with a N/P ratio equal to 1.17, three-electrodes configuration, pouch cell**

Figure 71 presents the potential versus time profile for a three-electrode system, where a potential drop below zero is observed. However, this drop is not as significant as in Figure 68.

When the potential of the SOX counter electrode slightly drops below zero during cycling, it indicates some level of polarization. In this case, a negative potential for the SOX suggests that lithium is being inserted into the electrode material beyond its stable operational range. This could lead to excessive lithium intercalation or even lithium plating on the surface of the SiO_x, especially if the electrolyte is not stable at low potential.

The N/P ratio in this configuration, representing the balance between the negative electrode (SOX) and the positive electrode (LFP), plays a key role in influencing cell performance. Since SOX has a much higher theoretical capacity than LFP, an improper N/P ratio can result in unbalanced cycling. A low N/P ratio may push the SOX electrode to operate in a region where lithium plating or significant volume expansion occurs, leading to faster degradation and capacity fade.

On the other hand, a high N/P ratio might underutilize the potential of the SOX, reducing the overall efficiency of the cell. Therefore, optimizing the N/P ratio is crucial for maintaining the balance between the two electrodes, especially given the complex volume changes, pulverization, and instability associated with SOX. Based on the results obtained, increasing the N/P ratio might reduce the potential drop below zero.
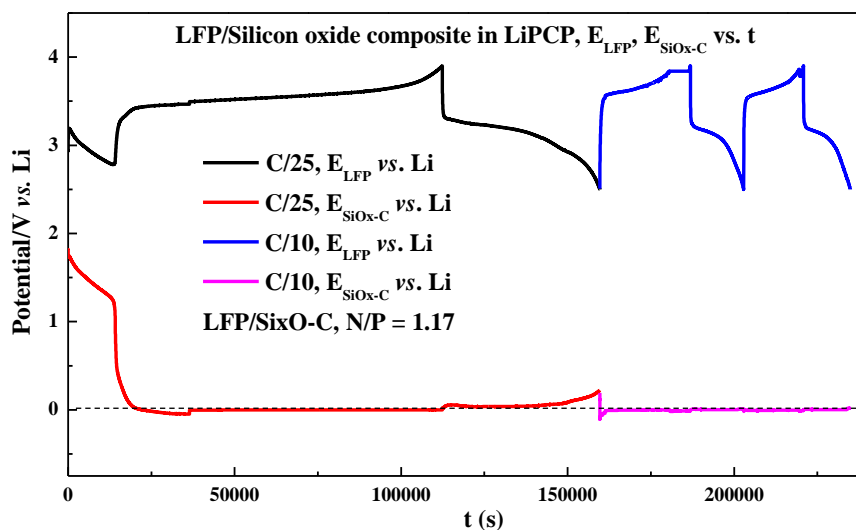
Figure 71. Time (s) vs. potential (v) of LFP/SOX with a N/P ratio equal to 1.17, three-electrodes configuration, pouch cell

Additionally, CMC/SBR-based binders, particularly Na-CMC, are known for their mechanical flexibility and ability to accommodate the significant volume expansion typically associated with silicon-based materials during lithiation. This helps maintain electrode integrity over cycling, reducing the risk of particle disconnection and improving the long-term cycling stability of the cell. However, at low concentration of Na-CMC may not fully prevent the mechanical stresses that arise during repeated cycling of the SOX, so further optimization of the electrode fabrication may be necessary.

Lastly, the fluorine-free electrolyte, LiPCP, might have some influence. This electrolyte is more environmentally friendly and may eliminate the formation of undesirable fluorinated species on the electrode surface. However, it is showing less stability at low potential, such as those experienced by the SOX when the potential drops below zero. This could lead to electrolyte reduction or unwanted side reactions, contributing to the observed capacity fade and performance loss. Therefore, while the fluorine-free electrolyte offers some benefits, its stability under such harsh cycling conditions needs careful consideration, particularly in systems involving silicon-based anodes or low potentials.

11.11.3. Influence of the electrolyte at low potentials on full-cell performance, fluorine-free Li-ion cells

This research project extensively explored the fabrication and optimization of aqueous-processed anodes and cathodes at both laboratory and pre-pilot scales. These battery components were designed to enhance overall cell performance and maximize the contribution of the LiPCP-based electrolyte.

In the initial phase of the study, the formulation of the electrolyte, incorporating various mixtures of organic carbonate solvents (refer to Figure 72), was investigated, alongside its electrochemical characterization. During this stage, it was observed that when the cell potential drops below 2 V, the electrolyte components undergo reduction, resulting in the generation of additional capacity (see Figure 73). However, this extra capacity is unsustainable, as the associated reactions are predominantly irreversible. In fluorinated electrolytes, the formation of a passivation layer is more efficient, which inhibits further decomposition. In contrast, in fluorine-free systems, a possible incomplete passivation leads to more substantial decomposition during the early charge-discharge cycles.
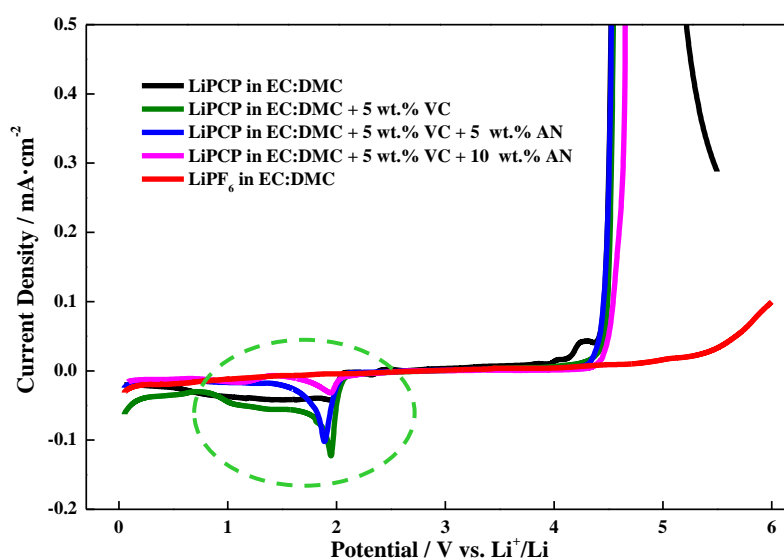
Figure 72. Electrolyte window stability at various electrolyte compositions

Figure 72 further indicates that optimizing the electrolyte formulation can minimize this reduction. The focus of this research was to introduce a novel electrolyte, evaluate its compatibility with aqueous-processed electrodes, and demonstrate its scalability to pouch cells, highlighting its potential for industrial applications. Future research and new formulations are expected to reduce or eliminate electrolyte reduction at low potential.

Another important factor is the formation of the SEI on the surface of the negative electrode, whether SG or SOX. Figure 73 illustrates the first cycle of LFP/SG and LFP/SOX in pouch cells. This first cycle is also referred to as the "formation cycle," involves the creation of this protective SEI layer, which consumes lithium cations. In this case, this process seems to result in an over-consumption of lithium, attributed to the electrolyte reduction, which leads to larger-than-expected capacity as more lithium than theoretically calculated is stored temporarily. This SEI formation is usually accompanied by reactions that are irreversible, which lead to capacity losses in subsequent cycles as the SEI stabilizes.
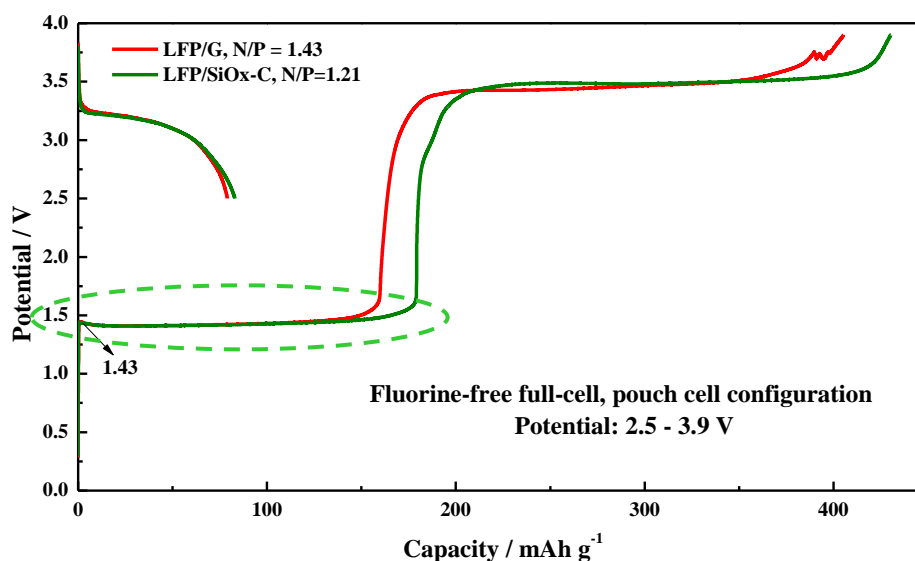
Figure 73. First cycle of full pouch cells, LFP/SG and LFP/SOX in LiPCP with EC:DMC (30:70 wt.%) and 5 wt.% of VC

In addition to SEI formation, the use of a fluorine-free LiPCP electrolyte introduces another potential cause of larger initial capacities. This electrolyte may present instability at low potentials, particularly below 2 V, where electrolyte reduction reactions can occur. These reactions contribute to the first-cycle capacity by generating extra charge storage from the reduction products of the electrolyte, which are typically undesirable and do not contribute to reversible capacity. Over time, these decomposition reactions stabilize, reducing the excessive capacity seen in the first cycle.

Figure 74 presents the first (C/25) and second (C/10) cycles for two half-cell systems: Li/SG and Li/SOX. Unlike cathode half-cells, anodes operate at lower potentials, making them more susceptible to electrolyte reduction.
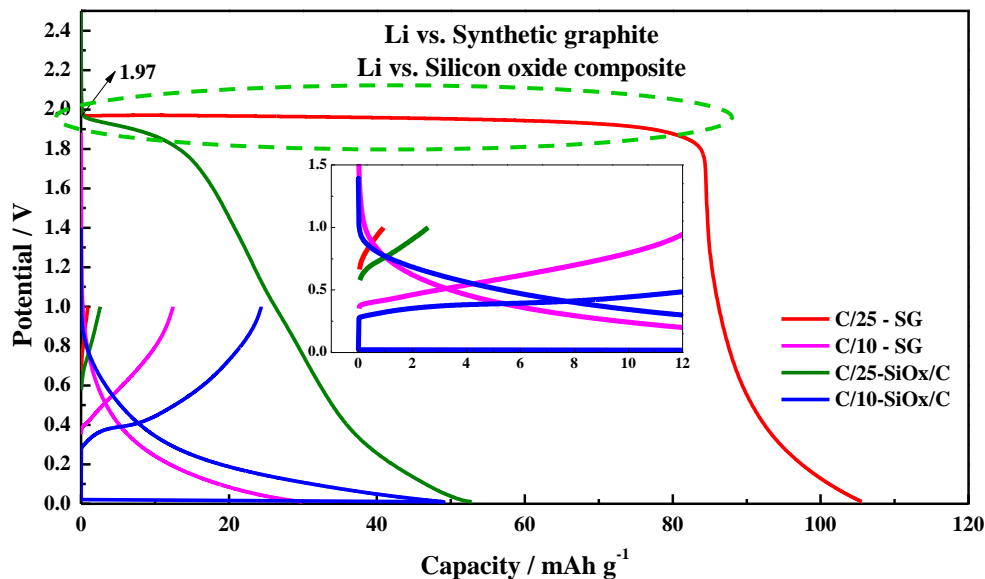
Figure 74. First and second cycle of half cells, Li/SG and Li/SOX in LiPCP with EC:DMC (30:70 wt.%) and 5 wt.% of VC

Both SG and SOX anodes initially absorb a significant amount of lithium cations due to their high theoretical capacity. Therefore, in both anodes a significant capacity depletion is observed after the first cycle. This can be attributed to the electrolyte reduction at low potentials, which can be clearly noted at 1.43 V when full cells are being tested, and at 1.97 V when anodes (half-cells) are cycled.

This process is also often accompanied by irreversible lithium consumption and mechanical degradation, such as cracking or pulverization of the AM. The mechanical effects, including temporary expansion, allow for greater lithium insertion during the initial cycle, resulting in a temporary capacity gain. However, subsequent cycles typically experience a decline in capacity due to material degradation.

In summary, the larger-than-theoretical capacities observed in the first cycle of LFP/SG and LFP/SOX cells (Figure 73) with fluorine-free LiPCP electrolyte can be attributed to several factors such as, the formation of the SEI, electrolyte reduction, irreversible lithium consumption in SiO_x, and potential assembly inaccuracies. The instability of fluorine-free electrolytes at low potentials (below 2 V) further exacerbates these effects by promoting unwanted side reactions, contributing to the initial capacity surplus. As these reactions stabilize, subsequent cycles tend to show capacities closely with theoretical values.

11.11.4. Pouch cells assembly configuration for electrochemical characterization

For electrochemical characterization and references samples Table 56 provide details of each pouch cell cycled with LFP as the cathode and the anode type is specified on the table, what was the purpose of each and the N/P ratio.

Acceptable N/P ratio considered at industrial level for commercial electrolyte $LiPF_6$-based is the range of 1.1–1.2, however, as it was shown before this range might be applicable only for $LiPF_6$, most commercial electrolyte.

Table 56.   Pouch cells codes and cell description

Channel CODE	Anode	N/P	OBS.
CL_PC3_002	G	1.15	Reference without cycling
CL_PC3_003	Si	1.12	Reference without cycling
CL_PC3_004	Si	1.17	3 Electrodes = 1 C/25, 2 C/10
CL_PC_005	G	1.27	64 Cycles
CL_PC_006	G	1.43	71 Cycles
CL_PC_007	Si	1.20	102 Cycles
CL_PC_011	Si	1.21	75 cycles
CL_PC_012	Si	1.18	Half-cycle
CL_PC3_014	Si	1.21	3 Electrodes = 1 C/25, 2 C/10
CL_PC3_016	G	1.23	3 Electrodes = 1 C/25, 2 C/10
CL_PC3_017	G	1.07	3 Electrodes = 1 C/25, 2 C/10
CL_PC_018	G	1.17	Half-cycle

Table 57 details specific characteristics of anode/cathode for cell assembly.

Table 57.   Areal capacity values for each electrode of assembled pouch cells

Channel CODE	Cathode (Pouch cell) = 37.5x64 = 20.25 cm^2				Anode (Pouch cell) = 39x65 = 21.80 cm^2			
	m_c = %AM*m_e (mg/cm^2)	C_{exp-E} (mAh/cm^2)	m_{AM} = m_c * A (mg)	C_{VMP3} (mAh)	m_c = %AM*m_a (mg/cm^2)	C_{exp-E} (mAh/cm^2)	Potential range (V)	N/P Ratio
CL_PC3_002	11.75	2.00	237.86	40.44	6.18	2.30	2.5 - 3.9	1.15
CL_PC3_003	10.35	1.76	209.63	35.64	3.92	1.96	2.5 - 3.9	1.12
CL_PC_006	9.60	1.63	194.40	33.01	6.25	2.33	2.5 - 3.9	1.43
CL_PC_007	12.43	2.11	251.71	42.79	5.06	2.53	2.5 - 3.9	1.20
CL_PC_011	13.31	2.26	269.56	45.83	5.46	2.73	2.5 - 3.9	1.21
CL_PC3_014	12.79	2.17	259.00	44.03	5.28	2.64	2.5 - 3.9	1.21
CL_PC_012	11.71	1.99	237.13	40.31	4.70	2.35	2.5 - 3.9	1.18
CL_PC3_016	12.74	2.17	257.99	43.87	7.17	2.67	2.5 - 3.9	1.23
CL_PC3_017	12.37	2.10	250.49	42.57	6.06	2.25	2.5 - 3.9	1.07
CL_PC_018	10.84	1.84	219.51	37.31	5.78	2.15	2.5 - 3.9	1.17

RESULTS AND DISCUSSION

SURFACE CHARACTERIZATION OF ELECTRODES

BEFORE AND AFTER CYCLING, POUCH CELLS

Aqueous-processed electrodes

Lithium iron phosphate (LFP)

Synthetic graphite (SG)

Silicon oxide composite (SOX)

C. SURFACE CHARACTERIZATION OF ELECTRODES BEFORE AND AFTER CYCLING, POUCH CELLS

11.12. Scanning electron microscope (SEM), surface characterization of LFP before and after cycling

This section focuses on the surface characterization of pouch cells electrodes before and after cycling. For this section, the electrodes presented are the electrodes optimized and under conditions explained in detail in previous sections.

Each section describes the characteristics of the electrodes after a number of cycles or when they were resting for 24 hours for electrolyte soaking and subsequent characterization.

11.12.1. LFP, cathode AM powder

The particle distribution and morphology of LFP/C is shown in Figure 75. The sample manifested as secondary micron-sized particles with diameters of 6–10 μm loosely aggregated by primary particles with sizes of 300–650 nm. The large-sized primary particles and agglomerates observed on the rough surface of secondary microspheres will result in a tap density of 1.45 ± 0.2 g cm^{-3}. Table 58 details the LFP powder chemical composition.

Table 58.   Details of the chemical composition of LFP/C powder

LFP/C	C (%)	Li (%)	Fe (%)	P (%)	O (%)	Impurity (Na, Ca, Ni) (%)
Chemical Compositions	1.15 ± 0.25	4.40 ± 0.50	34.5 ± 1.0	19.5 ± 1.0	40.4 ± 0.50	≤ 0.01

LFP/C, LFP powder
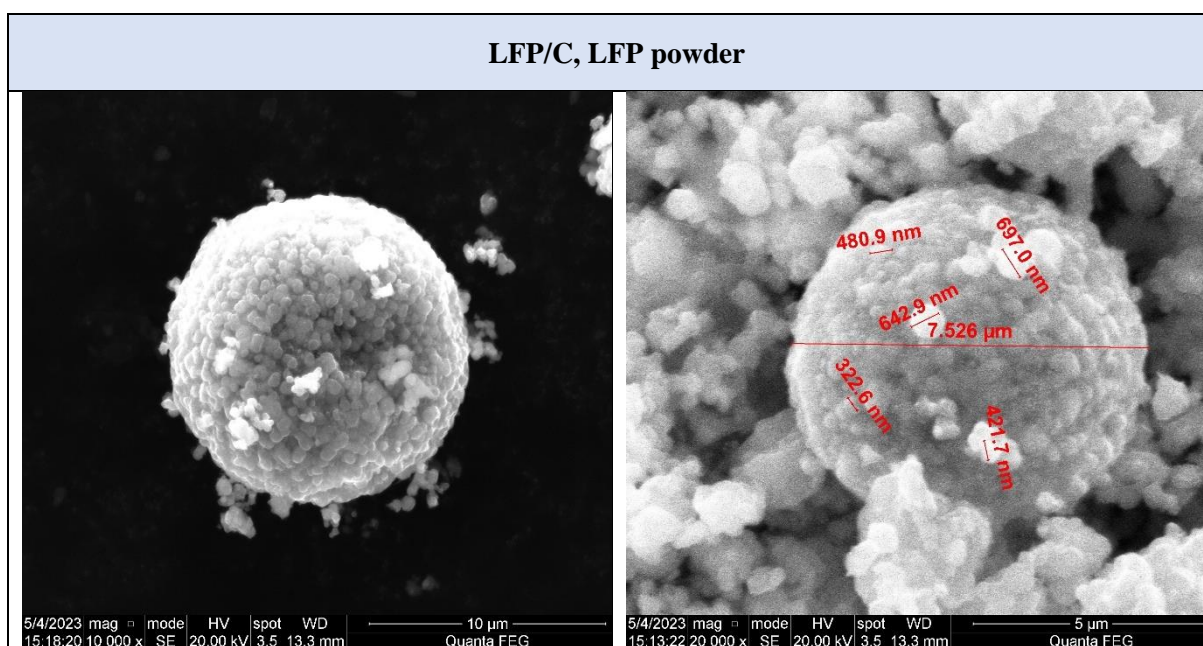
Figure 75. LFP AM powder morphology

11.12.2. LFP electrode, fluorine-free Li-ion pouch cell −before galvanostatic cycling

Surface characterization of the electrodes was conducted using Scanning Electron Microscopy (SEM) to analyze both pre-cycled and post-cycled pouch cells.

Before cycling, the electrodes were soaked in electrolyte for 24 hours. This procedure was crucial to replicate the conditions just before cycling begins, allowing for an accurate assessment of the initial state of the electrodes. Importantly, the electrolyte was not washed off prior to characterization. Since this is the first time a fluorine-free Li-ion cell has been characterized, there is no existing data on the surface content. Therefore, retaining all possible components on the surface before cycling was essential for comprehensive analysis.

Figures 76 and 78 present the surface morphology of the LFP electrode before cycling. Small particles dispersed across the surface were observed, which are likely to be AMs or CMs from the electrode itself. Additionally, dark spots were clearly visible under the microscope, distributed across the entire surface of the electrode. These dark spots, along with the small particles, were further examined using Energy Dispersive X-ray Spectroscopy (EDX) to determine their elemental composition.

PC3-002, LFP, N/P = 1.15, Electrode soaked in electrolyte for 24 hours.
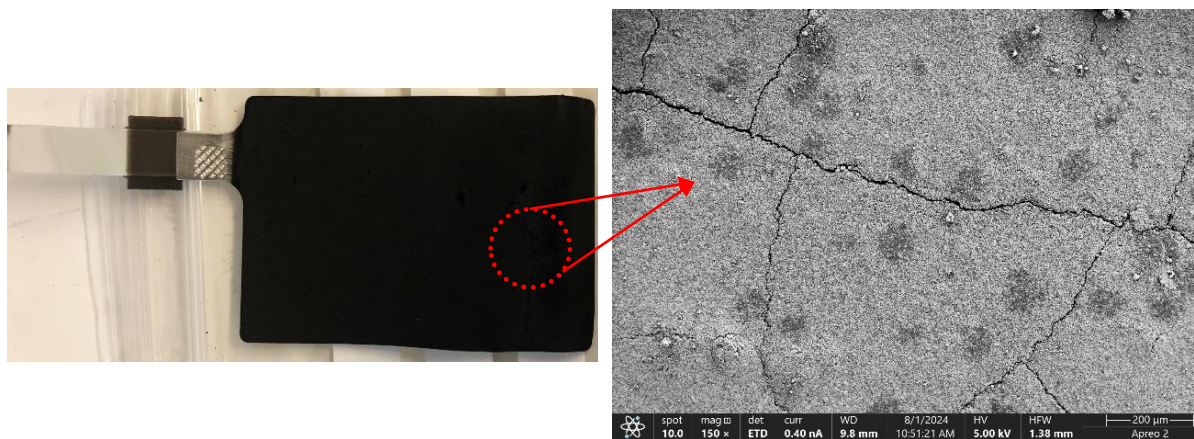
Figure 76. FLP electrode soaked in electrolyte for 24 hours

One significant observation was the presence of cracks on the electrode surface, despite the electrodes being calendered within a 10-15% range. These cracks, which were not visible to the unaided eye but became apparent at 150× magnification, formed thin channels across the surface. Unfortunately, these cracks negatively impacted cell performance, leading to capacity fading and a gradual decrease in capacity with each cycle.

The EDX analysis, as shown in Figure 77 and 79, identified the elements present on the cathode surface before cycling, including carbon (C), oxygen (O), nitrogen (N), phosphorus (P), iron (Fe), and sodium (Na). The presence of C, O, N, P, and Fe was expected; carbon and nitrogen are attributed to the electrolyte, while phosphorus, oxygen, and iron originate from the cathode material (LFP). However, the detection of sodium (Na) was unexpected. Sodium could possibly originate from the binder Na-CMC or be an impurity in the AM (LFP), as indicated in Table 58.

PC3-002, LFP, N/P = 1.15, Electrode soaked in electrolyte for 24 hours.
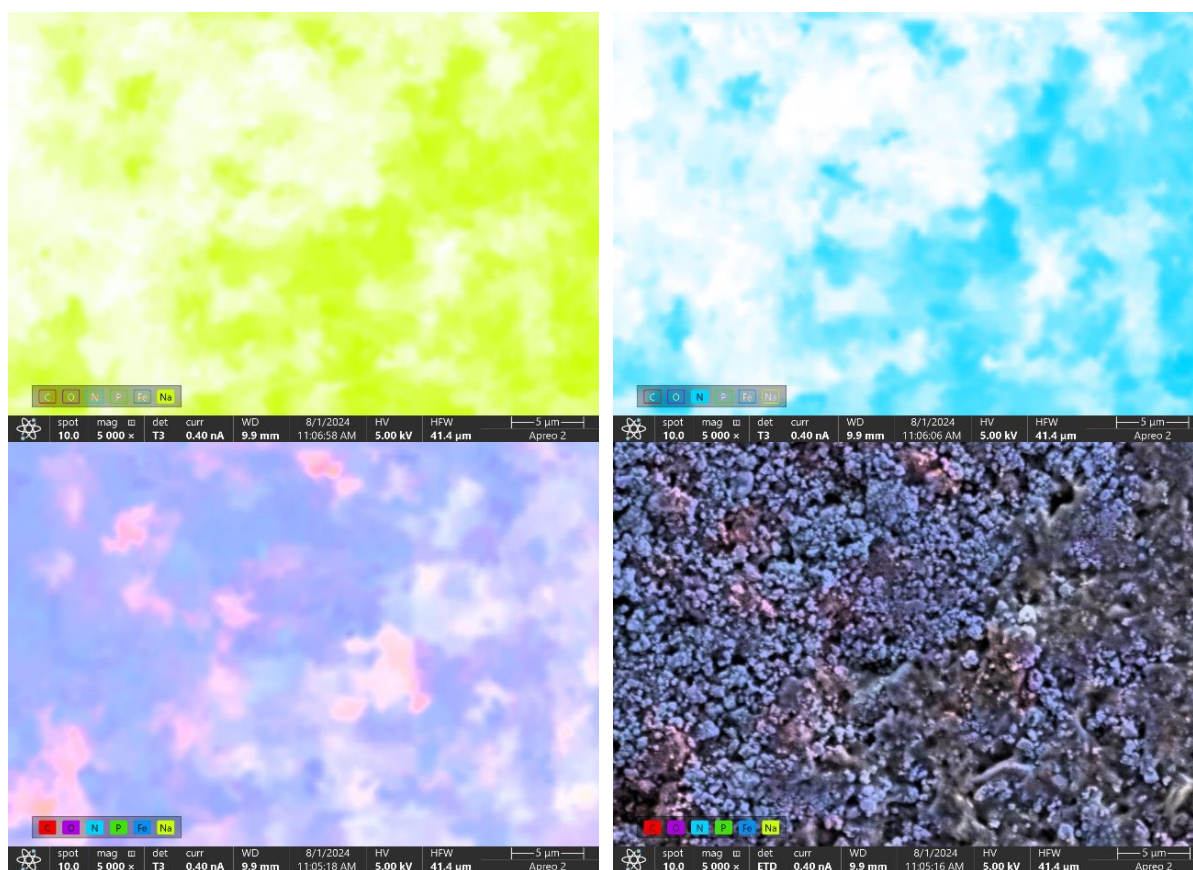
Figure 77. FLP electrode soaked in electrolyte for 24 hours, composition

Figures 76 and 78 reveal dark spots on the LFP cathode surface, which differ markedly from the typical distribution of AMs and CMs in the electrode. These spots, appearing as larger and elongated particles, show a notable presence of sodium (Na) and nitrogen (N). Na-CMC, commonly used as a binder in LFP electrodes, disperses sodium throughout the electrode surface. However, the significantly higher concentration of sodium in these specific particles suggests that the Na-CMC binder accumulates in these regions, or it had some interaction with the electrolyte.

PC3-003, LFP, N/P = 1.12, Electrode soaked in electrolyte for 24 hours.
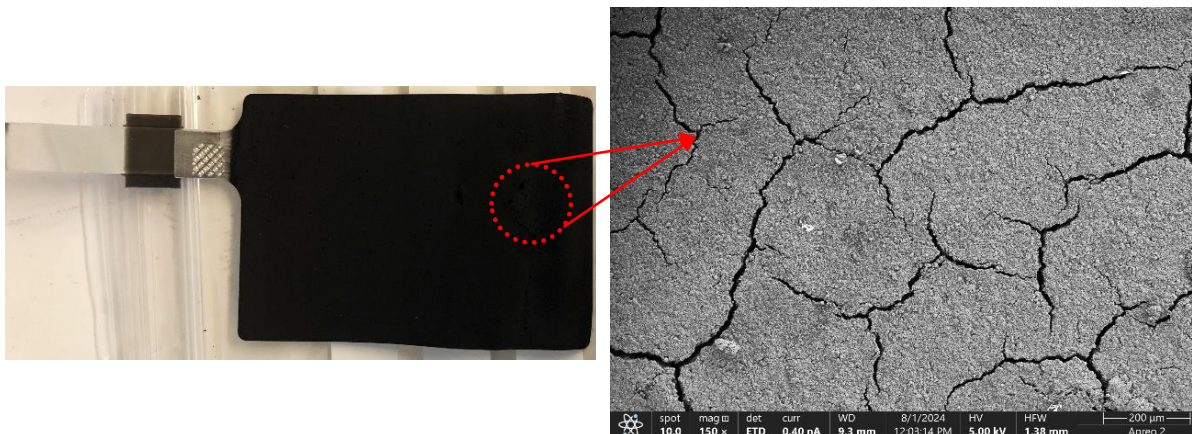
Figure 78. LFP electrode soaked in electrolyte for 24 hours,

This finding underscores the role of Na-CMC in the electrode microstructure, influencing the distribution and characteristics of the particles observed.

Additionally, the presence of sodium on the surface could further exacerbate these performance issues, potentially affecting the overall efficiency of the cell.
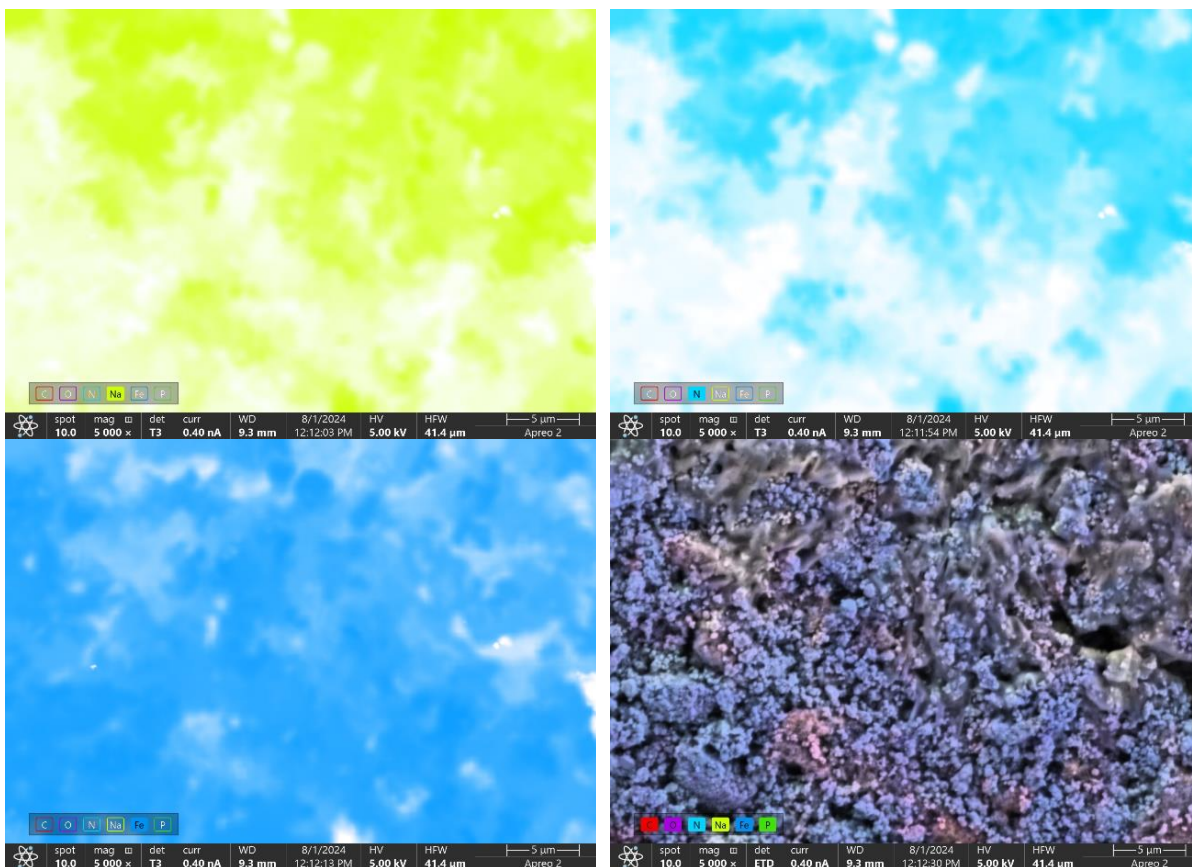
Figure 79. LFP electrode soaked in electrolyte for 24 hours, composition

11.12.3. LFP electrode, fluorine-free Li-ion pouch cell −post-cycling

Figures 80, 81, and 82 show the surface morphology of LFP electrodes after cycling, each focusing on specific features. Figure 80 illustrates the electrode surface after 60 cycles in a 2-electrode pouch cell configuration, with SG as the anode. In Figure 80a, the opened electrode reveals that most of the surface remained intact, with minimal delamination. The areas that did show delamination likely existed before cycling began. Additionally, several lighter grey spots are visible, scattered across the electrode surface. These spots stand out against the darker background of the electrode.
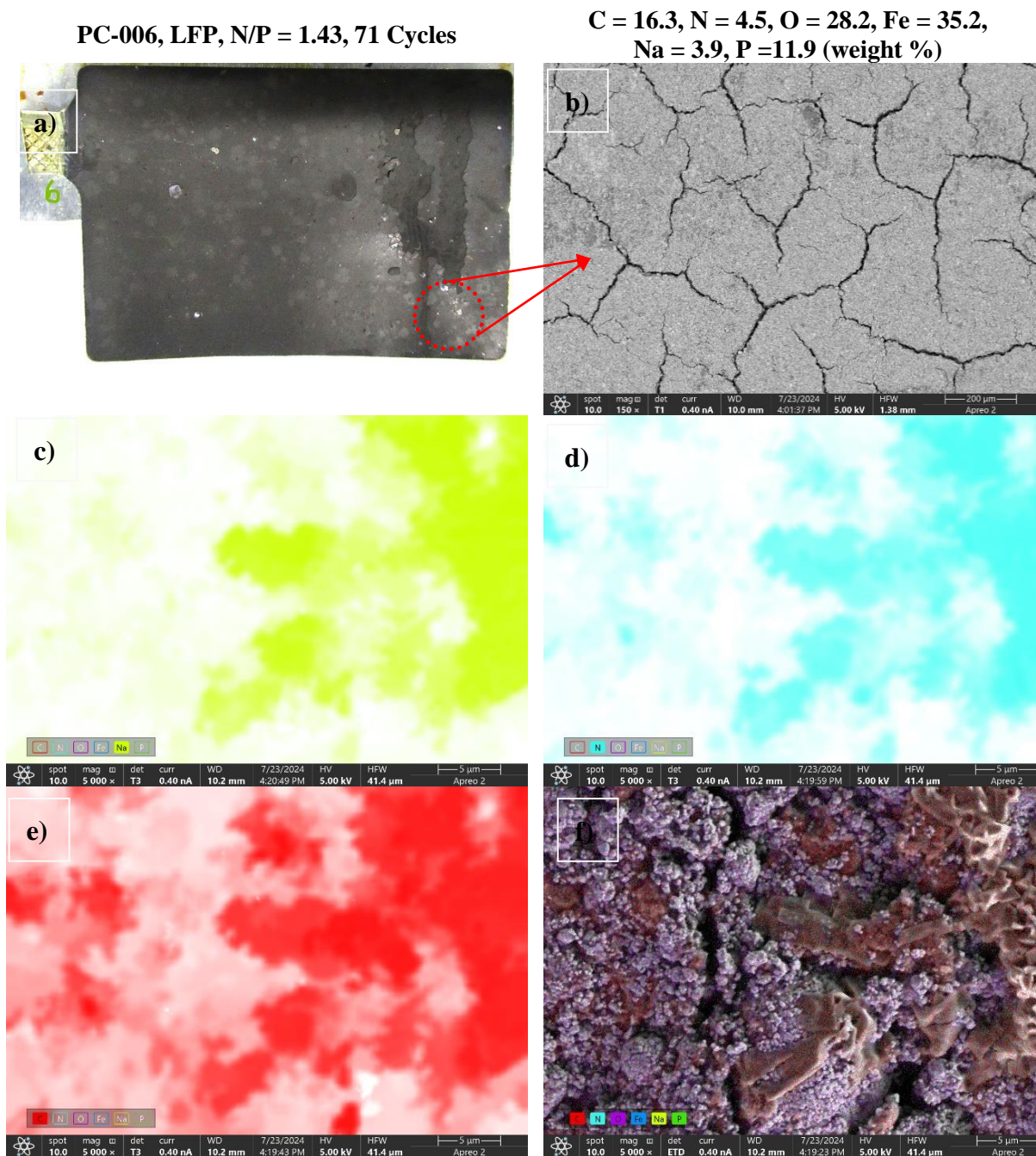
Figure 80. LFP electrode surface morphology after cycling with SG

Figure 80b provides an SEM image at 150× magnification, revealing cracks distributed throughout the electrode surface. These cracks could explain the observed capacity fading with each cycle and suggest significant electrolyte consumption and extraction during the initial cycle, potentially impacting future cell performance.

Figures 80c, 80d, and 80e present surface characterization of the dark spots, showing a high concentration of sodium (Na), nitrogen (N), and carbon (C), more so than in other areas of the surface, as indicated by the intense colorations. Figure 80f displays the overall elemental composition of the surface, including iron (Fe), phosphate (P), and oxygen (O), in addition to Na, N, and C. The higher concentration of Fe, P, and O on areas without dark spots suggests that these regions primarily consist of the AM.

Figure 81 examines the electrodes after 70 cycles using SOX as the anode in a similar 2-electrode pouch cell configuration.

Figure 81a shows the electrode after 70 cycles. Similar to the SG case, the cathode exhibits no delamination or loss of electrode material post-cycling. Light spots are present but are significantly fewer than those observed on the electrode cycled with SG. Figure 81b provides an SEM image of the cathode surface at 150× magnification, showing visible cracks. While dark spots are not visible at this magnification, increasing the magnification to 1300× reveals their presence, confirming the existence of other components as seen in the previous electrode analysis. Figures 81c and 81d identify the presence of sodium and nitrogen, respectively, with higher concentrations found in the dark spots compared to the rest of the electrode surface.

Figures 81e and 81f show the distribution of the remaining elements across the electrode surface, consistent with the findings in Figure 80.

Figure 82, as Figures 80 and 81, presents the post-cycling surface morphology of the electrode after three cycles (1 cycle of C/25 and 2 cycles of C/10) in a 3-electrode pouch cell configuration. In this setup, SG served as the counter-electrode, while lithium metal was used as the reference electrode. An initial observation showed the unexpected presence of sodium on the cathode surface, which was difficult to trace back to a definitive source. To further investigate, an additional Scanning Electron Microscopy (SEM) characterization was performed. For this sample higher voltage was applied to confirm whether sodium was embedded within the particles or merely distributed superficially across the cathode surface due to the CMC binder distributed on the electrode surface.

Figures 80 and 81 depict SEM results at 5 kV, providing a superficial view of the electrode surface. To penetrate deeper into the electrode structure, the voltage was increased to 20 kV in Figure 82, allowing for a more in-depth analysis of the particles formed.

The post-mortem images of the electrode revealed numerous surface particles. Initially, these particles resembled lithium metal, potentially formed during cycling due to observed overpotential in the 3-electrode configuration as shown in point 11.11.2.

PC-011, LFP, N/P = 1.21, 75 cycles
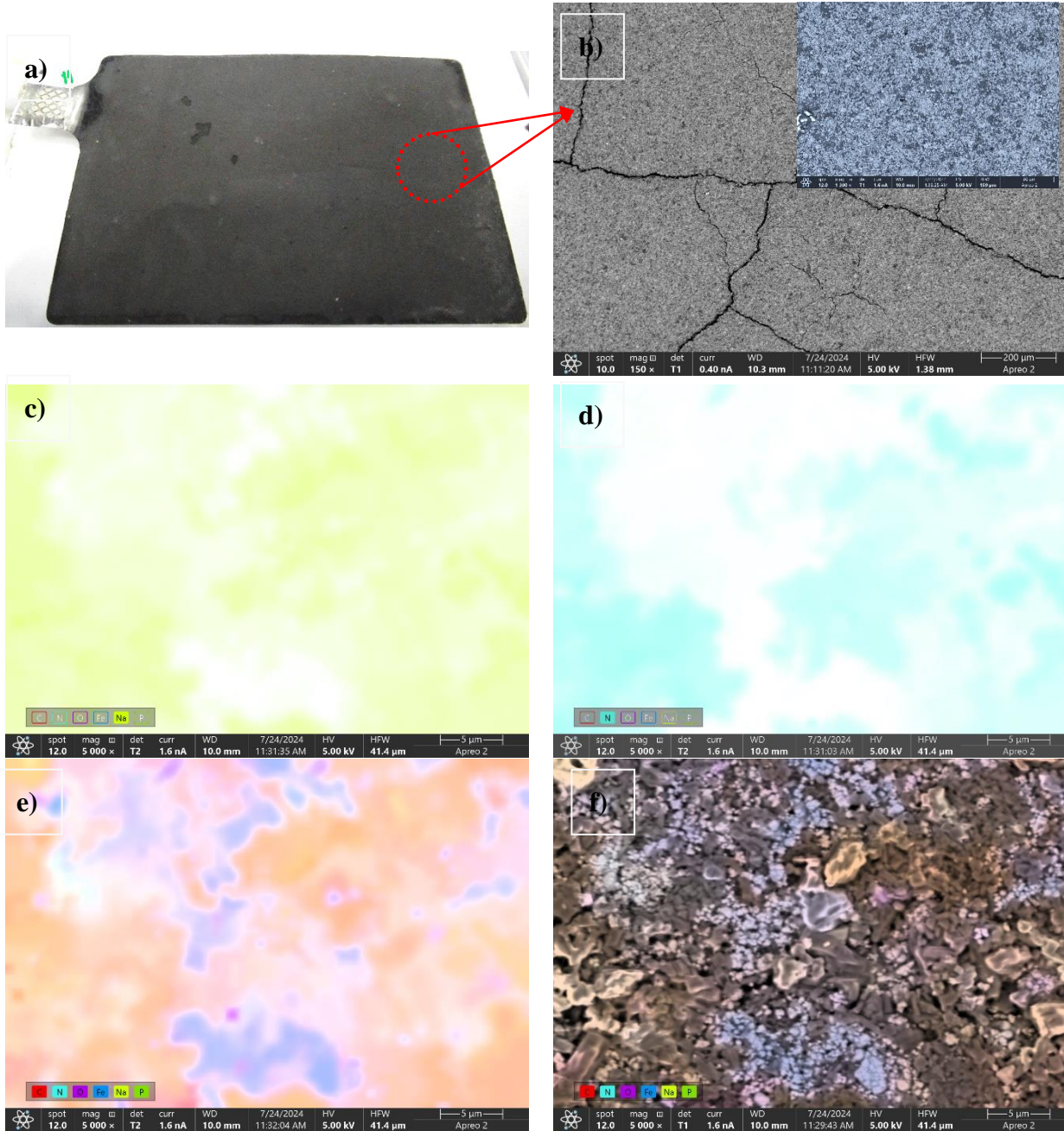
Figure 81. LFP electrode surface morphology after cycling with SOX

Despite applying higher potential for SEM analysis, as shown in Figure 82b (magnified 200× and 250×), the electrode surface displayed significant cracking. These cracks were more pronounced compared to the electrode surface before cycling. Moreover, crystal-like particles appeared, along with the previously noted dark spots. These particles were homogeneously distributed across the electrode, as illustrated in Figure 82a. Notably, an orange tint on the left side of the electrode suggests that the presence of lithium metal as the reference electrode the cycling process might have some effect, however, nothing different to the report was noticed.

PC3-017, LFP, N/P = 1.07, 3 Cycles
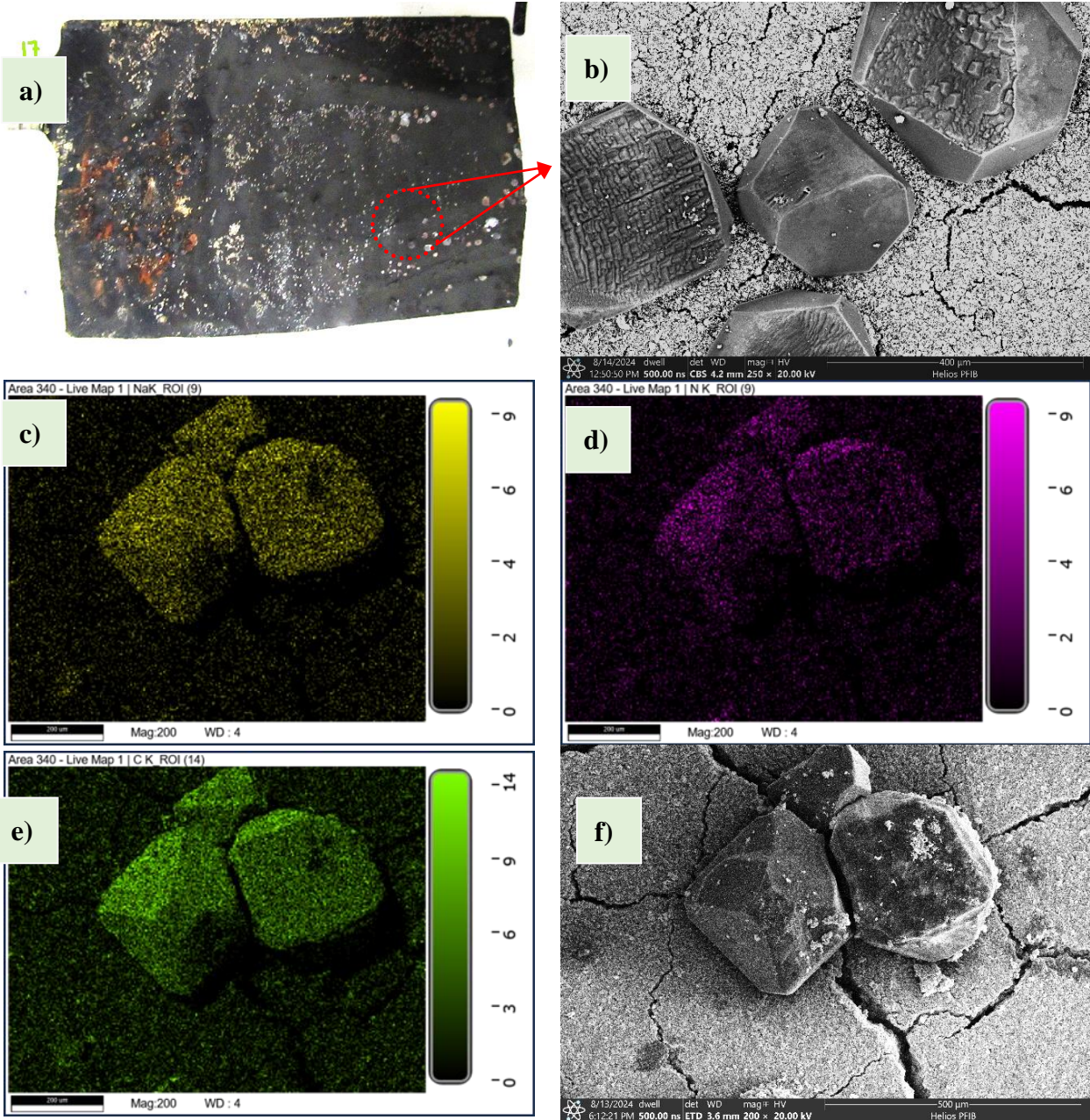
Figure 82. LFP electrode surface morphology after cycling with SG, three-electrode pouch cell configuration

Figures 82c, 82d, and 82e reveal the elemental composition of the particles. Sodium (Na), nitrogen (N), and carbon (C) concentrations were significantly higher within these particle formations than elsewhere on the electrode surface. This suggests that these elements are interacting, possibly leading to the formation of a salt compound after cycling.

From the cathode surface characterization before and after cycling, the following points can be highlighted:

Crack formation and impact on cell performance:

- The presence of cracks on the electrode surface both before and after cycling plays a critical role in the cell performance. These cracks are likely to contribute to capacity fading during cycling.
- The larger and more widespread the cracks, the greater the lithium depletion during the extraction and insertion processes. As a result, the electrode coulombic efficiency decreases significantly during each cycle.

Particle Formation and Potential Sources:

- The particles observed on the electrode surface may be attributed to impurities from the battery components (electrodes or electrolyte) prior to cycling, with sodium being a likely contaminant.
- Alternatively, these particles could result from chemical reactions during the SEI formation, or during the initial cycles of the cell.

The interaction of the novel LiPCP-based electrolyte with CMC-based processed electrodes (both anodes and cathodes) was a novel area of study. This doctoral project aimed to identify optimal formulations of electrolyte and electrodes compatible with the new electrolyte for the development of greener and more sustainable LIBs. The results here are indicative of some successful interactions but highlight the need for further investigation.

The main objective of this research was to assess the compatibility between the electrolyte and electrodes in pouch cells. While the study yielded valuable insights, no additional characterization of the pouch cells was performed after the cycling process.

11.13. Scanning electron microscope (SEM), surface characterization of SG anode before and after cycling

The surface characterization was performed using scanning electron microscopy (SEM) to examine the surface of the electrode in a pouch cell configuration. Both pre- and post-cycling characterization of the anode followed the same protocols applied to the cathodes to ensure consistency in experimental conditions and accurate comparison of results.

11.13.1. SG, fluorine-free Li-ion pouch cell pre-cycling

PC3-002, SG, N/P = 1.15, Electrode soaked in electrolyte for 24 hours.

Figure 83. SG electrode surface morphology pre-cycling with LFP, two-electrode monolayer pouch cell configuration
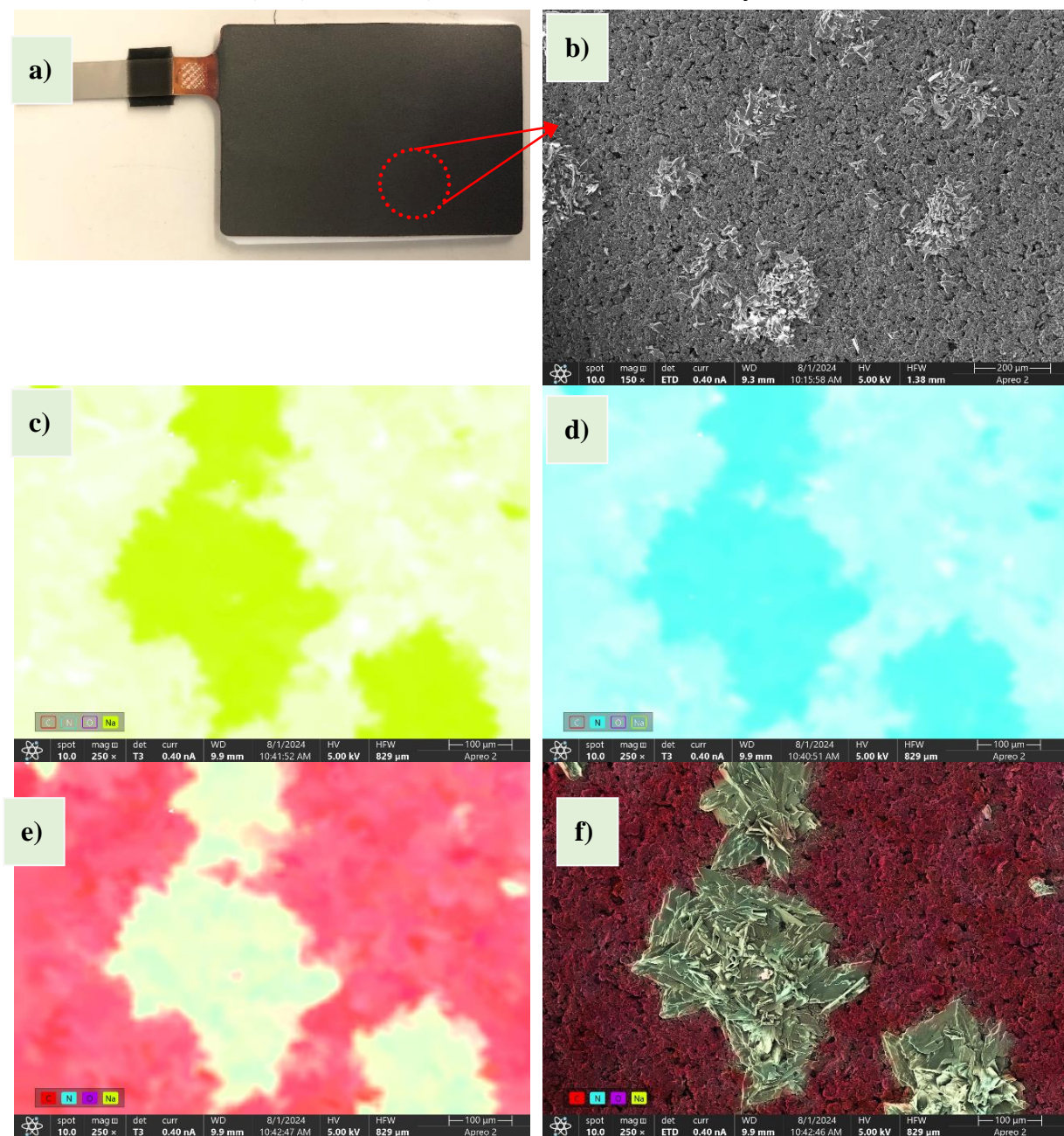
Figure 83a displays the surface of SG prior to electrochemical cycling, after being soaked in the electrolyte for 24 hours. As expected, sodium deposition on the anode surface was observed during this initial stage, likely due to the electrolyte composition and interaction with the graphite.

Figure 83b, captured at 150× magnification and 5 kV, provides a more detailed view of the surface, where a noticeable formation of crystals can be seen. These crystals are uniformly distributed across the anode surface, indicating that the process of sodium precipitation was even and homogeneous. This suggests that the amount of electrolyte used, specifically between 900 to 1000 µL of LiPCP-based electrolyte, might play a significant role in promoting the formation of these crystalline structures.

Upon closer examination, the smoothness and uniformity of the anode surface stand out, particularly the absence of any visible cracks. This smooth and crack-free surface is a crucial factor that could enhance the overall performance of the cell, as cracks could introduce performance degradation due to loss of AM or the creation of high-resistance regions. The absence of these defects suggests a stable electrode structure, which should contribute positively to the electrochemical behavior of the cell during cycling.

Figures 83c and 83d, at a magnification of 250× and 5 kV, further illustrate the presence of sodium and nitrogen on the anode surface. These elements appear to be uniformly distributed, with higher concentrations detected in the precipitated particles rather than on the rest of the surface. This indicates that the particles formed during soaking are predominantly composed of sodium-nitrogen compounds, which may be linked to electrolyte decomposition or side reactions during the soaking process.

Figure 83e provides a more comprehensive elemental analysis, showing the distribution of carbon, nitrogen, oxygen, and sodium on the anode surface. As expected, carbon is the dominant element due to the SG composition of the electrode. However, the carbon content is notably lower within the precipitated particles compared to the rest of the surface, suggesting that these particles primarily consist of electrolyte decomposition products or the influence of Na-CMC in the electrolyte. Figure 83f reinforces this conclusion, showing a clear distinction between the particle structures and the smooth underlying graphite surface. This analysis provides insight into the role of electrolyte and the CMC binder interactions in the formation of these crystalline deposits on the anode.

11.13.2. SG, fluorine-free Li-ion pouch cell post−cycling

Following electrochemical cycling, a post-mortem analysis was conducted on the SG anode. Figure 84a illustrates the surface morphology after more than 60 charge/discharge cycles. The surface now appears significantly different from the pre-cycling state, with considerable growth and more visible particles on the surface.
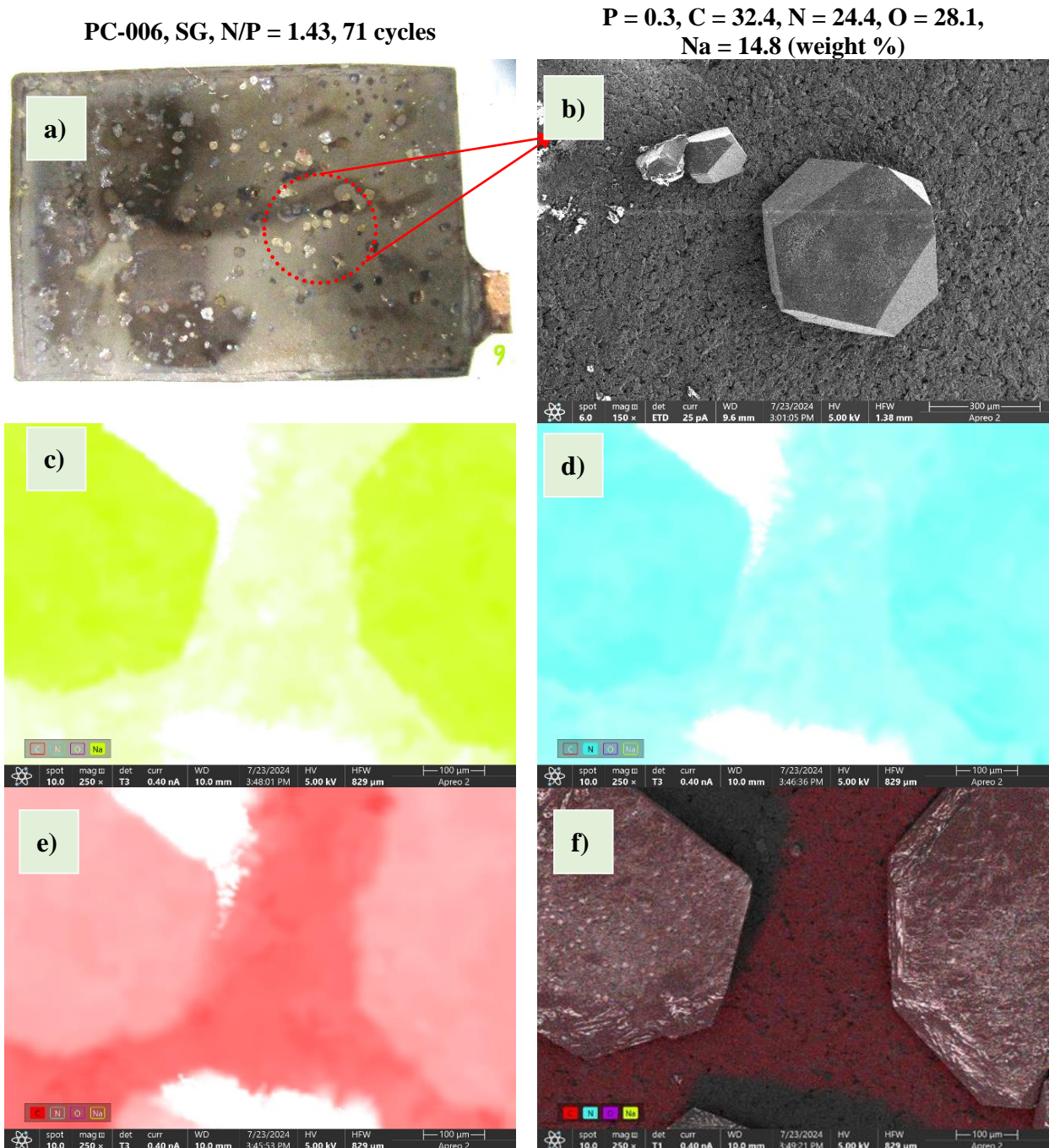
Figure 84. SG electrode surface morphology post-cycling with LFP, two-electrode monolayer pouch cell configuration

These particles are large enough to be observed without the need for high magnification, indicating that significant changes have occurred during cycling. The bright appearance of these particles initially suggested the formation of metallic lithium, as lithium plating is a common issue in cells undergoing cycling. To investigate this further, SEM analysis was employed. Figure 84b, taken at 150× magnification and 5 kV, shows the SG anode after cycling, first, confirming the absence of cracks on the surface, which indicates that the electrode has maintained its structural integrity.

The particles formed on the anode surface during cycling exhibit a crystal-like, hexagonal morphology. This shape is consistent across most particles, suggesting a uniform process of particle growth. To better understand their composition, elemental analysis was performed. Figures 84c, 84d, and 84e present the distribution of sodium, nitrogen, and carbon on the anode surface, respectively. As expected, sodium and nitrogen concentrations are higher in the precipitated particles, while carbon remains more abundant across the rest of the anode surface due to its SG nature.

The difference in color intensity between the particles and the surrounding surface (base electrode material) also provides clues about the possible nature of the formed particles and the surface. Interestingly, the crystalline shape of the particles suggests that lithium metal formation, initially suspected, can be ruled out, as lithium metal typically forms dendritic structures rather than the observed hexagonal crystals.

Figure 84f further corroborates this, showing the presence of carbon, nitrogen, oxygen, and sodium on both the particles and the anode surface, with similar morphology to the particles formed with the two-electrode pouch cell configuration.

To further confirm the identity of the particles formed after cycling, SEM analysis was conducted on a three-electrode pouch cell configuration due to its surface appearance.

Figure 85a shows the surface of the SG anode post-cycling, where significant changes are evident compared to the pre-cycling state. The surface now appears much rougher, and the influence of the lithium metal electrode is noticeable in the middle on the left side of the surface, altering the morphology of the graphite surface. Figure 85b, taken at 200× magnification and 20 kV exhibited a surface with small holes, likely caused by the interaction with the lithium reference electrode during the charge/discharge process. Figure 85f is the image used for analysis of Figures 85c, 85d, and 85e.

It is worth noting that these holes were not present in the two-electrode pouch cell configuration (pre- or post-cycling), suggesting that the third electrode (lithium metal) might introduce additional stress on the anode surface during cycling.

PC3-017, SG, N/P = 1.07, 3 cycles, 3-electrode configuration
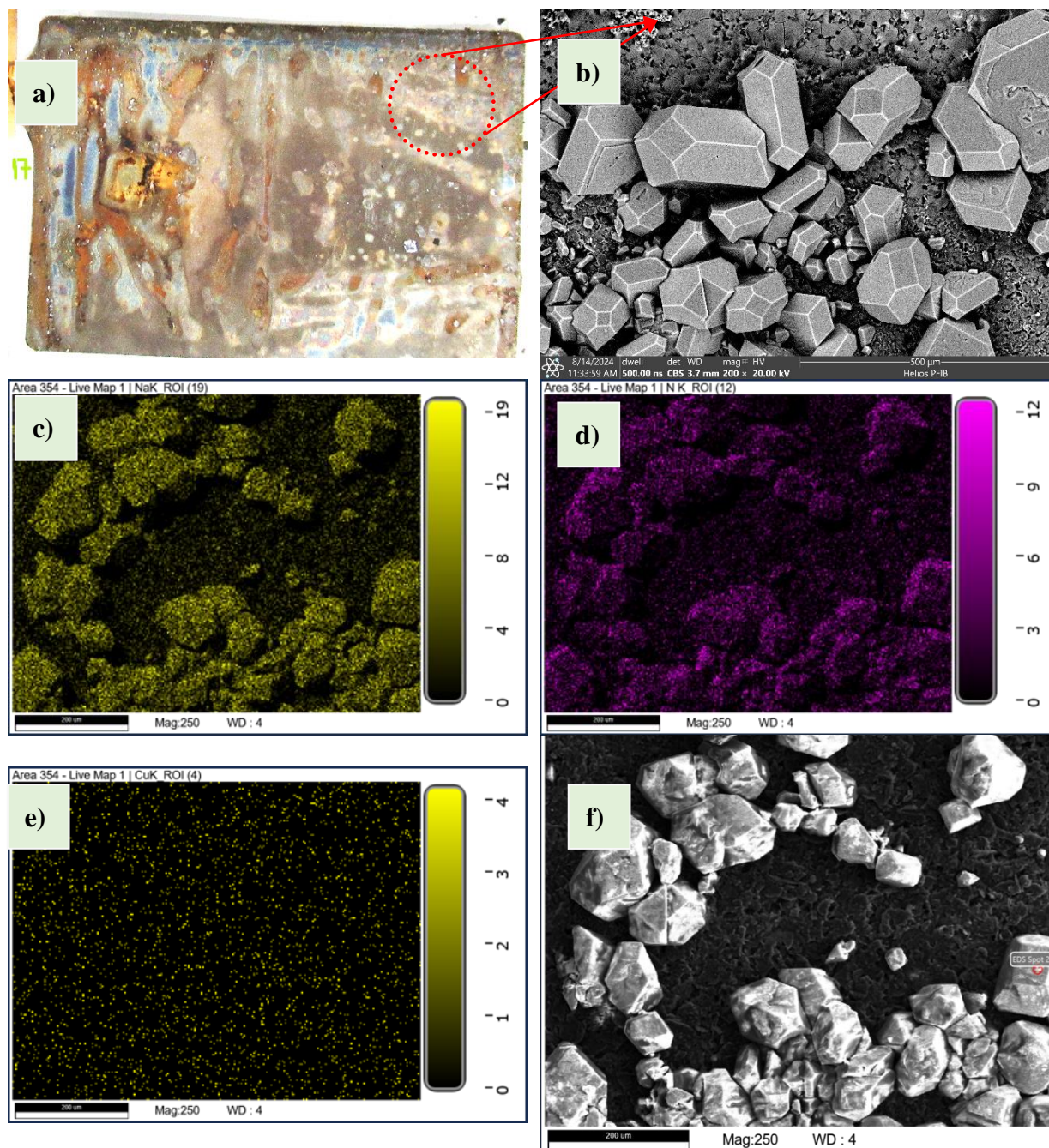
Figure 85. SG electrode surface morphology post-cycling with LFP, three-electrode pouch cell configuration

Figures 85c and 85d again demonstrate higher concentrations of sodium and nitrogen within the precipitated particles compared to the rest of the surface. This repeated observation across various electrodes suggests a consistent formation mechanism for these particles, likely related to side reactions involving sodium and nitrogen from the electrolyte.

Given the unusual surface morphology and particle distribution with this electrode, it was hypothesized that copper precipitation or dendrite formation might have occurred. Therefore, copper was also analyzed to rule out any potential copper compound formation during cycling. However, as shown in Figure 85e, taken at 250× magnification and 20 kV, no copper-related deposits were found. Instead, it confirms the uniform presence of copper across the entire anode surface. The homogeneous distribution was expected, as the anode was cast on copper foil as the current collector. The absence of localized copper accumulation indicates that no significant copper plating or compound formation occurred during the cycling process. This suggests that the observed surface modifications were primarily due to electrolyte interaction and side reactions, rather than copper-related degradation.

The comprehensive surface characterization of SG anodes before and after cycling revealed several important findings. The pre-cycling anode exhibited a smooth, crack-free surface with uniform particle deposition, indicating a well-optimized electrolyte interaction. Post-cycling analysis showed the formation of large crystalline particles, primarily composed of sodium and nitrogen compounds, with no evidence of lithium metal plating. The structural integrity of the anode was maintained throughout cycling, with no cracks observed, except for minor holes in the three-electrode configuration, likely due to the influence of the lithium reference electrode.

Furthermore, copper analysis confirmed that no copper compounds formed during the charge/discharge process, as the copper was uniformly distributed across the anode surface. The consistent presence of sodium and nitrogen-containing particles on both the cathode and anode surfaces suggests that these compounds are not specific to any one electrode but are likely a result of electrolyte interaction with Na-CMC, impurities or side reactions occurring during cycling. The formation of uniform, crystal-like particles during cycling is likely due to the applied electrochemical potential, but the exact source of these particles remains uncertain. Further investigation is needed to determine their origin and how they may impact long-term cell performance.

11.14. Scanning Electron Microscope (SEM), surface characterization of SOX anode pre- and post-cycling

This section focuses on the surface characterization of SOX anodes in pouch cells. Detailed analysis was conducted both before and after cycling with specific emphasis on the formation of particles on the surface and their elemental composition.

11.14.1. Pre-cycling surface characterization of SOX anode

PC3-003, SOX, N/P = 1.12, Electrode soaked in electrolyte for 24 hours.
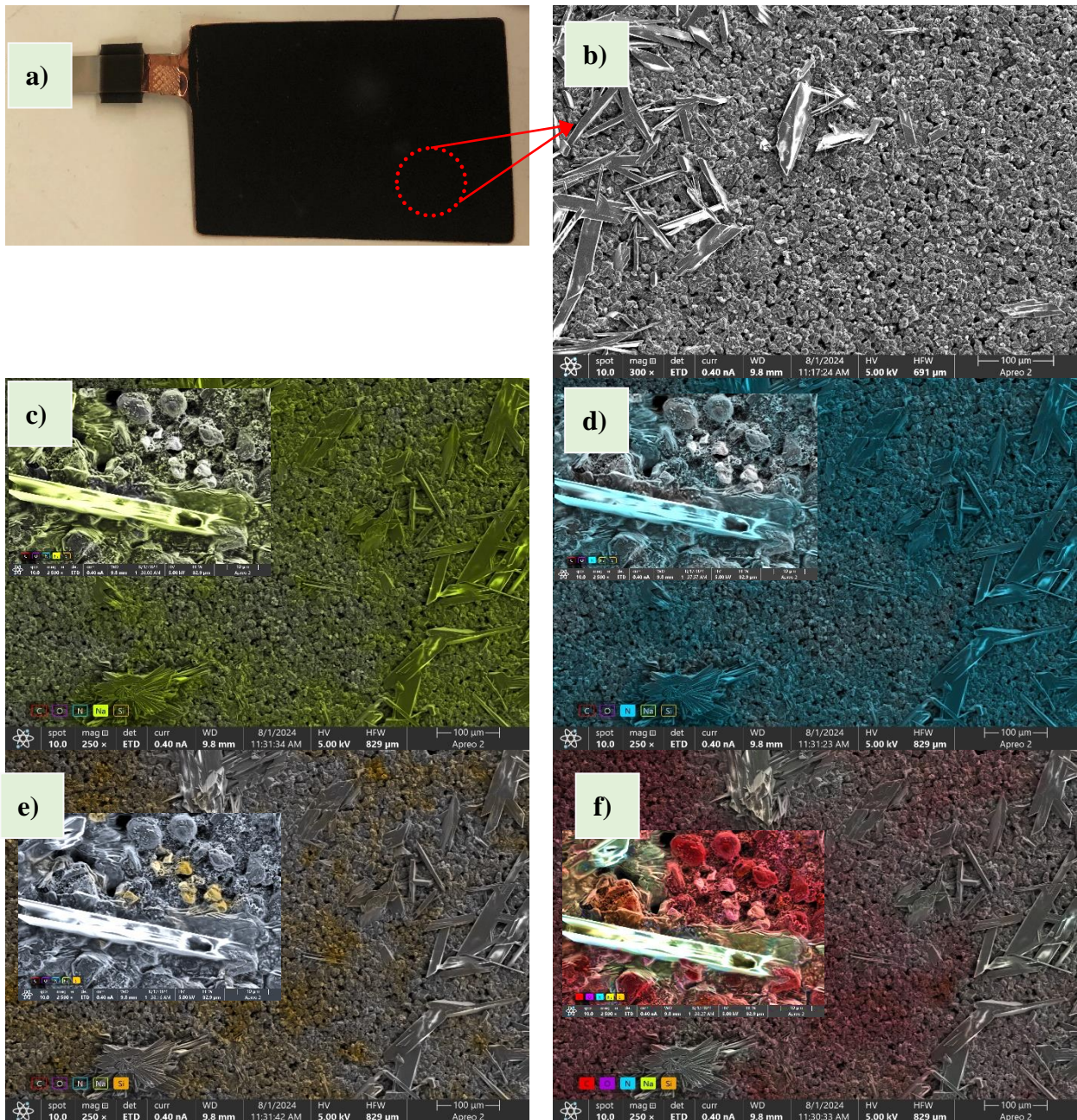
Figure 86. SOX electrode surface morphology before cycling with LFP, two-electrode monolayer pouch cell configuration

As part of the research, the SOX anode was investigated, with its surface analyzed before cycling. Figure 86a shows the surface of an open pouch cell, where the electrode had been soaked in electrolyte for 24 hours prior to opening. The surface reveals small, scattered particles, fewer in number and smaller in size than those observed on the SG electrode before cycling. This difference in particle size and distribution suggests that the interaction between the SOX and the electrolyte is distinct from that of the SG anode, likely due to the differing material properties of the AMs (SOX).

Figure 86b, captured at a magnification of 300× and 5.0 kV, offers a closer view of the SOX surface. The particles on this anode exhibit long, needle-like shapes, contrasting with the more regular crystalline formations seen on SG. This unique morphology indicates a different mechanism of particle formation, likely influenced by the surface chemistry and structure of the SOX.

Figures 86c, 86d, and 86e present the elemental distribution on the surface, focusing on sodium, nitrogen, and silicon, respectively. These images, captured at 250× and 2500× magnification and 5 kV, confirm that sodium and nitrogen are present across the entire surface but are more concentrated in the precipitated particles. The presence of silicon is primarily confined to the base electrode surface. This suggests that the precipitated particles are primarily composed of electrolyte decomposition products interacting with the Na-CMC aqueous binder rather than silicon compounds from the AM.

Additionally, Figure 86f displays the presence of carbon, oxygen, nitrogen, sodium, and silicon on the anode surface. The carbon and silicon (Si:C ratio to 1:9) content are clearly concentrated on the base surface, with minimal presence in the precipitated particles. This reinforces the idea that the particles are primarily composed of sodium-containing compounds, and their smaller size compared to the SG anode may be attributed to the electrolyte volume used and potential impurities from different components.

It is also important to note that the presence of sodium on the surface is expected due to the use of the aqueous binder Na-CMC in the electrode fabrication. However, impurities could have contributed to the formation of the homogeneously distributed, needle-like particles, influencing the overall surface characteristics.

11.14.2. After cycling, the surface of the SOX anode exhibited considerable changes compared to its pre-cycling state and the SG anode.

PC-011, SOX, N/P = 1.21, 75 cycles
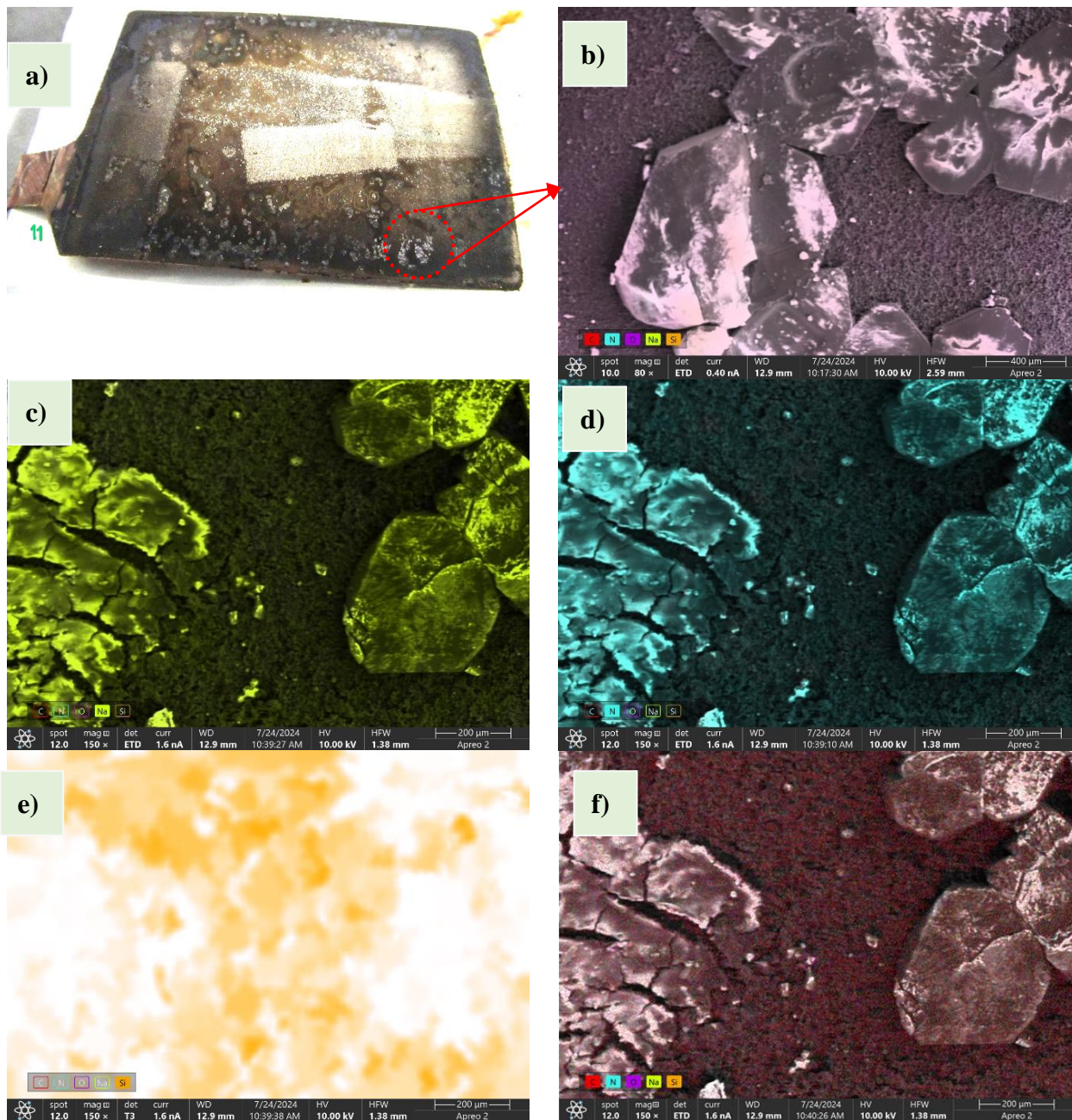
Figure 87. SOX electrode surface morphology post-cycling with LFP, 2-electrode monolayer pouch cell configuration

Figure 87a shows the post-cycling surface of the opened pouch cell, where bright particles are visible. Similar to the SG surface, these bright spots indicate particle formation during cycling.

In addition, part of the surface seems to have exposed the current collector, suggesting that some dissolution and pulverization of the AM may have occurred during the charge/discharge process. This dissolution could be a result of the electrochemical stress experienced by the electrode, leading to partial degradation of the SOX material.

Figure 87b, captured at 80× magnification with 10 kV, shows the absence of cracks on the anode surface after cycling. This crack-free surface implies good mechanical stability of the SOX during cycling, which is crucial for maintaining electrode performance. Interestingly, the analysis revealed two distinct types of precipitated particles: one type, similar to those seen on the SG anode, has a planar surface and large, flaky shapes; the other consists of smaller, clustered particles, as depicted in Figure 87f. The formation of these two types of particles suggests multiple reaction pathways during cycling, potentially due to various interactions between the electrolyte and the SOX and the number of cycling, probably existing more degradation in each cycle.

Figures 87c and 87d further analyze these precipitated particles, confirming that sodium and nitrogen are present in high concentrations in both types of particles. The uniform distribution of these elements across the surface and within the particles highlights the consistency of the deposition process, which is likely driven by electrolyte breakdown during cycling. Figure 87e provides insight into the silicon content on the surface, revealing that silicon is more concentrated in areas free of precipitated particles. This is expected, as the SOX forms the bulk of the electrode material. The lighter areas on the image, where no particles are present, confirm the presence of silicon, further distinguishing the base electrode surface from the precipitates.

Lastly, Figure 87f shows the distribution of carbon, nitrogen, oxygen, sodium, and silicon on the anode surface. Carbon is more prevalent in areas free from precipitates, which is consistent with the SOX's composition (containing Si:C ratio to 1:9). The elemental composition confirms that the particles are primarily sodium- and nitrogen-based, further suggesting that the electrolyte and binder interactions, rather than the AM itself, are responsible for particle formation.

11.14.3. Discussion and implications of sodium particle formation

The presence of sodium in the precipitated particles, both before and after cycling, is likely a result of the interaction between the aqueous binder Na-CMC and the LiPCP-based electrolyte. Nitrogen content in the precipitates also suggests that electrolyte decomposition

plays a role in particle formation. The presence of sodium as an impurity in the AM, particularly in LFP, has a significant impact on the growth and distribution of particles on both the SOX and SG anodes. During cycling, the continuous extraction and insertion of lithium cations appear to drive the precipitation process, leading to the growth of sodium-containing particles.

Furthermore, the applied current during charge and discharge cycles plays a critical role in particle formation. In all cases, the sodium-containing particles were smaller and more widely distributed before cycling, with their size increasing significantly post-cycling. This suggests that the electrochemical stress applied to the electrode accelerates the growth of these particles, likely due to side reactions involving the electrolyte and binder.

Furthermore, despite the use of aqueous-processed electrodes, no evidence of aluminum corrosion was found post-cycling, as detailed in the next section. Similarly, no copper corrosion was observed on the anode surface after cycling. This is a key finding, as both aluminum and copper corrosion can significantly degrade cell performance and stability.

In addition, based on the morphology of the particles and the absence of detectable lithium, it can be concluded that lithium metal dendrites did not form on the surface of the anode during cycling. The absence of lithium dendrites is a positive outcome, as dendrite formation can lead to short circuits and capacity fading in LIBs. This suggests that the electrodes proposed in this research maintained stable cycling behavior without forming hazardous lithium metal deposits.

The formation of sodium-containing particles, driven by the interaction between the aqueous binder and the electrolyte, was consistently observed across various cycling stages. Although the size and morphology of the precipitated particles varied between pre- and post-cycling states, the mechanical integrity of the SOX anode was maintained intact, with no cracks or significant material degradation.

These findings suggest that while some particle formation is inevitable due to the electrolyte interactions, the overall stability of fluorine-free full cells proposed are promising for future applications. Further research is needed to investigate the long-term effects of these precipitated particles on cell performance, particularly their impact on capacity retention and cycling efficiency. The optimization of both anodes and cathodes fabrication in aqueous-based processes is also important to improve the cell performance.

11.14.4. Scanning electron microscope (SEM), surface characterization of separator Celgard 2325 and current collector after cycling pouch cells

This section of the PhD investigation focuses on the post-cycling surface characterization of additional components of the pouch cell, such as the Celgard separator, aluminum and copper current collectors, and Teflon used in the three-electrode pouch cell assembly (see Figure 88). Detailed surface analysis and visual inspection were conducted to evaluate the effects of the cycling process on these materials.

Separator celgard 2325   **PC-006 LFP/SG**
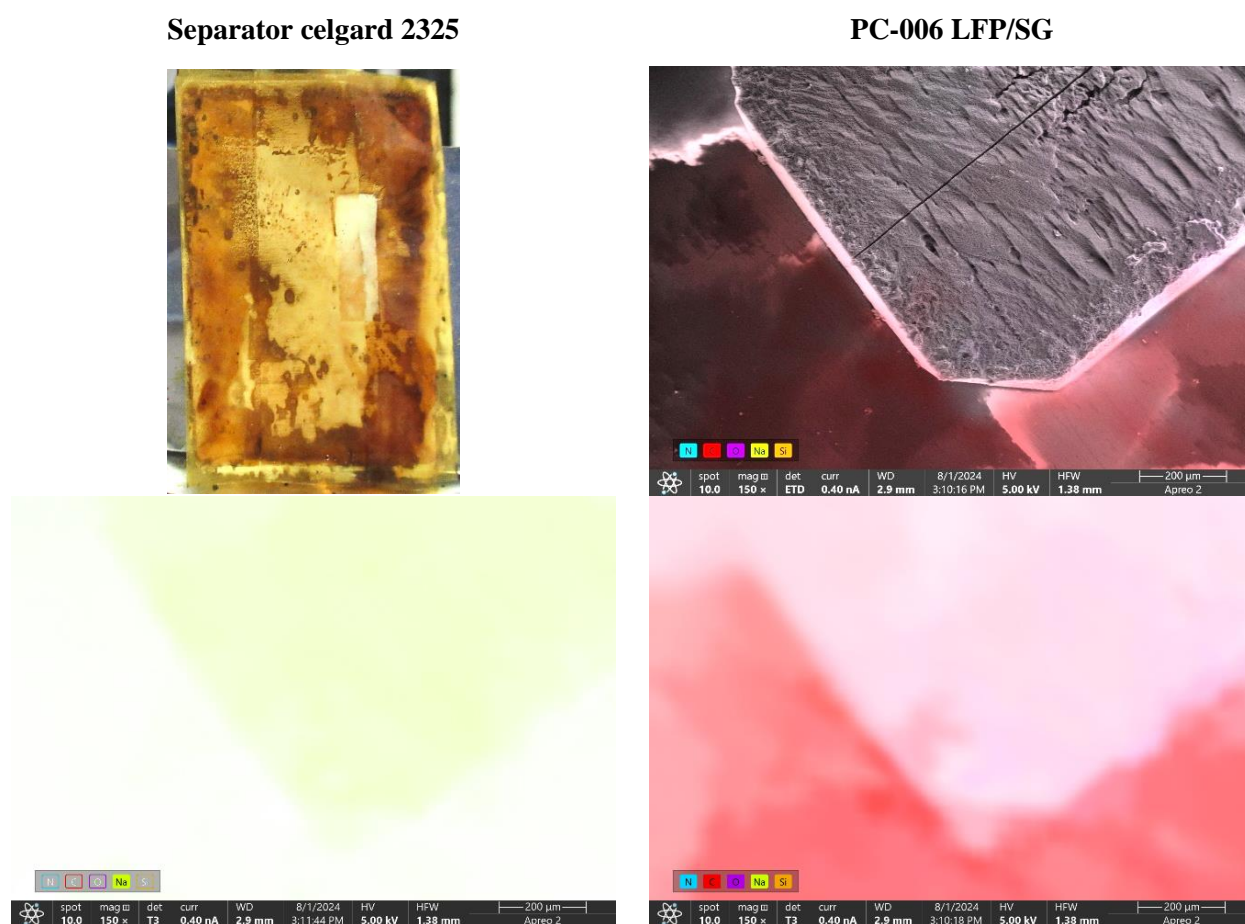
Figure 88. Separator surface post-cycling in the cell LFP/SG two-electrode pouch cell configuration

The Celgard separator, a key component that maintains separation between the anode and cathode while allowing ion transport, was analyzed after cycling in two different pouch cell configurations. Surface changes were noted in the separator, which could provide insights into electrolyte degradation and potential interactions with the AMs.

In Figure 88a, the Celgard separator from a LiPCP-based electrolyte cell with LFP/SG electrodes is shown post-cycling. A notable color change from yellow to brownish was

observed in the separator. Further surface characterization was performed on the separator, with Figure 88b highlighting the distribution of nitrogen, carbon, oxygen, and sodium across its surface at 150× magnification and 5 kV. In Figure 88c, sodium is found in particles on the surface of the separator, while Figure 88d shows an area with a higher concentration of carbon where no particles are present. The presence of carbon on the separator surface could suggest that some carbon from the electrode may have migrated during cycling, contributing to the change in electrolyte color and potentially affecting the cell performance and coulombic efficiency during each cycle. It also should be noted that polypropylene separator consists mostly of carbon, however, the separator itself could not be easily imaged with SEM due to its charging as it is not a conductive material. Based on the separator characteristics and the images obtained by SEM, the presence of carbon on the surface of the separator is at least partially the result of migration from the electrode.

Separator Celgard 2325 **PC-011 LFP/SOX composite**
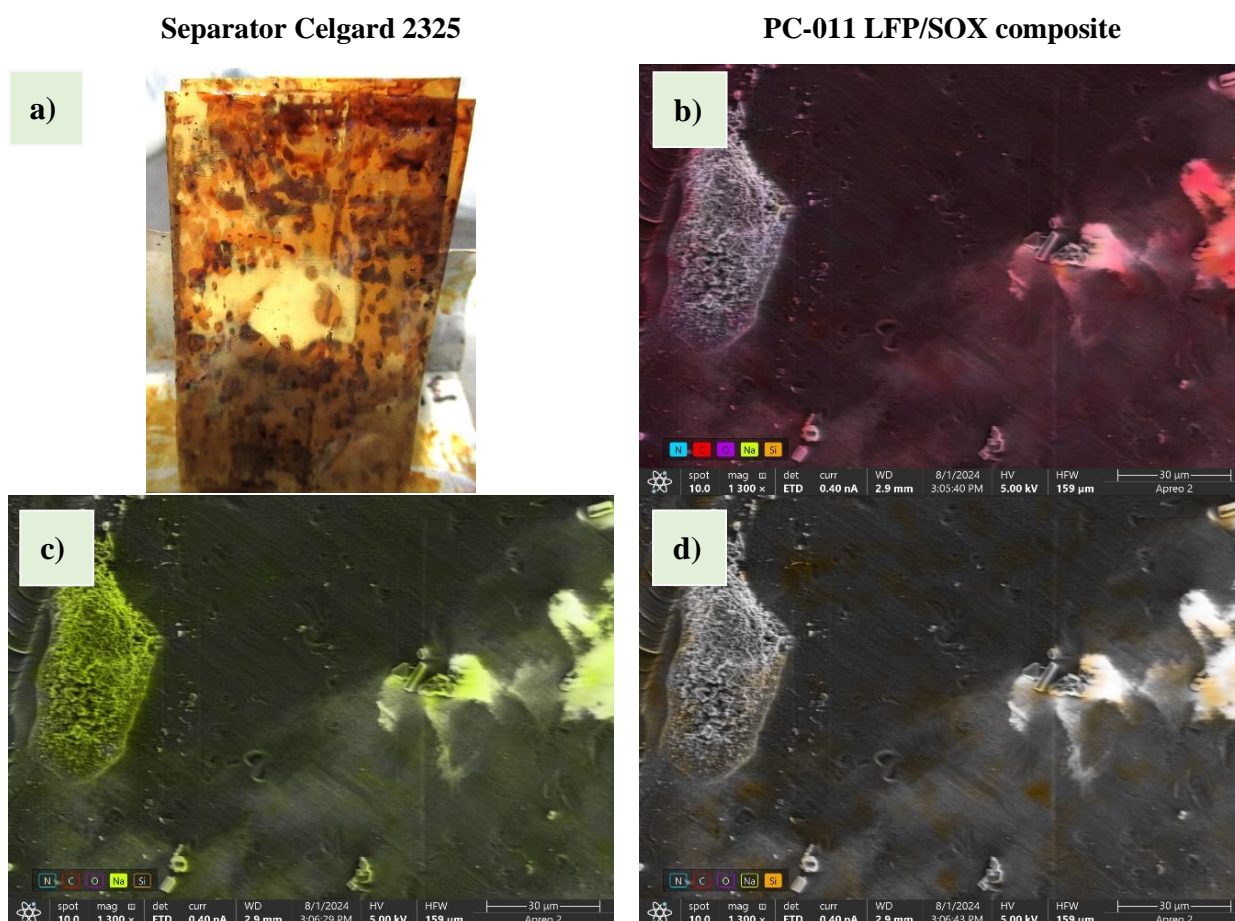
Figure 89. Separator surface post-cycling in the cell LFP/SOX two-electrode pouch cell configuration

In another configuration, the LFP/SOX full cell with a LiPCP electrolyte, similar findings were reported. Figure 89a shows the Celgard separator post-cycling, where the electrolyte color

also darkened. Figures 89b, 89c, and 89d reveal the presence of sodium, silicon, and carbon on the separator surface, respectively. These observations suggest similar degradation or interaction mechanisms across both cell configurations, which could impact the long-term stability of the separator and the cell.

It is important to note that analyzing the separator surface using electron microscopy posed challenges due to the separator's tendency to charge under the electron beam. This charging phenomenon hindered the ability to clearly visualize the surface and its components, making it difficult to perform detailed surface analysis in some areas.

The aluminum and copper current collectors, which serve as conductive substrates for the cathode and anode materials, were also analyzed for signs of corrosion or other surface changes after cycling.

In Figure 90a, the back of the aluminum current collector post-cycling is shown. Typically, when aqueous binders are used, aluminum corrosion is expected due to its reactivity in the presence of water. However, careful pH control during slurry preparation for electrode fabrication ensured that the pH remained within an acceptable range, preventing corrosion. The absence of corrosion after cycling the fluorine-free pouch cell highlights the importance of slurry formulation in maintaining the integrity of aluminum current collectors.

In contrast, the back of the copper current collector, used for anode fabrication, displayed some surface changes, as seen in Figure 90b. A slight color change was observed, which is expected given the cycling process. While copper is generally more resistant to corrosion in aqueous-processed systems, minor surface alterations may occur due to interactions with the electrolyte or the cycling conditions. These changes could influence the long-term conductivity and stability of the anode. The color change of the electrolyte after cycling was a recurring observation. Figure 90c illustrates the darker electrolyte color seen after cycling, consistent with previous findings from the separator analysis. This darkening likely results from electrolyte degradation, contamination, or side reactions occurring during the cycling process, potentially leading to reduced cell efficiency and capacity over time.

Interestingly, as shown in Figure 90d, there was no significant color change in the electrolyte after a 24-hour resting period prior to the start of the cycling process, suggesting that the color change occurs specifically during electrochemical cycling. This figure also shows the placement of the white Teflon used in the three-electrode pouch cell configuration, indicating its role in the assembly.

Aluminium current collector, back
Cathode (Pouch cell) = 37.5x64 = 20.25 cm²

Copper current collector, back
Anode (Pouch cell) = 39x65 = 21.80 cm²

Separator celgard 2325 after cycling

Opening pouch cells, Electrode soaked in electrolyte for 24 hours. (3 electrodes)
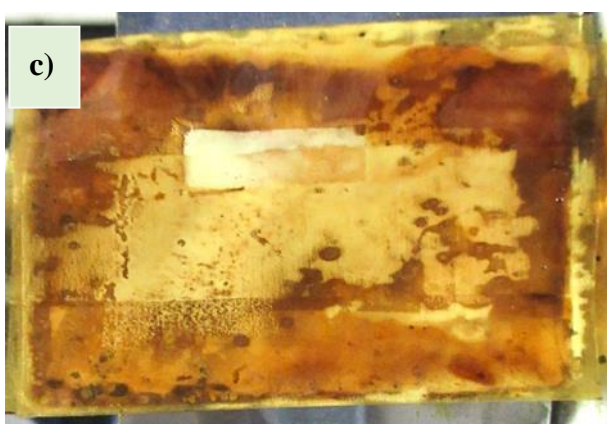
Plates of tetlon for 3 electrodes assembly, after cycling

Plates of teflon, washed after cycling

Figure 90. Aluminium and copper current collectors, Celgard separator after cycling, open three-electrode pouch cell configuration, Teflon used for three-electrode cell configuration post-cycling, and washed Teflon with water

Following cycling, the deposited electrolyte on the Teflon was examined. Figure 90e presents the deposited electrolyte on the Teflon surface post-cycling, revealing the extent of contamination or buildup of byproducts during the process.

After washing the Teflon with water, as shown in Figure 90f, the electrolyte was removed, and the surface returned to its original state. This suggests that while electrolyte residue may accumulate on the Teflon during cycling, it does not permanently affect the material, allowing for potential reuse in subsequent experiments.

In summary, the post-cycling surface characterization of the Celgard separator, current collectors, and Teflon revealed important findings regarding the effects of the cycling process on these components. The color change of the electrolyte and separator suggests electrolyte degradation or contamination during cycling, potentially affecting the cell efficiency and overall performance.

The absence of corrosion on the aluminum current collector, despite the use of aqueous binders, highlights the significance of maintaining appropriate pH levels during slurry preparation. However, minor surface changes on the copper current collector suggest that some interactions with the electrolyte may occur, though they do not appear to significantly impact its performance. Additionally, while the electrolyte residue on the Teflon indicated some contamination post-cycling, it was easily removed through washing, demonstrating that this material remains robust and reusable.

These observations provide insights into how various components of the pouch cell respond to electrochemical cycling and emphasize the need for careful material selection and process control to ensure the longevity and performance of the cell. Further studies could focus on minimizing the observed changes and understanding their implications for long-term cell stability and efficiency.

11.15. Sodium content on the surface of the electrodes, pouch-cells after cycling

The sodium content on the particles and electrode surfaces was quantified after cycling pouch cells. The sodium distribution on LFP, SG, and SOX electrodes is shown in Figures 91, 92, and 93, respectively.

To better understand the sodium and other components content distribution, different regions of the electrode were analyzed. Two main regions were identified based on their surface appearance: the surface of the electrode and the formed particles in the case of LFP and SG electrodes. In the SOX case, three different regions were identified under the same criteria (surface appearance).

	Atomic %		Atomic % Error	
Element	Region 1	Region 2	Region 1	Region 2
Na	14.3	0.0	0.3	-
C	44.1	7.3	0.5	0.3
N	28.6	0.0	1.9	-
O	13.0	58.1	0.8	0.8
Fe	0.0	19.2	-	0.8
P	0.0	15.4	-	0.4
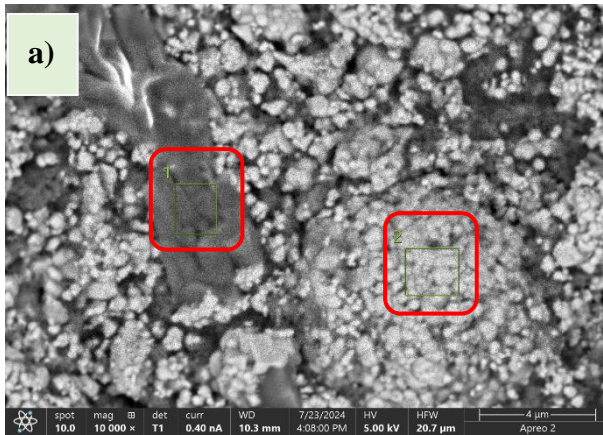
Element	Atomic %	Atomic % Error
C	29.4	0.1
N	7.0	0.1
O	38.1	0.2
Fe	13.6	0.1
Na	3.6	0.0
P	8.3	0.1

Total number of counts: 3 152, total acquisition time: 3 seconds, acceleration voltage: 5 kv

Total number of counts: 3 267 929, total acquisition time: 2274 seconds, acceleration voltage: 5 kv

Figure 91. Surface characterization, sodium content on (a) two specific regions and (b) the average content on the surface of the LFP cathode material, Pouch cell 06.

Figure 91(a) shows two regions, each with distinct surface topographies. Region 1 exhibited high levels of sodium, carbon, nitrogen, and oxygen, with no detectable LFP material. This suggests that region 1 consists of particles (crystals) formed after cycling, where the presence of sodium is significant. The atomic percentage (at.%) of iron (Fe) and phosphorus (P) was 0% in region 1, indicating that the particles fully cover the electrode surface. In contrast, sodium was present at approximately 14 at.% in the particles but was not detected in region 2, which had 0 at.% sodium.

Region 2 of Figure 91(a) features a rough, granulated surface, likely representing undissolved LFP cathode material. These particles are a consequence of incomplete distribution of active, conductive, and additive materials during slurry preparation. This region's topography confirms that the LFP material was not dissolved during the electrode fabrication.

Figure 91(b) provides a broader view of region 1 from Figure 91(a), reinforcing the high sodium, carbon, nitrogen, and oxygen content in the formed particles. The average sodium content across the entire section is about 3.6 at.%. This result highlights the importance of regional characterization: when only the particles were analyzed, sodium content reached

around 14%, but when both particles and the electrode surface are studied together, sodium presence averages are 3%. These results suggest that sodium migrates to the electrode surface during cycling, likely from two sources: impurities in the LFP material and the Na-CMC binder. The fact that the electrode did not delaminate or pulverize further supports the notion that sodium migration occurs when in contact with the electrolyte during cycling. Pointing out that the amount of Na-salts formed are small, representing less than 5% of the electrode surface.

Figure 92 illustrates the elemental composition of various regions on the surface of the graphite electrode after cycling. Both the particles formed, and the electrode surface were analyzed for elemental content, with a particular focus on carbon, nitrogen, oxygen, and sodium distribution, the content is shown in atomic % (at.%).
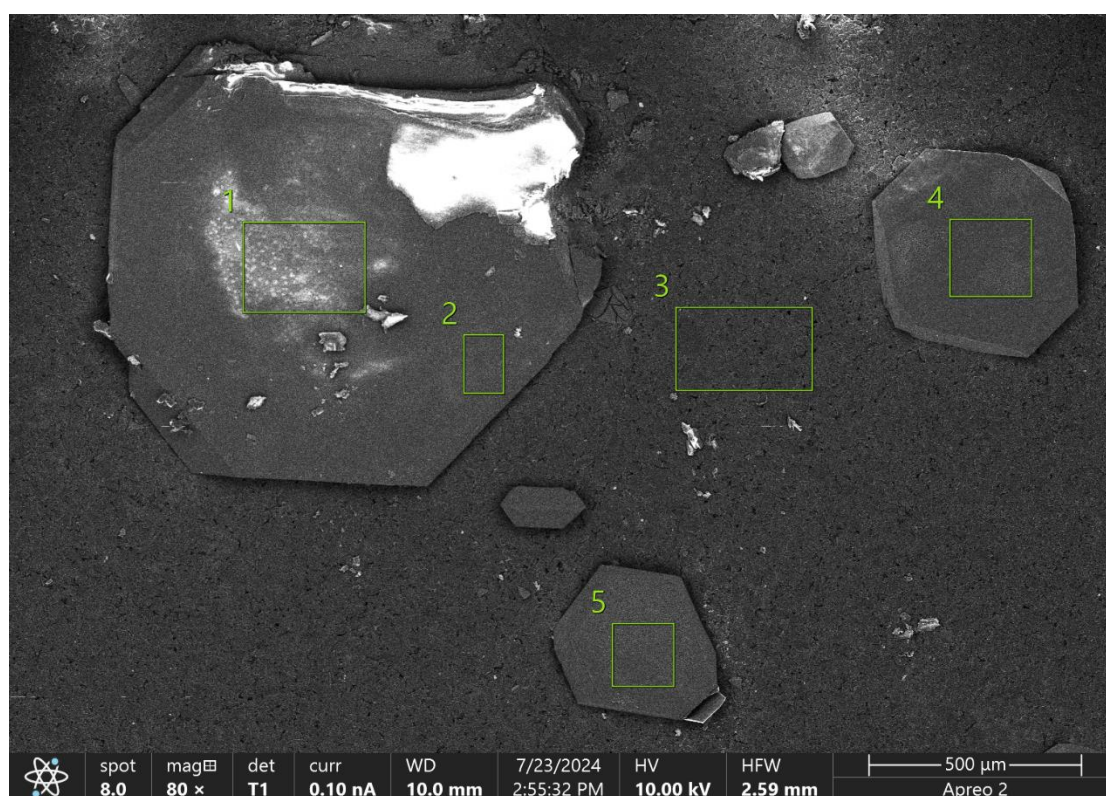
Element	Atomic %				
	Region 1	Region 2	Region 3	Region 4	Region 5
C	37.4	40.2	62.9	37.1	36.6
N	26.9	24.2	15.6	29.2	28.2
O	35.7	25.7	21.0	33.2	26.5
Na	0.0	9.9	0.0	0.0	8.7

Total Number of Counts: 27 384, Total Acquisition Time: 47 seconds
Acceleration Voltage: 10 kV

Figure 92. Surface characterization, sodium and other components content on five specific regions on the surface of the SG anode material, Pouch cell 06.

Sodium was detected at approximately 10 atomic percent (at.%) in regions 2 and 5, as expected from the formed particles. However, in region 4, sodium was not detected (0 at.%), which might be attributed to the short analysis time (less than one minute) across the five regions. A longer analysis duration could have yielded more precise values.

Based on this, the overall sodium content on the surface can be inferred to be slightly below 10 at.%, which aligns with expectations, as more particles formed on the surface of the SG anode compared to the LFP cathode.

The presence of sodium on the graphite anode surface can primarily be attributed to the Na-CMC binder used in the electrode's fabrication. During cycling, especially during the initial charge-discharge cycles, the low potential experienced by the anode lead to electrolyte decomposition and interaction with the electrode surface. This interaction results in the formation of the SEI layer, where sodium-containing salt might have precipitated. The relatively high sodium content on the graphite anode surface compared to the LFP cathode suggests that the low potential environment of the anode, coupled with the cycling process, increases sodium deposition through the formation of these salts.

This phenomenon is likely driven by sodium migration from the Na-CMC binder during SEI formation, where sodium is incorporated into the surface particles. The SEI layer plays a crucial role in protecting the anode from further electrolyte decomposition, and the detection of sodium suggests that it may also influence the composition and structure of the SEI. This is particularly important for the cycling stability and performance of the cell, as sodium in the SEI may affect ionic conductivity and electrochemical behavior over time. Further investigations into the exact mechanisms of sodium incorporation in the SEI layer could provide valuable insights into optimizing binder selection and electrode design and fabrication.

Figure 93 presents the analysis of three distinct regions on the surface of the SOX anode material after cycling: (1) a region with a modified surface topography resulting from pulverization of the silicon oxide (SOX) composite, likely due to mechanical stress during cycling, (2) the electrode surface, and (3) particles formed post-cycling. The active material pulverization alters the surface morphology, distinct from the regions where salts formed. Regions 1 and 3 exhibit salts on the surface, with minimal or no detection of silicon, suggesting significant surface modification in these areas.
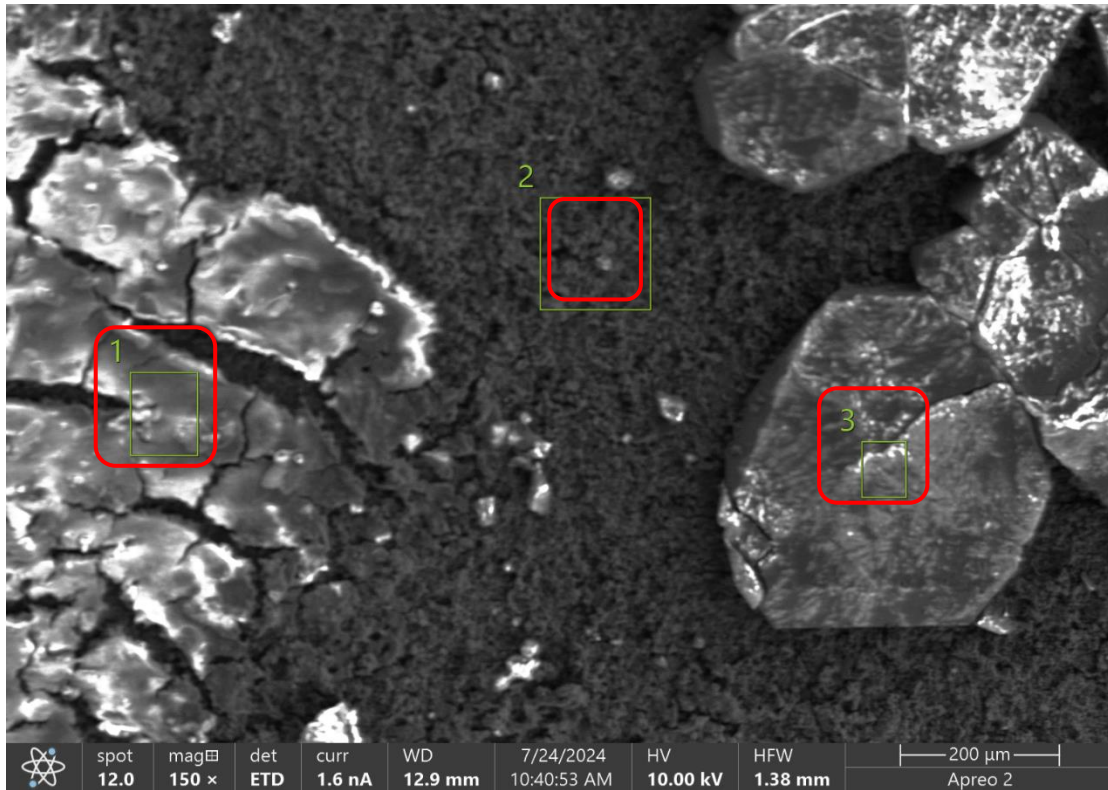
Element	Atomic %		
	Region 1	Region 2	Region 3
C	42.5	47.0	41.3
N	13.6	13.4	23.4
O	35.9	33.0	27.6
Na	7.9	5.8	7.7
Si	0.0	0.8	0.1

Total Number of Counts: 8 910, Total Acquisition Time: 15 seconds
Acceleration Voltage: 10 kV

Figure 93. Surface characterization, sodium and other components content on three specific regions on the surface of the SOX anode material, Pouch cell 11.

Sodium presence is approximately 8 at.% in regions 1 and 3, and slightly lower (below 6 at.%) on the surface of the electrode (Region 2), below 7 at.% in average. This relatively high sodium concentration, particularly in the particle regions, suggests that sodium is involved in the surface chemistry of the SOX anode, similar to what is observed in the SG anode.

The higher sodium content compared to the LFP cathode but similar to the SG anode might be attributed to the electrochemical environment, specifically the low potential experienced during cycling, especially in the early stages.

During the initial cycles, the SEI layer forms as a result of electrolyte decomposition at the SOX anode surface. Sodium, likely originating from the Na-CMC binder, migrates to the surface, incorporating into the SEI layer. Under low potential conditions, where sodium-containing salts precipitate, contributing to the formation of the SEI.

The pulverization of the SOX material introduces an additional layer of complexity. The altered surface topography may lead to increased surface area and defects, promoting more extensive interaction with the electrolyte and enhancing salt formation. This could explain the elevated sodium levels detected compared to LFP cathode. Further research is necessary to fully understand the implications of this pulverization on SOX electrode performance and to optimize electrode fabrication methods. The results indicate that the sodium presence and surface modification in the SOX anode require further investigation to draw definitive conclusions about the role of sodium in the cycling stability and performance of the electrode.

Summarizing the formation of sodium-containing salts on the surface of LFP, SG, and SOX electrodes fabricated with Na-CMC binder and analyzed after cycling, it is evident that sodium migrates to the surface of all three electrode materials during cycling. In the case of the LFP electrode, sodium deposits primarily in the form of surface particles, with an average sodium content around 3.6 at.% on the electrode surface. These particles are likely formed due to the interaction between the Na-CMC binder, LFP impurities, and the electrolyte during cycling, especially during the early stages when the SEI layer is developing. Similarly, in the SG anode, the sodium content is slightly higher, around 10 at.% as average.

For the SOX anode materials, the presence of sodium-containing salts is also significant, with sodium levels reaching up to 8 at.% in particle regions and about 6 at.% on the electrode surface. The pulverization of the SOX material during cycling further modifies the surface topography, contributing to more extensive salt formation and sodium deposition. These results suggest that sodium migration and salt formation are influenced by the nature of the electrode material, the electrochemical environment, and the mechanical stress experienced during cycling. The higher sodium content on the anode surfaces, particularly in SG and SOX electrodes, highlights the role of the Na-CMC binder in contributing to the SEI formation, where sodium salts are incorporated into the surface layer, affecting the cycling performance and stability of the electrodes.

12. CONCLUSIONS

This research aimed to demonstrate the viability and scalability of fluorine-free lithium-ion cells, transitioning from coin to pouch cells.

To achieve this goal, a novel fluorine-free electrolyte was developed, and aqueous-based anodes and cathodes were fabricated, tested for compatibility, optimized, and scaled up. Ionic conductivities were measured for different electrolytes, specifically 0.8 mol·kg^{-1} LiPCP in EC:DMC, EC:EMC, and EC:DMC at (30:70 wt.%), alongside 1 mol·kg^{-1} LiPF$_6$ in similar solvents, across a temperature range of 0 to 50°C.

The highest conductivities for both LiPCP and LiPF$_6$ were achieved with EC:DMC as the solvent. At 20°C, LiPCP in EC:DMC exhibited a conductivity of 9.6 mS·cm^{-1}, while LiPF$_6$ in EC:DMC showed a higher conductivity of 12.3 mS·cm^{-1}, a difference of approximately 28% in favor of the LiPF$_6$ solution. The optimal ionic conductivity for LiPCP was observed at a concentration of 0.8 mol·kg^{-1} in EC:DMC at 20°C. This finding demonstrates the electrolyte potential in specific temperature and concentration conditions.

Following this, the study investigated the compatibility of the fluorine-free electrolyte with aqueous-based electrodes. The cathodes selected were cobalt-free, and the anodes were made from more abundant raw materials. For the cathode, LiFePO$_4$ (LFP) was chosen, while SG and SOX were selected for the anode.

Various slurry formulations were tested for the cathode, with the optimal formulation for LFP being identified as 87:10:3 (LFP:KB:CMC). This was later optimized to 93.5:5:0.75:0.75 (LFP:KB:CMC:SBR) to improve the slurry viscosity, which in turn enhanced the solid content from 33.49% to 41.55%. This improvement significantly affected mass loading, resulting in an areal capacity of approximately 2 mAh·cm^{-2}, which was crucial for the assembly of pouch cells.

The pH of the LFP slurry averaged 8.5, falling within the acceptable range for LFP-based electrode fabrication. Calendering, an optimal compression of 15% was found, resulting in a smooth, crack-free electrode surface. Additionally, based on the electrochemical characterization, with a calendered LFP electrode, the cell exhibited a first-cycle coulombic efficiency of 93.5%, significantly higher than the 82.4% efficiency of an uncalendered electrode.

For the SG electrode, an initial slurry formulation of 95:3:2 (SG:CB:CMC) was found compatible with the LiPCP-based electrolyte. To further optimize the slurry, the formulation was adjusted to 95:2:1:2 (SG:C-45:CMC:SBR), increasing the solid content to 37.3%. The resulting mass loading of approximately 2.3 mAh·cm^{-2} allowed the cell to achieve an N/P ratio between 1.1 and 1.4, aligning with the characteristics of the fluorine-free electrolyte. The calendering process required minimal compression, below 10%, due to the favorable characteristics of the slurry and the electrode after casting, producing a smooth and homogeneous anode. The slurry pH for the SG and SOX electrodes remained between 7.5 and 8, ensuring consistency in the electrode fabrication process.

For the SOX electrode, the initial slurry formulation of 95:3:2 (SiOx/C:CB:CMC) was further refined to 92:6:1:1 (SiOx/C:C-45:CMC:SBR), which increased the solid content from 33.6% to 49.2%. This optimization improved the electrode's mass loading, reaching an average of 2.4 mAh·cm^{-2}, and produced an N/P ratio of approximately 1.20. After casting, the electrode surface was smooth and free of cracks, indicating the effectiveness of the slurry formulation.

The conductivity of all the aqueous-based electrodes was calculated at various thicknesses, revealing that electrode conductivity decreases as thickness increases. Additionally, the density of all the electrodes increased following the calendering process, contributing to improved mechanical stability and performance during cycling.

The cell configuration of LFP/SG was evaluated in both coin and pouch cells. For coin cells, at a C/10 rate and an N/P ratio of 1.18, the specific capacity averaged 60 mAh·g^{-1}, with a coulombic efficiency of around 90%. In pouch cells, under the same C/10 rate but with an N/P ratio of 1.43, the initial specific capacity was 84 mAh·g^{-1}, with a coulombic efficiency of 71%. After 64 cycles, the capacity stabilized around 63 mAh·g^{-1}, with a significantly improved coulombic efficiency of 98.2%.

In contrast, the LFP/SOX configuration demonstrated lower specific capacities. For coin cells at a C/10 rate and an N/P ratio of 1.12, the average specific capacity was 40 mAh·g^{-1}, with an average coulombic efficiency of 90%. Pouch cells at a C/10 rate and an N/P ratio of 1.21 initially delivered a specific capacity of 73 mAh·g^{-1} (coulombic efficiency of 50.3%), but this capacity dropped to 22 mAh·g^{-1} by the 75th cycle, with the coulombic efficiency improving to 95%. These results emphasize the critical impact of the N/P ratio on both the performance and safety of the cells.

In a three-electrode cell configuration, the LFP/SG system exhibited a significant drop in potential below zero, suggesting that the N/P ratio needs further optimization. Additionally, galvanostatic cycling showed that the fluorine-free electrolyte, LiPCP, might reduce at potentials below 2 V. This behavior is seen in both half-cells and full cells (coin and pouch configurations), indicating potential stability issues at lower potential. While the LiPCP electrolyte is more environmentally friendly and reduces the formation of harmful fluorinated species on electrode surfaces, it demonstrates reduced stability at low potentials, leading to undesirable side reactions, such as electrolyte reduction, which likely contributes to capacity fade and performance degradation. As was seen on the electrode surface, the formation of crystals before and after cycling. However, this can be reduced or eliminated with a different electrolyte formulation, considering different solvents, or electrolytes additives.

Summarizing, the electrochemical characterization indicates that fluorine-free lithium-ion cells exhibit promising properties at both laboratory and pre-pilot scale, presenting comparable results. This research represents the first comprehensive study on the viability and scalability of fluorine-free lithium-ion cells, aiming to develop a more sustainable and environmentally friendly battery. Furthermore, the results show the potential for easier recycling at the end of the battery life, offering significant advantages in terms of both sustainability and performance optimization.

13. REFERENCES

1.   N. Nitta, et al., *Li-ion battery materials: present and future.* Materials Today, 2015. 18(5): p. 252-264.

2.   A. Perner, and J. Vetter, *Lithium-ion batteries for hybrid electric vehicles and battery electric vehicles*, in *Advances in Battery Technologies for Electric Vehicles*. 2015. p. 173-190.

3.   J. Warner, *Lithium-Ion and Other Cell Chemistries*, in *The Handbook of Lithium-Ion Battery Pack Design*. 2015. p. 65-89.

4.   J.B. Goodenough and Y. Kim, *Challenges for Rechargeable Li Batteries.* Chemistry of Materials, 2009. 22(3): p. 587-603.

5.   J.B. Goodenough and K.S. Park, *The Li-ion rechargeable battery: a perspective.* J. Am. Chem. Soc., 2013. 135(4): p. 1167-1176.

6.   A. Yoshino, *The birth of the lithium-ion battery.* Chem. Int. Ed., 2012. 51: p. 5798-5800.

7.   J. Xie and Y.C. Lu, *A retrospective on lithium-ion batteries.* Nat. Commun., 2020. 11(1): p. 2499.

8.   Z. Chen, et al., *Toward greener lithium-ion batteries: Aqueous binder-based $LiNi_{0.4}Co_{0.2}Mn_{0.4}O_2$ cathode material with superior electrochemical performance.* J. Power Sources, 2017. 372: p. 180-187.

9.   S. Dühnen, et al., *Toward Green Battery Cells: Perspective on Materials and Technologies.* Small Methods, 2020. 4(7): p. 2000039.

10.   H.-J. Kim, et al., *A Comprehensive Review of Li-Ion Battery Materials and Their Recycling Techniques.* Electronics, 2020. 9(7): p. 1161.

11.   H. Bae and Y. Kim, *Technologies of lithium recycling from waste lithium ion batteries: a review.* Mater. Adv., 2021. 2(10): p. 3234-3250.

12.   H. Zhang, et al., *Fluorine-Free Noble Salt Anion for High-Performance All-Solid-State Lithium–Sulfur Batteries.* Adv. Energy Mater., 2019. 9(25): p. 1900763.

13.   G. Hernandez, et al., *Elimination of Fluorination: The Influence of Fluorine-Free Electrolytes on the Performance of $LiNi_{1/3}Mn_{1/3}Co_{1/3}O_2$/Silicon-Graphite Li-Ion Battery Cells.* ACS Sustain. Chem. Eng., 2020. 8(27): p. 10041-10052.

14.   T. Jin, et al., *Nonflammable, Low-Cost, and Fluorine-Free Solvent for Liquid Electrolyte of Rechargeable Lithium Metal Batteries.* ACS Appl. Mater. Interfaces, 2019. 11(19): p. 17333-17340.

15.   J. Zhao, et al., *Moving to Aqueous Binder: A Valid Approach to Achieving High-Rate Capability and Long-Term Durability for Sodium-Ion Battery.* Adv. Sci. (Weinh), 2018. 5(4): p. 1700768.

16.   P. Jezowski and P.L. Kowalczewski, *Starch as a Green Binder for the Formulation of Conducting Glue in Supercapacitors.* Polymers (Basel), 2019. 11(10): p. 1648.

17.   H.J. Chang, et al., *Effects of water-based binders on electrochemical performance of manganese dioxide cathode in mild aqueous zinc batteries.* Carbon Energy, 2020. 3(3): p. 473-481.

18.   J. Menzel, et al., *Agar-based aqueous electrolytes for electrochemical capacitors with reduced self-discharge.* Electrochim. Acta, 2020. 332: p. 135435.

19.   A. Rensmo, et al., *Lithium-ion battery recycling: a source of per- and polyfluoroalkyl substances (PFAS) to the environment?* Environ. Sci. Process. Impacts, 2023. 25(6): p. 1015-1030.

20.   F. Spyrakis and T.A. Dragani, *The EU's Per- and Polyfluoroalkyl Substances (PFAS) Ban: A Case of Policy over Science.* Toxics, 2023. 11(9): p. 721.

21.   S. Chu, et al., *Advanced cobalt-free cathode materials for sodium-ion batteries.* Chem. Soc. Rev., 2021. 50(23): p. 13189-13235.

22.   K. Chen, et al., *Cobalt-free composite-structured cathodes with lithium-stoichiometry control for sustainable lithium-ion batteries.* Nat. Commun., 2024. 15(1): p. 430.

23.   S. Lee and A. Manthiram, *Can Cobalt Be Eliminated from Lithium-Ion Batteries?* ACS Energy Lett., 2022. 7(9): p. 3058-3063.

24.   L. Qiu, et al., *Enhanced electrochemical properties of $LiFePO_4$ (LFP) cathode using the carboxymethyl cellulose lithium (CMC-Li) as novel binder in lithium-ion battery.* Carbohydr. Polym., 2014. 111: p. 588-591.

25.   A.K. Pahdi, et al., *Phospho-olivines as Positive-Electrode Materials for Rechargeable Lithium Batteries.* J. Electrochem. Soc., 1997. 144: p. 1188-1194.

26.   C. Wang, et al., *Electrochemical performance of modified artificial graphite as anode material for lithium ion batteries.* Ionics, 2012. 19(2): p. 221-226.

27.   B. Moradi and G.G. Botte, *Recycling of graphite anodes for the next generation of lithium ion batteries.* J. Appl. Electrochem., 2015. 46(2): p. 123-148.

28.   S.L. Glazier, et al., *An Analysis of Artificial and Natural Graphite in Lithium Ion Pouch Cells Using Ultra-High Precision Coulometry, Isothermal Microcalorimetry, Gas Evolution, Long Term Cycling and Pressure Measurements.* J. Electrochem. Soc., 2017. 164(14): p. A3545-A3555.

29.   C.-H. Yim, et al., *A high capacity silicon–graphite composite as anode for lithium-ion batteries using low content amorphous silicon and compatible binders.* J. Mater. Chem. A, 2013. 1(28): p. 8234-8243.

30.   N.-S. Choi, et al., *Recent Progress on Polymeric Binders for Silicon Anodes in Lithium-Ion Batteries.* J. Electrochem. Sci. Technol., 2015. 6(2): p. 35-49.

31.   R.E. Ruther, et al., *Chemical Evolution in Silicon-Graphite Composite Anodes Investigated by Vibrational Spectroscopy.* ACS Appl. Mater. Interfaces, 2018. 10(22): p. 18641-18649.

32.   J. Warner, *Lithium-Ion Battery Applications*, in *The Handbook of Lithium-Ion Battery Pack Design.* 2015. p. 177-209.

33. T. Kim, et al., *Lithium-ion batteries: outlook on present, future, and hybridized technologies.* J. Mater. Chem. A, 2019. 7(7): p. 2942-2964.

34. M. Armand, et al., *Lithium-ion batteries – Current state of the art and anticipated developments.* J. Power Sources, 2020. 479: p. 228708.

35. K. Xu, *Electrolytes and interphases in Li-ion batteries and beyond.* Chem. Rev., 2014. 114(23): p. 11503-618.

36. T.R. Jow, et al., *Electrolytes for Lithium and Lithium-Ion Batteries.* Modern Aspects of Electrochemistry 58, ed. 2014, New York, Springer.

37. X. Tian, et al., *"Water-in-Salt" Electrolytes for Supercapacitors: A Review.* ChemSusChem, 2021. 14(12): p. 2501-2515.

38. A. Vij, et al., *Some fluorine-containing nitrogen acids and their derivatives.* Coord. Chem. Rev., 1997. 158: p. 413-432.

39. L. Suo, et al., *Fluorine-donating electrolytes enable highly reversible 5-V-class Li metal batteries.* Proc. Natl. Acad. Sci. USA, 2018. 115(6): p. 1156-1161.

40. W. Wieczorek and J. Płocharski, *Designing Electrolytes for Lithium-Ion and Post-Lithium Batteries.* 2021, Singapur: Jenny Stanford Publishing Pte. Ltd.

41. N. Xu, et al., *Research progress of fluorine-containing electrolyte additives for lithium ion batteries.* J. Power Sources Adv., 2021. 7: p. 100043.

42. X. Liu, et al., *Research progress on preparation and purification of fluorine-containing chemicals in lithium-ion batteries.* Chinese J. Chem. Eng., 2022. 41: p. 73-84.

43. J.-P. Hoffknecht, et al., *Beyond fluorine: sustainable ternary polymer electrolytes for lithium batteries.* Green Chem., 2021. 23(24): p. 9935-9944.

44. O.V. Bushkova, et al., *New lithium salts in electrolytes for lithium-ion batteries (Review).* Russ. J. Electrochem., 2017. 53(7): p. 677-699.

45. A.M. Haregewoin, et al., *Electrolyte additives for lithium ion battery electrodes: progress and perspectives.* Energy Environ. Sci., 2016. 9(6): p. 1955-1988.

46. P. Zhu, et al., *Insights into architecture, design and manufacture of electrodes for lithium-ion batteries.* Mater. Des., 2022. 223: p. 111208.

47. D. Surovtseva, et al., *Toward a life cycle inventory for graphite production.* J. Ind. Ecol., 2022. 26(3): p. 964-979.

48. B.E. Lebrouhi, et al., *Critical materials for electrical energy storage: Li-ion batteries.* J. Energy Storage, 2022. 55: p. 105471.

49. Z. Zhang, et al., *A comparative study of different binders and their effects on electrochemical properties of $LiMn_2O_4$ cathode in lithium ion batteries.* J. Power Sources, 2014. 247: p. 1-8.

50. D. Mazouzi, et al., *Critical roles of binders and formulation at multiscales of silicon-based composite electrodes.* J. Power Sources, 2015. 280: p. 533-549.

51.   P. Jankowski, et al., *SEI-forming electrolyte additives for lithium-ion batteries: development and benchmarking of computational approaches.* J. Mol. Model., 2017. 23(1): p. 6.

52.   M. Wang, et al., *Challenges in Recycling Spent Lithium-Ion Batteries: Spotlight on Polyvinylidene Fluoride Removal.* Glob. Chall., 2023. 7(3): p. 2200237.

53.   S. Simons, et al., *Advanced concepts*, in *Thermal, Mechanical, and Hybrid Chemical Energy Storage Systems*. 2021. p. 569-596.

54.   B. Wang, et al., *Post-Lithium-Ion Battery Era: Recent Advances in Rechargeable Potassium-Ion Batteries.* Chemistry, 2021. 27(2): p. 512-536.

55.   H. Adenusi, et al., *Lithium Batteries and the Solid Electrolyte Interphase (SEI)— Progress and Outlook.* Adv. Energy Mater., 2023. 13(10): p. 2203307.

56.   X. Zhang, et al., *Review on the production of high-purity lithium metal.* J. Mater. Chem. A, 2020. 8(43): p. 22455-22466.

57.   K. Brandt, *Development of secondary lithium batteries.* Solid State Ionics, 1994. 69: p. 173-183.

58.   K. Brandt, *Historical development of secondary lithium batteries.* Solid State Ionics, 1994. 69: p. 173-183.

59.   S.N. Bryntesen, et al., *Opportunities for the State-of-the-Art Production of LIB Electrodes—A Review.* Energies, 2021. 14(5) p. 1406.

60.   J. Zhang, et al., *Progress in electrolytes for beyond-lithium-ion batteries.* J. Mater. Sci. Technol., 2020. 44: p. 237-257.

61.   F. Wu and G. Yushin, *Conversion cathodes for rechargeable lithium and lithium-ion batteries.* Energy Environ. Sci., 2017. 10(2): p. 435-459.

62.   S.A. Khan, et al., *Advanced cathode materials and efficient electrolytes for rechargeable batteries: practical challenges and future perspectives.* J. Mater. Chem. A, 2019. 7(17): p. 10159-10173.

63.   A. Manthiram, *A reflection on lithium-ion battery cathode chemistry.* Nat. Commun., 2020. 11(1): p. 1550.

64.   D. Stampatori, et al., *Li-Ion Batteries: A Review of a Key Technology for Transport Decarbonization.* Energies, 2020. 13(10): p.2638.

65.   D. Aurbach, et al., *Design of electrolyte solutions for Li and Li-ion batteries: a review.* Electrochim. Acta, 2004. 50(2-3): p. 247-254.

66.   S.S. Zhang, et al., *Study of $LiBF_4$ as an electrolyte salt for a Li-ion battery.* J. Electrochem. Soc. 2002, 149(5): p. A586-A590

67.   R. Yazami and A. Martinent, *Fluorinated anions and electrode/electrolyte stability in lithium batteries*, in *Fluorinated Materials for Energy Conversion*, 2005, Elsevier: New York, p. 173-194.

68.   K. Zaghib, et al., *Safe Li-ion polymer batteries for HEV applications.* J. Power Sources, 2004. 134: p. 124-129.

69. C. Arbizzani, et al., *Battery parameters for hybrid electric vehicles*, in *Advances in Battery Technologies for Electric Vehicles*. Woodhead Publising 2015. p. 55-72.

70. L. Niedzicki, et al., *New covalent salts of the 4+V class for Li batteries.* J. Power Sources, 2011. 196(20): p. 8696-8700.

71. P. Burk, et al., *Superacidity of neutral Brönsted acids in gas phase.* J. Comp. Chem., 1996. 17: p. 30-41.

72. G.A. Olah, et al., *Superacids: Acids up to billions of times stronger than sulfuric acid have opened up fascinating new areas of chemistry.* Science, 1979. 206: p. 13-20.

73. I.A. Koppel, et al., *The gas-phase acidities of very strong neutral Brønsted acids.* J. Am. Chem. Soc., 1994. 116: p. 3047-3057.

74. A. Kütt, et al., *Equilibrium acidities of superacids.* J. Org. Chem., 2011. 76: p. 391-395.

75. V. Aravindan, et al., *Lithium-ion conducting electrolyte salts for lithium batteries.* Chem. Eur. J., 2011. 17: p. 14326-14346.

76. Q. Li, et al., *Progress in electrolytes for rechargeable Li-based batteries and beyond.* Green Energy & Environment, 2016. 1(1): p. 18-42.

77. P.G. Bruce, et al., *Conductivity and transference number measurements on polymer electrolytes.* Solid State Ionics, 1988. 28–30: p. 918-922.

78. M.A. Aboudzadeh, et al., *Ionic conductivity and molecular dynamic behavior in supramolecular ionic networks; the effect of lithium salt addition.* Electrochim. Acta, 2015. 175: p. 74-79.

79. J. Tong, et al., *The Effect of Concentration of Lithium Salt on the Structural and Transport Properties of Ionic Liquid-Based Electrolytes.* Front. Chem., 2019. 7: p. 945.

80. A. Méry, et al., *A Critical Review for an Accurate Electrochemical Stability Window Measurement of Solid Polymer and Composite Electrolytes.* Materials (Basel), 2021. 14(14): p. 3840.

81. M. Ströbel, et al., *Investigation of a Novel Ecofriendly Electrolyte-Solvent for Lithium-Ion Batteries with Increased Thermal Stability.* Batteries, 2021. 7(4): p. 72.

82. U.S. Meda, et al., *Solid Electrolyte Interphase (SEI), a boon or a bane for lithium batteries: A review on the recent advances.* J. Energy Storage, 2022. 47: p. 103564.

83. A.V. Plakhotnyk, et al., *Hydrolysis in the system $LiPF_6$—propylene carbonate—dimethyl carbonate—H_2O.* J. Fluor. Chem., 2005. 126: p. 27-31.

84. T. Kawamura, et al., *Decomposition reaction of $LiPF_6$-based electrolytes for lithium ion cells.* J. Power Sources, 2006. 156: p. 547-554.

85. J.B. Goodenough and J. Kim, *Challenges for rechargeable Li batteries.* Chem. Mater., 2010. 22: p. 587-603.

86. H. Yang, et al., *Thermal stability of $LiPF_6$ salt and Li-ion battery electrolytes containing $LiPF_6$.* J. Power Sources, 2006. 161: p. 573-579.

87. M.-H. Ryou, et al., *Effects of lithium salts on thermal stabilities of lithium alkyl carbonates in SEI layer.* Electrochim. Acta, 2012. 83: p. 259-263.

88. H. Yang and X.-D. Shen, *Dynamic TGA–FTIR studies on the thermal stability of lithium/graphite with electrolyte in lithium-ion cell.* J. Power Sources, 2007. 167: p. 515-519.

89. S.F. Lux, et al., *The mechanism of HF formation in LiPF₆ based organic carbonate electrolytes.* Electrochem. Commun., 2012. 14: p. 47-50.

90. S. Steudte, et al., *Hydrolysis study of fluoroorganic and cyano-based ionic liquid anions – consequences for operational safety and environmental stability.* Green Chem., 2012. 14: p. 2474-2483.

91. J. Wu, et al., *Influence of hydrofluoric acid formation on lithium ion insertion in nanostructured V₂O₅.* J. Phys. Chem., 2012. 116: p. 21208-21215.

92. F.W. Dampier, S.B. Brummer, *The cycling behavior of the lithium electrode in LiAsF6/methyl acetate solutions.* Electrochim. Acta, 1977. 22: p. 1339-1345.

93. V.R. Koch, *Reactions of tetrahydrofuran and lithium hexafluoroarsenate with lithium.* J. Electrochem. Soc., 1979. 126: p. 181-187.

94. Statista Research Department *Production of arsenic worldwide from 2010 to 2023.* 2024 [cited 2024 2024]; https://www.statista.com/statistics/797505/arsenic-worldwide-production/].

95. R. Gond, et al., *Non-flammable liquid electrolytes for safe batteries.* Mater. Horiz., 2021. 8(11): p. 2913-2928.

96. X. Zuo, et al., *Lithium tetrafluoroborate as an electrolyte additive to improve the high voltage performance of lithium-ion battery.* J. Electrochem. Soc., 2013. 160: p. A1199-A1204.

97. L. Péter and J. Arai, *Anodic dissolution of aluminium in organic electrolytes containing perfluoroalkylsulfonyl imides.* J. Appl. Electrochem., 1999. 29: p. 1053-1061.

98. M. Ishikawa, et al., *Charge/discharge characteristics of carbon fiber with graphite structure in organic electrolytes containing lithium trifluoromethanesulfate and lithium hexafluorophosphate.* J. Electrochem. Soc., 1994. 141: p. 1105-1108.

99. J. Foropoulos Jr. and D.D. DesMarteau, *Synthesis, properties, and reactions of bis((trifluoromethyl)sulfonyl) imide, (CF₃SO₂)₂NH.* Inorg. Chem., 1984. 23: p. 3720-3723.

100. T. Kawamura, et al., *Decomposition reaction of LiPF₆-based electrolytes for lithium ion cells.* J. Power Sources, 2006. 156(2): p. 547-554.

101. M.H. Fu, et al., *Lithium difluoro(oxalato)borate/ethylene carbonate+propylene carbonate+ethyl(methyl) carbonate electrolyte for LiMn₂O₄ cathode.* J. Power Sources, 2010. 195(3): p. 862-866.

102. X. Xie, et al., *Reductive Decomposition Kinetics and Thermodynamics That Govern the Design of Fluorinated Alkoxyaluminate/Borate Salts for Mg-Ion and Ca-Ion Batteries.* J. Phys. Chem. C, 2022. 126(49): p. 20773-20785.

103. V. Nilsson, et al., *Critical evaluation of the stability of highly concentrated LiTFSI - Acetonitrile electrolytes vs. graphite, lithium metal and LiFePO$_4$ electrodes.* J. Power Sources, 2018. 384: p. 334-341.

104. P. Jankowski, et al., *Designing High-Performant Lithium Battery Electrolytes by Utilizing Two Natures of Li$^+$ Coordination: LiTDI/LiTFSI in Tetraglyme.* Batteries & Supercaps, 2020. 4(1): p. 205-213.

105. M. Kasprzyk, et al., *Non-crystallizing solvent mixtures and lithium electrolytes for low temperatures.* Solid State Ionics, 2017. 308: p. 22-26.

106. L. Li, et al., *Transport and electrochemical properties and spectral features of non-aqueous electrolytes containing LiFSI in linear carbonate solvents.* J. Electrochem. Soc., 2011. 158: p. A74-A82.

107. I.A. Koppel, et al., *Generalized principle of designing neutral superstrong Brønsted acids.* J. Am. Chem. Soc., 2002. 124: p. 5594-5600.

108. M.S. Ding and T.R. Jow, *How conductivities and viscosities of PC-DEC and PC-EC solutions of LiBF$_4$, LiPF$_6$, LiBOB, Et$_4$NBF$_4$, and Et$_4$NPF$_6$ differ and why.* J. Electrochem. Soc., 2004. 151: p. A2007-A2015.

109. H.-B. Han, et al., *Lithium bis(fluorosulfonyl)imide (LiFSI) as conducting salt for nonaqueous liquid electrolytes for lithium-ion batteries: Physicochemical and electrochemical properties.* J. Power Sources, 2011. 196: p. 3623-3632.

110. M. Armand, *Process for the synthesis of sulfonylimidides.* EP0419647B1 1990.

111. M. Armand and P. Johansson, *Novel weakly coordinating heterocyclic anions for use in lithium batteries.* J. Power Sources, 2008. 178(2): p. 821-825.

112. J. Scheers, et al., *Novel Lithium Imides; Effects of -F, -CF$_3$, and -C≡N Substituents on Lithium Battery Salt Stability and Dissociation.* Electrochem., 2012. 80(1): p. 18-25.

113. M. Armand, et al., *Review—Development of Hückel Type Anions: From Molecular Modeling to Industrial Commercialization. A Success Story.* Journal of The Electrochemical Society, 2020. 167(7): p. 070562.

114. H.V. Venkatasetty, *New and novel lithium imide electrolytes and copolymers: Synthesis and characterization for lithium rechargeable batteries*, in *Annual Battery Conference on Applications and Advances.* 2001: 16th Long Beach, CA, United States. p. 277-282.

115. L.J. Krause, et al., *Corrosion of aluminum at high voltages in non-aqueous electrolytes containing perfluoroalkylsulfonyl imides; New lithium salts for lithium-ion cells.* J. Power Sources 1997. 68: p. 320-325.

116. E. Zygadło-Monikowska, et al., *Synthesis and characterization of lithium-salt complexes with difluoroalkoxyborates for application as lithium electrolytes.* Electrochim. Acta, 2015. 175: p. 104-112.

117. G. Hernández, et al., *Polyimide-polyether binders–diminishing the carbon content in lithium sulfur batteries.* Materials Today Energy, 2017. 6: p. 264-270.

118. B. Boz, et al., *Review—Electrolyte and Electrode Designs for Enhanced Ion Transport Properties to Enable High Performance Lithium Batteries.* Journal of The Electrochemical Society, 2021. 168(9): p. 090501.

119. X. Min, et al., *Highly Oxidative-Resistant Cyano-Functionalized Lithium Borate Salt for Enhanced Cycling Performance of Practical Lithium-Ion Batteries.* Angew Chem Int Ed Engl, 2023. 62(34): p. e202302664.

120. R. Marom, et al., *Revisiting $LiClO_4$ as an electrolyte for rechargeable lithium-ion batteries.* J. Electrochem. Soc., 2010. 157: p. A972-A983.

121. G.H. Newman, et al., *Hazard investigations of $LiClO_4$/dioxolane electrolyte.* J. Electrochem. Soc., 1980. 127: p. 2025-2027.

122. H. Yang, et al., *Aluminum corrosion in lithium batteries. An investigation using the electrochemical quartz crystal microbalance.* J. Electrochem. Soc., 2000. 147: p. 4399-4407.

123. C.W. Park and S.M. Oh, *Performances of Li/Li_xCoO_2 cells in $LiAlCl_4·3SO_2$ electrolyte.* J. Power Sources, 1997. 68: p. 338-343.

124. T. Gao, et al., *$LiAlCl_4·3SO_2$: a promising inorganic electrolyte for stable Li metal anode at room and low temperature.* Ionics, 2019. 25(9): p. 4137-4147.

125. C. Chauvin, et al., *Lithium salts based on oligoether sulfate esters.* Electrochim. Acta, 2005. 50: p. 3843-3852.

126. C. Chauvin, et al., *NMR and electrochemical study on lithium oligoether sulfate in polymeric and liquid electrolytes.* ChemPhysChem, 2006. 7: p. 1921-1929.

127. L. Schafzahl, et al., *Long-Chain Li and Na Alkyl Carbonates as Solid Electrolyte Interphase Components: Structure, Ion Transport, and Mechanical Properties.* Chemistry of Materials, 2018. 30(10): p. 3338-3345.

128. J.S. Gnanaraj, et al., *A comparison among $LiPF_6$, $LiPF_3(CF_2CF_3)_3$ (LiFAP), and $LiN(SO_2CF_2CF_3)_2$ (LiBETI) solutions: Electrochemical and thermal studies.* J. Power Sources, 2003. 119–121: p. 799-904.

129. H. Lee, et al., *Comparison of voltammetric responses over the cathodic region in LiPF6 and LiBETI with and without HF.* J. Electrochem. Soc., 2005. 152: p. A1193-A1198.

130. Z. Xiao, et al., *Lithium bis(oxalate)borate additive in the electrolyte to improve Li-rich layered oxide cathode materials.* Materials Chemistry Frontiers, 2020. 4(6): p. 1689-1696.

131. C. Zor, et al., *Guide to Water Free Lithium Bis(oxalate) Borate (LiBOB).* J. Phys. Chem. C, 2021. 125(21): p. 11310-11317.

132. W. Xu and C.A. Angell, *LiBOB and Its Derivatives: Weakly Coordinating Anions, and the Exceptional Conductivity of Their Nonaqueous Solutions.* Electrochem. Solid-State Lett., 2001. 4: p. E1-E4.

133. X. Wang, et al., *Lithium bis(oxalate)borate crosslinked polymer electrolytes for high-performance lithium batteries.* Journal of Energy Chemistry, 2021. 55: p. 228-235.

134. A. Swiderska-Mocek and D. Naparstek, *Physical and electrochemical properties of lithium bis(oxalate)borate—organic mixed electrolytes in Li-ion batteries.* Electrochim. Acta, 2016. 204: p. 69-77.

135. S.S. Zhang and T.R. Jow, *Aluminum corrosion in electrolyte of Li-ion battery.* J. Power Sources, 2002. 109: p. 458-464.

136. C. Li, et al., *Phosphorus-Containing $C_{12}H_{27}O_4P$ as Functional Electrolyte Additives for High-Voltage $LiNi_{0.5}Mn_{1.5}O_4$/Graphite Li-Ion Batteries with Excellent Electrochemical Performance.* Advanced Materials Interfaces, 2020. 8(3): p. 2001588.

137. M. Schmidt, et al., *Lithium fluorophosphates: A new class of conducting salts for electrolytes for high energy lithium-ion batteries.* J. Power Sources, 2001. 97–98: p. 557-560.

138. N. Nanbu, et al., *Lithium Tris[3-fluoro-1,2-benzenediolato(2-)-O,O']phosphate as a Novel Lithium Salt for Lithium Battery Electrolytes.* 2002. 5: p. A202-A205.

139. P.G. Balbuena, *Electrolyte materials - Issues and challenges.* 2014. p. 82-97.

140. L. Niedzicki, et al., *LiTDI and solvent mixture based electrolytes for lithium-ion cells.* Electrochim. Acta, 2015. 174: p. 625-629.

141. S. Paillet, et al., *Power capability of LiTDI-based electrolytes for lithium-ion batteries.* J. Power Sources, 2015. 294: p. 507-515.

142. L. Niedzicki, et al., *Lithium cation conducting TDI anion-based ionic liquids.* Phys Chem Chem Phys, 2014. 16(23): p. 11417-25.

143. S.R. Batten, et al., *Coordination polymers of small cyano anions.* Chimia (Aarau), 2013. 67(6): p. 379-82.

144. H. Yoon, et al., *Lithium electrochemistry and cycling behaviour of ionic liquids using cyano based anions.* Energy Environ. Sci., 2013. 6(3): p. 979-986.

145. A.M. Khil, et al., *Hydrolytic Heterocyclization of the 1,1,2,3,3-Pentacyanopropene Salts.* J. Heterocycl. Chem., 2014. 52(3): p. 688-691.

146. Y. An, et al., *Effects of Position and Quantity of the Cyano Group in Organic Electrode Materials on Electrochemical Performance.* Batteries & Supercaps, 2022. 6(2): p. e202200463.

147. A. Bitner-Michalska, et al., *Fluorine-free electrolytes for all-solid sodium-ion batteries based on percyano-substituted organic salts.* Sci. Rep., 2017. 7: p. 40036.

148. J. Scheers, et al., *All fluorine-free lithium battery electrolytes.* J. Power Sources, 2014. 251: p. 451-458.

149. C. Richardson and C.A. Reed, *Exploration of the pentacyano-cyclo-pentadienide ion, $C_5(CN)_5^-$, as a weakly coordinating anion and potential superacid conjugate base. Silylation and protonation.* Chem. Commun. (Camb), 2004(6): p. 706-707.

150. L. Niedzicki, et al., *Modern generation of polymer electrolytes based on lithium conductive imidazole salts.* J. Power Sources, 2009. 192(2): p. 612-617.

151. F. Ye and R.E. Noftle, *Preparation of fluorinated imides.* J. Fluor. Chem., 1997. 81: p. 193-196.

152. L. Niedzicki, et al., *New type of imidazole based salts designed specifically for lithium ion batteries.* Electrochim. Acta, 2010. 55(4): p. 1450-1454.

153. D.S. Hall, et al., *Exploring Classes of Co-Solvents for Fast-Charging Lithium-Ion Cells.* J. Electrochem. Soc., 2018. 165(10): p. A2365-A2373.

154. V. Garcia-Melgarejo, et al., *Parametrization with Explicit Water of Solvents Used in Lithium-Ion Batteries: Cyclic Carbonates and Linear Ethers.* J. Phys. Chem. B, 2020. 124(23): p. 4741-4750.

155. D. Pritzl, et al., *Analysis of Vinylene Carbonate (VC) as Additive in Graphite/LiNi$_{0.5}$Mn$_{1.5}$O$_4$ Cells.* J. Electrochem. Soc., 2017. 164(12): p. A2625-A2635.

156. Y. Yin and X. Dong, *Electrolyte engineering and material modification for graphite-based lithium-ion batteries operated at low temperature.* Interdisciplinary Materials, 2023. 2(4): p. 569-588.

157. M. Nie, et al., *Effect of Vinylene Carbonate and Fluoroethylene Carbonate on SEI Formation on Graphitic Anodes in Li-Ion Batteries.* J. Electrochem. Soc., 2015. 162(13): p. A7008-A7014.

158. S. Ahn, et al., *Effect of fluoroethylene carbonate and vinylene carbonate additives on full-cell optimization of Li-ion capacitors.* Electrochem. Commun., 2021. 122: p. 106905.

159. J. Khan, et al., *A new approach to study combination mixture organic solvent ethylene carbonate with lithium-ion for alkali-ion battery: A density functional theory.* J. Mater. Res. Technol., 2021. 11: p. 1672-1677.

160. K. Kuboto, et al., *Novel inorganic ionic liquids possessing low melting temperatures and wide electrochemical windows: Binary mixtures of alkali bis(fluorosulfonyl)amides.* Electrochem. Commun., 2008. 10: p. 1886-1888.

161. S. Tsuzuki, et al., *Origin of the low viscosity of [EMIm][(FSO$_2$)$_2$N] ionic liquid and its lithium salt mixture: Experimental and theoretical study of self-diffusion coefficients, conductivities, and intermolecular interactions.* J. Phys. Chem. B 2010. 114: p. 16329-16336.

162. W. Wang and P. Alexandridis, *Composite Polymer Electrolytes: Nanoparticles Affect Structure and Properties.* Polymers (Basel), 2016. 8(11): p. 387.

163. S.S. Zhang, et al., *Designing safer lithium-based batteries with nonflammable electrolytes: A review.* eScience, 2021. 1(2): p. 163-177.

164. X. Feng, et al., *New nonflammable tributyl phosphate based localized high concentration electrolytes for lithium metal batteries.* Sustain. Energy Fuels, 2022. 6(9): p. 2198-2206.

165. H. Niu, et al., *Recent Advances in Application of Ionic Liquids in Electrolyte of Lithium Ion Batteries.* J. Energy Storage, 2021. 40: p.102659.

166. K. Karuppasamy, et al., *Ionic Liquid-Based Electrolytes for Energy Storage Devices: A Brief Review on Their Limits and Applications.* Polymers (Basel), 2020. 12(4) p. 918.

167.   K. Deng, et al., *Nonflammable organic electrolytes for high-safety lithium-ion batteries.* Energy Storage Mater., 2020. 32: p. 425-447.

168.   C.M. Timperley, et al., *Fluorinated phosphorus compounds Part 1. The synthesis and reactions of some fluoroalkyl phosphoryl compounds.* J. Fluor. Chem., 2000. 104: p. 215-223.

169.   T. Satyavani, et al., *Methods of synthesis and performance improvement of lithium iron phosphate for high rate Li-ion batteries: A review.* Eng. Sci. Technol., an International Journal, 2016. 19(1): p. 178-188.

170.   Y. Chen, et al., *A review of lithium-ion battery safety concerns: The issues, strategies, and testing standards.* J. Energy Chem., 2021. 59: p. 83-99.

171.   J.L. Tebbe, et al., *Degradation of Ethylene Carbonate Electrolytes of Lithium Ion Batteries via Ring Opening Activated by LiCoO₂ Cathode Surfaces and Electrolyte Species.* ACS Appl. Mater. Interfaces, 2016. 8(40): p. 26664-26674.

172.   B. Flamme, et al., *Guidelines to design organic electrolytes for lithium-ion batteries: environmental impact, physicochemical and electrochemical properties.* Green Chem., 2017. 19(8): p. 1828-1849.

173.   H. Zhang, et al., *Electrolyte Additives for Lithium Metal Anodes and Rechargeable Lithium Metal Batteries: Progress and Perspectives.* Angew. Chem. Int. Ed. Engl., 2018. 57(46): p. 15002-15027.

174.   H. Haruna, et al., *Accurate Consumption Analysis of Vinylene Carbonate as an Electrolyte Additive in an 18650 Lithium-Ion Battery at the First Charge-Discharge Cycle.* J. Electrochem. Soc., 2016. 164(1): p. A6278-A6280.

175.   O. Borodin, et al., *Oxidative stability and initial decomposition reactions of carbonate, sulfone, and alkyl phosphate-based electrolytes.* J. Phys. Chem., 2013. 117: p. 8661-8682.

176.   D. Zhou, et al., *Polymer Electrolytes for Lithium-Based Batteries: Advances and Prospects.* Chem, 2019. 5(9): p. 2326-2352.

177.   H. Zhao, et al., *Film-forming electrolyte additives for rechargeable lithium-ion batteries: progress and outlook.* J. Mater. Chem. A, 2019. 7(15): p. 8700-8722.

178.   S.S. Zhang, *A review on electrolyte additives for lithium-ion batteries.* J. Power Sources, 2006. 162(2): p. 1379-1394.

179.   M.J. Lain, et al., *Electrolyte Additives in Lithium Ion EV Batteries and the Relationship of the SEI Composition to Cell Resistance and Lifetime.* Electrochem., 2020. 1(2): p. 200-216.

180.   T. van Ree, *Electrolyte additives for improved lithium-ion battery performance and overcharge protection.* Curr. Opin. Electrochem., 2020. 21: p. 22-30.

181.   B. Tong, et al., *Sulfur-containing compounds as electrolyte additives for lithium-ion batteries.* InfoMat, 2021. 3(12): p. 1364-1392.

182.   L. Xia, et al., *Review-recent advances in non-aqueous liquid electrolytes containing fluorinated compounds for high energy density lithium-ion batteries.* Energy Storage Mater., 2021. 38: p. 542-570.

183. V.A. Nguyen and C. Kuss, *Review-Conducting Polymer-Based Binders for Lithium-Ion Batteries and Beyond.* J. Electrochem. Soc., 2020. 167(6): p. 065501.

184. J. Wagner-Henke, et al., *Knowledge-driven design of solid-electrolyte interphases on lithium metal via multiscale modelling.* Nat. Commun., 2023. 14(1): p. 6823.

185. T. Li, et al., *Insight into the Contribution of Nitriles as Electrolyte Additives to the Improved Performances of the $LiCoO_2$ Cathode.* J. Phys. Chem. Lett., 2022. 13(37): p. 8801-8807.

186. K. Duan, et al., *Synergistic Inorganic-Organic Dual-Additive Electrolytes Enable Practical High-Voltage Lithium-Ion Batteries.* ACS Appl. Mater. Interfaces, 2022. 14(8): p. 10447-10456.

187. K. Periyapperuma, et al., *Fluorine-free ionic liquid electrolytes for sustainable neodymium recovery using an electrochemical approach.* Green Chem., 2021. 23(9): p. 3410-3419.

188. P. Kulkarni, et al., *Recent progress in 'water-in-salt' and 'water-in-salt'-hybrid-electrolyte-based high voltage rechargeable batteries.* Sustain. Energy Fuels, 2021. 5(6): p. 1619-1654.

189. L. Suo, et al., *"Water-in-Salt" electrolytes enable green and safe Li-ion batteries for large scale electric energy storage applications.* J. Mater. Chem. A, 2016. 4(17): p. 6639-6644.

190. K. Oldiges, et al., *Understanding transport mechanisms in ionic liquid/carbonate solvent electrolyte blends.* Phys Chem Chem Phys, 2018. 20(24): p. 16579-16591.

191. A.S. Shaplov, et al., *Recent Advances in Innovative Polymer Electrolytes based on Poly(ionic liquid)s.* Electrochim. Acta, 2015. 175: p. 18-34.

192. G.T. Kim, et al., *Development of ionic liquid-based lithium battery prototypes.* J. Power Sources, 2012. 199: p. 239-246.

193. S. Ko, et al., *Electrolyte design for lithium-ion batteries with a cobalt-free cathode and silicon oxide anode.* Nat. Sustain., 2023. 6(12): p. 1705-1714.

194. S. Yuan, et al., *Advanced Electrolyte Design for High-Energy-Density Li-Metal Batteries under Practical Conditions.* Angew. Chem. Int. Ed. Engl., 2021. 60(49): p. 25624-25638.

195. B.E. Murdock, et al., *A Perspective on the Sustainability of Cathode Materials used in Lithium-Ion Batteries.* Adv. Energy Mater., 2021. 11(39) p. 2102028.

196. A. Chakraborty, et al., *Layered Cathode Materials for Lithium-Ion Batteries: Review of Computational Studies on $LiNi_{1-x-y}Co_xMn_yO_2$ and $LiNi_{1-x-y}Co_xAl_yO_2$.* Chem. Mater., 2020. 32(3): p. 915-952.

197. R. Zhang, et al., *Compositionally complex doping for zero-strain zero-cobalt layered cathodes.* Nature, 2022. 610(7930): p. 67-73.

198. J.-H. Kim, et al., *A method of increasing the energy density of layered Ni-rich $Li[Ni_{1-2x}Co_xMn_x]O_2$ cathodes (x = 0.05, 0.1, 0.2).* J. Mater. Chem. A, 2019. 7(6): p. 2694-2701.

199. S. Buechele, et al., *Identification of Redox Shuttle Generated in LFP/Graphite and NMC811/Graphite Cells.* J. Electrochem. Soc., 2023. 170(1) p. 010511.

200. M. Bichon, et al., *Study of Immersion of LiNi$_{0.5}$Mn$_{0.3}$Co$_{0.2}$O$_2$ Material in Water for Aqueous Processing of Positive Electrode for Li-Ion Batteries.* ACS Appl. Mater. Interfaces, 2019. 11(20): p. 18331-18341.

201. O. Touag, et al., *One-pot synthesis of LiAlO2-coated LiNi$_{0.6}$Mn$_{0.2}$Co$_{0.2}$O$_2$ cathode material.* Energy Adv., 2023. 2(5): p. 701-711.

202. P. Laine, et al., *Co-precipitation of Mg-doped Ni$_{0.8}$Co$_{0.1}$Mn$_{0.1}$OH$_2$: effect of magnesium doping and washing on the battery cell performance.* Dalton Trans., 2023. 52(5): p. 1413-1424.

203. F. Schipper, et al., *Review-Recent Advances and Remaining Challenges for Lithium Ion Battery Cathodes.* J. Electrochem. Soc., 2016. 164(1): p. A6220-A6228.

204. S. Ghosh, et al., *A Review on High-Capacity and High-Voltage Cathodes for Next-Generation Lithium-ion Batteries.* Journal of Energy and Power Technology, 2021. 4(1): p. 1-1.

205. A. Hebert and E. McCalla, *The role of metal substitutions in the development of Li batteries, part I: cathodes.* Mater. Adv., 2021. 2(11): p. 3474-3518.

206. N. Bensalah and H. Dawood, *Review on Synthesis, Characterizations, and Electrochemical Properties of Cathode Materials for Lithium Ion Batteries.* J. Mater. Sci. Eng., 2016. 5(4).

207. Y. Han, et al., *Effects of Al doping on the electrochemical performances of LiNi$_{0.83}$Co$_{0.12}$Mn$_{0.05}$O$_2$ prepared by coprecipitation.* Ceram. Int., 2021. 47(9): p. 12104-12110.

208. K. Zhou, et al., *An in-depth understanding of the effect of aluminum doping in high-nickel cathodes for lithium-ion batteries.* Energy Storage Mater., 2021. 34: p. 229-240.

209. Z. Ahaliabadeh, et al., *Extensive comparison of doping and coating strategies for Ni-rich positive electrode materials.* J. Power Sources, 2022. 540.p. 231633

210. F.I. Saaid, et al., *Ni-rich lithium nickel manganese cobalt oxide cathode materials: A review on the synthesis methods and their electrochemical performances.* Heliyon, 2024. 10(1): p. e23968.

211. R. Fan, et al., *Construction of high performance N-doped carbon coated LiMn$_{0.8}$Fe$_{0.2}$PO$_4$ nanocrystal cathode for lithium-ion batteries.* J. Alloys Compd., 2021. 876: p. 160090.

212. G. Yang, et al., *Integrated co-modification of PO$_4^{3-}$ polyanion doping and Li$_2$TiO$_3$ coating for Ni-rich layered LiNi$_{0.6}$Co$_{0.2}$Mn$_{0.2}$O$_2$ cathode material of Lithium-Ion batteries.* Chem. Eng. J., 2021. 421: p. 129964.

213. H.H. Sun, et al., *Transition metal-doped Ni-rich layered cathode materials for durable Li-ion batteries.* Nat. Commun., 2021. 12(1): p. 6552.

214. T. Entwistle, et al., *Co-precipitation synthesis of nickel-rich cathodes for Li-ion batteries.* Energy Rep., 2022. 8: p. 67-73.

215. T. Le Thi, et al., *Modified Coprecipitation Synthesis of Nickel-Rich NMC (Li$_{1.0}$Ni$_{0.6}$Mn$_{0.2}$Co$_{0.2}$O$_2$) for Lithium-Ion Batteries: A Simple, Cost-Effective, Environmentally Friendly Method.* ACS Omega, 2023. 8(48): p. 45414-45427.

216. N. Loeffler, et al., *In Situ Coating of Li[Ni$_{0.33}$Mn$_{0.33}$Co$_{0.33}$]O$_2$ Particles to Enable Aqueous Electrode Processing.* ChemSusChem, 2016. 9(10): p. 1112-1117.

217. Y. Xie, et al., *Li-rich layered oxides: Structure, capacity and voltage fading mechanisms and solving strategies.* Particuology, 2022. 61: p. 1-10.

218. L. Silvestri, et al., *Li-Rich Layered Oxides: Structure and Doping Strategies to Enable Co-Poor/Co-Free Cathodes for Li-Ion Batteries.* Crystals, 2023. 13(2): p. 204.

219. S. Kim, et al., *A stable lithium-rich surface structure for lithium-rich layered cathode materials.* Nat. Commun., 2016. 7(1): p. 128.

220. A. Celeste, et al., *Pushing Stoichiometries of Lithium-Rich Layered Oxides Beyond Their Limits.* ACS Appl. Energy Mater., 2022. 5(2): p. 1905-1913.

221. C. Wang, et al., *Li$_2$ZrO$_3$ coated LiNi$_{1/3}$Co$_{1/3}$Mn$_{1/3}$O$_2$ for high performance cathode material in lithium batteries.* Electrochim. Acta, 2014. 119: p. 236-242.

222. S. Sun, et al., *Li$_2$ZrO$_3$-coated LiNi$_{0.6}$Co$_{0.2}$Mn$_{0.2}$O$_2$ for high-performance cathode material in lithium-ion battery.* Ionics, 2015. 21(7): p. 2091-2100.

223. W.-H. Ryu, et al., *Electrochemical properties of nanosized Li-rich layered oxide as positive electrode materials for Li-Ion batteries.* RSC Adv., 2013. 3(22): p. 8527-8534.

224. Y. Meng, et al., *A phytic acid derived LiMn$_{0.5}$Fe$_{0.5}$PO$_4$/Carbon composite of high energy density for lithium rechargeable batteries.* Sci. Rep., 2019. 9(1): p. 6665.

225. P. Selinis and F. Farmakis, *Review-A Review on the Anode and Cathode Materials for Lithium-Ion Batteries with Improved Subzero Temperature Performance.* J. Electrochem. Soc., 2022. 169(1): p. 010526.

226. H. Zhang, et al., *Recent progress in advanced electrode materials, separators and electrolytes for lithium batteries.* J. Mater. Chem. A, 2018. 6(42): p. 20564-20620.

227. Z. He, et al., *Optimally designed interface of lithium rich layered oxides for lithium ion battery.* J. Alloys Compd., 2017. 708: p. 1038-1045.

228. P. Chandan, et al., *Voltage fade mitigation in the cationic dominant lithium-rich NCM cathode.* Commun. Chem., 2019. 2(1): p. 120.

229. W. Hua, et al., *Structural insights into the formation and voltage degradation of lithium- and manganese-rich layered oxides.* Nat. Commun., 2019. 10(1): p. 5365.

230. T. Liu, et al., *Rational design of mechanically robust Ni-rich cathode materials via concentration gradient strategy.* Nat. Commun., 2021. 12(1): p. 6024.

231. T. Yang, et al., *Ultrahigh-nickel layered cathode with cycling stability for sustainable lithium-ion batteries.* Nat. Sustain., 2024. 7(9): p. 1204-1214.

232. Z. Ye, et al., *Nickel-Rich Layered Cathode Materials for Lithium-Ion Batteries.* Chemistry, 2021. 27(13): p. 4249-4269.

233. J.P. Pender, et al., *Electrode Degradation in Lithium-Ion Batteries.* ACS Nano, 2020. 14(2): p. 1243-1295.

234. H. Wang, et al., *Formation and modification of cathode electrolyte interphase: A mini review.* Electrochem. Commun., 2021. 122: p. 106870.

235. H.J. Song, et al., *Artificial cathode-electrolyte interphases on nickel-rich cathode materials modified by silyl functional group.* J. Power Sources, 2019. 416: p. 1-8.

236. I. Takahashi, et al., *Cathode Electrolyte Interphase Formation and Electrolyte Oxidation Mechanism for Ni-Rich Cathode Materials.* J. Phys. Chem. C, 2020. 124(17): p. 9243-9248.

237. P. Minnmann, et al., *Designing Cathodes and Cathode Active Materials for Solid-State Batteries.* Adv. Energy Mater., 2022. 12(35): p. 2201425.

238. C. Misiewicz, et al., *Formation of a Cathode Electrolyte Interphase on High-Voltage Li-ion Cathodes.* Chem. Mater., 2024. 36(19): p. 9729-9740.

239. S. Wang, et al., *Enabling stable and high-rate cycling of a Ni-rich layered oxide cathode for lithium-ion batteries by modification with an artificial Li$^+$-conducting cathode-electrolyte interphase.* J. Mater. Chem. A, 2021. 9(19): p. 11623-11631.

240. A. Mauger and C.M. Julien, *Olivine Positive Electrodes for Li-Ion Batteries: Status and Perspectives.* Batteries, 2018. 4(3): p. 39.

241. B. Ramasubramanian, et al., *Recent Development in Carbon-LiFePO$_4$ Cathodes for Lithium-Ion Batteries: A Mini Review.* Batteries, 2022. 8(10): p. 133.

242. K. Zaghib, et al., *LiFePO$_4$ safe Li-ion polymer batteries for clean environment.* J. Power Sources 2005. 146: p. 380-385.

243. S.U. Chang, et al., *Preparation and Performances of C-LiFePO$_4$/Polytriphenylamine Composite as Cathode Material for Lithium-Ion Batteries.* Acta Physico-Chimica Sinica, 2014. 30(1): p. 88-94.

244. W. Yu, et al., *Textured LiFePO$_4$ Bulk with Enhanced Electrical Conductivity.* J. Am. Ceram. Soc., 2016. 99(10): p. 3214-3216.

245. M.S.Javed, et al., *Recent Progress in Capacity Enhancement of LiFePO$_4$ Cathode for Li-Ion Batteries.* J. Electrochem. Energy Convers. Storage, 2021. 18(1): p. 010801.

246. W. Duan, et al., *Enhanced charge transport properties of an LFP/C/graphite composite as a cathode material for aqueous rechargeable lithium batteries.* RSC Adv., 2023. 13(36): p. 25327-25333.

247. X.-F. Sun, et al., *Optimizing the Hydrothermal Synthesis of Micro-Sized Olivine LiFePO$_4$.* Acta Physico-Chimica Sinica, 2012. 28(12): p. 2885-2892.

248. K.K. Halankar, et al., *Optimization of lithium content in LiFePO$_4$ for superior electrochemical performance: the role of impurities.* RSC Adv., 2018. 8(2): p. 1140-1147.

249. D. Goonetilleke, et al., *Structural evidence for Mg-doped LiFePO$_4$ electrode polarisation in commercial Li-ion batteries.* J. Power Sources, 2018. 394: p. 1-8.

250. S.-P. Chen, et al., *Review on Defects and Modification Methods of LiFePO₄ Cathode Material for Lithium-Ion Batteries.* Energy & Fuels, 2022. 36(3): p. 1232-1251.

251. H. Erabhoina and M. Thelakkat, *Tuning of composition and morphology of LiFePO₄ cathode for applications in all solid-state lithium metal batteries.* Sci. Rep., 2022. 12(1): p. 5454.

252. Y. Zhu, et al., *Insights on the degradation mechanism for large format prismatic graphite/LiFePO₄ battery cycled under elevated temperature.* J. Energy Storage, 2023. 60: p. 106624.

253. C. Huber and R. Kuhn, *Thermal management of batteries for electric vehicles*, in *Advances in Battery Technologies for Electric Vehicles*. 2015. p. 327-358.

254. F.-Y. Tsai, et al., *Dispersion, agglomeration, and gelation of LiFePO₄ in water-based slurry.* J. Power Sources, 2016. 310: p. 47-53.

255. J. Hu, et al., *Research Progress into the Structure and Performance of LiFePO₄ Cathode Materials.* Acta Physico-Chimica Sinica, 2019. 35(4): p. 361-370.

256. N. Aguilo-Aguayo, et al., *Water-based slurries for high-energy LiFePO₄ batteries using embroidered current collectors.* Sci. Rep., 2020. 10(1): p. 5565.

257. K. Hoang and M. Johannes, *Tailoring Native Defects in LiFePO₄: Insights from First-Principles Calculations.* Chem. Mater., 2011. 23(11): p. 3003-3013.

258. A.V. Kubarkov, et al., *Engendering High Energy Density LiFePO₄ Electrodes with Morphological and Compositional Tuning.* Nanomaterials (Basel), 2023. 13(11): p. 1771.

259. H. Kim, et al., *High-performance electrode materials for lithium-ion batteries for electric vehicles*, in *Advances in Battery Technologies for Electric Vehicles*. 2015. p. 191-241.

260. L. Yang, et al., *Olivine LiMn$_x$Fe$_{1-x}$PO₄ cathode materials for lithium ion batteries: restricted factors of rate performances.* J. Mater. Chem. A, 2021. 9(25): p. 14214-14232.

261. E. Lyle, et al., *Melt Synthesis of Lithium Manganese Iron Phosphate: Part I. Composition, Physical Properties, Structural Analysis, and Charge/Discharge Cycling.* J. Electrochem. Soc., 2022. 169(6): p. 060526.

262. T.-F. Yi, et al., *Improving the cycling stability and rate capability of LiMn$_{0.5}$Fe$_{0.5}$PO₄/C nanorod as cathode materials by LiAlO₂ modification.* J. Mater., 2020. 6(1): p. 33-44.

263. Z. Chen, et al., *Highly efficient synthesis of nano LiMn$_{0.90}$Fe$_{0.10}$PO₄/C composite via mechanochemical activation assisted calcination.* Ceram. Int., 2023. 43: p. 18483-18490.

264. E. Lyle, et al., *Melt Synthesis of Lithium Manganese Iron Phosphate: Part II. Particle Size, Electrochemical Performance, and Solid-State Lithium Diffusion.* J. Electrochem. Soc., 2022. 169(6): p. 060527.

265. H. Shen, et al., *Hierarchical LiMn$_{0.5}$Fe$_{0.5}$PO$_4$/C nanorods with excellent electrochemical performance synthesized by rheological phase method as cathode for lithium ion battery.* Ionics, 2015. 22(2): p. 193-200.

266. M. Bakierska, et al., *Nature of the Electrochemical Properties of Sulphur Substituted LiMn$_2$O$_4$ Spinel Cathode Material Studied by Electrochemical Impedance Spectroscopy.* Materials (Basel), 2016. 9(8): p. 30066.

267. T. Van Le, et al., *Fabrication of Cathode Materials Based on LiMn$_2$O$_4$/CNT and LiNi$_{0.5}$Mn$_{1.5}$O$_4$/CNT Nanocomposites for Lithium – Ion Batteries Application.* Mater. Res., 2015. 18(5): p. 1044-1052.

268. J.B. Goodenough, *Jahn-Teller phenomena solids.* Annu. Rev. Mater. Sci., 1998. 28: p. 1–27.

269. S. Chen, et al., *Surfactant-assisted synthesis of LiMn$_2$O$_4$ particles as high-rate and long-life cathode materials for lithium-ion batteries.* Ionics, 2017. 24(6): p. 1553-1560.

270. U. Pal, et al., *Developing a High-Performing Spinel LiMn$_2$O$_4$ Cathode Material with Unique Morphology, Fast Cycling and Scaled Manufacture.* Batteries & Supercaps, 2024. 7(6): p. e202400072.

271. Y. Hai, et al., *Facile Controlled Synthesis of Spinel LiMn$_2$O$_4$ Porous Microspheres as Cathode Material for Lithium Ion Batteries.* Front. Chem., 2019. 7: p. 437.

272. L. Wen, et al., *Effect of Formation Potentials on Gassing of LiMn$_2$O$_4$//Li$_4$Ti$_5$O$_{12}$/C Batteries.* J. Electrochem. Soc., 2018. 166(3): p. A5033-A5037.

273. C. Xu, et al., *The improved performance of spinel LiMn$_2$O$_4$ cathode with micro-nanostructured sphere-interconnected-tube morphology and surface orientation at extreme conditions for lithium-ion batteries.* Electrochim. Acta, 2020. 358: p. 136901.

274. J. Lee, et al., *The Complex Role of Aluminium Contamination in Nickel-Rich Layered Oxide Cathodes for Lithium-Ion Batteries.* Batteries & Supercaps, 2021. 4(12): p. 1813-1820.

275. L. Azhari, et al., *Underlying limitations behind impedance rise and capacity fade of single crystalline Ni-rich cathodes synthesized via a molten-salt route.* J. Power Sources, 2022. 545: p. 231963.

276. I.A. Moiseev, et al., *Single crystal Ni-rich NMC cathode materials for lithium-ion batteries with ultra-high volumetric energy density.* Energy Adv., 2022. 1(10): p. 677-681.

277. X. Zhu, et al., *High-Voltage Spinel Cathode Materials: Navigating the Structural Evolution for Lithium-Ion Batteries.* Adv. Mater., 2024. 36(30): p. 2403482.

278. L. Hanf, et al., *Investigating the oxidation state of Fe from LiFePO$_4$-based lithium ion battery cathodes via capillary electrophoresis.* Electrophor., 2020. 41(18-19): p. 1549-1556.

279. J. Lu, et al., *High-Performance Anode Materials for Rechargeable Lithium-Ion Batteries.* Electrochem. Energy Rev., 2018. 1(1): p. 35-53.

280. D. Li and H. Zhou, *Two-phase transition of Li-intercalation compounds in Li-ion batteries.* Mater. Today, 2014. 17(9): p. 451-463.

281. J. Collins, et al., *Carbon surface functionalities and SEI formation during Li intercalation.* Carbon, 2015. 92: p. 193-244.

282. C. Mao, et al., *Selecting the Best Graphite for Long-Life, High-Energy Li-Ion Batteries.* J. Electrochem. Soc., 2018. 165(9): p. A1837-A1845.

283. S. Menkin, et al., *Toward an Understanding of SEI Formation and Lithium Plating on Copper in Anode-Free Batteries.* J. Phys. Chem. C Nanomater. Interfaces, 2021. 125(30): p. 16719-16732.

284. H. Wang, et al., *Underpotential lithium plating on graphite anodes caused by temperature heterogeneity.* Proc. Natl. Acad. Sci. USA, 2020. 117(47): p. 29453-29461.

285. L. Zhang, et al., *Parameter Sensitivity Analysis of Cylindrical $LiFePO_4$ Battery Performance Using Multi-Physics Modeling.* J. Electrochem. Soc., 2014. 161(5): p. A762-A776.

286. M. Mancini, et al., *Study of the electrochemical behavior at low temperatures of green anodes for Lithium ion batteries prepared with anatase TiO_2 and water soluble sodium carboxymethyl cellulose binder.* Electrochim. Acta, 2012. 85: p. 566-571.

287. A. Birrozzi, et al., *Scaling up "Nano" $Li_4Ti_5O_{12}$ for High-Power Lithium-Ion Anodes Using Large Scale Flame Spray Pyrolysis.* J. Electrochem. Soc., 2015. 162(12): p. A2331-A2338.

288. L. Zhao, et al., *Revisiting the Roles of Natural Graphite in Ongoing Lithium-Ion Batteries.* Adv Mater, 2022. 34(18): p. e2106704.

289. D.-H. Yoon, et al., *Study of the Binder Influence on Expansion/Contraction Behavior of Silicon Alloy Negative Electrodes for Lithium-Ion Batteries.* J. Electrochem. Soc., 2020. 167(16): p. 160537.

290. M.H. Hossain, et al., *Advances of lithium-ion batteries anode materials-A review.* Chem. Eng. J. Adv., 2023. 16: p. 100569.

291. J. Zhang, et al., *Uniform SiOx/graphene composite materials for lithium ion battery anodes.* J. Alloys Compd., 2019. 809: p. 151798.

292. R. Väli, et al., *Alkali-Metal Insertion Processes on Nanospheric Hard Carbon Electrodes: An Electrochemical Impedance Spectroscopy Study.* J. Electrochem. Soc., 2017. 164(11): p. E3429-E3437.

293. F. Dou, et al., *Silicon/Carbon Composite Anode Materials for Lithium-Ion Batteries.* Electrochem. Energy Rev., 2019. 2(1): p. 149-198.

294. J. Li, et al., *Performance of Amorphous Lithium Phosphate Coated Lithium Titanate Electrodes in Extended Working Range of 0.01-3.00 V.* J. Inorg. Mater., 2021. 36(9): p. 180762.

295. Q. Wang, et al., *Interface chemistry of an amide electrolyte for highly reversible lithium metal batteries.* Nat. Commun., 2020. 11(1): p. 4188.

296.   C. Huang, et al., *Hierarchical porous $Li_4Ti_5O_{12}$–TiO_2 composite anode materials with pseudocapacitive effect for high-rate and low-temperature applications.* J. Mater. Chem. A, 2018. 6(29): p. 14339-14351.

297.   Y.-J. Zhang, et al., *New Research Progress of the Electrochemical Reaction Mechanism, Preparation and Modification for $LiFePO_4$.* Acta Physico-Chimica Sinica, 2017. 33(6): p. 1085-1107.

298.   Y. Wang, et al., *Enhanced Rate Performance of $Li_4Ti_5O_{12}$ Anode for Advanced Lithium Batteries.* J. Electrochem. Soc., 2018. 166(3): p. A5014-A5018.

299.   F. Zou and A. Manthiram, *A Review of the Design of Advanced Binders for High-Performance Batteries.* Adv. Energy Mater., 2020. 10(45): p. 2002508.

300.   K. Siwińska-Stefańska and B. Kurc, *Preparation and application of a titanium dioxide/graphene oxide anode material for lithium–ion batteries.* J. Power Sources, 2015. 299: p. 286-292.

301.   D.V. Carvalho, et al., *Study of Water-Based Lithium Titanate Electrode Processing: The Role of pH and Binder Molecular Structure.* Polymers (Basel), 2016. 8(8): p. 276.

302.   Q. Huang, et al., *Mechanisms of the decrease in low-temperature electrochemical performance of $Li_4Ti_5O_{12}$-based anode materials.* Sci. Rep., 2017. 7(1): p. 15292.

303.   P.U. Nzereogu, et al., *Anode materials for lithium-ion batteries: A review.* Appl. Surf. Sci. Adv., 2022. 9: p. 100233.

304.   H. Cheng, et al., *Recent progress of advanced anode materials of lithium-ion batteries.* J. Energy Chem., 2021. 57: p. 451-468.

305.   T. Yuan, et al., *Recent Advances in Titanium Niobium Oxide Anodes for High-Power Lithium-Ion Batteries.* Energy & Fuels, 2020. 34(11): p. 13321-13334.

306.   B. Scrosati and J. Garche, *Lithium batteries: Status, prospects and future.* J. Power Sources, 2010. 195(9): p. 2419-2430.

307.   W. Tao, et al., *Strategies for improving the storage performance of silicon-based anodes in lithium-ion batteries.* Nano Res., 2019. 12(8): p. 1739-1749.

308.   M.A. Azam, et al., *Recent advances of silicon, carbon composites and tin oxide as new anode materials for lithium-ion battery: A comprehensive review.* J. Energy Storage, 2021. 33: p. 102096.

309.   Y. Yan, et al., *Nano-Sn embedded in expanded graphite as anode for lithium ion batteries with improved low temperature electrochemical performance.* Electrochim. Acta, 2016. 187: p. 186-192.

310.   H. Yamauchi, et al., *Performance of Lithium-Ion Battery with Tin-Phosphate Glass Anode and Its Characteristics.* J. Electrochem. Soc., 2013. 160(10): p. A1725-A1730.

311.   B. Zhao, et al., *Atomic Layer Deposition of SnO_2-Based Composite Anodes for Thin-Film Lithium-Ion Batteries.* Front. Energy Res., 2020. 8: p. 609417.

312.   H. Chen, et al., *A mechanically robust self-healing binder for silicon anode in lithium ion batteries.* Nano Energy, 2021. 81: p. 105654.

313.   M. Salah, et al., *Doped and reactive silicon thin film anodes for lithium ion batteries: A review.* J. Power Sources, 2021. 506: p. 230194.

314.   Y.M. Zhao, et al., *Advances of polymer binders for silicon-based anodes in high energy density lithium-ion batteries.* InfoMat, 2021. 3(5): p. 460-501.

315.   G.F.I. Toki, et al., *Recent progress and challenges in silicon-based anode materials for lithium-ion batteries.* Ind. Chem. Mater., 2024. 2(2): p. 226-269.

316.   P. Haberzettl, et al., *Processing of Aqueous Graphite–Silicon Oxide Slurries and Its Impact on Rheology, Coating Behavior, Microstructure, and Cell Performance.* Batteries, 2023. 9(12): p. 581.

317.   Z. Hu, et al., *High performance germanium-based anode materials.* Coord. Chem. Rev., 2016. 326: p. 34-85.

318.   D. Kwon, et al., *Germanium-based multiphase material as a high-capacity and cycle-stable anode for lithium-ion batteries.* RSC Adv., 2016. 6(92): p. 89176-89180.

319.   H. Choi, et al., *Germanium and Tin Precursors for Chalcogenide Materials Containing N-Alkoxy Thioamide Ligands.* ACS Omega, 2024. 9(26): p. 28707-28714.

320.   Y.-P. Deng, et al., *The Current State of Aqueous Zn-Based Rechargeable Batteries.* ACS Energy Lett., 2020. 5(5): p. 1665-1675.

321.   X. Du, et al., *Core-shell structured ZnS-C nanoparticles with enhanced electrochemical properties for high-performance lithium-ion battery anodes.* Electrochim. Acta, 2017. 225: p. 129-136.

322.   L. He, et al., *Electrochemical characteristics and intercalation mechanism of ZnS/C composite as anode active material for lithium-ion batteries.* Electrochim. Acta, 2011. 56(3): p. 1213-1218.

323.   Z. Gao, et al., *Influencing factors of low- and high-temperature behavior of Co-doped Zn_2SnO_4–graphene–carbon nanocomposite as anode material for lithium-ion batteries.* J. Electroanal. Chem., 2017. 791: p. 56-63.

324.   C. Yuan, et al., *Mixed transition-metal oxides: design, synthesis, and energy-related applications.* Angew. Chem. Int. Ed. Engl., 2014. 53(6): p. 1488-504.

325.   X. Tian, et al., *An Investigation into the Charge-Storage Mechanism of MnO@Graphite as Anode for Lithium-Ion Batteries at Low Temperature.* ChemElectroChem, 2019. 6(8): p. 2248-2253.

326.   Y. Xue, et al., *MnO@N–C/flake graphite composite featuring bottom-top charge transfer channels and superior Li-storage performance at low-temperature.* J. Alloys Compd., 2020. 848: p. 156571.

327.   S. Li, et al., *Self-assembly of 2D sandwich-structured $MnFe_2O_4$/graphene composites for high-performance lithium storage.* Mater. Res. Bull., 2015. 61: p. 369-374.

328. J.G. Han, et al., *Interfacial Architectures Derived by Lithium Difluoro(bisoxalato) Phosphate for Lithium-Rich Cathodes with Superior Cycling Stability and Rate Capability.* ChemElectroChem, 2016. 4(1): p. 56-65.

329. K.-A. Kwon, et al., *α-Fe₂O₃ Submicron Spheres with Hollow and Macroporous Structures as High-Performance Anode Materials for Lithium Ion Batteries.* J. Phys. Chem. C, 2014. 118(6): p. 2897-2907.

330. M. Zou, et al., *Silver-incorporated composites of Fe₂O₃ carbon nanofibers as anodes for high-performance lithium batteries.* J. Power Sources, 2014. 270: p. 468-474.

331. S. Zhu, et al., *Highly uniform Fe₃O₄ nanoparticle–rGO composites as anode materials for high performance lithium-ion batteries.* RSC Adv., 2017. 7(87): p. 54939-54946.

332. Q. Chen, et al., *Fe₃O₄ nanorods in N-doped carbon matrix with pseudo-capacitive behaviors as an excellent anode for subzero lithium-ion batteries.* J. Alloys Compd., 2019. 772: p. 557-564.

333. Y. Teng, et al., *MoS₂ Nanosheets Vertically Grown on Graphene Sheets for Lithium-Ion Battery Anodes.* ACS Nano, 2016. 10(9): p. 8526-35.

334. X. Liu, et al., *A MoS₂/Carbon hybrid anode for high-performance Li-ion batteries at low temperature.* Nano Energy, 2020. 70: p. 104550.

335. R. Hu, et al., *Porous Co3O4 nanofibers surface-modified by reduced graphene oxide as a durable, high-rate anode for lithium ion battery.* Electrochim. Acta, 2017. 228: p. 241-250.

336. L. Tan, et al., *Stable Lithium Storage at Subzero Temperatures for High-capacity Co₃O₄@graphene Composite Anodes.* ChemNanoMat, 2020. 7(1): p. 61-70.

337. M. Lu, et al., *Remarkable High-temperature Performance of Hollow Co 9 S 8 Nanoparticles Integrated with Carbon Materials for Lithium-ion Batteries.* Electrochim. Acta, 2017. 250: p. 196-202.

338. W. Yang, et al., *NiO nanorod array anchored Ni foam as a binder-free anode for high-rate lithium ion batteries.* J. Mater. Chem. A, 2014. 2(47): p. 20022-20029.

339. Z. Bai, et al., *Two-Dimensional NiO@C-N Nanosheets Composite as a Superior Low-Temperature Anode Material for Advanced Lithium-/Sodium-Ion Batteries.* ChemElectroChem, 2020. 7(17): p. 3616-3622.

340. F. Luo, et al., *A review on green and sustainable carbon anodes for lithium ion batteries: utilization of green carbon resources and recycling waste graphite.* Green Chem., 2023. 25(22): p. 8950-8969.

341. H.S. Majdi, et al., *Nano and Battery Anode: A Review.* Nanoscale Res. Lett., 2021. 16(1): p. 177.

342. H. Zhang, et al., *Graphite as anode materials: Fundamental mechanism, recent progress and advances.* Energy Storage Mater., 2021. 36: p. 147-170.

343. T. Insinna, et al., *Graphite Anodes for Li-Ion Batteries: An Electron Paramagnetic Resonance Investigation.* Chem. Mater., 2023. 35(14): p. 5497-5511.

344. S.X.Drakopoulos, et al., *Formulation and manufacturing optimization of lithium-ion graphite-based electrodes via machine learning.* Cell Rep. Phys. Sci., 2021. 2(12): p. 100683.

345. J.U. Hwang, et al., *Characteristics of an artificial graphite anode material for rapid charging: manufactured with different coke particle sizes.* J. Mater. Sci.: Mater. Electron., 2022. 33(25): p. 20095-20105.

346. M. Lu, et al., *A comparison of solid electrolyte interphase (SEI) on the artificial graphite anode of the aged and cycled commercial lithium ion cells.* Electrochim. Acta, 2008. 53(9): p. 3539-3546.

347. J.U. Hwang, et al., *Properties of synthetic graphite from boric acid-added pitch: performance as anode in lithium-ion batteries.* SN Applied Sciences, 2021. 3(6): p. 600.

348. C. Ma, et al., *Synthesis and electrochemical properties of artificial graphite as an anode for high-performance lithium-ion batteries.* Carbon, 2013. 64: p. 553-556.

349. Y.-B. Wang, et al., *Strategies of binder design for high-performance lithium-ion batteries: a mini review.* Rare Met., 2021. 41(3): p. 745-761.

350. M. Liu, et al., *Influence of Binder on Impedance of Lithium Batteries: A Mini-review.* J. Electr. Eng. Technol., 2021. 17(2): p. 1281-1291.

351. S. Li, et al., *A review of rational design and investigation of binders applied in silicon-based anodes for lithium-ion batteries.* J. Power Sources, 2021. 485: p. 229331.

352. W. Huang, et al., *Overcoming the fundamental challenge of PVDF binder use with silicon anodes with a super-molecular nano-layer.* J. Mater. Chem. A, 2021. 9(3): p. 1541-1551.

353. N. Lingappan, et al., *The significance of aqueous binders in lithium-ion batteries.* Renew. Sustain. Energy Rev., 2021. 147: p. 111227.

354. W. Zhu, et al., *Progress of Binder Structures in Silicon-Based Anodes for Advanced Lithium-Ion Batteries: A Mini Review.* Front. Chem., 2021. 9: p. 712225.

355. A. Cholewinski, et al., *Polymer Binders: Characterization and Development toward Aqueous Electrode Fabrication for Sustainability.* Polymers (Basel), 2021. 13(4): p. 631.

356. J. Yoon, et al., *Polymeric Binder Design for Sustainable Lithium-Ion Battery Chemistry.* Polymers (Basel), 2024. 16(2): p. 254.

357. J. Xing, et al., *A Review of Nonaqueous Electrolytes, Binders, and Separators for Lithium-Ion Batteries.* Electrochem. Energy Rev., 2022. 5(4): p. 14.

358. L.-M. Yu, et al., *Water-based binder with easy reuse characteristics for silicon/graphite anodes in lithium-ion batteries.* Polymer J., 2021. 53(8): p. 923-935.

359. M. Ndour, et al., *The formulation of a CMC binder/silicon composite anode for Li-ion batteries: from molecular effects of ball milling on polymer chains to*

consequences on electrochemical performances. Mater. Adv., 2022. 3(23): p. 8522-8533.

360.   K.C. Kil and U. Paik, *Lithium salt of carboxymethyl cellulose as an aqueous binder for thick graphite electrode in lithium ion batteries.* Macromol. Res., 2015. 23(8): p. 719-725.

361.   D. Versaci, et al., *New eco-friendly low-cost binders for Li-ion anodes.* J. Solid State Electrochem., 2017. 21(12): p. 3429-3435.

362.   S. Müllner, et al., *Effect of Water-Soluble CMC/SBR Binder Ratios on Si-rGO Composites Using µm- and nm-Sized Silicon as Anode Materials for Lithium-Ion Batteries.* Batteries, 2023. 9(5): p. 248.

363.   M. Akhlaq, et al., *Carboxymethyl cellulose-based materials as an alternative source for sustainable electrochemical devices: a review.* RSC Adv., 2023. 13(9): p. 5723-5743.

364.   X. Wu, et al., *Effects of functional binders on electrochemical performance of graphite anode in potassium-ion batteries.* Ionics, 2018. 25(6): p. 2563-2574.

365.   J. Park, et al., *How the interaction between styrene-butadiene-rubber (SBR) binder and a secondary fluid affects the rheology, microstructure and adhesive properties of capillary-suspension-type graphite slurries used for Li-ion battery anodes.* Coll. Surf. A: Physicochem. Eng. Asp., 2019. 579: 123692.

366.   C.R. Birkl, et al., *Degradation diagnostics for lithium ion cells.* J. Power Sources, 2017. 341: p. 373-386.

367.   M.M. Kabir and D.E. Demirocak, *Degradation mechanisms in Li-ion batteries: a state-of-the-art review.* Int. J. Energy Res., 2017. 41(14): p. 1963-1986.

368.   X. Han, et al., *A review on the key issues of the lithium ion battery degradation among the whole life cycle.* eTransportation, 2019. 1: p. 100005.

369.   E.R. Fadel, et al., *Role of solvent-anion charge transfer in oxidative degradation of battery electrolytes.* Nat. Commun., 2019. 10(1): p. 3360.

370.   N. Kirkaldy, et al., *Lithium-Ion Battery Degradation: Measuring Rapid Loss of Active Silicon in Silicon-Graphite Composite Electrodes.* ACS Appl. Energy Mater., 2022. 5(11): p. 13367-13376.

371.   R. Sazinas, et al., *Towards understanding of electrolyte degradation in lithium-mediated non-aqueous electrochemical ammonia synthesis with gas chromatography-mass spectrometry.* RSC Adv., 2021. 11(50): p. 31487-31498.

372.   X. Lin, et al., *Lithium Plating Mechanism, Detection, and Mitigation in Lithium-Ion Batteries.* Prog. Energy Combust. Sci., 2021. 87: p. 100953.

373.   J.G. Han, et al., *An Antiaging Electrolyte Additive for High-Energy-Density Lithium-Ion Batteries.* Adv. Energy Mater., 2020. 10(20): p. 2000563.

374.   J.S. Edge, et al., *Lithium ion battery degradation: what you need to know.* Phys Chem Chem Phys, 2021. 23(14): p. 8200-8221.

375.   M.A. Danzer, et al., *Aging of lithium-ion batteries for electric vehicles*, in *Advances in Battery Technologies for Electric Vehicles.* 2015. p. 359-387.

376. C. Lin, et al., *Aging Mechanisms of Electrode Materials in Lithium-Ion Batteries for Electric Vehicles.* J. Chem., 2015. 2015: p. 1-11.

377. M. Woody, et al., *Strategies to limit degradation and maximize Li-ion battery service lifetime - Critical review and guidance for stakeholders.* J. Energy Storage, 2020. 28: p. 101231.

378. R. Sahore, et al., *Towards Understanding of Cracking during Drying of Thick Aqueous-Processed $LiNi_{0.8}Mn_{0.1}Co_{0.1}O_2$ Cathodes.* ACS Sustain. Chem. Eng., 2020. 8(8): p. 3162-3169.

379. F. Leng, et al., *Hierarchical degradation processes in lithium-ion batteries during ageing.* Electrochim. Acta, 2017. 256: p. 52-62.

380. N. Pavlin, et al., *The Role of Cellulose Based Separator in Lithium Sulfur Batteries.* J. Electrochem. Soc., 2018. 166(3): p. A5237-A5243.

381. L. Guo, et al., *Degradation in lithium ion battery current collectors.* J. Phys.: Energy, 2021. 3(3): p. 032015.

382. H. Sonoki, et al., *Effect of Anion Species in Early Stage of SEI Formation Process.* J. Electrochem. Soc., 2019. 166(15): p. A3593-A3598.

383. E. Peled and S. Menkin, *Review—SEI: Past, Present and Future.* J. Electrochem. Soc., 2017. 164(7): p. A1703-A1719.

384. A. Wang, et al., *Review on modeling of the anode solid electrolyte interphase (SEI) for lithium-ion batteries.* Npj Comput. Mater., 2018. 4(1): p. 15.

385. Y. Abe, et al., *Electrochemical Impedance Spectroscopy on the Performance Degradation of LiFePO4/Graphite Lithium-Ion Battery Due to Charge-Discharge Cycling under Different C-Rates.* Energies, 2019. 12(23): p. 4507.

386. X. Yu and A. Manthiram, *Sustainable Battery Materials for Next-Generation Electrical Energy Storage.* Adv. Energy Sustainability Res., 2021. 2(5): p. 2000102.

387. C. Julien, et al., *Lithium Batteries Science and Technology.* 2016, Switzerland: Springer International Publishing.

388. X. Su, et al., *A new strategy to mitigate the initial capacity loss of lithium ion batteries.* J. Power Sources, 2016. 324: p. 150-157.

389. B.F. Song, et al., *Evaluating the capacity ratio and prelithiation strategies for extending cyclability in porous silicon composite anodes and lithium iron phosphate cathodes for high capacity lithium-ion batteries.* J. Energy Storage, 2020. 28: p. 101268.

390. D. Di Lecce, et al., *Lithium-ion batteries for sustainable energy storage: recent advances towards new cell configurations.* Green Chem., 2017. 19(15): p. 3442-3467.

391. C.-S. Kim, et al., *Effects of Capacity Ratios between Anode and Cathode on Electrochemical Properties for Lithium Polymer Batteries.* Electrochim. Acta, 2015. 155: p. 431-436.

392.   P. Štrbac, et al., *Salts of 1,1,2,3,3-pentacyanopropenide carbanion with aromatic cations 28th* in *Croatian-Slovenian Crystallographic Meeting*. 2022: Poreč. p. 1.

393.   W.J. Middleton, et al., *Cyanocarbon Chemistry V. Cyanocarbon Acids and their Salts.* Central Research Department, Experimental Station, E. I. Du Pont de Nemours and Co., 1958. 1(439): p. 12.

394.   R.H. Boy, *Cyanocarbon Chemistry XXIII. The ionization behaviour of cyanocarbon acids.* J. Phys. Chem., 1963. 4: p. 737–744.

395.   L. Niedzicki, et al., *Salts for electrolytes for galvanic cells, especially lithium-ion and sodium-ion salts and the method of their preparation.* PL232856B1 2019: Poland.

396.   M.W. Rupich, et al., *Characterization of Reactions and Products of the Discharge and Forced Overdischarge of Li - SO$_2$ Cells.* J. Electrochem. Soc., 1982. 129: p. 1857-1861.

397.   Y. Yamada, et al., *Unusual stability of acetonitrile-based superconcentrated electrolytes for fast-charging lithium-ion batteries.* J Am Chem Soc, 2014. 136(13): p. 5039-46.

398.   Z. Li, et al., *High Volumetric Energy Density of LiFePO$_4$/KB Cathode Materials Based on Ketjen Black Additive.* ChemElectroChem, 2020. 7(9): p. 2174-2183.

399.   H. Wang, et al., *Effects of oxidized Ketjen Black as conductive additives on electrochemical performance of the LiMn$_2$O$_4$@Al$_2$O$_3$ cathode in lithium-ion batteries.* J. Alloys Compd., 2021. 860: p. 158482.

400.   L. Ouyang, et al., *The effect of solid content on the rheological properties and microstructures of a Li-ion battery cathode slurry.* RSC Adv., 2020. 10(33): p. 19360-19370.

401.   S. Lim, et al., *The effect of binders on the rheological properties and the microstructure formation of lithium-ion battery anode slurries.* J. Power Sources, 2015. 299: p. 221-230.

402.   W. Bauer and D. Nötzel, *Rheological properties and stability of NMP based cathode slurries for lithium ion batteries.* Ceram. Int., 2014. 40(3): p. 4591-4598.

403.   Y. Sheng, et al., *Effect of Calendering on Electrode Wettability in Lithium-Ion Batteries.* Front. Energy Res., 2014. 2: p. 56.

404.   C. Meyer, et al., *Characterization of the calendering process for compaction of electrodes for lithium-ion batteries.* J. Mater. Process. Technol., 2017. 249: p. 172-178.

405.   M. Abdollahifar, et al., *Insights into Influencing Electrode Calendering on the Battery Performance.* Adv. Energy Mater., 2023. 13(40): p. 2300973.

406.   C. Meyer, et al., *Process modeling of the electrode calendering of lithium-ion batteries regarding variation of cathode active materials and mass loadings.* J. Energy Storage, 2018. 18: p. 371-379.

14. APPENDICES

Table A.1. Conductivity of LiPCP at different concentrations

Concentration (mol·Kg⁻¹) LiPCP (3EC/7DMC)	κ/mS·cm⁻¹ (0°C)	κ/mS·cm⁻¹ (10°C)	κ/mS·cm⁻¹ (20°C)	κ/mS·cm⁻¹ (30°C)	κ/mS·cm⁻¹ (40°C)	κ/mS·cm⁻¹ (50°C)
0.1	2.29	2.75	3.20	3.65	4.03	4.47
0.2	3.28	3.96	4.54	5.01	5.75	6.54
0.3	3.43	4.09	4.77	5.54	6.31	7.15
0.4	4.77	5.79	6.80	7.82	8.75	9.76
0.5	4.83	5.63	6.31	7.23	8.37	9.75
0.6	6.19	7.35	8.84	10.06	11.56	12.76
0.7	5.84	7.36	8.58	9.88	11.73	13.54
0.8	6.48	7.99	9.63	11.38	13.41	15.02
0.9	4.80	6.05	7.47	8.81	10.31	12.04
1.0	4.93	6.37	7.97	9.61	11.41	13.29
1.1	3.02	4.42	5.85	7.28	8.67	10.51
1.2	4.43	5.82	7.39	8.82	10.69	12.35

Table A.2. Conductivity of LiPCP and LiPF₆ at different temperatures and carbonate mixture solvents

Electrolyte (mol·Kg⁻¹)	κ/mS·cm⁻¹ (0°C)	κ/mS·cm⁻¹ (10°C)	κ/mS·cm⁻¹ (20°C)	κ/mS·cm⁻¹ (30°C)	κ/mS·cm⁻¹ (40°C)	κ/mS·cm⁻¹ (50°C)
0.8 LiPCP in 3EC:7DMC	6.48	7.99	9.63	11.38	13.41	15.02
0.8 LiPCP in 3EC:7DEC	2.92	3.69	4.48	5.46	6.44	7.38
0.8 LiPCP in 3EC:7EMC	4.39	5.35	6.36	7.57	8.78	10.21
1.0 LiPF₆ in 3EC:7DMC	8.16	10.13	12.30	14.52	16.91	19.58
1.0 LiPF₆ in 3EC:7DEC	3.89	4.95	6.14	7.41	8.87	10.48
1.0 LiPF₆ in 3EC:7EMC	5.45	6.74	7.76	8.83	9.85	11.13

Table A.3. % Difference of LiPCP and LiPF₆ conductivities

%Difference of LiPF₆/LiPCP	T / °C					
	0°C	10°C	20°C	30°C	40°C	50°C
% Diff. EC:DMC	25.95	26.82	27.75	27.60	26.03	30.35
% Diff. EC:DEC	33.45	34.21	37.05	35.87	37.76	41.93
% Diff. EC:EMC	24.07	25.84	21.93	16.63	12.14	9.02
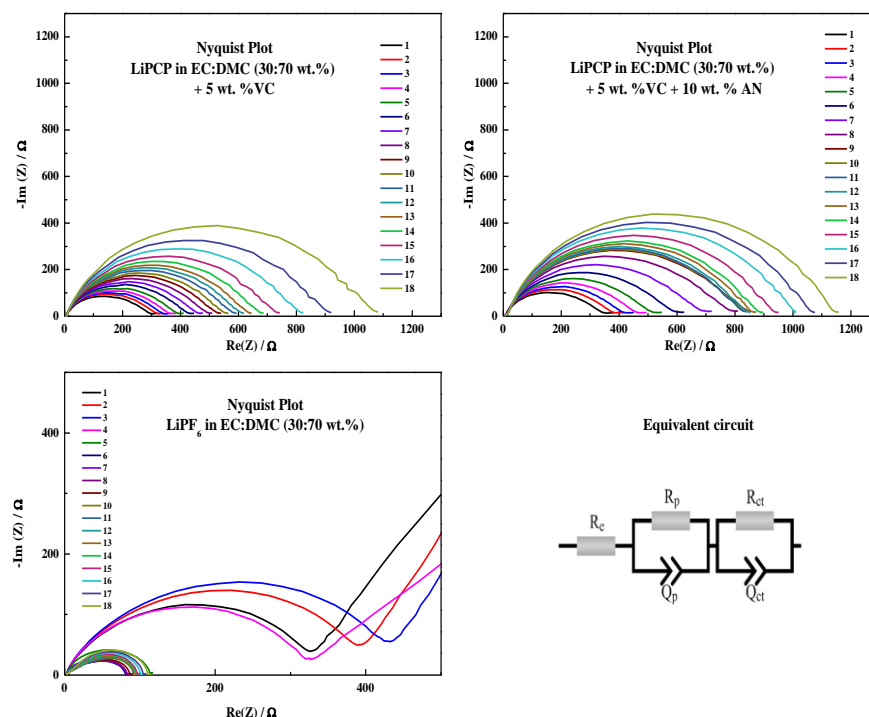
**Figure A.1. a) Nyquist Plots of 0.8 mol·kg⁻¹ LiPCP in EC:DMC (30:70 wt.%) with 5 wt.%
of VC, b) Nyquist Plots of 0.8 mol·kg⁻¹ LiPCP in EC:DMC (30:70 wt.%) with 5 wt.% of VC + 10
wt.% of AN, c) Nyquist Plots of LiPF₆ in ED:DMC (30:70 wt.%), d) Equivalent circuit used for
analysis of impedance spectra**

Resistivities measured in the equipment and the conductivities calculated for each sample
are detailed in Figure 46.

Table A.4. Resistivities measured and conductivities calculated at various LFP slurry
formulations and various electrode sheet thicknesses, LFP S1, S2 and S3.

	LFP S1		LFP S2		LFP S3	
	$1/\kappa$ ($\Omega \cdot$ cm)	κ (mS·cm⁻¹)	$1/\kappa$ ($\Omega \cdot$ cm)	κ (mS·cm⁻¹)	$1/\kappa$ ($\Omega \cdot$ cm)	κ (mS·cm⁻¹)
L1			1.1	869.62	0.910	1099.26
L2	1.9	522.38	1.2	813.32	0.746	1339.67
L3	4.0	251.00	1.4	722.20	0.953	1049.04
L4	4.6	218.20	1.7	598.44	1.325	754.53

Table A.5. Resistivities measured and conductivities calculated at various LFP slurry
formulations and various electrode sheet thicknesses, LFP S4, S5, S6 and S10.

	LFP S4		LFP S5		LFP S6		LFP S10	
	$1/\kappa$ ($\Omega \cdot$ cm)	κ (mS·cm⁻¹)	$1/\kappa$ ($\Omega \cdot$ cm)	κ (mS·cm⁻¹)	$1/\kappa$ ($\Omega \cdot$ cm)	κ (mS·cm⁻¹)	$1/\kappa$ ($\Omega \cdot$ cm)	κ (mS·cm⁻¹)
L1	2.341	427.26	3.797	263.39	3.608	277.19	4.490	222.72
L2	2.096	477.21	4.700	212.77	4.375	228.55	4.273	234.05
L3	2.356	424.54	5.470	182.82	3.950	253.14		

LIST OF FIGURES

LIST OF TABLES

LIST OF APPENDICES